UNIVERSITY OF OKLAHOMA

GRADUATE COLLEGE

VAPOR PHASE UPGRADING OF RENEWABLE CARBOXYLIC ACIDS AND OXYGENATES OVER BRØNSTED ZEOLITES

A DISSERTATION

SUBMITTED TO THE GRADUATE FACULTY

in partial fulfillment of the requirements for the

Degree of

DOCTOR OF PHILOSOPHY

By

ABHISHEK GUMIDYALA
Norman, Oklahoma
2017

VAPOR PHASE UPGRADING OF RENEWABLE CARBOXYLIC ACIDS AND OXYGENATES OVER BRØNSTED ZEOLITES

A DISSERTATION APPROVED FOR THE
SCHOOL OF CHEMICAL, BIOLOGICAL AND MATERIALS ENGINEERING

BY

_____
Dr. Steven P. Crossley, Chair

_____
Dr. Daniel E. Resasco

_____
Dr. Lance L. Lobban

_____
Dr. Bin Wang

_____
Dr. David A. Sabatini

I want to dedicate this work to my mother Padmavathi Gumidyala and my father Subhash Gumidyala as they are the best parents one could ask for.

Acknowledgements

I want to express my sincere gratitude and acknowledge the support, guidance and help provided by the following people.

The unconditional love and support of my mother Padmavathi Gumidyala and father Subhash Gumidyala made me the person I am today. They taught me the morals and values of life and made me understand the importance of education. They held themselves together during some of the difficult times recently and continued to encourage me to achieve my dreams.

My caring elder sister Dr. Preethi Gumidyala is the best human being. I am astonished by the belief she has in my abilities to succeed in life.

My brother-in-law Dr. Rakesh Kacharla has been a pillar of support when I am so far away from home. He took my role as a son to my parents when they needed the most. I want to take this opportunity and thank him for taking care of my family.

My niece Shanvi Kacharla, is a blessing from God to our family. She has brought joy and came as an angel into my life. Her innocent smile and cute gestures kept me going even on the most stressful days.

My loving younger sister Shruthi Kandi is always there for me in one way or the other. My childhood would have been boring without the annoying fights I had with her. I want to thank my brother-in-law Saimani Kandi for his support in this trip.

Manasa Godavarthy, a great friend with whom I have been associated for almost 9 years now. She has seen ups and downs in my life very closely but never wavered from believing in me. I want to thank her for providing the strength I needed in this

journey. I am glad that she pursued Masters at OU during same time as mine as she made the long boring hours in lab fun and joyful.

Dr. Steven Crossley has been an excellent human being and a great advisor. I am very honored and privileged to be his student. I am very grateful to him for believing in me and providing an opportunity to pursue PhD and do research in his group. One of the many qualities that he imparted into me is to critically retrospect one's own results and validate them which has immensely helped me to have some great research findings and yielded several high impact publications.

Dr. Daniel Resasco has been a real role model. Even after achieving such greater heights in the field of catalysis his zeal to work hard has been an inspiration. Interactions with him through several group meetings has helped me grow as researcher. His critical analysis of my work has guided me in the right direction. He has been a strong advocate for me during my stay as a graduate student.

Dr. Lance Lobban is one of the very warm hearted personality I ever met. I want to thank him for being on my committee and for providing me with continuous guidance.

Dr. Bin Wang has been a great collaborator. His theoretical studies and simulations helped me understand my findings in depth. He always made himself available whenever I had any questions and always patiently explained several concepts of DFT.

Dr. David Sabatini for teaching a great class on surfactants right in my first semester of grad school. His class helped me learn and understand on how to

understand concepts in detail. I want to sincerely thank him for agreeing to be on my committee.

Dr. Tawan Sooknoi, Dr. Richard Mallinson and Dr. Rolf Jentoft for providing advice during different phases of this program and help me step forward towards completing my research.

I wanted to thank Chandramouli Vaddepalli for being my advocate when I applied to graduate school at OU. He assisted me to understand the research approach here which gave me a heads-up of things to expect and prepare well to have a smoother transition.

I wanted to specially thank Dr. Taiwo Omotoso and Dr. Tu Pham for helping me start in the lab during my early days. They have been great friends and help outside lab too. They provided me with great advices in research and during my job search process.

I made some special friends in this journey Nikhil Reddy Nandaram, Joel Reddy Kooduru, Divyateja Pamarthi, Ramakrishna Prabhala, Rajiv Reddy Janupala. I want to thank them for the association in creating some beautiful lifetime memories.

I am very grateful to my colleagues and friends at OU biofuel group Dr. Miguel Gonzalez, Dr, Anh To, Dr. Lei Nei, Dr. Christopher Waters, Dr. Dachuan Shi, Dr. Ali Mehdad, Dr. Shaolong Wan, Dr. Priscilla De Souza, Dr. Nick Briggs, Dr. Daniel Santhanaraj, Dr. Wesley Tennyson, Felipe Anaya, Tyler Vann, Adam Stevens, Daniel Dixon, Nhung Duong, Tuong Bui, Valeria Herrera, Santiago Umberilla, Zhao Zheng, Reda Bababrik, Lawrence Barrett, Duong Ngo, Gap Warakunwit, Xiang Wang, Tong Mou, Yen Pham, Diken Jain, Anvit Vartak, Chase Brown, Cristian, Adam Avion,

Galveston Begaye, Monica Chidurala for their cooperation and help in the lab and off the lab.

Terri Colliver, Wanda Gress, Vernita Farrow, Donna King, and Madena McGinnis for helping with all the documentation and financial advices. They always have a warm smile even though we visited them with work.

Alan Miles for providing the knowledge and help for building and fixing equipment in the lab.

I want to specially acknowledge the funding source for my work and the University of Oklahoma for the opportunity to study and perform this research.

Table of Contents

Acknowledgements iv

List of Tables xiv

List of Figures xv

Abstract xxiv

Chapter 1: Introduction 1

Chapter 2: Selective ketonization of acetic acid over HZSM-5: The importance of acyl species and the influence of water 4

Abstract 4

Introduction 5

Experimental 9

Catalyst preparation 9

Catalyst characterization 10

Continuous flow reactions 11

Acetic acid TPRx experiments 12

IR experiments 13

Results and discussion: 14

Reaction mechanism and evidence for stable acyl species 14

Identification of selective ketonization regime under continuous flow 18

Effect of water on catalyst deactivation rates 20

Reaction kinetics and identification of rate-determining step 24

Conclusions: 30

Acknowledgements: 31

Chapter 3: Direct carbon-carbon coupling of furanics with acetic acid over Brønsted zeolites 32
Abstract: 32
Introduction 33
Materials and methods 35
Results and discussion 37
Evidence for direct acylation of furanics and reaction kinetics 37
Evaluating Rate determining step and reaction energies from DFT 43
Conclusion 46
Chapter 4: Kinetics and mechanism of acetic acid ketonization over HZSM-5 49
Introduction 49
Experimental 51
Catalyst preparation. 51
Catalyst characterization. 51
Continuous flow reactions 52
Density functional theory calculations 53
Results and discussion 54
Acetic acid ketonization reaction mechanism and identifying kinetically relevant step 54
Langmuir-Hinshelwood kinetic model and fitting 60
Evaluation of kinetic parameters from theoretical calculations 67
Conclusion 69
Chapter 5: Acylation of oxygenates with acetic acid over Brønsted zeolites 70

Introduction 70
Materials and methods 71
Results and discussion 72
m-cresol acylation with acetic acid 73
Toluene acylation with acetic acid 76
Furan acylation with acetic acid 79
Conclusion 81
Chapter 6: Effect of water on cracking reaction 83
Introduction 83
Experimental and Theoretical Methods 86
Catalytic materials 86
Vapor and Liquid phase reactions 88
Results and discussion 88
Ab-initio molecular dynamics (AIMD) simulations 93
Conclusions 95
Chapter 7: Synthesis of ZSM-5 Nanoparticles Encapsulated within an Ultrathin Silicalite-1 Coating of Tunable Thickness 96
Abstract 96
Introduction 97
Experimental Section 100
Materials 100
Synthesis of ZSM-5 Seeds 100
Synthesis of ZSM-5@silicalite-1 101

Preparation of H-Zeolites 102
Materials Characterization 103
Material Testing in a Fixed Bed Reactor 105
Results and discussion 107
Preparation of ZSM-5@silicalite-1 107
Validation of the Silicalite-1 Shell Structure 112
Tailoring the Silicalite-1 Shell Thickness. 117
Conclusions 123
Acknowledgment 124
Chapter 8 :- Mechanism of Ketonization of Carboxylic acids over ZSM 5 – role of Alpha Hydrogen 126
Introduction 126
Experimental Methods 128
Catalyst preparation 128
Catalyst characterization 128
Flow experiments 129
Temperature programmed reactions 130
Results and Discussion 131
Characterization results 131
Flow reaction results 131
Conclusions: 139
Chapter 9: Synthesis of thin layers of ZSM-5 over carbon nanotubes for improved selectivities 141

Introduction 141
Experimental Details 143
VMWNTs Synthesis 143
Zeolite Synthesis: 143
Nitrogen Adsorption for Surface Area Measurements 144
IPA-TPD 144
X-Ray Diffraction 145
Reaction Studies 145
Electron Microscopy 146
Results and Discussion 146
Catalyst 146
Reactions 151
Modification of the Zeolite Catalyst 153
Conclusion 155
Chapter 10: The Role of Diffusion Path on the Catalytic Upgrading of Biomass Pyrolysis Vapors over ZSM-5 156
Introduction 156
Results and Discussion 158
Catalyst Characterization 158
Catalyst Activity 163
Role of Extra-Framework Alumina 165
Effect of Acid Washing and Mesopores 166
Deactivation 171

Conclusions 171
Experimental Section..... 172
Catalyst Synthesis..... 172
Mesopore Creation 173
Acid Washing 173
Catalyst characterization 174
Pyrolysis GCMS-FID 175
Pyroprobe conditions..... 176
Acknowledgements 177
References 178
Appendix-A : Supporting information for chapter-2..... 194
Appendix-B :- Supporting information for chapter-3 206
Appendix-C :- Supporting information for chapter-7 219

List of Tables

Table 1 :- Adsorption enthalpy and entropy of acetic acid, acetone, water and CO_2 calculated from Van't Hoff's plot 64

Table 2 :- Activation enthalpy, entropy and free energy for the carbon-carbon coupling step in acetic acid ketonization reaction over CBV8014..... 66

Table 3 :- Rate enhancement for cumene cracking at 0 time on stream..... 90

Table 4 :- Si/Al ratios and Shell thickness δ for HZSM-5 (core) and HZSM-5@Silicalite-1 (core-shell) 114

Table 5 :- Nitrogen adsorption results for mesopore series..... 161

Table 6 :- Measured Brønsted sites and calculated Si/Al ratio for mesopore series[a] ... 163

Table 7 :- Hydrothermally synthesized samples 173

List of Figures

Figure 1 :- Acetic acid IR on CBV8014 shows the regeneration of Brønsted acid sites. 15

Figure 2 :- Acetic acid TPD on CBV8014 showing an initial dehydration step involved in the reaction pathway followed the decomposition of the intermediate to acetone and CO_2. 16

Figure 3 :- Acetic acid IR on CBV8014 after adsorption of acetic acid at 50°C and subsequent heating to 150°C. The IR spectra are offset for clarity. 17

Figure 4 :- Proposed mechanism for acetic acid ketonization on CBV8014 18

Figure 5 :- Flow reaction studies of acetic acid on CBV8014 at 300°C showing very high selectivity to acetone and CO_2. The flowrate of acetic acid is maintained at 0.0000728 mol/min with a catalyst weight of 120mg. 19

Figure 6 :- Flow reaction studies of acetic acid on CBV8014 showing yields of acetone and carbon balance as a function of temperature. The acetic acid partial pressure was maintained at 10.67 Torr. Rates at each temperature were taken at 30 min TOS. 20

Figure 7 :- Acetic acid flow reactions at 300°C and 320°C showing a sudden drop in conversion when water was introduced. Catalyst weight 0.025g and 0.014g were used for reaction at 300°C and 320°C respectively to match the initial rates, with an acetic acid flow of $7.28 * 10^{-5}$ mol/min at a partial pressure acetic acid of 10.8 Torr. Water was introduced at a 1:1 molar ratio. 23

Figure 8 :- Order of reaction rate with respect to water as measured at varying TOS values. Conditions are vs. water concentration over CBV8014 at 300°C, 0.025 g catalyst, with initial rates extrapolated to 0 min TOS. Conditions are identical to those

in Figure 11. Eror bars represent ±1 standard error value of the reaction order coefficient. 23
Figure 9 :- Dependence of acetic acid reaction rate over carrier gas flow rate at constant W/F=0.095 h and reactant concentration over CBV8014 at 310°C and 30min TOS..... 25
Figure 10 :- Rate of acetic acid conversion as a function of the density of Brønsted acid sites at a constant W/F=0.095 h over CBV8014 at 300°C and 30min TOS. The concentration of Brønsted acid sites were varied via Na exchange of CBV8014. 25
Figure 11:- Natural logarithm of the rate of reaction vs. acetic acid concentration over CBV8014 at 300°C, 0.025 g catalyst, with rates extrapolated to 0 min TOS. 26
Figure 12 :- Natural logarithm of the rate of reaction vs. water concentration over CBV8014 at 300°C, 0.025 g catalyst, with initial rates extrapolated to 0 min TOS. Acetic acid partial pressure is maintained at 10.8 Torr. 28
Figure 13 :- TOF values for acetic acid, and it's deuterated counterparts in the OD position (D1) and fully deuterated (D4). Reaction conditions are described in section 2.3. 30
Figure 14 :- Direct acylation of methylfuran with acetic acid over HZSM-5. (A), Schematic of 2-methyl furan acylation with acetic acid over HZSM-5. (B), TPD experiment over HZSM-5 showing 5-acetyl 2-methyl furan desorbing with 2-methyl furan pulses from catalyst bed saturated with surface acyl species at 220 °C. 39
Figure 15 :- Reaction kinetics of methylfuran acylation with acetic acid over HZSM-5. Natural logarithm of acylation reaction rate vs. (A) concentration of acetic acid (B) concentration of 2-methyl furan and (C) concentration of water over CBV8014 at a reaction temperature of 250 °C, 0.05mg catalyst and 30min time on stream. The

included table (D) shows conversion and product selectivities observed upon passing 2-methyl furan and acetic acid over HZSM-5 after 30min time on stream at a constant W/F of 0.19 h with respect to acetic acid fed. (E) Turnover frequency of 2-methyl furan acylation with acetic acid over HZSM-5 and Hβ as a function of time at 250 °C and 0.05mg catalyst (F) Apparent activation energy of acetic acid acylation over HZSM-5 estimated for a temperature range of 220-250 °C. 41

Figure 16 :- Density-functional-theory calculations of acylation of 2-methyl furan with acetic acid. All the values are reported in kJ/mol. The transition states are shown as the insets with C, O, H, Si, and Al atoms colored cyan, red, grey, black and green, respectively. The results calculated using the HSE hybrid functional (red) is also shown to compare with the PBE results (black). The reaction path is schematically shown at the bottom. 44

Figure 17 :- Charge transfer and density of states (DOS) calculated using the hybrid functional. (A), charge transfer between the molecules (the desorbed acyl and MF) and the zeolite framework in the transition state of the C-C coupling step. (B), the same charge transfer in the absence of the MF molecule. Red and Blue indicates charge accumulation (negative charge) and charge depletion (positive charge). The isosurface corresponds to a charge density of ±0.015 $eÅ^{-3}$. (C-D), plane-averaged charge transfer (see methods in supporting information) of the same area as in (A-B). Electron depletion at the desorbed acyl (indicated by dashed circles) via the Bader charge analysis is also shown. (E) Projected DOS onto the desorbed acyl species (acylium ion) in (A) and (B). 45

Figure 18 (a,b,c,d) :- Evolution of acetic acid and acetone as a function of W/Fat 30min time on stream over CBV8014 at temperature of 280, 290, 300 and 310 °C..... 63
Figure 19 :- Evaluating activation enthalpy and entropy of acetic acid ketonization over CBV8014 using Eyring-Polanyi plot..... 66
Figure 20 :- DFT-calculated reaction profile for ketonization reaction between two acetic acid molecules in HZSM-5. All the values are reported in kJ/mol. The transition states are shown as the insets. The C, O, H, Si, and Al atoms are colored cyan, red, grey, black and green, respectively. The results calculated using the HSE hybrid functional (red) is also shown to compare with the PBE results (black). The reaction path is schematically shown at the bottom. In the C-C coupling step and decarboxylation of β-keto acid, a hydrogen transfer step is needed. The hydrogen atom involved in the hydrogen transfer is highlighted in orange in the schematics. 67
Figure 21 :- Acylation of m-cresol over CBV8014 at different temperatures 74
Figure 22 :- Apparent barrier estimation for m-cresol acylation with acetic acid over HZSM-5..... 76
Figure 23 :- Arrhenius plot of toluene acylation with acetic acid over cbv8014 at different tempeartures. The ratio of acetic acid to toluene is 1:0.258. 78
Figure 24 :- Moles of acylated product formed as function of times at different temperatures. The ratio of acetic acid to toluene is 1:2. 78
Figure 25 :- Apparent barrier estimation for toluene acylation with acetic acid over HZSM-5..... 79
Figure 26 :- Yields of acetyl furan product as a function of time at different temperatures. 80

Figure 27 :- Arrhenius plot for furan acylation with acetic acid over HZSM-5..... 81
Figure 28 :- Comparing the rates of acylation of m-cresol, m-furan, furan and toluene with acetic acid as acylating agent over HZSM-5..... 81
Figure 29 (a,b,c) :- Cumene conversion over CBV2314 at a reaction temperature of 300, 285,275 °C with water and without water. 90
Figure 30 :- Conversion of cumene as a function of time on stream with intermittent cofeeding of water at a reaction temperature of 275 °C over CBV2314 catalyst. 91
Figure 31 :- Conversion of cumene to products as a function of time on stream in presence of water at 275 °C over CBV2314. Water was intermittently stopped and started back to observe the activity behavior. 92
Figure 32 :- Snapshots in AIMD simulations. (A) water hexamer forms a chain between two acid sites. (B) the water hexamer breaks to form two clusters, a dimer and a tetramer. In both cases, the protons are delocalized in the H-bonded environment. The Si, Al, O, H are colored grey, blue, red and green, respectively. 94
Figure 33 :- Electron microscopy images of ZSM-5 (core) and ZSM-5@silicalite-1 (core-shell) crystals prepared without thermal annealing. (A) SEM image of ZSM-5 crystals prepared at 100 °C for 60 h. (B) SEM image of ZSM-5@silicalite-1 prepared with a 10 nm shell thickness. (C) TEM image of a core-shell particle shows the rough crystal surface comprised of protrusions with dimensions spanning ca. 5 to 20 nm. (D) HRTEM image of the core-shell particle reveals the presence of lattice fringes with translation symmetry extending from the exterior to interior of the crystal (1.2 nm periodicity, white lines). 109

Figure 34 :- Characterization of ZSM-5 (core) and ZSM-5@silicalite-1 (core-shell) crystals prepared with thermal annealing. (A) SEM image of ZSM-5 crystals after 170 °C annealing for 12 days. (B) SEM image of ZSM-5@silicalite-1 crystals after 170 °C annealing of the core for 12 days and growth of a 10 nm silicalite-1 layer. (C) TEM image of a ZSM-5@silicalite-1 crystal reveals a smooth, faceted surface. (D) Powder XRD patterns confirm the crystallinity of annealed (i) ZSM-5 and (ii) ZSM-5@silicalite-1 as having the MFI structure (Pnma space group). XRD data are offset along the y-axis for visual clarity. 111

Figure 35 :- (A) Superimposed EDS mapping of annealed ZSM-5@silicalite-1 crystals prepared with a 10 nm silicalite-1 shell. The elements are color coded: Al (red) and Si (green). (B) HRTEM image of a core-shell crystal reveals the presence of lattice fringes that extend from the exterior to the interior of the particle without any discontinuity. The orientation of fringes (1.1 nm periodicity) is highlighted by the white lines. HRTEM images confirm the translational symmetry between the core and shell due to the epitaxial growth of a silicalite-1 layer on the surface of ZSM-5 seeds. 113

Figure 36 :- ^{27}Al NMR was used to quantify the amount of extra-framework alumina in H-ZSM5 (core) and H-ZSM5@silicalite-1 (core-shell). The intensities at 60 ppm and 0 ppm correspond to framework and extra-framework alumina, respectively. 115

Figure 37 :- Gas phase turnover frequency (TOF) in a flow reactor of (A) triisopropylbenzene and (B) acetic acid over H-ZSM-5@silicalite-1 prepared with a 10 nm silicalite-1 shell, as well as the annealed H-ZSM-5 core. The reactions were performed at 1 atm after pre-treating the catalyst in He flow at 300 °C for one hour to remove physisorbed water from the catalyst surface. Cracking of triisopropylbenzene

(A) was done at 400 °C and ketonization of acetic acid (B) was done at 320 °C. The outlet stream from the flow reactor is connected to a GC-FID equipped with innowax column to quantify the products. The number of Brønsted sites was estimated via IPA TPD (excluding extra-framework Al from ^{27}Al NMR)..... 117
Figure 38 :- Ex situ DLS measurements of ZSM@silicalite-1 growth. The temporal change in hydrodynamic diameter D_H was analyzed by heating a 1 wt% dispersion of ZSM-5 seeds (D_H = 156 nm) in a silicalite-1 growth solution with molar composition 14 TEOS:7 TPAOH:9500 H_2O. Samples were removed from the oven (100 ± 1 °C) at periodic times and were quenched to room temperature for DLS analysis. The symbols are an average of three measurements with standard deviation of ± 2 nm. The slope of linear regression (solid line) reveals a 3.8 nm/h rate of silicalite-1 growth, which agrees with a prior study by Li et al.. [135]..... 119
Figure 39 :- (A) Kinetic phase diagram of silicalite-1 growth solutions comprised of two regimes: Region I contains soluble silica molecules (monomers and oligomers) and Region II is comprised of soluble species in quasi-equilibrium with silica nanoparticle precursors.[187] The CAC (solid line) divides the two regions. The pH was measured for solutions used to prepare core-shell particles (diamond symbols), to estimate ce (blue circle), and to assess a silica-free solution (red triangle). The dashed line is interpolated between data points and the dotted line is an estimated solubility of silicalite-1. The color coded segments in Region II illustrate the progressive increase in shell thickness with increased silica supersaturation. (B) Synthesis conditions used to tailor the shell thickness of ZSM-5@silicalite-1. Growth solutions of molar composition x TEOS:14 TPAOH: 9500 H2O and ZSM-5 crystals (0.25 g seeds per 25 g growth

solution) were heated for 24 hours at 100 °C, followed by 12 days of 170 °C annealing. The solid line is a linear regression (R2 = 0.97) extrapolated to zero shell thickness, which corresponds to ce of silicalite-1 (i.e., x = 13 TEOS). 121

Figure 40 :- Benzoic acid TPD on HZSM-5 showing an initial dehydration step 132

Figure 41 :- Flow reaction studies co-feeding acetic acid with benzoic acid at T=300C showing formation of two ketones 134

Figure 42 :- a, b: Benzoic acid TPD studies pulsing in acetic acid on benzoyl adsorbed HZSM5 showing acetone and acetophenone respectively 135

Figure 43 :- Flow reaction studies co feeding Pivalic acid and acetic acid at T=300^{o}C 137

Figure 44 :- Pivalic acid TPD on HZSM-5 showing decomposition into isobutylene, water and CO_2..... 138

Figure 45 :- a, b: TPD studies pulsing in acetic acid on ^{13}C benzoyl adsorbed HZSM5 139

Figure 46 :- (a) VMWNTs grown between mica sheets and (b &c) after growth of zeolites on the VMWNTs. 147

Figure 47 :- Images of zeolites after burning out the carbon nanotube template. (a) Low magnification image of the the middle of the VMWNT array (b) high magnification image of the middle of the VMWNT array, (c) low magnication image of the end of a VMWNT array, and (d) high magnification image of the end of the VMWNT array. 148

Figure 48 :- TEM images of sample Z-CNT-3 (a) low magnification showing arrays of zeolites and (b & c) high magniciation showing the channels created where the VMWNTs once resided. 149

Figure 49: Nitrogen adsorption used to calculate the volume of the micropores and mesopores for sample Z-CNT-1. 150
Figure 50: Average pore diameter of the Z-CNT-1 sample. 150
Figure 51: Conversion and carbon balance for HZSM5 with a Si/Al=40. 152
Figure 52: For HZSM5 with a Si/Al=11 the (a) conversion and carbon balance and (b) the selectivity for propylene and benzene. 152
Figure 53: Reactions results for Z-CNT-1 (a) selectivity and (b) conversion and carbon balance. 153
Figure 54: SEM images of samples (a & b) Z-CNT-1, (c & d) Z-CNT-2, (e & f) Z-CNT-3, (g & h) Z-CNT-4. 154
Figure 55 : SEM images of the ZSM-5 samples (A,B,C), mesoporous sample C and acid washed sample C. 160
Figure 56 : XRD of parent and mesoporous zeolite 162
Figure 57 :- 1st biomass pulse alkyl benzenes for mesopore series on a per acid site basis 163
Figure 58 :- Alkyl benzenes in crystallite size series 164
Figure 59 :- Napthalenes in crystallite size series 165
Figure 60 :- Alkyl benzenes in mesopore series 167
Figure 61 :- Naphthalenes in mesopore series 167
Figure 62 :- Acetic acid conversion mesopore series 169
Figure 63 :- Syringol conversion mesopore series 170
Figure 64 :- Acetic acid reacted per site basis on mesopore series 170
Figure 65 :- Syringol converted per site basis on mesopore series 171

Abstract

Ketonization of acetic acid is a powerful route to convert these problematic acids into stable building blocks to produce fuels and chemicals. This reaction is investigated over HZSM-5 via a combination of temperature programmed techniques (TP), IR, and reaction kinetics. TP experiments demonstrate the generation of stable acyl intermediates that require higher temperatures to facilitate C-C coupling with a second acetic acid molecule. Isotope labeling experiments reveal that the rate-determining step is the formation of the C-C bond rather than the activation of the second acid. A detailed Langmuir Hinshelwood kinetic modelling revealed the thermodynamic and kinetic parameters involved in the reaction. All the experimental data is verified with theoretical calculations using density functional theory.

Though ketonization is an effective C-C coupling technique the inevitable production of CO_2 during the reaction reduces carbon yield and increase greenhouse gas emissions. This study report the direct acylation of methylfuran with acetic acid in the presence of water, all of which can be readily produced from biomass. This direct coupling limits unwanted polymerization of furanics while producing acetyl methyl furan. Reaction kinetics and density functional theory calculations illustrate that the dehydration of the acid to form surface acyl species is rate limiting. We show that furanic species effectively stabilize the charge of the transition state, therefore lowering the overall activation barrier. These results demonstrate a promising new route to C-C bond forming reactions to produce higher value products from biomass.

Chapter 1: Introduction

Utilization of biomass for the production of biofuels and chemicals is being studied extensively in recent years. Fuels and chemicals produced from biomass has a potential to serve as alternative energy source and mitigate environmental challenges by reducing net CO_2 emissions. Bio-oil derived from the fast pyrolysis of biomass is a complex mixture of chemically incompatible oxygenated compounds typically furanics, phenolics, carboxylic acids, and other small oxygenates [1, 2]. The efficient conversion of molecules present in bio-oil to useful fuel and chemical precursors is a daunting task. First of the two significant challenges associated with upgrading bio-oil is the fact that it is thermally unstable, with compounds polymerizing upon aging even at room temperature. The second challenge is, due to the large amounts of light C_2–C_3 oxygenates that are converted to low-value light gases after conventional upgrading via hydrotreating, limits the potential for incorporation of the biomass-derived species into the gasoline/diesel fuel range.

Acetic acid is largely responsible for both of these challenges. It is the most abundant compound among the light oxygenates yielded from bio-oil [3]. Its acidity is known to present corrosion problems and promote polymerization of other species present in the mixture. Mild thermal approaches such as torrefaction can selectively decompose hemicellulose and cellulose in biomass[3], and is a very effective strategy for separating phenolics from the other pool of molecules. But still this tactic yields a blend of furanic and carboxylic acid species that are difficult to separate.

Decarboxylative ketonization reaction is a well-known and effective route for stabilizing carboxylic acid, predominantly acetic acid, as it converts two organic acids

to a ketone. This route has received a great deal of attention for stabilizing carboxylic acids as it produces ketones that can undergo sequential coupling reactions to generate longer-chain hydrocarbons. Ketonization of carboxylic acids over basic and reducible oxides has been extensively studied[4-7]. In contrast, the mechanism involved in ketonization of carboxylic acids over acidic zeolites remain unexplored, while some reported ketenes as intermediates over Brønsted zeolites[8]. The reaction intermediates responsible for the conversion as well as the specific role of protons in the zeolite on the mechanism is far from being totally understood. In addition, while water is present in bio-oil streams, the role of water on this reaction has not been clearly identified or studied in the literature. Zeolites, especially MFI framework zeolites, are among the most promising and commonly employed catalysts for the conversion of bio-oil to fuels and chemicals.

Understanding the conversion of most abundant and problematic species acetic acid to stable molecules over widely used catalyst is of great importance. In this contribution an effort was made by our group to understand the mechanism for conversion of acetic acid to acetone over HZSM-5 catalyst [9]. Proposed reaction mechanism over HZSM-5 involved initial dehydration of the acid to form acyl species which upon subsequent heating interact with other activated carboxylic acids to form acetone. A detailed kinetic model was developed and kinetic parameters were estimated by regressed fittings. This data will be verified by theoretical calculations using DFT.

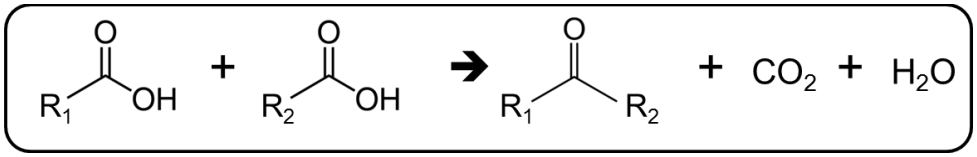

The major drawback in this strategy is the stoichiometric formation of carbon dioxide as a byproduct, accounting to 25% of the carbon in acetic acid. Therefore, an alternative strategy for stabilizing the torrefaction stream by direct C-C coupling of acids and furanic compounds while yielding thermally stable intermediates would lead to a step change in the upgradation process. Direct dehydration of acetic acid to form acyl intermediates followed by coupling to a furanic substrate would be very appealing. While furanic species have shown to couple with acetic anhydride under very mild anhydrous conditions[10], direct coupling of furanic species with acid has not been reported. Furanic species are known to undergo a wide range of side reactions over Brønsted acid sites, many of which can lead to uncontrolled polymerization and coke formation[11]. This chemistry over HZSM-5 zeolites can potentially result in production of fuel precursors and specialty chemicals from biomass without losing any carbon.

Chapter 2: Selective ketonization of acetic acid over HZSM-5: The importance of acyl species and the influence of water

This work is published in Journal of catalysis. Complete article and supporting information can found using the citation "Gumidyala, A., Sooknoi, T., & Crossley, S. (2016). Selective ketonization of acetic acid over HZSM-5: The importance of acyl species and the influence of water. Journal of Catalysis, 340, 76-84."

Abstract

The ketonization of acetic acid is investigated over HZSM-5 via a combination of temperature programmed techniques (TP), IR, and reaction kinetics. TP experiments demonstrate the generation of stable acyl intermediates that require higher temperatures to facilitate C-C coupling with a second acetic acid molecule. Near exclusive selectivities for the ketonization reaction devoid of significant sequential aldol condensation are observed at temperatures ranging from 270-330°C. The rate-determining step is proposed to involve the interaction of an acyl group with a second acid, with an apparent reaction order of 1.6. This order can be explained by a second order rate-determining step that is reduced as a result of acid-derived surface species. Isotope labeling experiments reveal that the rate-determining step is the formation of the C-C bond rather than the activation of the second acid. The rate of reaction per gram scales with the concentration of Brønsted sites present, with the exchange of Brønsted sites with Na resulting in a corresponding drop in activity. The ketonization reaction exhibits a -0.46 order with respect to water, but this loss in activity is accompanied by a significant increase in catalyst stability.

Introduction

Bio-oil derived from the fast pyrolysis of biomass is a complex mixture of oxygenated compounds typically containing furanics, phenolics, carboxylic acids, and other small oxygenates[1, 2, 12-22]. In recent years, upgrading bio-oil has gained significant interest due to its potential as an alternative energy source and mitigate environmental challenges. Two very significant challenges are associated with the upgrading of bio-oil to fuels and chemicals. The first is the fact that it is thermally unstable, with compounds condensing to solids upon aging at room temperature. The second challenge is due to the large amounts of light C_2-C_3 oxygenates are converted to low value light gases after conventional upgrading via hydrotreating, limiting the potential for incorporation of the biomass derived species into the gasoline/diesel fuel range [23].

Acetic acid is largely responsible for both of these challenges. It is the most abundant single compound in bio-oil [2, 24], and its acidity is known to present corrosion problems and promote polymerization of other species present in the mixture. The resulting solids are not readily upgraded and accelerate catalyst deactivation, which is a major concern for upgrading of pyrolysis oils [1, 2, 12-22]. In addition, the fact that acetic acid contains only two carbon atoms in its backbone means that conversion via hydrotreating will yield low value C_1 and C_2 hydrocarbons.

The conversion of acetic acid to a stable, non-acidic molecule with a longer C-C backbone is highly desirable. The ketonization reaction is a well-known and effective method for carboxylic acid upgrading as it converts two organic acids to a ketone while removing oxygen in the form of water and CO_2 [4-7, 25-30]. This reaction is very

appealing as the stable ketones formed can be further converted to produce longer-chain hydrocarbons via aldol condensation/hydrogenation [6, 7, 28-30].

The ketonization of carboxylic acids via the decomposition of salts [22, 31-33] as well as over basic and reducible oxides has been extensively studied. While several reactive surface intermediates have been proposed over high lattice reducible oxides involving ketenes, ketene like species, carboxylates, and even anhydrides [4-7, 25-30], consensus is slowly growing toward the importance of a β-ketoacid intermediate. In contrast, the reactive intermediates responsible for this transformation over acidic zeolites remains unexplored, while some similar surface intermediates such as ketenes have been reported over Brønsted zeolites [8]. Despite the fact that ketones have been observed as products from the transformation of acetic acid over zeolites since the early 1980's, specific details of the reaction mechanism still remain elusive [34-38]. While ketones are reported in several cases, conditions that yield high selectivity to acetone while minimizing sequential aldol condensation reactions have yet to be identified. In addition to uncertainty surrounding the mechanism, the critical role of water, which is present in significant quantities in virtually all streams that contain acetic acid, has not been investigated for this reaction. Zeolites, especially MFI framework zeolites, are one of the most promising and commonly employed catalysts for the conversion of bio-oil to fuels and chemicals. The fact that so little is known about the mechanism of conversion of the most abundant species in bio-oil over this catalyst is surprising, and warrants further investigation.

The few studies investigating the ketonization reaction over zeolites have operated under conditions that also involve a variety of secondary reactions such as

aldol condensation and aromatization[38], making it difficult to come to mechanistic conclusions. In addition to these sequential and parallel products, the intrinsic ability of a zeolite to activate various oxygenated species, such as acetic acid, can be clouded by the rapid deactivation that is associated with the subsequent conversion of reaction products such as acetone, as has been illustrated by Kresnawahjuesa et al. [39]. As early as 1983, Chang *et al.* [36] offered the suggestion that the ketonization reaction over zeolites may occur via a nucleophilic attack of an acylium ion with an acetate. Due to the rapid deactivation observed over zeolites, they proposed that these acetate species were formed from the decomposition of acylium species by dehydroxylation of the zeolite, leading to an inherent irreversible deactivation of the catalyst. Martens et al. [35] proposed a similar mechanism involving a surface acyl intermediate similar to Chang et al. Rather than forming an activated acetate via dehydroxylation of the zeolite, they speculated that a second acid could interact directly with the basic site on the zeolite generated via the formation of a surface acyl group to dissociate the O-H bond on the carboxylic acid and regenerate the Brønsted site and form a carboxylate anion. The location of the surface acyl species during this process is not specified. They proposed that this carboxylate anion subsequently interacts with the positively charged acyl cation to form the ketone.

Other types of reactive intermediates have been proposed for reactions involving acyl species and the acylium ions. Of particular relevance to this reaction are ketenes. Surface acyl species are in equilibrium with acylium ions, as well as gas phase ketenes in low abundance. Ketenes are often proposed as important reactive intermediates for reactions involving carboxylic acids and acyl groups[8]. Specifically for the

ketonization reaction, it has been shown that over oxides such as TiO_2, gas phase ketenes are parallel side products that do not lead to ketone formation as discussed in depth in a recent review on the topic[7]. Martinez et al. argued against a sequential ketene based mechanism, using a monolith reactor while varying the contact time[20]. Similarly, Pestman et al. [5] used ^{13}C labeled acids to perform cross ketonization reactions between a carboxylic acid capable of forming a ketene with another carboxylic acid lacking an alpha hydrogen and thus incapable of forming a gas phase ketene. They showed by labeling the carbonyl carbon of carboxylic acids that gas phase ketenes are not responsible for the ketonization reaction over TiO_2.

Surface bound acyl species and their corresponding acylium ions have long been proposed as intermediates for similar C-C coupling reactions as well, such as acylation reactions with aromatics over zeolites [40-45]. Corma et al.[46] proposed that surface acyl species and acylium ions are important intermediates involved in aromatic acylation reactions. This claim was later challenged by Bonati et al.[47, 48] who, upon the observance of ketenes in trace levels, argued that ketenes were responsible for these reactions. Deuterium labeling studies by the same group later showed that while ketenes are produced in parallel to acyl groups and acylium ions, they are not intermediates in the acylation reaction[49], but rather side products that contribute to catalyst deactivation via coke formation.

In this contribution, we report the ketonization of acetic acid over HZSM-5 under conditions that selectively yield acetone. A systematic variation of temperature gives insight into the mechanism of acetone production and the resulting changes in selectivity. Temperature programmed desorption and IR studies combined with reaction

kinetics are used to investigate the reaction pathway and the possible reaction intermediates. The role of water on the ketonization mechanism and its impact on catalyst deactivation, competitive adsorption and interaction with intermediate surface species is also discussed.

Experimental

Catalyst preparation

ZSM-5 (CBV-8014) with a SiO_2/Al_2O_3=80 purchased from Zeolyst International in the ammonium form was calcined at 600°C for 5 hours in dry air to obtain the protonated HZSM-5 by thermal decomposition of NH_4^+ to NH_3 and H^+. Silicalite-1 was hydrothermally synthesized from the gel composition of tetrapropylammonium hydroxide (TPAOH):SiO_2:H_2O:EtOH=9:25:477:100 by following the procedure outlined in reference [50]. Reagents used for the synthesis include tetraethyl orthosilicate (TEOS, Sigma Aldrich, reagent grade, 98%), tetrapropylammonium hydroxide (TPAOH, Alfa Aesar, 40% w/w aq. soln.) and deionized water. The gel was stirred at ambient temperature for 24 hours and then hydrothermally treated for 24 hours at 80°C in an autoclave. The synthesized sample was washed and filtered by centrifugation followed by drying overnight (12hrs) at 80°C. The dried sample was then calcined at 600°C for 5hrs to remove the template. Both catalysts after calcination were pelletized and subsequently crushed and sieved to particles with sizes ranging from 90-250 μm.

Na exchange was conducted on the samples to titrate a portion of the Brønsted sites and test for diffusion limitations. A fraction of the Brønsted acid sites were poisoned with sodium dosing as per the procedure reported in literature[51]. Three different

samples (referred to as sample 1,2, and 3) were prepared by varying the amount of sodium loading using 0.5M $NaNO_3$ solution as the sodium source. Double-distilled water and commercial $NaNO_3$ (Sigma Aldrich, ReagentPlus®, ≥99.0%) were used to prepare 0.5M $NaNO_3$ solution. All samples were characterized by IPA-TPD for quantification of the resulting Brønsted acid site density.

Catalyst characterization

The crystallinity of the samples was investigated by X-Ray Diffraction using a Rigaku automatic diffractor (Model D-MAX A) with a curved crystal monochromator. It had Cu Kα as radiation source and was operated at 40kV and 35mA between the angle range of 5-55°. For analysis, a well ground catalyst sample was placed on a plastic slide and spread evenly to obtain a flat surface.

Scanning electron microscopy (SEM) measurements of the samples were performed by a Zeiss-NEON FEG-SEM instrument to estimate the particle diameter. To prepare SEM samples, a small amount of the zeolite aqueous suspension was placed on carbon tape and dried for one hour.

Isopropyl amine (IPA) temperature-programmed desorption (TPD) experiments were conducted on the zeolites used in this study to investigate the concentration of Brønsted acid sites. 50mg of catalyst was taken in a quartz reactor (1/4" OD) and flushed at 300°C for one hour with helium as a carrier gas at a flow rate of 20ml/min. After pre-treatment, the temperature was reduced to 100°C and 2 μL pulses of IPA were injected into the reactor through a septum using a syringe. To ensure saturation of all the acid sites in the catalyst bed with IPA, the mass to charge ratio (m/z) of 44 and 58 were tracked at the exit of the reactor with a MKS Cirrus 200 quadrupole mass

spectrometer (MS). IPA pulses were continued until a constant peak height corresponding to m/z=44 and 58 was observed as sequential pulses were injected. After adsorption of IPA on to the catalyst bed, helium carrier gas was flushed over the bed at a rate of 20ml/min at 100°C for 4 hours to remove physically adsorbed IPA, after which the temperature was ramped from 100°C to 600°C at a rate of 10°C/min. The products desorbing from the reactor during the temperature ramp were tracked via MS. Products were quantified through the calibration of the MS signal using standards and a sample loop.

Continuous flow reactions

Flow reaction studies were performed in a quartz tube reactor (1/4" OD) at atmospheric pressure and temperatures varying from 250-340°C. The catalyst sample was packed in the reactor between quartz wool and the reactor was filled with acid washed glass beads with a diameter of 1mm from the inlet of the reactor to the catalyst bed. The inlet of the reactor was heated to create a vaporization zone and the outlet stream of the reactor, which was connected to a six port valve for sampling, was heated to 250°C to prevent condensation. The temperature of the catalyst bed was controlled by a thermocouple attached to the outer wall of the reactor. The catalyst was preheated and flushed with helium flowing at 50 ml/min for one hour at 300°C before introducing acetic acid (Sigma Aldrich, ACS reagent, ≥99.7%) via a syringe pump. The results and product distribution at the desired time on stream (TOS) were analyzed using a Hewlett Packard 6890 gas chromatograph equipped with a flame ionization detector and an innowax column of dimensions 30m and 0.25 μm. The vapors downstream of the six

port valve were condensed in a sample bubbler using ice and water as a coolant medium.

External mass transfer limitations in the flow reactions were tested at 300°C by varying the helium carrier gas flow rate from 50 to 125 ml/min. It is important to mention that the W/F (weight of catalyst in g/feed flow rate in g/h) and the partial pressure of acetic acid were maintained constant during this study. When measured rates are controlled by external mass transport limitations, the rate increases linearly with increasing (carrier gas flow/particle diameter (dp))$^{0.5}$ [52]. This test was used to ensure that all data used to obtain kinetic parameters were not corrupted by external mass transfer limitations.

The kinetic isotope effect on ketonization of acetic acid over HZSM-5 was studied in this flow reactor at a reaction temperature of 300 °C and atmospheric pressure. Two different isotopically labeled acetic acid probe molecules were tested, acetic acid-d (Aldrich, 99 atom % D) and acetic acid-d_4 (Aldrich, 99.5 atom % D). As with the previous runs, the catalyst bed was preheated and flushed with helium at 300 °C for one hour before feeding the reactant. Acetic acid was fed to the reactor through a syringe pump with a rate of 0.0000728 mol/min at a reactant partial pressure of 10.67 Torr. A catalyst weight of 0.025g was used for these experiments. Products at the desired time on stream (TOS) were analyzed using the Hewlett Packard 6890 gas chromatograph described above.

Acetic acid TPRx experiments

The temperature-programmed reaction of acetic acid over Brønsted acid sites of CBV8014 was studied in the similar reactor setup used for IPA TPD explained in the

section 2.2. 50mg of catalyst was packed in a quartz reactor (1/4" OD) and flushed at 300°C for one hour with helium at a flowrate of 50 ml/min. It is important to mention that a moisture trap was installed in the helium line to avoid the introduction of moisture with the gas stream. It was ensured that the catalyst bed was completely dried after flushing with dry helium by tracking water (m/z=18) at the exit of the reactor via MS. After pre-treatment, the temperature was reduced to 100°C and glacial acetic acid was pulsed using a syringe in 2 μL increments. The catalyst bed was saturated with acetic acid as confirmed by analyzing exit gases from the reactor using MS. m/z=60 was tracked for acetic acid to ensure a constant signal per pulse in the exit stream of the reactor. After adsorption of acetic acid, the catalyst bed was flushed at 100°C with dry helium at a flow rate of 50 ml/min for 4 hrs after which the temperature was ramped from 100 to 600°C at 10°C/minute. The products desorbing from the reactor during the temperature ramp were tracked by MS and were quantified by injecting standards.

IR experiments

Infrared spectroscopy study of acetic acid over CBV8014 was conducted in a PerkinElmer Spectrum 100 FT-IR Spectrometer equipped with a Harrick Praying Mantis^{TM} chamber. After pre-treating CBV8014 at 300 °C in helium flow 50ml/min for 1 h, the temperature was reduced to 50°C and a blank spectrum of the zeolite surface was taken as a reference. Acetic acid was then adsorbed onto the surface for 30 min at 50°C through a sample bubbler maintained at -7°C while flowing helium at a rate of 50 mL/min. This was followed by flushing for 2 h at 50°C under a flow of 50 mL/min to remove physically adsorbed acetic acid. After flushing, the spectrum of the CBV8014 surface adsorbed with acetic acid was collected at 50°C and then the temperature was

raised at a steady rate of 10°C/min. Analysis at each desired temperature was conducted by stopping the ramp and holding at the desired temperature and performing 64 scans to obtain the spectrum prior to continuing the temperature ramp.

Results and discussion:

Reaction mechanism and evidence for stable acyl species

A simple analysis of the Brønsted acid sites post reaction provides insight into the nature of activation of the carboxylic acids before the ketonization reaction. Figure 1 shows that the Brønsted sites are clearly recovered after desorption of acetic acid and produced ketones at 300°C, demonstrating that irreversible dehydroxylation of the zeolite is not a prerequisite to activation of the acids for this reaction. The peak at 3605 cm^{-1} corresponding to Brønsted acid sites disappears after adsorbing acetic acid. A subsequent temperature ramp to 300°C is sufficient to desorb the ketones that were produced. The reappearance of the Brønsted sites indicates the absence of zeolite dehydroxylation to form an acetate as a necessary step for the ketonization reaction. A similar reappearance of IR bands corresponding to Brønsted sites was reported by Martens *et al.* upon exposure of HT zeolite to butyric acid followed by evacuation at 300°C [35].

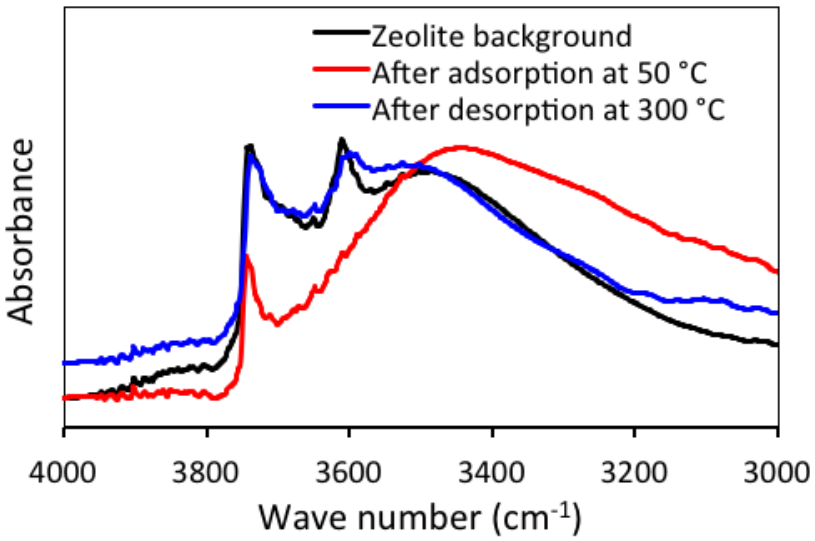

Figure 1 :- Acetic acid IR on CBV8014 shows the regeneration of Brønsted acid sites.

A temperature programmed desorption (TPD) experiment of acetic acid over CBV8014 was conducted to probe the reaction mechanism. Water (m/z=18), CO_2 (m/z=44), acetone (m/z=58) and m/z=43 (a fragment of both acetic acid and acetone) correspond to the most abundant species produced in this experiment. This profile, shown in Figure 2**,** clearly indicates that an initial dehydration step occurs in the reaction pathway. This would likely result in the formation of an acyl intermediate as had been speculated in previous studies [34-36]. It is important to note that CO_2 has a lower heat of adsorption on HZSM-5 as compared to that of water [53], so re-adsorption or bed effects could not explain the evolution of water prior to CO_2. Quantification of the water produced during the dehydration step amounts to 16.75 μmoles, which corresponds to the dehydration of an acid on >82% of the 20.3 μmoles of Brønsted acid sites present in the catalyst bed.

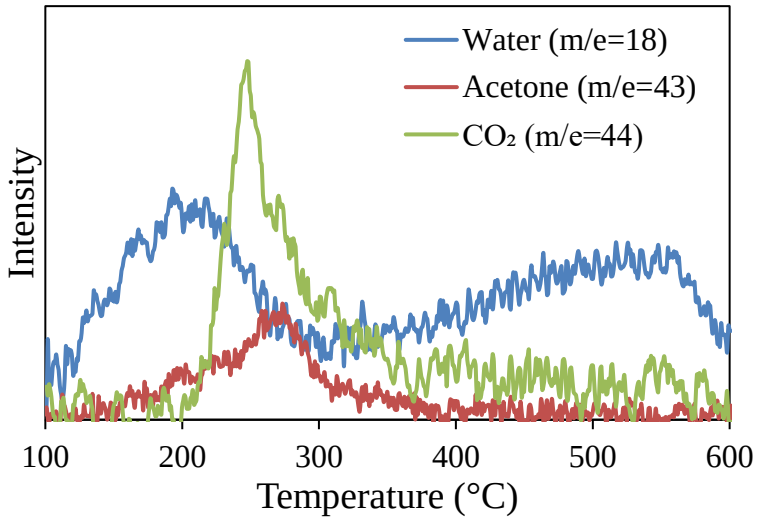

Figure 2 :- Acetic acid TPD on CBV8014 showing an initial dehydration step involved in the reaction pathway followed the decomposition of the intermediate to acetone and CO_2.

FTIR analysis of the catalyst after exposure to acetic acid and subsequent heating enables better understanding of the surface species formed during the course of the reaction. Initially the IR spectrum of the catalyst surface after pretreatment was taken as shown in Figure 3. After introducing acetic acid to the catalyst at 50°C via a saturated vapor stream, a significant peak was observed at ~1720 cm^{-1} as indicated by the solid vertical line, which is associated with surface adsorbed acetic acid [54-56]. After ramping the temperature at a steady rate to 150°C, the peak at ~1720 cm^{-1} shifts to lower wave number along with another peak appearing at 1755 cm^{-1} as indicated by the two dashed lines, which have been attributed to acetyl species [57]. It is important to note that the Brønsted acid sites are not recovered in this temperature range, as indicated by the lack of reappearance of the band at 3605 cm^{-1} after heating to 150°C as can be seen in Figure S3 of Appendix-A. This indicates that the acyl species remain bound to the zeolites under these conditions.

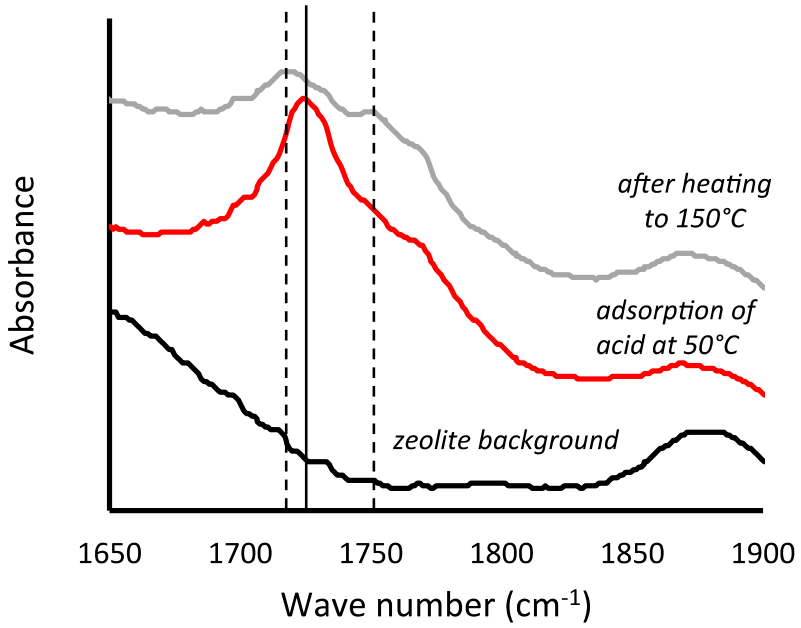

Figure 3 :- **Acetic acid IR on CBV8014 after adsorption of acetic acid at 50°C and subsequent heating to 150°C. The IR spectra are offset for clarity.**

The IR results presented in Figure 3 indicate the presence of a stable acyl intermediate, and the TPD results in Figure 2 suggest that the dehydration step is not the rate-determining step for the overall coupling reaction. A reaction mechanism can be proposed as shown in Figure 4. The coupling step on the left may be a combination of several steps in series. Dashed bonds are not meant to represent a proposed transition state, but simply to illustrate the bonds involved in a possible route to the formation of a β-keto acid, which can subsequently decompose to form acetone. A rate determining step involving a surface acyl group and another acid will yield a second order kinetic dependence with respect to acetic acid as will be discussed in section 3.4. This is true if the rate determining step involves (a) the tautomerization or activation of the second acid, or (b) the formation of a C-C bond with the acyl. Further insight may be obtained

through kinetic fitting to determine the reaction order and deduce a rate-determining step.

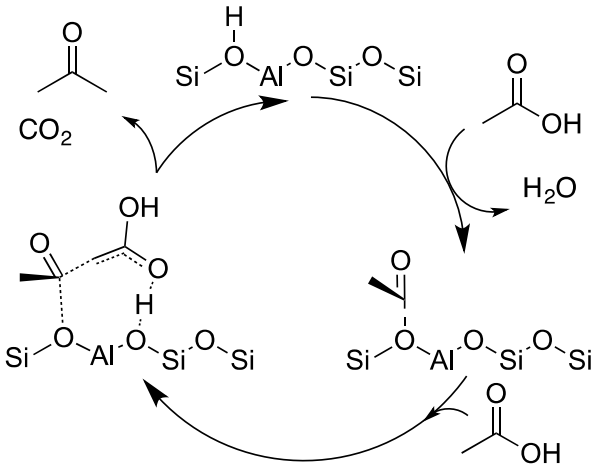

Figure 4 :- Proposed mechanism for acetic acid ketonization on CBV8014

Identification of selective ketonization regime under continuous flow

Subsequent aldol condensation and aromatization of acetone often complicates the kinetic analysis of the ketonization reaction. The conversion of acetic acid in a flow reactor over CBV8014 at 300°C yields near 100% selectivity to acetone and CO_2 as shown in Figure 5**.** After accounting for the CO_2 generated during the ketonization reaction for each mole of acetone produced [4-7, 25-30, 34-38], over a 95% carbon balance was observed for each reaction unless otherwise noted. The fact that most studies report a variety of subsequent aldol condensation products can clearly be mitigated by operating at milder temperatures under the conditions used in this study.

The ketonization reaction over zeolites is surprisingly selective over a broad range of temperatures. Figure 6 shows the flow reaction of acetic acid on CBV8014 at various temperatures with W/F being constant for all of the runs. These experiments were performed at temperatures ranging from 270-340°C and, as expected, the yield of acetone increased with increasing temperature. High carbon balances were observed

only up to a temperature of 330°C, beyond which a significant amount of carbon was lost due to the formation of heavier species that do not desorb from the catalyst. Vervecken *et al.* [30] and later Martens *et al.*[34, 35] reported a similar effect, with higher yields to aldol condensation products at elevated temperatures. Though no condensation products were observed in our study, the drop in carbon balance at 330°C indicates their formation. Higher temperatures may be required to desorb these species from the active site and leave the catalyst particle at a rate greater than subsequent condensation reactions that ultimately lead to coke formation. The lack of aldol condensation products observed at lower temperatures could be due to a combination of the reduced rate for this reaction as well as a lower population of vacant sites for acetone readsorption at lower reaction temperatures.

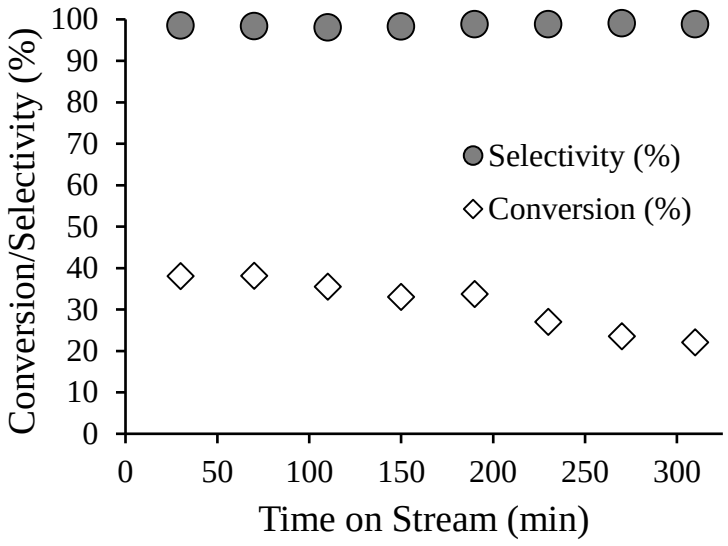

Figure 5 :- Flow reaction studies of acetic acid on CBV8014 at 300°C showing very high selectivity to acetone and CO_2. The flowrate of acetic acid is maintained at 0.0000728 mol/min with a catalyst weight of 120mg.

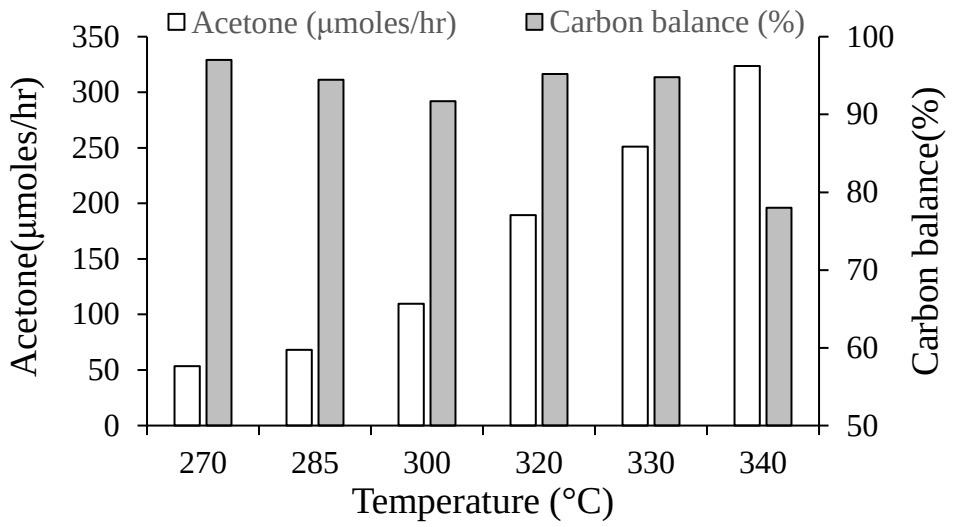

Figure 6 :- Flow reaction studies of acetic acid on CBV8014 showing yields of acetone and carbon balance as a function of temperature. The acetic acid partial pressure was maintained at 10.67 Torr. Rates at each temperature were taken at 30 min TOS.

Figure 5 and Figure 6 show that stable conversions may be achieved under more moderate conditions, with deactivation resulting from consecutive reactions, as well as potentially through parallel reactions involving ketene species. This loss in activity as a function of time on stream (TOS) can be recovered by a simple calcination. Figure S4 of Appendix-A highlights the reaction rate as a function of TOS across both the fresh and regenerated catalyst. After the catalyst has been exposed to acetone at 300°C for 105 minutes, the carbonaceous deposits are removed by temperature-programmed oxidation. The catalyst is then placed back in the reactor and the initial catalyst activity is recovered. This provides further support that irreversible dehydroxylation of the zeolite does not significantly occur under these conditions.

Effect of water on catalyst deactivation rates

Most streams that contain acetic acid are also accompanied by high amounts of water. Bio-oil produced from the pyrolysis of lignocellulosic biomass contains

approximately 60% water by weight, therefore understanding the role of water on the ketonization reaction is critical for any practical application utilizing these renewable streams. The mechanism outlined in Figure 4 implies that water may inhibit the formation of acylium species. However, a second order step may be rate-determining as will be discussed in more detail below. The role of water on this reaction can be twofold, by interacting with surface acyl species or desorbed ketenes to re-form acids, as well as by competing for adsorption sites.

Figure 7 shows a flow reaction conducted at 300°C during which water co-fed at a 1:1 molar ratio with acetic acid is introduced after a TOS of 100 min. A sudden drop in conversion is observed upon the introduction of water. When water co-feeding is stopped, the activity is recovered to a level equal to that observed prior to water introduction to the system, showing no measureable irreversible effect of water on the catalyst. The drop in the activity by water co-feeding could be due to either (i) the reversible reaction of acylium formation i.e, the surface acyl interacting with water to form acetic acid or (ii) competition between water and acetic acid for the active sites on the catalyst. The same experiment is repeated at a higher temperature of 320°C with a reduced W/F to maintain the same conversion levels as those observed at 300°C. Upon the addition of water at the higher temperature, the impact of water on the rate of ketonization is less pronounced.

Any influence of competitive adsorption for active sites will become less pronounced at higher temperatures, therefore the role of water on competition for active sites cannot be ruled out. Similarly, if the dehydration step to form an surface acyl species is endothermic, as was shown to be the case upon studying the Koch reaction

over H-MOR zeolites by Boronat et al. [58], higher temperatures will favor a greater equilibrium concentration of acyl groups on the surface. A more detailed analysis of water partial pressure on the reaction rate is presented in the next section.

The rate of acetone formation after the catalyst has been exposed to water co-feeding shown in Figure 7 indicates that water inhibits deactivation of the catalyst. While water competes for active sites and decreases the rate of the reaction, the stability of the catalyst may actually be improved. The positive influence of water on inhibiting the deactivation rate is more pronounced when evaluating the reaction order with respect to water as a function of time on stream. Figure 8 shows that the reaction order increases when measured at later TOS values. This indicates that, when extrapolating to 0 TOS, the -0.46 order with respect to water is a measure of the true impact that water has on the reaction rate. At later TOS as the catalyst begins to deactivate, the overall order is shifted by the influence that water has on the catalyst decay rate, with the apparent order approaching -0.2. This can be observed more directly by evaluating the exponential dependence of the rate as a function of time. By considering the exponential dependence of rate in terms of a deactivation coefficient, kd, it can clearly be observed that water inclusion positively impacts the catalyst stability. The rates fit to decay curves, as well as the deactivation coefficients as a function of water partial pressure can be found in the supplemental information in Figure S8 of Appendix-A. This positive influence of water on catalyst stability has very promising practical implications for real renewable streams that are often accompanied by significant amounts of water.

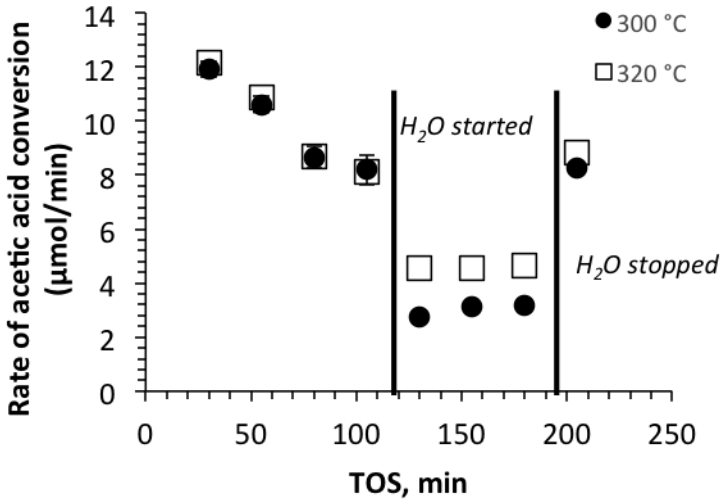

Figure 7 :- Acetic acid flow reactions at 300°C and 320°C showing a sudden drop in conversion when water was introduced. Catalyst weight 0.025g and 0.014g were used for reaction at 300°C and 320°C respectively to match the initial rates, with an acetic acid flow of 7.28 *10^{-5} mol/min at a partial pressure acetic acid of 10.8 Torr. Water was introduced at a 1:1 molar ratio.

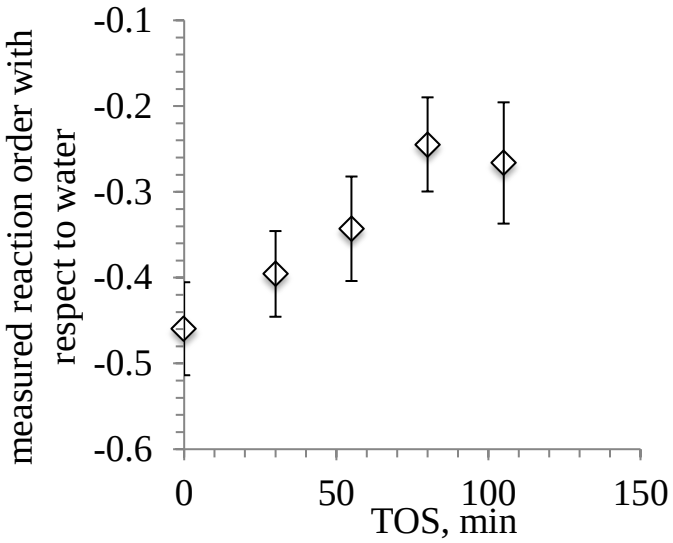

Figure 8 :- Order of reaction rate with respect to water as measured at varying TOS values. Conditions are vs. water concentration over CBV8014 at 300°C, 0.025 g catalyst, with initial rates extrapolated to 0 min TOS. Conditions are identical to those in Figure 11. Eror bars represent ±1 standard error value of the reaction order coefficient.

Reaction kinetics and identification of rate-determining step

Tests were conducted to ensure that the kinetic data is not limited by mass transfer. The reaction rate at 310°C as a function of helium carrier gas flow rate is shown in Figure 9. At low flow rates, the rate increases with increasing carrier gas flow, indicating that the rate is controlled by external mass transport to the catalyst surface. This effect disappears above 100 ml/min of gas flow suggesting the reaction is devoid of external diffusion corruptions above this flow rate. All kinetic experiments were therefore conducted with a carrier gas flowrate of 125 ml/min. This includes the experiments reporting reaction orders vs. TOS as described in the previous section.

The necessity of Brønsted acid sites for this reaction to proceed was confirmed by passing acetic acid over silicalite-1 at 300°C, with no measurable conversion observed over silicalite-1, as shown in Figure S5 of Appendix-A**.** This was further confirmed by Na exchange of the HZSM-5, (Samples 1,2,3 in Table 1 in Appendix-A). The activity dropped proportional to the concentration of Brønsted sites passivated by Na as shown in Figure 10, with a constant TOF of 1.03 ± 0.09 min^{-1} per Brønsted site over all of the catalysts tested. This confirms that the measured rates are not limited by internal or external mass transfer under these conditions. This result also demonstrates that any Lewis acidity introduced by the incorporation of Na cations does not accelerate the rate-determining step.

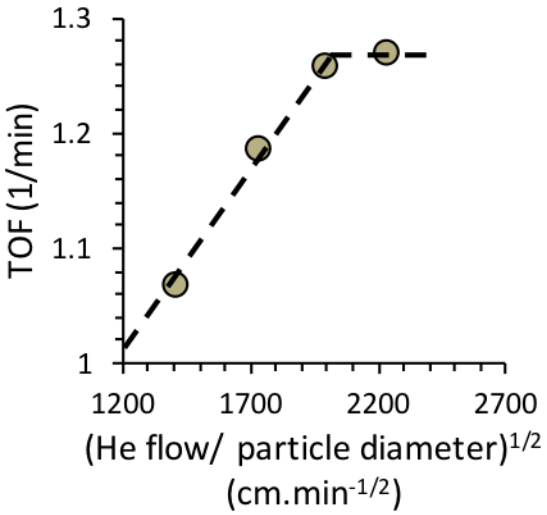

Figure 9 :- Dependence of acetic acid reaction rate over carrier gas flow rate at constant W/F=0.095 h and reactant concentration over CBV8014 at 310°C and 30min TOS.

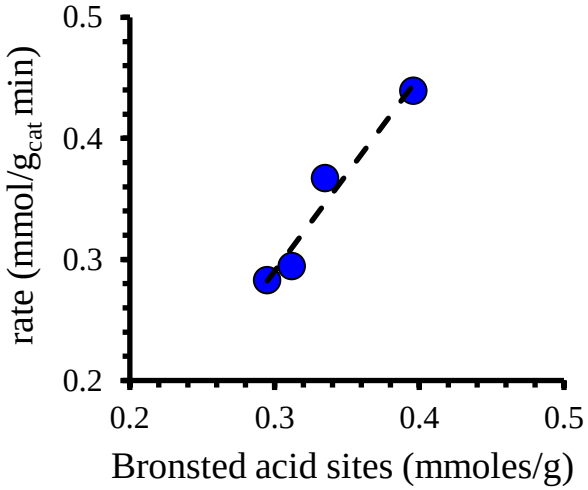

Figure 10 :- Rate of acetic acid conversion as a function of the density of Brønsted acid sites at a constant W/F=0.095 h over CBV8014 at 300°C and 30min TOS. The concentration of Brønsted acid sites were varied via Na exchange of CBV8014.

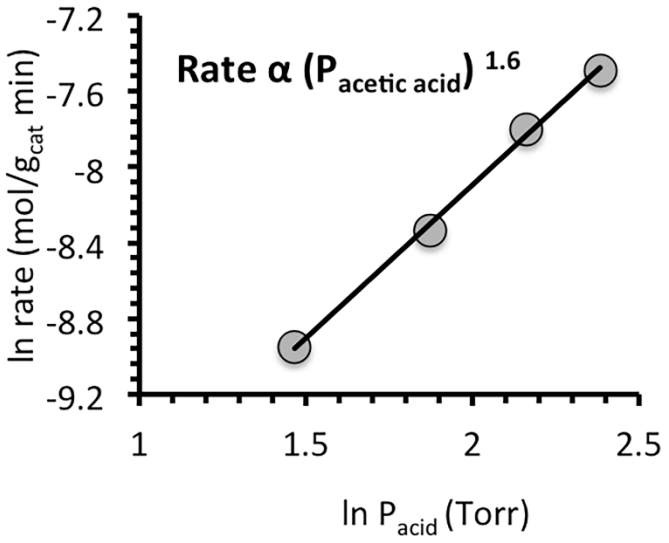

Figure 11:- Natural logarithm of the rate of reaction vs. acetic acid concentration over CBV8014 at 300°C, 0.025 g catalyst, with rates extrapolated to 0 min TOS.

By varying the concentration of acetic acid fed, we observe that the order of the ketonization reaction is greater than one. Rates were found by extrapolating the conversion to initial TOS values to eliminate effects of catalyst deactivation as described in the previous section. The fact that the reaction appears to be greater than 1st order as shown in Figure 11 implies a rate-determining step involving two acid-derived species. The reason for an observed order with respect to acetic acid less than two could be due to coverage of acetic acid and acid derived surface species. This behavior is very similar to that observed when measuring the apparent reaction order for coupling of acids over reducible oxides, where the second order coupling exhibits a fractional apparent order [6, 7].

Combining the observance of water evolution in Figure 2 along with acyl surface species at 150°C in Figure 3 implies that the dehydration of an acetic acid molecule to form a surface acylium species is not the rate-determining step. The further

observance of CO_2 (m/z=44) and acetone (m/z=43) evolution at 250°C in Figure 2 indicates that an intermediate formed between an acylium ion and an activated carboxylic acid can couple and subsequently decompose to yield CO_2 and acetone. The kinetic order greater than one further supports a second order rate-limiting step. This second order dependence that is manifested as an apparent 1.6 order rate dependence on acetic acid partial pressure can be explained by examination of a rate law derived assuming that an adsorbed acid and an adsorbed acyl interact during the rate-determining step to form acetone.

$$RCOOH / RCO^{+} \xrightarrow{k} RCOR \bullet H^{+} + CO_2$$

An expression highlighting the second order dependence of this rate-determining step is derived in the supplemental information, resulting in the following equation:

$$rate = \frac{kK_{Com}K_{equilibrium}K_{Acid}P_{Acid}^{2}}{P_{H2O}\left(1 + K_{Acid}P_{Acid} + \frac{K_{equilibrium}K_{Acid}P_{Acid}}{P_{H2O}} + \frac{K_{Com}K_{equilibrium}K_{Acid}P_{Acid}^{2}}{P_{H2O}} + K_{Ketone}P_{Ketone} + K_{H_2O}P_{H_2O} + K_{CO_2}P_{CO_2}\right)} \quad (1)$$

Several scenarios depicting variants of most abundant surface intermediates (MASI) are highlighted in the supplemental information. One can clearly see by inspection of (1) that a fractional order of 1.6 with respect acetic acid can be attributed to contributions to the rate equation by a combination of surface acetic acid, acetic acid/acyl complex, and surface acyl groups (corresponding to the three terms in the denominator that increase with the partial pressure of acetic acid).

Further insight may be gained by investigating the dependence of water on the rate expression. By varying the water partial pressure, and extrapolating data to initial TOS values, the rate of acetone production exhibits a -0.46 order with respect to water

as shown in Figure 12**.** Based on rate equation (1), competitive adsorption of water alone would not be able to account for the -0.46 order observed. Further simplification of expression (1), where the surface is completely saturated with adsorbed water species would simplify to:

$$rate = \frac{kK_{Com}K_{equilibrium}K_{Acid}P_{Acid}^{2}}{\left(K_{H_2O}P_{H_2O}^{2}\right)} \qquad (2)$$

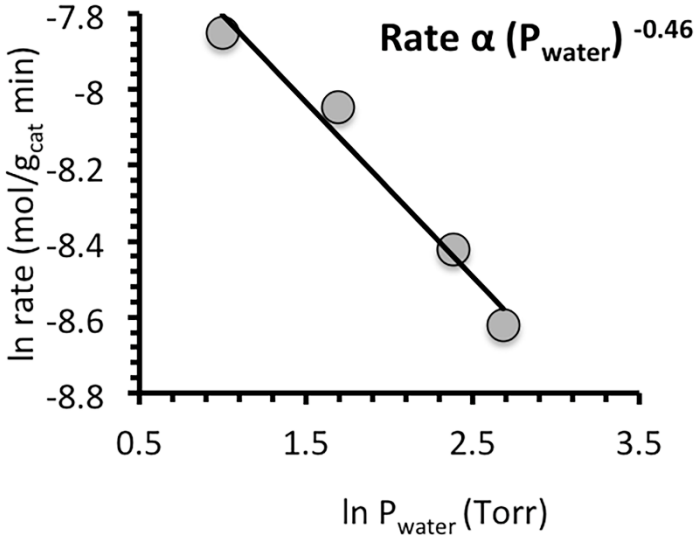

Figure 12 :- Natural logarithm of the rate of reaction vs. water concentration over CBV8014 at 300°C, 0.025 g catalyst, with initial rates extrapolated to 0 min TOS. Acetic acid partial pressure is maintained at 10.8 Torr.

Rate equation (2) does not agree with the observed experimental rate. Lower coverages of water, without considering the possibility of surface acyl species would yield an order with respect to water that varies from -1 to -2 as discussed in the supplemental information. Similarly, if the surface were completely saturated with surface acyl and acid/acyl species, the order with respect to acetic acid would range from 0 to 1. An order of 1.6 with respect to acetic acid indicates that sites are not all occupied by acyl groups or an acyl/acid complex, but clearly a significant fraction of the sites are

occupied by these species in order to justify an order with respect to water that is between 0 and -1.

Ison et al. [53] measured a heat of adsorption of water over HZSM-5 as -51 kJ/mol at low coverage while Kresnawahjuesa *et al.* of the same group[59] later reported the heat of adsorption of acetic acid over HZSM-5 as -139 kJ/mol. This indicates that while water could potentially compete for adsorption sites at high enough concentrations, excluding entropic contributions, water is not expected to occupy the majority of Brønsted sites under these conditions. While we cannot exclude the possibility that a significant portion of the negative order attributed to water in the reaction rate is due to competition for active sites, it is a reasonable assumption that a greater proportion of Brønsted sites are occupied by acyl species than water under these conditions based on the proposed rate expression. While we have eliminated the influence of water on catalyst deactivation rates with this analysis, the possibility of water interacting with transition states and facilitating proton transfer has not been investigated. If, for example, the tautomerization of the carboxylic acid in proximity to an acyl group is a limiting step in this reaction, water could play yet another positive role on this reaction.

The kinetic consequences of a rate determining step involving the activation of the alpha hydrogen, either through direct abstraction or tautomerization, may be probed by examining the variation in reaction rate with deuterated acid feed molecules. It should be noted that these rates are not limited by internal or external diffusion, as illustrated by Figure 10. A rate determining step that involves the direct cleavage of either an OH or a CH bond will exhibit a primary KIE of approximately 3.2 or 2.6 at the reaction temperature, respectively [60, 61]. The absence of a primary kinetic isotope effect based

on the insignificant shift in TOF upon replacing acetic acid with either OD or fully deuterated acetic acid shows that activation of the alpha hydrogen is not the rate-determining step. This, coupled with the second order dependence of the rate on acetic acid, demonstrates that the rate-determining step is the formation of the C-C bond between an acyl and an activated acid.

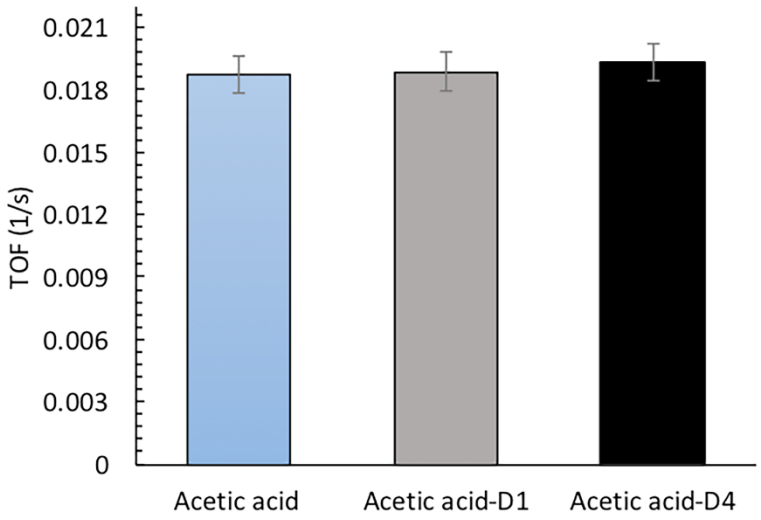

Figure 13 :- TOF values for acetic acid, and it's deuterated counterparts in the OD position (D1) and fully deuterated (D4). Reaction conditions are described in section 2.3.

Conclusions:

Conditions necessary to convert acetic acid to acetone over HZSM-5 in the gas phase with near 100% selectivity to the ketonization reaction have been identified. Significant sequential condensation of acetone was observed at a temperature beyond 320°C as indicated by a decrease in the carbon balance. An initial dehydration step is involved in the reaction pathway to yield a surface acyl species in equilibrium with an acylium ion. This acylium ion couples with a second acid, with a step involving two acetic acid derived species serving as the rate-determining step as supported by IR, TPD

and kinetic data. The lack of a primary kinetic isotope effect upon introducing deuterated reactants reveals that the rate-determining step is the formation of the C-C bond. Water inhibits the reaction exhibiting a -0.46 order on the reaction rate, but also has a positive influence on the catalyst stability under the conditions reported here.

Acknowledgements:

Financial support from the American Chemical Society (grant PRF 54107-DNI5) and the Department of Energy (Grant DE-EE0006287) is gratefully acknowledged.

Chapter 3: Direct carbon-carbon coupling of furanics with acetic acid over Brønsted zeolites

All the work in this chapter is performed at University of Oklahoma. The DFT calculations as a part of this work were performed by Dr. Bin Wang. This work is published in Science Advances journal. Complete article and supporting information can found using the citation "Gumidyala, A., Wang, B., & Crossley, S. (2016). Direct carbon-carbon coupling of furanics with acetic acid over Brønsted zeolites. Science Advances, 2(9), e1601072."

Abstract:

Effective carbon-carbon coupling of acetic acid to form larger products while minimizing CO_2 emissions is critical to achieving a step change in efficiency for the production of transportation fuels from sustainable biomass. Here we report the direct acylation of methylfuran with acetic acid in the presence of water, all of which can be readily produced from biomass. This direct coupling limits unwanted polymerization of furanics while producing acetyl methyl furan. Reaction kinetics and density functional theory calculations illustrate that the dehydration of the acid to form surface acyl species is rate limiting. Water inhibits the overall rate but selectivity to acylated products is not affected. We show that furanic species effectively stabilize the charge of the transition state, therefore lowering the overall activation barrier. These results demonstrate a promising new route to C-C bond forming reactions to produce higher value products from biomass.

Introduction

Heteroaromatic functionalization via Friedel-Crafts acylation to attach a carbonyl group to the aromatic rings is important for the production of several specialty chemicals and drugs[43]. Acylation is commonly carried out with acyl chlorides or anhydrides as acylating agents due to their ease of activation. While efforts have been made to use carboxylic acids directly to minimize waste and improve efficiency, the more severe conditions that are required often lead to undesired side reactions with negative consequences for specialty chemical synthesis. Studies carried out with the direct use of carboxylic acids as acylating agents are therefore the vast minority, with understanding of the consequential influence of water on said reaction rates nearly nonexistent.

For the upgrading of biomass streams, however, the direct activation of acetic acid, which is the most abundant compound present in many biomass derived streams[2, 24], may be a prerequisite for obtaining adequate yields of high value products. The efficient conversion of molecules present in streams derived from biomass to useful fuel and chemical precursors is a daunting task. Thermochemical routes such as pyrolysis, torrefaction, and solvolysis that transform the polymers in lignocellulosic biomass to monomeric species yield a complex mixture of chemically incompatible compounds[14, 62-66]. While mild thermal approaches such as torrefaction can selectively decompose hemicellulose and cellulose, this still yields a blend of furanic and carboxylic acid species that are difficult to separate[65, 66]. The acidity introduced by acetic acid facilitates the polymerization of furanic species at room temperature, creating obvious storage and transportation challenges[2, 16, 24, 65, 67, 68].

Stabilization through severe hydrodeoxygenation decomposes these acids, which consist of predominantly acetic acid, to low value C_1 and C_2 containing species. While this approach yields a stable product, the excessive requirement of hydrogen and low yields of products that are liquid at room temperature hinders the economics of the overall process[69-71]. Excessively high temperatures with acid catalysts with the aim of producing deoxygenated products suffers from similar consequences of excessive amounts of carbon wasted as coke and light compounds.

One promising route to improve yields is to couple carboxylic acids, predominantly acetic acid, in the vapor phase to produce larger products. Decarboxylative ketonization is one route that has received a great deal of attention for stabilizing these acids to form ketones that can undergo sequential coupling such as aldol condensation to generate useful compounds[5, 7, 26, 34, 36]. Perhaps the most significant drawback of this reaction is the stoichiometric formation of carbon dioxide as a byproduct, corresponding to 25% of the carbon in the acetic acid. An alternative approach to pre-stabilize the blend of oxygenates via selective C-C coupling of acids and furanic compounds while yielding thermally stable intermediates would lead to a step change in the field.

Direct dehydration of acetic acid to form acyl intermediates followed by coupling to a furanic substrate would be very appealing. Friedel-Crafts acylation has been the subject of several reviews, with the vast majority of studies concerning carboxylic acids focused on coupling with aromatic or phenolic compounds in the absence of co-fed water for specialty chemicals synthesis [43, 72, 73]. While furanic species have shown to couple with acetic anhydride under very mild anhydrous conditions[10], direct coupling of furanic species such as furan or methyl furan with acetic acid has not been

reported. Furanic species are known to undergo a wide range of side reactions over Brønsted acid sites, many of which can lead to uncontrolled polymerization and coke formation [11].

In this study, we report the direct vapor phase coupling of acetic acid with furanic species over HZSM-5 zeolites resulting in fuel range products without losing CO_2 in the process, increasing the overall amount of carbon in the biomass retained in transportation fuel precursors in the form of C-C bonds [74, 75]. Methyl furan is chosen as a probe molecule as it can be generated from the selective C-O cleavage of furfural[76], which is abundant in biomass degradation streams. Under conditions more mild than necessary for ketonization, acylation of methyl furan occurs with high selectivity under a wide range of concentrations. The kinetics of this reaction as well as influence of water on the reaction rate is discussed. Temperature programmed desorption (TPD) experiments and density functional theory (DFT) calculations are used to explain the mechanism of this promising reaction, highlighting the important role of confinement on the overall reaction and the acyl formation as the rate-determining step. Finally, we demonstrate the important influence of methyl furan on the stabilization of the charge of the acylium ion at the transition state, which facilitates C-C bond formation. These results have a broader influence on C-C coupling through Friedel-Crafts reactions over zeolites.

Materials and methods

A typical procedure for gas acylation flow reactions of 2-methyl furan with acetic acid over HZSM-5 is as follows. Catalyst was packed between quartz wool in a 1/4 inch quartz reactor and pretreated at 300 °C for one hour under a helium flow of 125 ml/min

to remove physisorbed water. A thermocouple was attached on outside wall of the reactor near the catalyst bed to maintain the reactor temperature. After pretreatment the temperature was adjusted to the required reaction temperature and reactants were fed through a syringe pump. The inlet of the reactor is heated to create a vaporization zone for the reactants and the outlet of the reactor and downstream lines are heated to 250 °C to prevent condensation of products. Samples were taken via a six port valve connected to a HP 6890GC equipped with flame ionization detector and innowax column for analysis.

Temperature programmed desorption studies of reactants are performed in the same system used for IPA TPD (see supporting information section 1.2 for details). The catalyst bed was pretreated in helium flow of 20 ml/min at 300 °C for one hour and then the temperature was cooled to 100 °C. Several 2µl pulses of acetic acid was injected into the reactor using a syringe and saturation of catalyst bed was ensured by following m/e=60 in the MS. This was followed by flushing for 2 hours in helium to remove physisorbed acetic acid, after which temperature was ramped to 220 °C using a steady ramp rate of 10 °C/min. Then methyl furan was pulsed and the products were tracked using MS.

The density functional theory (DFT) calculations were carried out using the VASP package[77]. The PBE-GGA (Perdew-Burke-Ernzerhof-Generalized-Gradient-Approximation) exchange-correlation potential[78] was used, and the electron-core interactions were treated in the projector augmented wave (PAW) method[79, 80]. The van der Waals interaction has been taken into account through the so-called DFT-D3 semi-empirical methods via a pair-wise force field[81, 82]. A HSE (Heyd-Scuseria-

Ernzerhof) hybrid functional[83, 84] was used as well to calculate the total energy of the initial, transition and final states that have already been optimized by DFT-D3 calculations to reduce underestimation of the reaction barriers caused by the charge delocalization error of the local and semi-local exchange-correlation functionals[85]. The nudged elastic band (NEB)[86] method has been used to find the transition state and calculate reaction barriers. The transition states have been further verified by vibrational calculations.

All the calculations have been performed using a ZSM5 unit cell including 96 Si and 192 O atoms. One Si atom at the T12 site, which is located at the intersection and more accessible to reactions [87], is replaced by one Al atom, so the Si/Al ratio is 95/1. The proton was initially attached to the O that is between the Al and the nearest T12 Si atom. The structure of unit cell was taken from an experimental work (a = 20.078 Å, b = 19.894 Å, c = 13.372 Å)[88] and fixed during the calculation. Atomic relaxation has been performed using a single Γ point of the Brillouin zone with a kinetic cut off energy of 400 eV. Further increase of k-point sampling to (1 × 1 × 2) doesn't change the reaction energetics. All the atoms (zeolite and the molecules) were fully relaxed until the atomic forces were smaller than 0.02 eV $Å^{-1}$.

Results and discussion

Evidence for direct acylation of furanics and reaction kinetics

A schematic of the direct acylation of methyl furan with acetic acid over HZSM-5 is shown in Figure 14 (A). The resulting product, acetyl methyl furan, contains significance both as a specialty chemical as well as a fuel precursor. By saturating the surface of HZSM-5 (CBV8014, Zeolyst international, SiO_2/Al_2O_3=80) with acetic acid

followed by a temperature ramp, two distinct regimes have been reported [9]. The first step involves the dehydration of the acid to form acyl species. Upon subsequent heating of the sample, these acyl species interact further with activated carboxylic acids to form ketone products. The latter step has a greater activation energy and can be avoided by operating at lower temperatures.

Evidence for direct acylation with furanic species via acetic acid can be obtained by conducting a similar experiment while pulsing methylfuran across a surface populated with acyl groups. By saturating a HZSM-5 catalyst surface with acetic acid at 100 °C in a TPD system (see supporting information section 1.2 in Appendix-B for experimental setup) followed by a temperature ramp to 220 °C results in dehydration of acids to produce surface acyl species. Observation of self-coupling of acetic acid does not begin to occur until 250 °C[9]. Results of product evolution following methyl furan pulses across the acyl saturated catalyst at 220 °C are shown in Figure 14 (B). With each pulse of methyl furan, acetyl methyl furan is observed desorbing from the catalyst surface. The peak intensity decays with increasing pulse number indicating a drop in the amount of acylation products formed, likely due to an extinction of surface acyl species. This experiment suggests that acetic acid dehydrates on a Brønsted acid site to form surface acyl species that attack the ring of methyl furan.

The acylation of 2-methyl furan with acetic acid occurs over the same HZSM-5 catalyst at temperatures ranging from 220-300 °C in an atmospheric pressure fixed bed flow reactor. This reaction is exclusively selective to acetyl methylfuran isomers over a broad range of temperatures. As shown in Figure 15 (D), product yield is dominated by acetyl-methylfuran isomers with detectable concentrations of acetone observed at a

reaction temperature of 300 °C. The carbon balance for each of the reactions tabulated in Figure 15 (D) is over 95%, therefore the conversions reported are same as the yields. The furan ring is predominantly acylated at the ortho position forming 5-acetyl 2-methyl furan though traces of 4-acetyl 2-methyl furan are produced with selectivity to the latter increasing at elevated temperatures. A minor increase in the selectivity to 3-acetyl-5-methyl furan, from ~4 to 12% of the acylated products, is observed with an increase in temperature suggesting a higher barrier to acylate in this position.

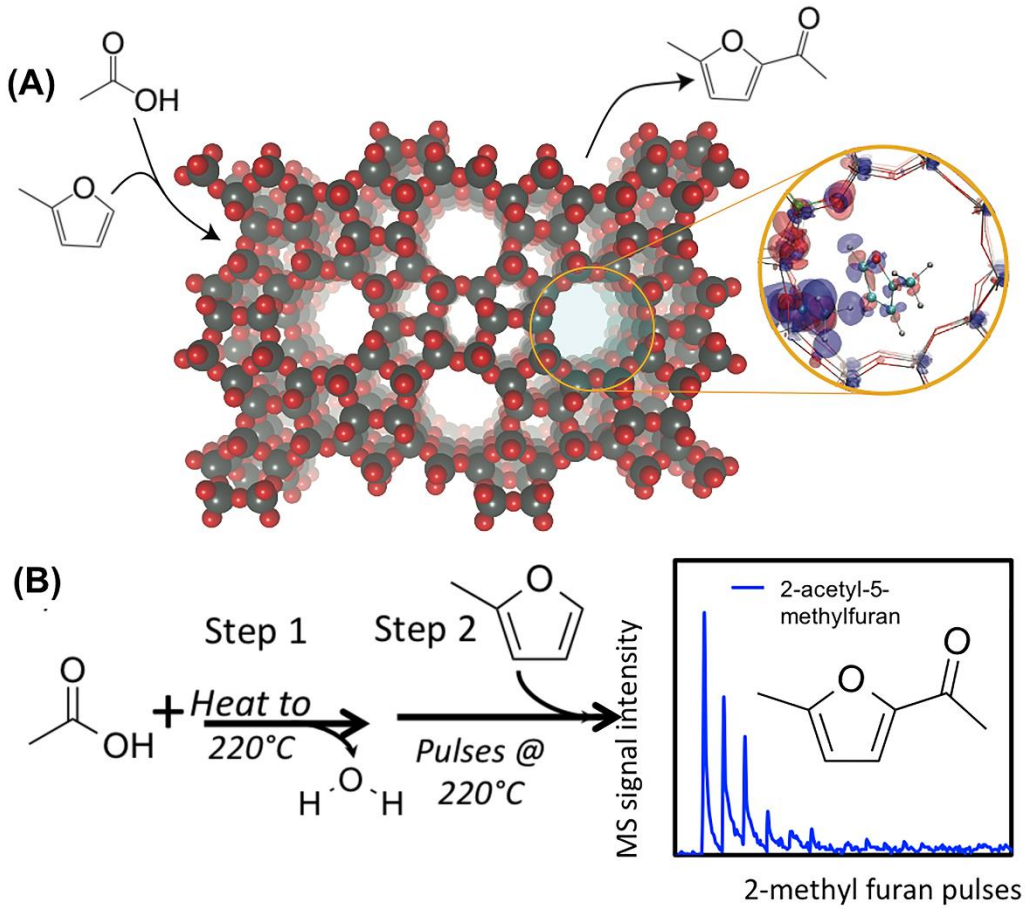

Figure 14 :- Direct acylation of methylfuran with acetic acid over HZSM-5. (A), Schematic of 2-methyl furan acylation with acetic acid over HZSM-5. (B), TPD experiment over HZSM-5 showing 5-acetyl 2-methyl furan desorbing with 2-methyl furan pulses from catalyst bed saturated with surface acyl species at 220 °C.

The acylation reaction order was estimated at 250 °C reaction temperature by varying the concentration of acetic acid and 2-methyl furan independently. As shown in Figure 15 (A,B), the reaction is first order with respect to both reactants. Further, the effect of water was studied by co-feeding water with 2-methyl furan and acetic acid. As seen in Figure 15 (C), water inhibits acylation with an order of -0.7. This does not preclude biomass derived streams that include water in the vapor phase, as increasing concentrations of water, even when water concentrations exceed methylfuran concentrations in the feed, appear to have no detrimental influence on the catalyst's selectivity or stability as shown in Fig. S4. In fact, under more severe temperatures where an abundance of ketenes may be present, water has been shown to inhibit catalyst deactivation for acid coupling reactions[9]. The enhancement in stability was explained by the potential reaction of water with trace ketene species in the gas phase that can lead to rapid catalyst deactivation.

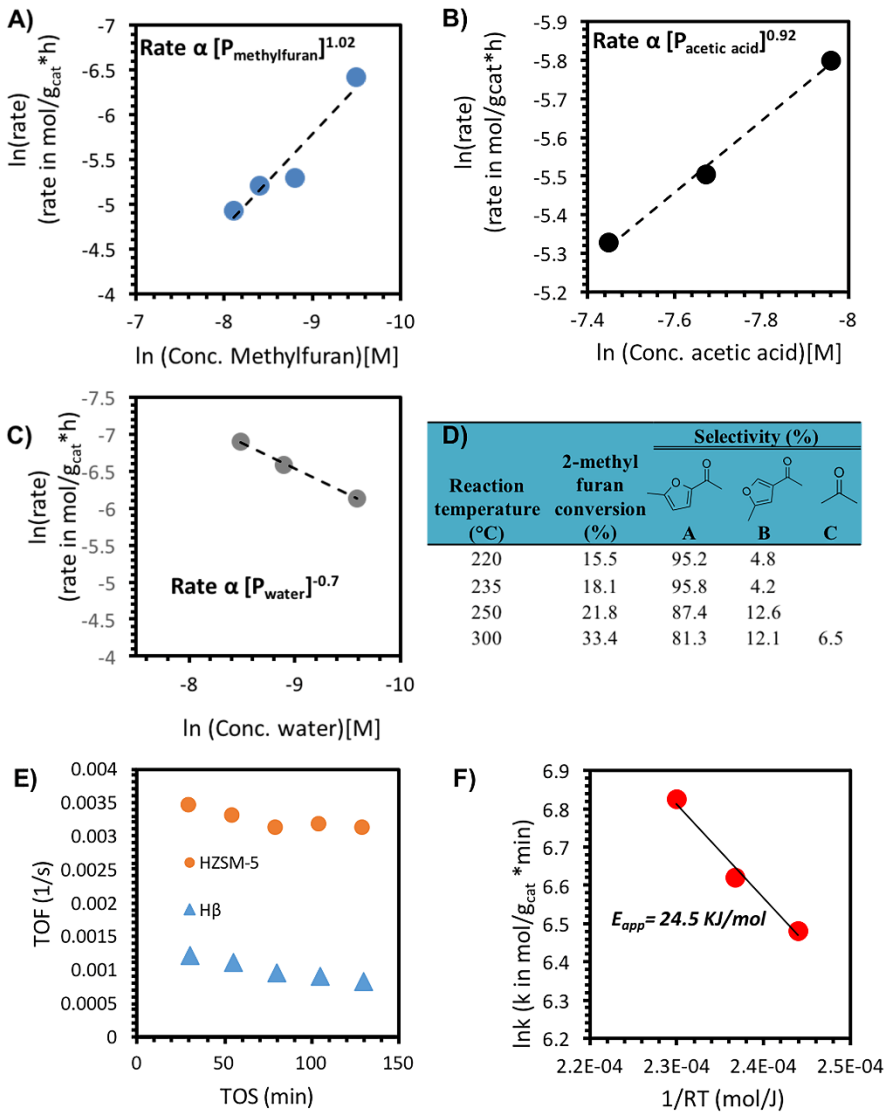

Figure 15 :- Reaction kinetics of methylfuran acylation with acetic acid over HZSM-5. Natural logarithm of acylation reaction rate vs. (A) concentration of acetic acid (B) concentration of 2-methyl furan and (C) concentration of water over CBV8014 at a reaction temperature of 250 °C, 0.05mg catalyst and 30min time on stream. The included table (D) shows conversion and product selectivities observed upon passing 2-methyl furan and acetic acid over HZSM-5 after 30min time on stream at a constant W/F of 0.19 h with respect to acetic acid fed. (E) Turnover frequency of 2-methyl furan acylation with acetic acid over HZSM-5 and Hβ as a function of time at 250 °C and 0.05mg catalyst (F) Apparent activation energy of acetic acid acylation over HZSM-5 estimated for a temperature range of 220-250 °C.

The role of zeolite topology was investigated through comparing the catalytic activity over HZSM-5 with Hβ zeolite (CP814C, Zeolyst international, SiO_2/Al_2O_3=38). Figure 15 (E) shows the turnover frequency (TOF) for 2-methyl furan acylation with acetic acid over these two zeolites. Surprisingly, HZSM-5 has far better activity in comparison with the larger pored Hβ.

The apparent activation energy for acylation was estimated using an Arrhenius plot over the temperature range of 220-250 °C. The obtained apparent activation energy corresponds only to acylation reaction, as no side reactions were observed under these conditions. As shown in Figure 15 (F), the estimated apparent barrier is 24.5 kJ/mole. By contrast the apparent energy for the ketonization of acetic acid over HZSM-5 was 67 kJ/mole, as shown in the supplemental information (Fig. S9). We have previously shown that acetic acid selectively undergoes decarboxylative ketonization at temperatures above 250 °C in the absence of a co-reactant that may react with surface acyl species. Temperature programmed desorption experiments and infrared spectroscopy reveals an initial dehydration step that produces surface bound acyl species on Brønsted acid sites of HZSM-5. The acetone reported in this study at 300 °C is due to this ketonization reaction. The apparent barrier for acylation is significantly lower than that of ketonization, which could suggest the energy required to couple an acyl with methylfuran is significantly lower than the coupling of an acyl with a carboxylic acid to yield a β-keto acid once adsorption energies are considered.

Evaluating Rate determining step and reaction energies from DFT

Further information regarding the coupling pathway and resulting energetics are gained through dispersion-corrected DFT calculations (see detailed methods in supplemental materials). Hybrid functional calculations have also been performed because DFT calculations may underestimate the reaction barriers caused by the charge delocalization error of the approximate exchange-correlation functionals.[85] The whole acylation reaction occurs on two oxygen atoms bound to the same Al atom (Figure 16). First, acetic acid adsorbs on HZSM-5 by forming H-bonds with Brønsted acid sites, and subsequently, acyl species and water form with a true energy barrier of 104 kJ/mol or an apparent barrier of 16 kJ/mol due to very exothermic adsorption of acetic acid resulting from both the H-bond and the structural confinement. We obtain an enhanced apparent barrier of 40 kJ/mol using the hybrid functional [83, 84]. It should be noted that all of the calculated adsorption enthalpy values are very similar between DFT and hybrid calculations, while the transition states are more stabilized by the semi-local PBE functional[78] due to the charge delocalization. The apparent activation energy obtained experimentally of 24.5 kJ/mole while 1st order with respect to the reactants (Figure 15) agrees well with the apparent barrier from DFT and hybrid functional calculations suggesting that acyl formation is the rate-limiting step. Rapid evolution of acetyl methyl furan upon pulsing methylfuran over an isothermal acyl covered surface (Figure 14 B) also indicates that C-C coupling between methylfuran and a surface acyl exhibits a lower barrier than acetic acid self coupling, which is in agreement with acyl formation as the rate-limiting step. Contrasting these results with those observed over Hβ zeolite, as shown in Fig. S8 in Appendix-B, the adsorption of acetic acid is more

strongly stabilized in HZSM-5. This subsequently leads to a higher activation energy barrier for Hβ when referencing the gas phase acid and the transition state for acyl formation. Because this step appears to be the rate-determining step, all subsequent discussion will focus on HZSM-5.

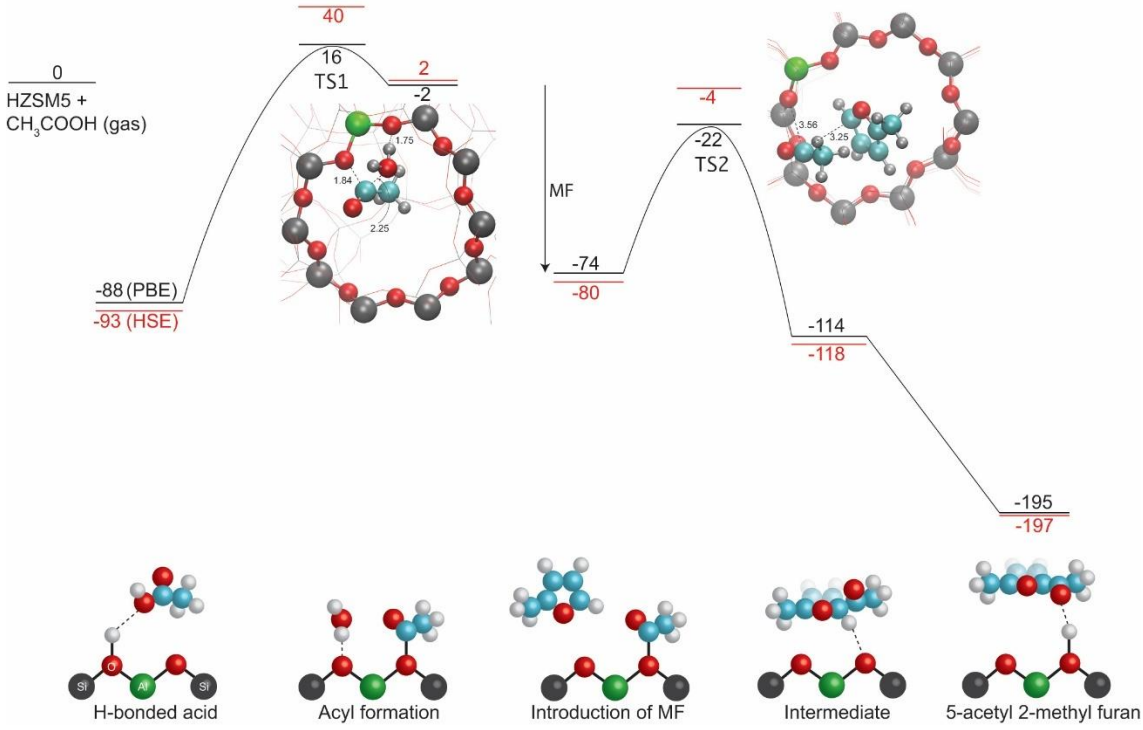

Figure 16 :- Density-functional-theory calculations of acylation of 2-methyl furan with acetic acid. All the values are reported in kJ/mol. The transition states are shown as the insets with C, O, H, Si, and Al atoms colored cyan, red, grey, black and green, respectively. The results calculated using the HSE hybrid functional (red) is also shown to compare with the PBE results (black). The reaction path is schematically shown at the bottom.

When 2-methyl furan (MF) is introduced, MF reacts with the surface acyl group to form an intermediate species, which is deprotonated subsequently to recover both the molecular aromaticity and the Brønsted acid site leading to a large energy gain. The apparent barrier of formation of 5-acetyl 2-methy furan from MF and acyl becomes negative due to the large heat of adsorption of MF. The overall barrier of acylation is

thus determined by the acyl formation rather than the C-C coupling, the latter of which may be more pronounced in ketonization.

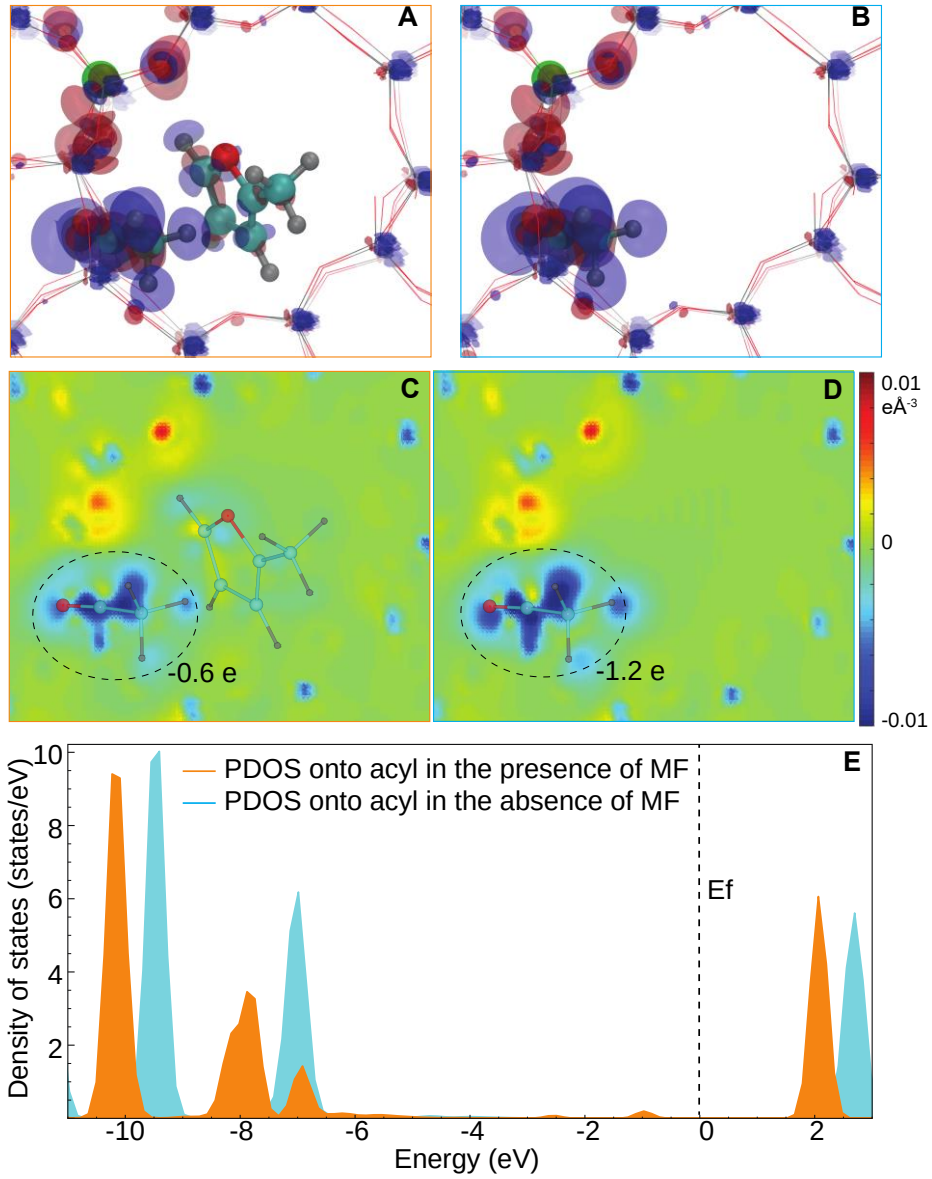

Figure 17 :- Charge transfer and density of states (DOS) calculated using the hybrid functional. (A), charge transfer between the molecules (the desorbed acyl and MF) and the zeolite framework in the transition state of the C-C coupling step. (B), the same charge transfer in the absence of the MF molecule. Red and Blue indicates charge accumulation (negative charge) and charge depletion (positive charge). The isosurface corresponds to a charge density of ±0.015 eÅ^{-3}. (C-D), plane-averaged charge transfer (see methods in supporting information) of the same area as in (A-B). Electron depletion at the desorbed acyl (indicated by dashed circles) via the Bader charge analysis is also shown. (E) Projected DOS onto the desorbed acyl species (acylium ion) in (A) and (B).

The direct desorption of the acyl species in the absence of 2-methy furan is very endothermic with an energy cost of 116 kJ/mol, which is much larger than the true activation barrier of 76 kJ/mol for the C-C coupling step. Figure 17 (A) shows the charge transfer between the complex (the desorbed acyl and MF) and the zeolite framework in the transition state of the C-C coupling step. To compensate the charge in the zeolite framework, a certain number of electrons flow from the complex to zeolite, evidenced by the charge depletion in the desorbed acyl and the MF molecule and charge accumulation at the oxygen atoms bonded to the Al. Integration of the charges via Bader analysis gives a total number of electron transfer of 1.2 electrons to the zeolite framework including 0.6 electrons from the desorbed acyl (acylium ion), as shown in Figure 17 (C), and 0.6 electrons from the MF. In the absence of MF, the integrated charge of 1.2 electrons is all located at the acylium ion (Figure 17 (D)). In addition, the interaction between the acylium ion and the MF molecule broadens the occupied states (close to the Fermi level) of the acylium ion as shown in the Projected Density of States (PDOS) in Figure 17 (E). This charge delocalization and electronic hybridization caused by MF in the proximity stabilizes the acylium ion and lowers the activation barrier in the C-C coupling step.

Conclusion

The results presented here illustrate the stable and selective C-C coupling of two biomass derived species, acetic acid and methyl furan, that when introduced alone to Brønsted zeolite catalysts lead to polymerization and coke formation [9, 89]. This is a promising new route for the conversion of biomass derived streams to higher value fuels and chemicals without sacrificing carbon as CO_2 in the process. Alternative

approaches to upgrading of acetic acid such as ketonization exhibit a larger apparent barrier for C-C coupling. The high abundance of surface acyl groups present when acetic acid is introduced alone to a zeolite are in equilibrium with ketene species that lead to uncontrollable coke formation and catalyst deactivation[9]. Furanic species are known to polymerize over of Brønsted acid sites even under ambient conditions [89]. In the scenario presented here, the low activation barrier for methyl furan coupling to acyl species allows for the stable production of C-C bonds while avoiding these undesired side reactions.

Flow reaction studies show that the direct acylation of 2-methyl furan with acetic acid over HZSM-5 is a relatively stable reaction, to produce predominantly 5-acetyl 2-methyl furan. Acetone is observed as a side product with insignificant concentrations at temperatures below 300 °C under the reactant concentrations used here. Water inhibits the rate, but does not detrimentally influence selectivity. Further, as shown with high partial pressures of acetic acid, water may improve catalyst stability at higher temperatures [9]. Streams consisting primarily of acetic acid, furfural, and water can be produced from the torrefaction of lignocellulosic biomass[74], and the conversion of furfural has been shown to selectively produce furan or methylfuran over a variety of catalysts[76, 90]. It should be noted that furfural conversion has shown to not be inhibited by the presence of acetic acid[91]. This implies that this selective acylation reaction could be applied to upgrade biomass-derived streams containing water.

Results in Figure 15 (E) emphasize the importance of topology for this reaction. HZSM-5, with a smaller pore size than Hβ zeolites, exhibits a higher turnover frequency and improved catalyst stability for this reaction. Apesteguia et al.[92], upon

studying the acylation of phenol with zeolites also reported superior performance for HZSM-5 compared to larger pored HY zeolites. This suggests that confinement plays an important role in this reaction.

Charge analysis from DFT (Figure 17) implies that the ability of the methylfuran molecule to compensate the charge of the acylium ion in the transition state may significantly reduce the barrier for C-C coupling. In the case of methylfuran, the reduction in the barrier is significant enough to shift the rate determining step to the rate of acid dehydration. This could explain the stability of the catalyst under these conditions, as the rapid coupling of methylfuran with surface acyl groups will decrease the population of surface acyl species that could otherwise convert to ketenes and subsequently carbonaceous deposits. In addition, low partial pressures of methylfuran and a high coverage of acetic acid will likely avoid the excessive furan polymerization over Brønsted zeolites. These calculations demonstrate the importance of the ability of methylfuran to stabilize the charge of the acylium ion at the transition state, which may be generally true for other C-C coupling reactions involving a charged species.

Chapter 4: Kinetics and mechanism of acetic acid ketonization over HZSM-5

All the data presented in this chapter is obtained at University of Oklahoma. The DFT calculations as a part of this work were performed by Dr. Bin Wang.

Introduction

Fossil fuels are concentrated organic compounds created from the remains of plants and animals that lived millions of years ago in the form of concentrated biomass. These resources make our modern day life possible by providing energy to generate electricity, power transportation systems and manufacture commercial goods. The usage of these fuels has an adverse effect on environment due to the greenhouse gas (carbon dioxide CO_2) emissions leading to climate changes and global warming. The need of the hour is to replace fossil fuel with alternative energy source and reduce the greenhouse gas emissions. Thus, bio-fuel produced from renewable energy resources like switchgrass or oak is a perfect substitute as it lowers the net CO_2 emission into the atmosphere. Most efficient method proposed to generate bio-oil is by rapid heating of lignocellulosic biomass (switchgrass or oak) in absence of oxygen a process known as pyrolysis. Upgrading of bio-oil to fuels and chemicals is not a simple process, as bio-oil is a complicated mixture and contains wide variety of compounds. The highly reactive carboxylic acids groups present in bio-oil makes it very unstable and complicates the process of further upgradation. These acids mainly acetic acid quantify to approximately 10% by weight in bio-oil, therefore converting them to light gases by traditional processes

is not economical and limits the amount carbon that can be incorporated into gasoline or diesel.

Several groups have worked extensively to convert these acids to more stable ketones through ketonization reaction and in process removes oxygen in the form of water and CO_2. This surface catalyzed reaction is well understood over reducible oxides and metal-oxides. In the recent past there is a decent agreement regarding the mechanism involved for this reaction with rate limiting step being C-C coupling producing betaketoacid type intermediate. Ketones produced from this reaction are good building block to increase the carbon chain length via aldol condensation followed by hydro-deoxygenation to yield fuels and chemicals.

The possibility of this reaction is least explored over zeolite catalysts which are proved to be promising catalysts in upgrading bio-oil. The ability of Brønsted acid sites to readily activate ketones and formation of ketenes under certain conditions complicates a detailed understanding of this reaction over zeolites. In our recent study, we have shown possibility of converting acetic acid selectively to acetone over Brønsted acid zeolites with MFI framework. Based on experimental evidence we have reported intermediates for ketonization reaction over HZSM-5. The overall mechanism is found to be very different from reducible oxides. Adsorption of acetic acid over a Brønsted acid site leads to dehydration producing water and leaving a reactive acyl group on the surface. This acylium ion which is in equilibrium with the surface acyl attacks another activated acid to yield a dimer which is kinetically relevant step.

In this current study, we attempt to obtain a detailed understanding of the acetic acid ketonization mechanism and reaction intermediates involved via kinetic modelling. A

detailed kinetic investigation, using a Langmuir–Hinshelwood model kinetic fitting involving single Brønsted site, combined with the transition state theory analysis is performed to calculate the activation energy barrier for ketonization reaction over HZSM-5. Here we are reporting kinetic and thermodynamic parameters after rigorous catalytic kinetics analysis of the experimental data. Computational simulations using density functional theory are done to confirm the authenticity of parameters obtained from experimental fitting. Theoretical calculations validate the assumption of rate limiting step for this reaction being a C-C coupling of acylium ion and an enolate. A good agreement is observed for kinetic and thermodynamic parameters between kinetic fitting and DFT study.

Experimental

Catalyst preparation.

All the experimental studies in the article have been carried out over ZSM-5 catalyst (CBV-8014) with a SiO_2/Al_2O_3=80 purchased from Zeolyst International. The commercial form of CBV8014 is in the ammonium form which is converted to proton form upon calcining in dry air at 600 °C for 5 hours. After calcination the catalyst is pelletized using a hydraulic press and subsequently crushed and sieved to particles with sizes ranging from 90-250 μm.

Catalyst characterization.

A detailed characterization for H-form of CBV8014 has been reported in a recent publication from our group. X-Ray Diffraction study ensured the catalyst has retained crystallinity and has not collapsed upon calcination. The particle diameter of CBV8014

was estimated from Scanning electron microscopy (SEM) using Zeiss-NEON FEG-SEM instrument shows a distribution of particles ranging from 100-500nm. Isopropyl amine (IPA) temperature-programmed desorption (TPD) experiment revealed the concentration of Brønsted acid sites in CBV8014. Quantifying the propylene desorbing from the zeolite bed saturated with IPA upon heating gives a measure of number of protons per gram of catalyst.

Continuous flow reactions

Experimental reaction data was obtained by performing reactions in a quartz tube reactor (1/4" OD) at atmospheric pressure and temperatures varying from 280-310°C. Measured amount of catalyst was diluted with acid washed glass beads of same size as catalyst pellets and packed in the quartz tube reactor between quartz wool. The temperature of the catalyst bed was controlled by attaching a thermocouple to the wall of the reactor. The temperature of the inlet of the reactor was maintained was maintained at 90 °C to create vaporization zone for the acetic acid (Sigma Aldrich, ACS reagent, ≥99.7%) being fed through syringe and septum. The outlet of the reactor, which was connected to a six-port valve for sampling, is heated to 250°C to avoid condensation of unconverted reactants and products. Before introducing acetic acid on to the catalyst bed, it was flushed in helium flow of 125 ml/min for one hour at 300 °C to remove water. The outlet stream leaving the reactor is analyzed at the desired time on stream (TOS) using a Hewlett Packard 6890 gas chromatograph equipped with a flame ionization detector and an innowax column of dimensions 30m and 0.25 µm. The vapors downstream of the six-port valve were condensed in a sample bubbler using ice and water as a coolant medium.

Density functional theory calculations

DFT calculations were carried out using the VASP (Vienna ab initio simulation) package. The PBE generalized gradient approximation exchange-correlation potential was used, and the electron-core interactions were treated in the projector augmented wave method. The van der Waals interaction was taken into account through the so-called DFT-D3 semiempirical methods via a pairwise force field. An HSE hybrid functional was also used to calculate the total energy of the initial, transition, and final states that were already optimized by DFT-D3 calculations to reduce underestimation of the reaction barriers caused by the charge delocalization error of the local and semilocal exchange-correlation functionals. The nudged elastic band method was used to find the transition state and calculate the reaction barriers. The transition states were further verified by vibrational calculations. All the calculations were performed using a ZSM-5 unit cell including 96Si and 192O atoms. One Si atom at the T12 site, which was located at the intersection and more accessible to reactions, as replaced by one Al atom; thus, the Si/Al ratio is 95:1. The proton was initially attached to the O atom that was between the Al atom and the nearest T12 Si atom. The structure of the unit cell was taken from an experimental work (a = 20.078 Å; b = 19.894 Å; c = 13.372 Å and fixed during the calculation. Atomic relaxation was performed using a single G point of the Brillouin zone with a kinetic cutoff energy of 400 eV. A further increase of k-point sampling to (1 × 1 × 2) does not change the reaction energetics. All the atoms (zeolite and the molecules) were fully relaxed until the atomic forces were smaller than 0.02 eV Å−1.

Results and discussion

Acetic acid ketonization reaction mechanism and identifying kinetically relevant step

In our previous study conditions necessary to convert acetic acid to acetone over HZSM-5 in the gas phase with nearly 100% selectivity to the ketonization reaction were identified. Formation of aldol condensation products from acetone were negligible within a reaction temperature range of 270-330 °C. Temperature programmed desorption studies along with Infrared spectroscopy studies revealed an initial dehydration step is involved in the reaction pathway to yield a surface acyl species in equilibrium with an acylium ion. This acylium ion couples with a second acid followed by decarboxylation to yield acetone and CO_2. Nature of activation of second acid is speculated to be in the form of a enolate like species. Upon varying concentration of acetic acid fed, ketonization reaction order is observed to be 1.6 with respect to surface adsorbed acetic acid.

Scheme-1 describes all the elementary steps involved acetic acid ketonization over CBV8014. Brønsted acid sites in the zeolite are believed to be the active sites for this reaction. It was found that the ketonization reaction rate reduced as the Brønsted acid sites were converted to Lewis sites upon exchange with sodium. The drop in turnover frequency correlated with the number of sites being exchanged. Thus, it can be deduced that only Brønsted sites are responsible for producing acetone from acetic acid and Lewis sites created by sodium exchange do not necessarily affect the reaction rate. The probable sequence of ketonization elementary steps in scheme-1 is assumed to be involving one Brønsted site. The adsorption and equilibrium constants will be denoted

by capital letter “K” with a subscript indicating the step, while the rate constant for the rate limiting step of the reaction is described as small letter “k”.

Initial adsorption of acetic acid occurs through O-atom of the OH group in the acid molecule over a Brønsted site (O-Al-O) (step-1 in Scheme-1). The proton from the Brønsted site is then abstracted to form water and acylium ion which is in equilibrium with the surface compensating the charge on zeolite surface (step-2 in Scheme-1). Dehydration to form water was initially evidenced by the evolution of water peak in TPD and further supported by the appearance of acyl peak in Infrared spectroscopy when CBV8014 saturated with acetic acid was heated to 150°C. Formation of acylium ion is a reversible step and also water is known to compete for Brønsted site. Thus presence of water can potentially shift the equilibrium away from dehydration step and reduce the concentration of acyl species on the surface. Over acid zeolite catalysts acetic acid is reported to make ketene like species which are generally considered as coke precursor and are largely responsible for catalyst deactivation. These ketene species can react with acetic acid to produce acetic anhydride. In Freidel-Craft acylation reactions, acetic anhydride is used as an acylating agent that can readily decompose to form surface acyl species and acetic acid over Brønsted and Lewis acid catalysts. If ketonization reaction mechanism follows via acetic anhydride pathway, co-feeding anhydride along with acid should enhance the reaction rate. But in our study it was observed that introduction of acetic anhydride kills the activity of the catalyst for ketonization reaction almost instantaneously before witnessing any yields of product. This suggests that the ease of activation anhydride populates the surface with ketene-like species and these intermediates are not involved in ketonization reaction

mechanism. Therefore, the overall forward reaction rate is driven by formation of acylium ion upon dehydration followed by the coupling of acylium ion with second acid. Direct C-C coupling of acylium ion and carboxylic acid is energetically unfavorable which will be discussed in detail in section-3.3.

The path of least energy barrier involves activation of second acid to form an enolate and followed by coupling of enolate with acylium ion. Formation of enolate is initiated by the adsorption of second acid on to the neighboring O-atom of the same O-Al-O site via H-bonding as demonstrated in step-3a in Scheme-1. This is followed by the alpha hydrogen cleavage to form a surface bound enolate species (step-3b in Scheme-1). Rate of forward and reverse reaction for these two sub steps 3(a,b) in forming enolate are a function of partial pressure of acetic acid and are in equilibrium. Therefore, the constants for these steps can be combined and one adsorption constant for the formation of enolate can be defined as $K_{complex}=K_{acid2}K_{enolate}$. The acylium ion nucleophically attacks the carbon in the methyl function of the enolate to form a complex dimer containing a new C-C bond. This complex is highly reactive and dissociates very rapidly forming acetone and CO_2 by decarboxylation and subsequently regenerates the proton on the zeolite surface.

1. Adsorption of acetic acid over a Brønsted acid site (O-Al-O)

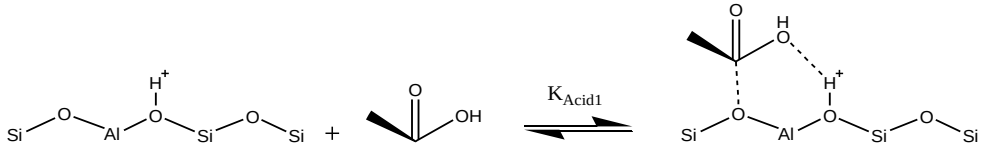

2. Dehydration of adsorbed acetic acid to form water and acylium ion equilibrium with zeolite surface

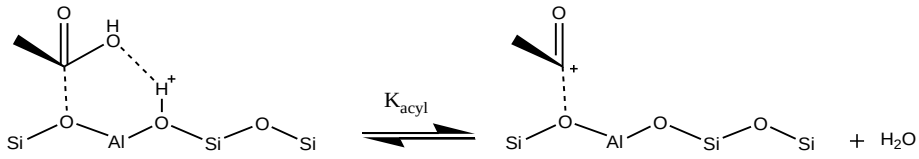

3. (a) Co-adsorption of second acetic acid molecule on the same O-Al-O site via hydrogen bonding

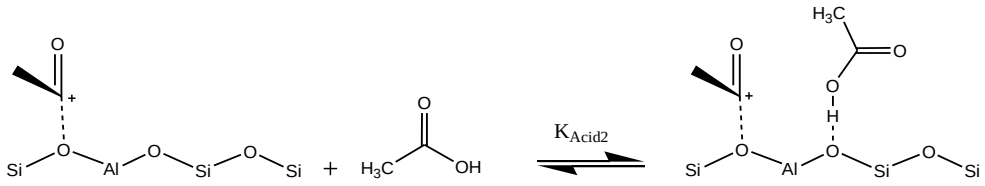

(b) Abstraction of Alpha-C-H and formation of O-H bond to a surface bound enolate

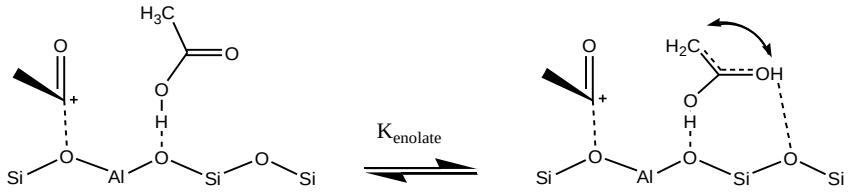

4. Coupling of surface acyl with enolate to forming a new C-C bond

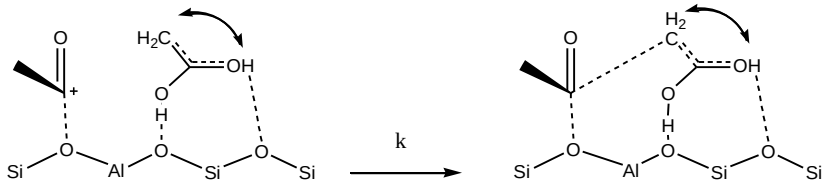

5. Decarboxylation of the dimer yielding acetone and CO_2 after regenerating the Brønsted acid site by the donating proton back to the surface

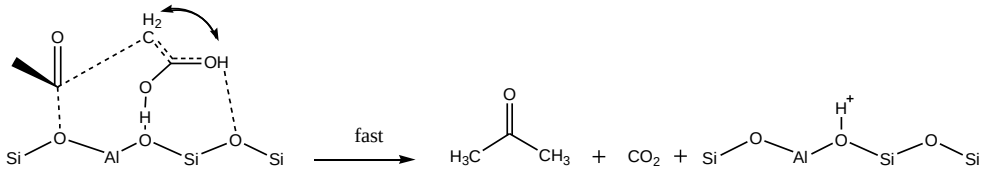

6. Adsorption of acetone over a Brønsted acid site (O-Al-O)

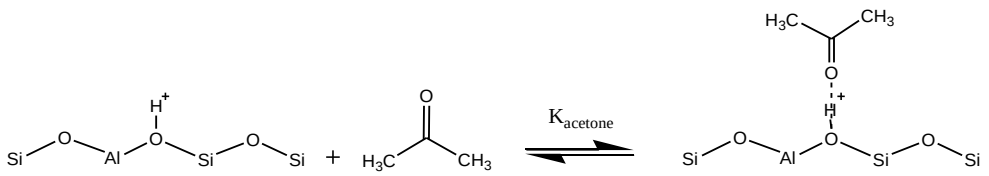

7. Adsorption of CO_2 over a Brønsted acid site (O-Al-O)

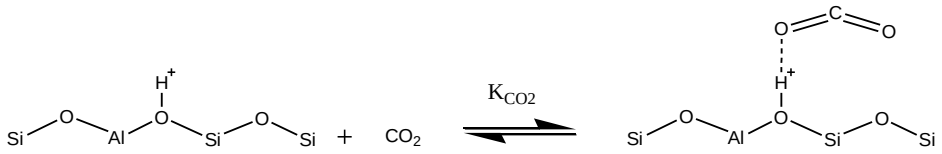

8. Adsorption of water over a Brønsted acid site (O-Al-O)

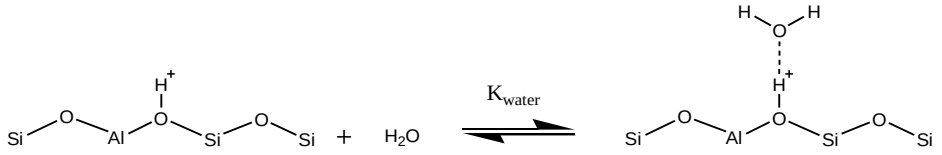

Our previous study reported second order dependence of acetic acid ketonization rate with respect to surface concentration of adsorbed acid on CBV8014. While in TPD experiment C-C coupling products appeared at 250 °C compared to dehydration product

which were observed at 150 °C suggesting dehydration is a faster step in reaction mechanism and needs less energy. Studying acylation of 2-methylfuran with acetic acid as acylating agent the apparent barrier for the acylation reaction is reported to be 24.5 kJ/mol, while the apparent barrier for ketonization reaction is 67 kJ/mol. Both reaction pathways are involving dehydration of acetic acid to form surface acyl. The kinetically relevant step for acylation reaction is speculated to be formation of surface acyl from dehydration of acetic acid over a Brønsted site. If ketonization of acetic acid also has the same rate determining step, then the apparent barriers for acylation and ketonization reactions should not be very different. This higher barrier requirement to form C-C products in ketonization reaction and second order dependence of rate on acid concentration advocates that two acid molecules are involved in determining ketonization reaction rate. These results suggest that the rate of acetic acid ketonization reaction is not limited by formation of acylium ion. Therefore, activation of second acid to form an enolate (step-3 in scheme-1), C-C coupling of surface acyl and enolate (step-4 in scheme-1) and decarboxylation of the complex dimer (step-5 in scheme-1) formed after C-C coupling are the only possible rate limiting steps.

Nucleophilic attack of acylium ion with second activated acid producing acetone and CO_2 involves formation of new C-C bond. Activation of second acid to form enolate is associated with breakage of alpha carbon-hydrogen bond and formation of a new O-H bond. Both these steps could potentially influence the reaction rate of acetic acid ketonization over CBV8014. If breaking of C-H bond or formation of O-H bond is a kinetically relevant step, then the exchange of H with Deuterium should exhibit a primary kinetic isotope effect (KIE). We reported that replacing acetic acid with

deuterium exchanged acetic acid exhibited no primary KIE. This shows that C-H and O-H bond does not significantly determine the rate of acetic acid ketonization reaction. Therefore, the formation of C-C between acylium ion and enolate or the decarboxylation of the complex dimer could be the rate determining step. Dissociation of these complex intermediates like beta-keto acid is reported to be a very fast reaction which happens instantaneously. All the kinetic fitting in the next section are done based on the assumption that surface reaction between acylium ion and enolate is the only rate limiting step. This is also demonstrated by DFT calculations in the later sections while studying the energetics involved the reaction.

Langmuir-Hinshelwood kinetic model and fitting

The elementary steps derived in scheme-1 are incorporated in a Langmuir-Hinshelwood kinetic model to describe acetic acid ketonization reaction kinetics involving one Brønsted acid site. The following assumptions were made in developing the kinetic model (1) All the Brønsted acid sites are equivalent and independent of surface coverage (2) All the reactants and products are equally likely to occupy the active site (3) Carbon-Carbon coupling between the acylium ion and enolate is the rate determining step (4) Decarboxylation of C-C coupled dimer is fast and irreversible (5) All the steps are in equilibrium except C-C coupling and decarboxylation. The rate expression for the acetic acid ketonization reaction over CBV8014 is shown in eq-1. A detailed derivation of rate equation has been shown in supporting information. The numerator in the rate equation shows the strong dependence of the rate on the partial pressure of acetic acid.

$$rate = \frac{kK_{Acid1}K_{Acyl}K_{complex}P_{Acid}^2}{P_{H_2O}\left(1 + K_{Acid1}P_{Acid} + \frac{K_{Acyl}K_{Acid1}P_{Acid}}{P_{H_2O}} + \frac{K_{Acyl}K_{Acid1}K_{complex}P_{Acid}^2}{P_{H_2O}} + K_{Ketone}P_{Ketone} + K_{H_2O}P_{H_2O} + K_{CO_2}P_{CO_2}\right)}$$

Extensive experimental data for acetic acid ketonization reaction was obtained by performing vapor phase reaction in an atmospheric plug flow reactor at reaction temperatures of 280, 290, 300 and 310 °C. W/F for the reactions was varied by changing the catalyst weight and maintaining the partial pressure of acetic acid constant. The experimental data obtained to fit with the kinetic model was collected under the conditions without external and internal mass transfer limitations. In our previous study we have identified and reported the kinetic limited regime for the ketonization reaction of acetic acid over HZSM-5. To evaluate the reaction is not external mass transfer limited the carrier gas flowrate was varied keeping the partial pressure of acetic acid same. By poisoning the active sites with sodium internal mass transfer limitations were evaluated. Complete details of mass transfer limitation tests are reported. In the current study, partial pressure acetic acid was kept constant at 0.0043 mol/hr and helium was used as carrier gas at 125 ml/min.

Figure 18 (a,b,c,d) shows the evolution of partial pressures of acetic acid and acetone for acetic acid ketonization reaction as a function of W/F for reaction temperatures 280, 290, 300 and 310 °C. The solid symbols in the figure-1 represents the experimentally obtained data while the solid lines in each case depicts fitted partial pressures using the Langmuir–Hinshelwood model described above. The adsorption/equilibrium constants are obtained at different temperatures from regressed kinetic fitting of experimental data. By using conventional Van't Hoff equation these constants are plotted as a function of temperature to obtain enthalpies (ΔH) and

entropies (ΔS) of adsorption from slope and intercept respectively. The equilibrium adsorption enthalpies and entropies for the acetic acid, acetone, water, CO_2 and complex resulting from the fitting at different temperatures are summarized in Table 1. Detailed plots of the fitting are reported in supporting information.

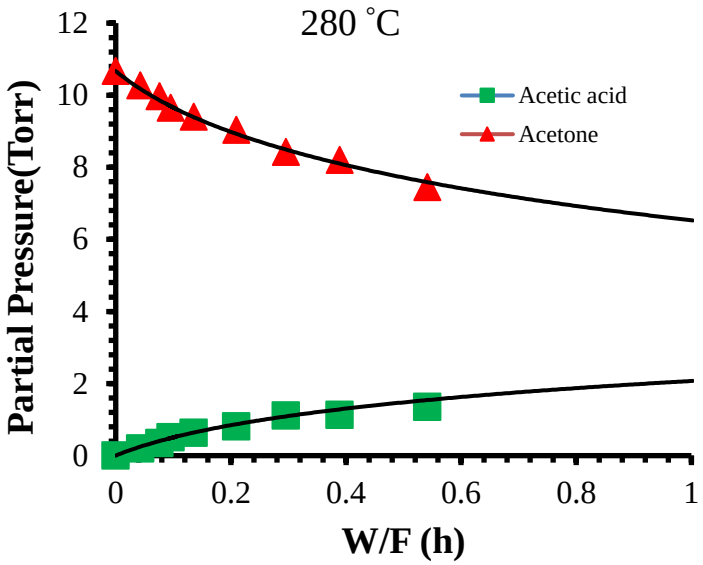

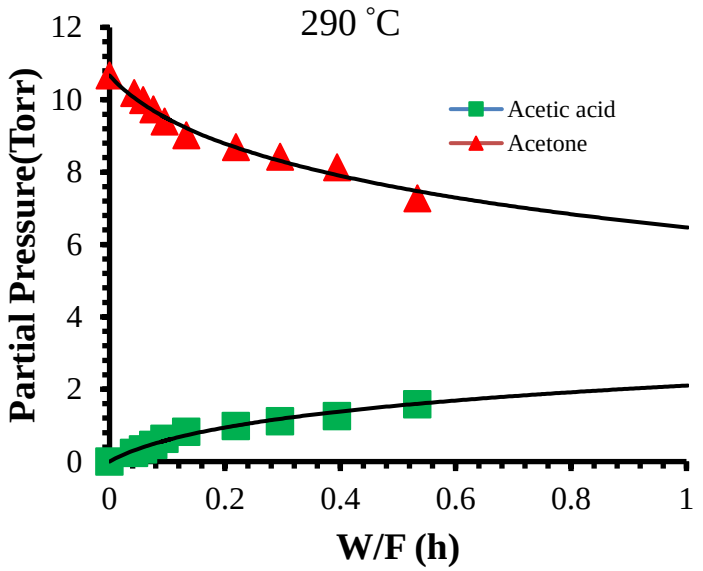

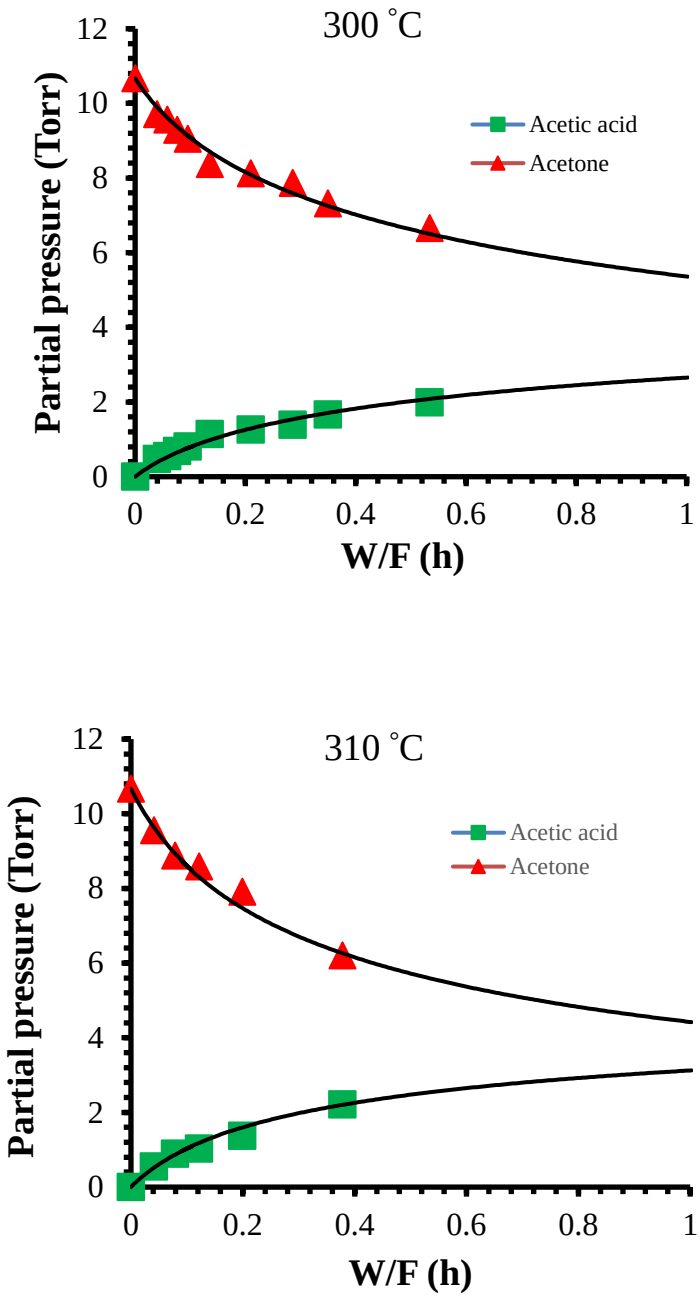

Figure 18 (a,b,c,d) :- Evolution of acetic acid and acetone as a function of W/Fat 30min time on stream over CBV8014 at temperature of 280, 290, 300 and 310 °C.

	ΔH ads, (kJ/mol)	ΔS ads, (J/mol K)
Acetic acid	**-138**	**-247**
Acetone	**-112**	**-210**
Water	**-50**	**-105**
CO_2	**-32**	**-121**
Complex	**-100**	**-232**

Table 1 :- Adsorption enthalpy and entropy of acetic acid, acetone, water and CO_2 calculated from Van't Hoff's plot

Similar to reducible metal oxides acetic acid exhibited stronger adsorption enthalpy over zeolite too in comparison with acetone, water and CO_2. From micro calorimetry studies Kresnawahjuesa et al measured heat of adsorption of acetic acid over HZSM-5 to be -139 kJ/mol, which is in perfect agreement with the value obtained in the current study. Similarly adsorption enthalpies of acetone, water and CO_2 are in line with the values reported in the literature by various groups. Equilibrium constant of the complex which is a dependent on the coverage of second acid has lower heat of adsorption of -100 kJ/mol in contrast to adsorption of first acid over a Brønsted acid site. This weak binding of second acid is understood to be due to the presence of acylium ion over the active site.

The structure and configuration of transition state for acetic acid ketonization reaction over CBV8014 can be speculated to be similar to the complex illustrated in step-4 of scheme-1. This activated complex which is in equilibrium with the reactants readily converts into C-C coupled dimer upon single vibration. The transition state

theory can provide a physical justification to the kinetic parameters derived from the fitting as well as some insight into the structure and configuration of the transition state involved in the chemical reaction. As proposed earlier, the rate-limiting step can be described in terms of transition state theory by the following equation-2.

$$RCO^{+} + RCOOH \xleftrightarrow{K^{\#}} [RCO^{+}/RCOOH] \xrightarrow{\nu^{\#}} [RCORCOOH]^{+} \qquad (2)$$

The rate expression for acetic acid ketonization reaction from transition state theory can be expressed as shown in equation-3 where k_B and h are the Boltzmann and Planck constants, respectively. $K^{i\#}$ is the transition state equilibrium constant can be evaluated using Eyring-Polanyi expression. This $K^{i\#}$ value reflects the enthalpy ($\Delta H^{\#}$) and entropy ($\Delta S^{\#}$) of activation for the reaction. Thus equation-3 can be transpired to the following workable equation-4, where $\Delta G^{\#}$ represents the free energy of the rate limiting step for ketonization reaction.

$$rate = \nu^{\#} \frac{k_B T}{h \nu^{\#}} K'^{\#}[RCO^{+}/RCOOH] = \frac{k_B T}{h} K'^{\#}[RCO^{+}/RCOOH] \qquad (3)$$

$$k = \frac{k_B T}{h} \times e^{-\Delta G^{\#}/RT} = \frac{k_B T}{h} \times e^{-\Delta H^{\#}/RT} \times e^{\Delta S^{\#}/R} \qquad (4)$$

The values of rate constant (k) in equation-4 are obtained from regressed fitting of experimental data using the kinetic model at different temperatures. Figure 19 shows the plot of these rate constants for rate determining step as a function of temperature. From this plot the activation enthalpy and entropy of the kinetically relevant step for acetic acid ketonization reaction are calculated to be 127 kJ/mol and -46 J/(mol. K) respectively. These kinetic parameters will be validated from theoretical calculations in the later section. The free energy of activation for carbon-carbon coupling step with

respect to adsorbed dimer is calculated at different temperatures and presented in Table 2. Negative activation entropy with respect to the adsorbed state indicates that the intermediate goes through a transition state with an entropy loss. The tighter confinement of the zeolite pore confines and stabilizes the transition state thereby causing the loss of entropy.

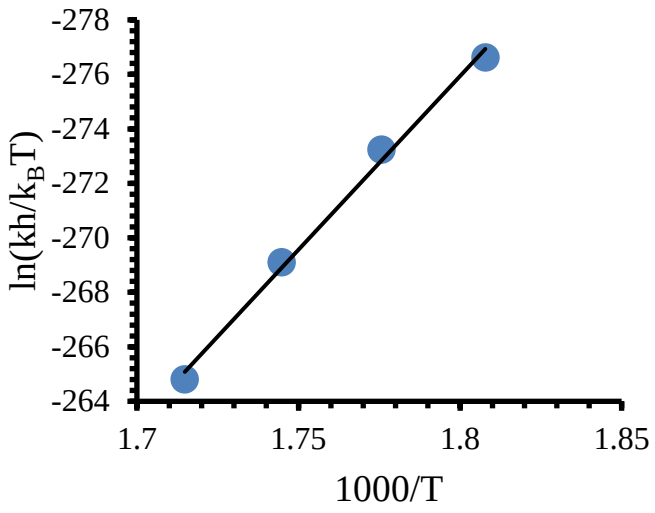

Figure 19 :- Evaluating activation enthalpy and entropy of acetic acid ketonization over CBV8014 using Eyring-Polanyi plot

Temperature (K)	*Activation enthalpy, ΔH (kJ/mol)*	*Activation entropy, ΔS (J/(mol. K))*	*Free energy of activation, ΔG (kJ/mol)*
553	***127***	***-46***	***152.4***
563			***152.9***
573			***153.4***
583			***153.8***

Table 2 :- Activation enthalpy, entropy and free energy for the carbon-carbon coupling step in acetic acid ketonization reaction over CBV8014.

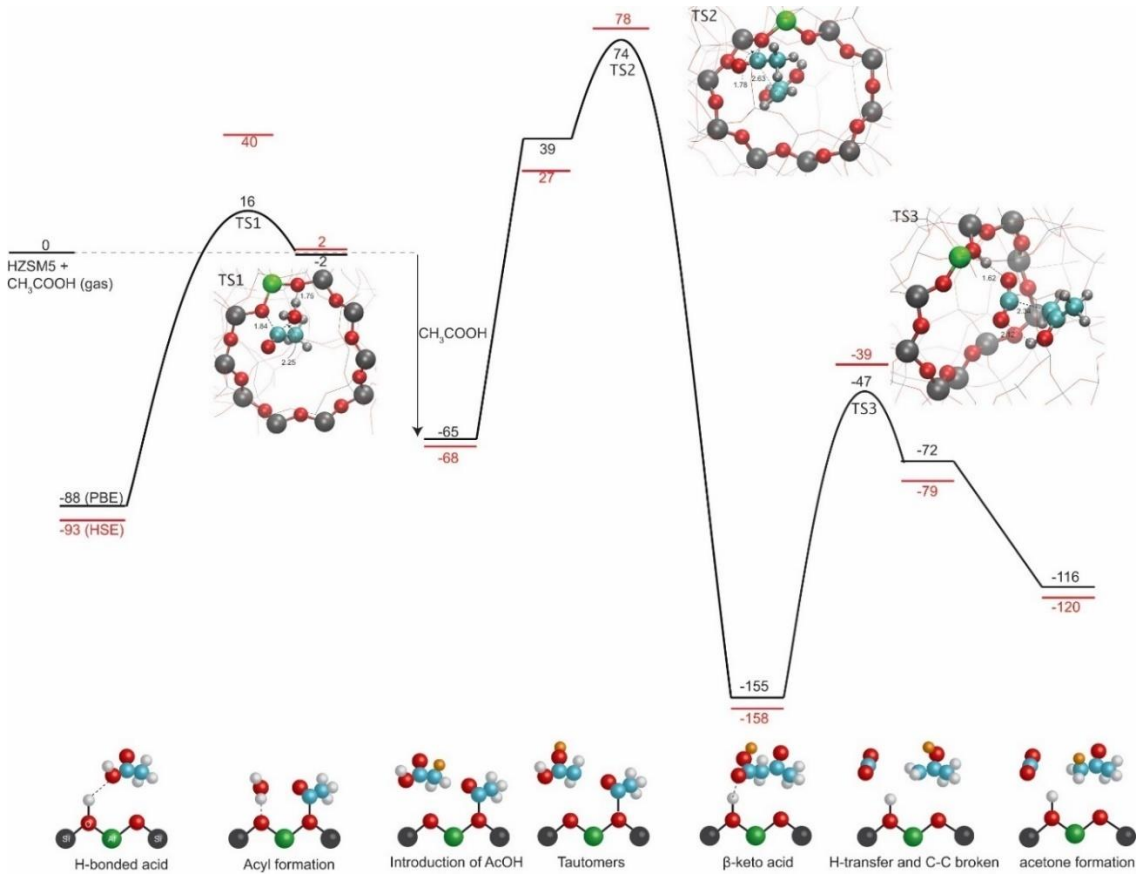

Figure 20 :- DFT-calculated reaction profile for ketonization reaction between two acetic acid molecules in HZSM-5. All the values are reported in kJ/mol. The transition states are shown as the insets. The C, O, H, Si, and Al atoms are colored cyan, red, grey, black and green, respectively. The results calculated using the HSE hybrid functional (red) is also shown to compare with the PBE results (black). The reaction path is schematically shown at the bottom. In the C-C coupling step and decarboxylation of β-keto acid, a hydrogen transfer step is needed. The hydrogen atom involved in the hydrogen transfer is highlighted in orange in the schematics.

DFT calculations have been performed in order to reveal the reaction mechanism using both the PBE functional[78] and the HSE hybrid function[83]. Details of calculation methods have been reported elsewhere[93]. We find the overall reaction involves a few elementary steps – acyl formation from the first acetic acid molecule, formation of a

tautomer from the second acetic acid molecule, C-C coupling between the acyl group and the tautomer to form a β-keto acid intermediate, and decarboxylation of the β-keto acid to form acetone. The acyl formation step has an apparent barrier of 16 kJ/mol from a DFT-PBE calculation[93]. To proceed the C-C coupling step, The hydrogen within (H_3)C-O(=C) in the acetic acid molecule is transferred to form a tautomer (H_2)C-OH(-C). This hydrogen transfer step is barrier less. The formed tautomer couples with the surface acyl group to form a β-keto acid intermediate, which forms a H-bond with the Brønsted acid site. Decomposition of the β-keto acid proceeds in two steps – (1) a cyclic H-transfer from the carboxyl group to the ketone group accompanied by simultaneously breaking the C-C bond and (2) an addition H-transfer to form the acetone product, the latter of which is barrier less. The reaction step to break the C-C bond has a true barrier of 108 kJ/mol from a PBE calculation. We also tried a concerted reaction path for the decarboxylation step, that is, simultaneously breaking C-C bonds with H-transfer from the carboxyl to the CH_2 group, and find a much higher true activation barrier of 307 kJ/mol. Therefore, the two-step decarboxylation reaction is more kinetically favorable. The overall reaction profile shown in Figure 20 suggests the rate-limiting step is the C-C coupling step between the second acetic acid and the surface acyl group with an apparent barrier of 74 kJ/mol. Calculations using the HSE hybrid functional agree with the PBE calculations, and, in most cases, reduce the over-stabilization of the transition states caused by charge delocalization error in semi-local functionals such as PBE[85], and overestimate the molecular adsorption energies[94, 95]. Therefore, calculations using the HSE functional provide higher true activation barriers than ones obtained

from PBE calculations. The HSE-calculated overall reaction barrier for the same reaction profile is 78 kJ/mol as shown in Figure 20.

Conclusion

A detailed reaction scheme was developed involving all the intermediates of the ketonization reaction over HZSM-5. Using these elementary a Langmuir Hienshelwood kinetic model was developed with overall reaction involving one Brønsted site. A systematic kinetic investigation, by regressed fitting of experimental data with Langmuir–Hinshelwood model revealed the adsorption energies involved in this reaction which are in perfect agreement with values reported in literature. Using transition state theory analysis activation enthalpy for ketonization reaction over HZSM-5 was found to be 127 kJ/mol with a negative entropy indicating the tighter transition state due to the confinement. Computational simulations using density functional theory are done to confirm the authenticity of parameters obtained from experimental fitting. Theoretical calculations validate the assumption of rate limiting step for this reaction being a C-C coupling of acylium ion and an enolate. A good agreement is observed for kinetic and thermodynamic parameters between kinetic fitting and DFT study.

Chapter 5: Acylation of oxygenates with acetic acid over Brønsted zeolites

All the data presented in this chapter is obtained at University of Oklahoma. The DFT calculations as a part of this work were performed by Dr. Bin Wang.

Introduction

The carbon efficient conversion of biomass to renewable fuels and chemicals is plagued by highly inefficient processes. One of the greatest contributors to this is the highly abundant acetic acid, which contributes to the formation of humins upon storage. Upgrading of acetic acid to form higher value products is appealing, with perhaps the most promising approach a kinetic decarboxylation to form the stable building block acetone. The primary drawback of this approach is CO_2 that is generated during this coupling reaction. A process that both neutralizes acids while not sacrificing CO_2 in the process would be highly advantageous.

In this contribution, we report that surface intermediates formed in the ketonization reaction, acyl species, [1,2] can be selectively coupled at elevated temperatures with a variety of renewable oxygenates over zeolites. This process does not yield CO_2 as a byproduct, and couples acetic acid to furanic [3] and phenolic rings to yield transportation fuel and commodity chemical precursors. We present a detailed kinetics analysis coupled with DFT calculations to reveal that the rate determining step shifts significantly with the chemical nature of the acyl accepting group. The rate determining step can shift from dehydration to form surface acyls to C-C coupling as we will discuss, with water playing an important role in the degree of rate control of each step. We discuss the influence of water, site proximity, and confinement on this

important reaction, and the implications of these findings on the production of transportation fuel precursors from biomass.

Materials and methods

The catalyst used for this study is CBV8014 which is a commercial ZSM-5 zeolite purchased from Zeolyst international. It has a Si/Al ratio of 40 which is confirmed by characterization using IPA-TPD technique. The catalyst when purchased is in ammonium form and is calcined in air at 600 °C to make proton form of ZSM-5 A detailed characterization of CBV8014 is given Appendix-A.

A typical procedure for gas phase acylation flow reactions of different oxygenates with acetic acid over HZSM-5 is as follows. Catalyst was packed between quartz wool in a 1/4 inch quartz reactor and pretreated at 300 °C for one hour under a helium flow of 125 ml/min to remove physisorbed water. A thermocouple was attached on outside wall of the reactor near the catalyst bed to maintain the reactor temperature. After pretreatment the temperature was adjusted to the required reaction temperature and reactants were fed through a syringe pump. The inlet of the reactor is heated to create a vaporization zone for the reactants and the outlet of the reactor and downstream lines are heated to 250 °C to prevent condensation of products. Samples were taken via a six port valve connected to a HP 6890GC equipped with flame ionization detector and innowax column for analysis.

The density functional theory (DFT) calculations were carried out using the VASP package[77]. The PBE-GGA (Perdew-Burke-Ernzerhof-Generalized-Gradient-Approximation) exchange-correlation potential[78] was used, and the electron-core interactions were treated in the projector augmented wave (PAW) method[79, 80]. The

van der Waals interaction has been taken into account through the so-called DFT-D3 semi-empirical methods via a pair-wise force field[81, 82]. A HSE (Heyd-Scuseria-Ernzerhof) hybrid functional[83, 84] was used as well to calculate the total energy of the initial, transition and final states that have already been optimized by DFT-D3 calculations to reduce underestimation of the reaction barriers caused by the charge delocalization error of the local and semi-local exchange-correlation functionals[85]. The nudged elastic band (NEB)[86] method has been used to find the transition state and calculate reaction barriers. The transition states have been further verified by vibrational calculations.

All the calculations have been performed using a ZSM5 unit cell including 96 Si and 192 O atoms. One Si atom at the T12 site, which is located at the intersection and more accessible to reactions [87], is replaced by one Al atom, so the Si/Al ratio is 95/1. The proton was initially attached to the O that is between the Al and the nearest T12 Si atom. The structure of unit cell was taken from an experimental work (a = 20.078 Å, b = 19.894 Å, c = 13.372 Å)[88] and fixed during the calculation. Atomic relaxation has been performed using a single Γ point of the Brillouin zone with a kinetic cut off energy of 400 eV. Further increase of k-point sampling to (1 × 1 × 2) doesn't change the reaction energetics. All the atoms (zeolite and the molecules) were fully relaxed until the atomic forces were smaller than 0.02 eV $Å^{-1}$.

Results and discussion

In Chapter-3 we have shown the possibility of a new route to directly couple methyl-furan and acetic acid via acylation reaction. From preliminary kinetic data and

theoretical calculations it was suggested that formation of acyl was rate determining step in contrast to carbon-carbon coupling for decarboxylative ketonization reaction. Both the reactions proceed with the same initial step of dehydration of first acetic acid over an acid site to yield surface acyl group. The shift in rate limiting step was observed to be due to the ability of second species i.e., methyl furan to stabilize the charge on the surface acyl by donating the electrons. This ability of methyl furan shifts the kinetically relevant step to acyl formation and reduces the apparent barrier of reaction from 67 kJ/mol to 24.5 kJ/mol. It would be very interesting to study different molecules with the ability to couple with surface acyl. Studying the rates and barriers of this acylation reaction with different acyl acceptors present in biomass torrefaction streams will show insights into this novel approach for direct coupling reaction and convert biomass to fuels and chemicals.

m-cresol acylation with acetic acid

Phenolics are the major compounds present in lignocellulosic biomass torrefaction stream-3[3]. For this study, we have selected m-cresol as an acyl acceptor which is a phenolic representative and acetic acid will be the acylating agent. The ratio of acetic acid to m-cresol was chosen to be 1: 0.22 to reduce the competition by m-cresol for surface active sites thereby reducing the side reactions. This reaction was studied in an atmospheric vapor phase reactor with CBV8014 as the catalyst at three different reaction temperatures (200 °C, 250 °C and 300 °C). The two major products observed in this study are m-tolyl acetate (ester) and acetophenone. The selectivity towards ester was very high at lower temperature of 200 °C while reducing with increase in temperature. This suggests that the formation of ester has a much lower

barrier. Figure 21 shows the selectivities of the products formed at different temperature at a time on stream of 30 min. It is to be noted that the W/F for these reactions were kept constant, so the conversions are slightly different. At higher temperature of 300 °C as expected and discussed in Chapter 2, 3 and 4 ketonization reaction takes place and we observe formation of acetone.

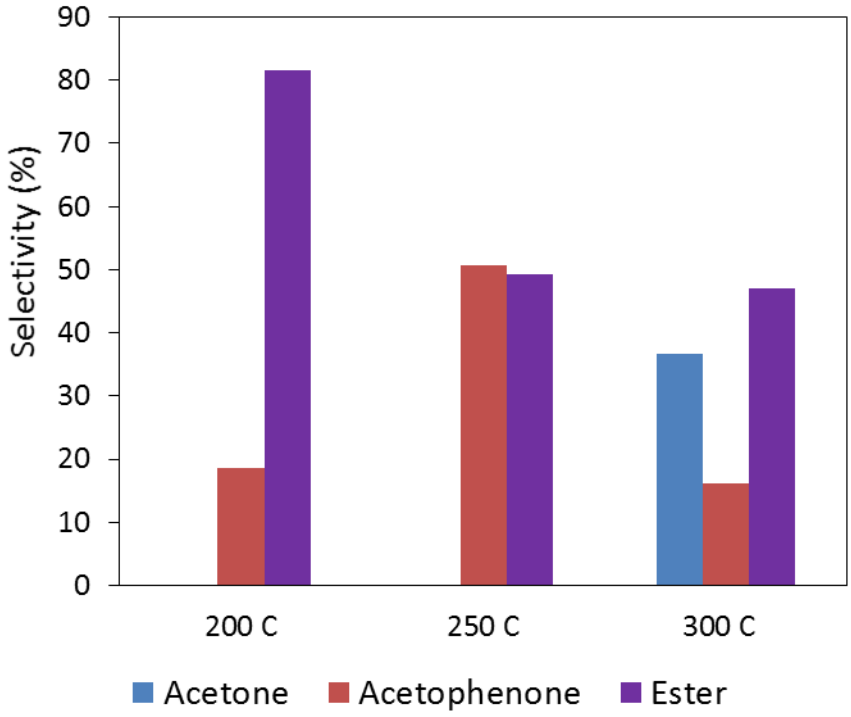

Figure 21 :- Acylation of m-cresol over CBV8014 at different temperatures

Aspeteguia et al. [92] in their study of m-cresol acylation in liquid phase over different type of zeolites observed also observed major products as ester and acetophenone. They speculated the formation of acetophenone as a sequential reaction i.e., after formation of ester by O-acylation the molecule undergoes rearrangement known as “Fries rearrangement” to yield acetophenone. Ester could also decompose to form acyl group and m-cresol which would then attack the ring to form acetophenone.

Resasco et al[96], in their publication of m-cresol acylation using acetic acid over H-beta zeolite also observed formation of ester even without catalyst in liquid phase, suggesting esterification is a non-catalyzed thermal reaction. This explains the higher selectivities towards ester product at lower temperatures and the shift to ring acylation at higher temperatures. The apparent barrier for this reaction was estimated to be 21 kJ/mol using Arrhenius plot as shown in Figure 22. The barrier for m-cresol acylation is similar to the barrier observed for m-furan acylation suggesting the mechanism could be very similar. That is formation of acyl by acetic acid is followed by the stabilization and C-C coupling of intermediate with m-cresol which eventually yields acetophenone. Decoupling the rates of esterification from direct ring acylation is very complex as the ester can also decompose/rearrange to yield same ring acylated product. Thus conclusive evidence regarding the mechanism couldn’t be drawn from study.

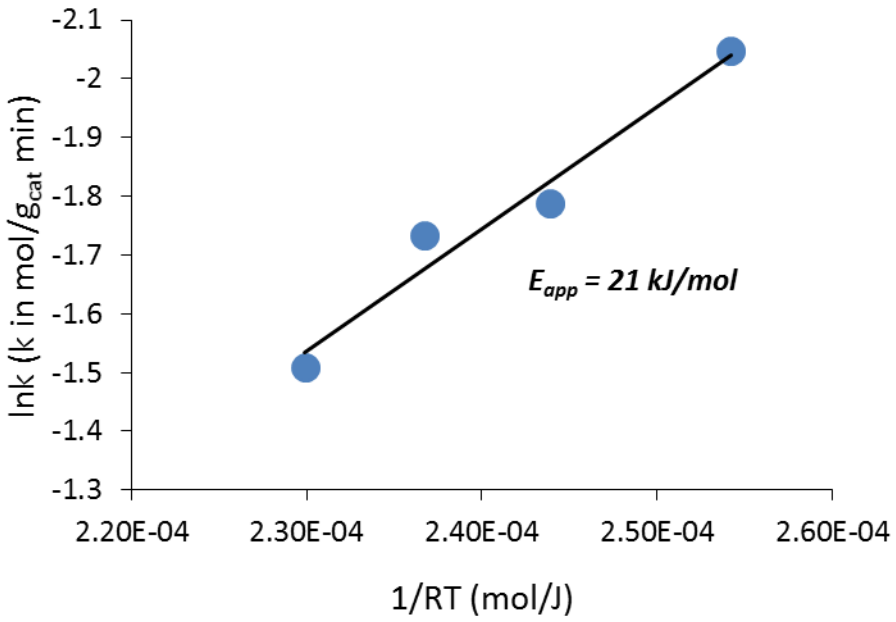

Figure 22 :- Apparent barrier estimation for m-cresol acylation with acetic acid over HZSM-5

Toluene acylation with acetic acid

A small fraction of aromatics are also present in stream 2 and 3 of torrefaction of biomass and they are also produced from side reactions like oligomerization during upgrading process. By acylating the ring with acetic acid to produce acetyl aromatic can increase the carbon chain length which is a high value fuel and specialty chemical. In this study we will use toluene and xylene as aromatic representative and acetic acid as acylating agent. The ratio of acetic acid and toluene was maintained at 1:0.258 which is like cresol acylation and m-furan acylation studies. The partial pressures of acylating agents and acyl acceptors are kept constant to compare rates of acylation reaction for different substrates. The reaction was performed at different temperatures over CBV8014 and the data is shown in the Arrhenius plot in Figure 23. As we see the rate of toluene acylation is very low even with increasing temperatures. If we further

increase the temperature the reaction was shifting towards ketonization. The apparent barrier measured for ketonization reaction is 119 kJ/mol which is very close to the true barrier measured from kinetics in Chapter-4. This suggests the catalyst surface is completely saturated by acetic acid. The rates of acetic acid ketonization we are measuring is in zero order regime thus giving a true barrier.

Activating an aromatic ring is a challenge due its high stability and unavailability of free electrons. Previous studies of acylation of aromatics with anhydrides as acylating agent in liquid phase has also shown very low turnovers as a function of temperature using acidic zeolite catalyst. Therefore to study aromatic acylation reaction we have to increase the partial pressures of toluene a lot so that it can compete with ketonization reaction and we can have measurable rates of acylation. The next set of reactions were performed at three different temperatures using a ratio acetic acid to toluene of 1:2. The data shown in Figure 24 is the yield of acylated toluene product formed at different temperatures as a function of time. The data at 30 min time on stream was to make an Arrhenius plot for this reaction to measure the apparent activation barrier. As shown in Figure 23 the barrier was measured to be 98 kJ/mol which is very high compared to m-furan acylation, m-cresol acylation and ketonization reactions. If toluene acylation reaction has a similar mechanism as m-furan or m-cresol acylation the rate should depend on the formation of surface acyl upon dehydration. But this very high apparent barrier suggests the shift in rate determining step to C-C coupling similar to what we observed for ketonization reaction. Since toluene ring is very stable it does not share the charge of surface acyl thereby making C-C coupling step more difficult to occur.

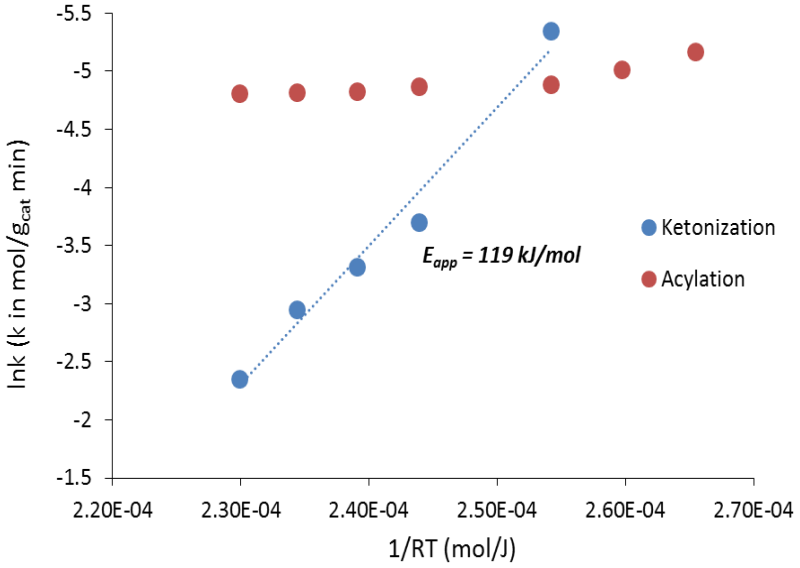

Figure 23 :- Arrhenius plot of toluene acylation with acetic acid over cbv8014 at different tempeartures. The ratio of acetic acid to toluene is 1:0.258.

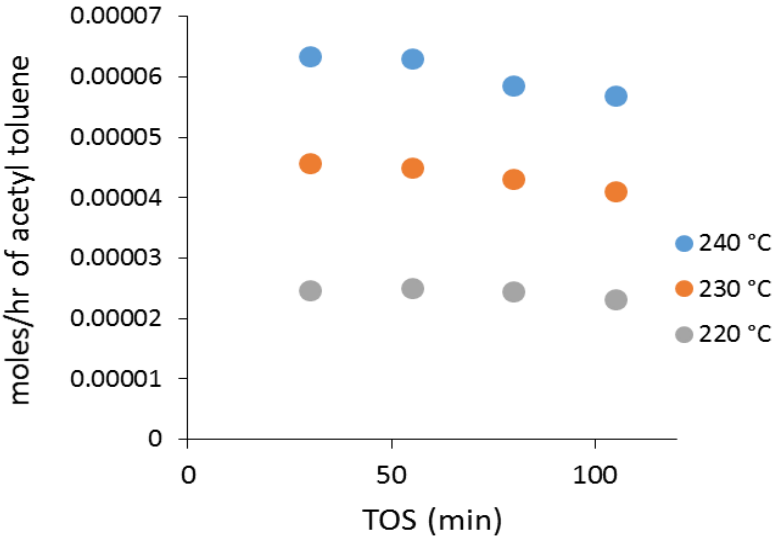

Figure 24 :- Moles of acylated product formed as function of times at different temperatures. The ratio of acetic acid to toluene is 1:2.

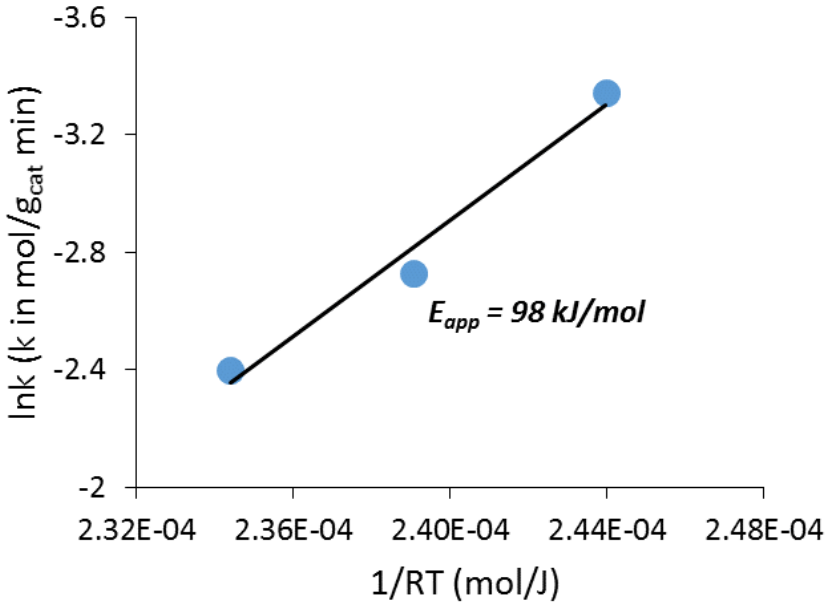

Figure 25 :- Apparent barrier estimation for toluene acylation with acetic acid over HZSM-5

Furan acylation with acetic acid

Acylation reaction is nucleophilic attack of the substrate with acyl cation. Therefore the substitution on the aromatic or furan ring should make the substrate more negative and increase the rate of nucleophilic substitution. In contrast the rate should drop in the absence of electron donating group on the ring.

To study this we performed acylation studies of furan and compared the data with methyl-furan acylation reaction. The ratio of acetic acid and furan are maintained constant at 1:0.258 in both the cases. Figure 26 shows yields of acetyl furan formed during the reaction as a function of time on stream. Apparent barrier for this reaction is estimated using data at 30 min time on stream to minimize the deactivation effects on the barrier. Methyl-furan acylation at similar partial pressures had a barrier of 24.5 kJ/mol while the furan acylation reaction barrier increased to 51 kJ/mol shown in Figure

27. This increase in barrier and drop in the rate can be attributed to the presence of electron donating group in methyl furan. This functional group helps in stabilizing the intermediates thereby reducing the barrier by coupling step. This data does not conclusively state about the rate determining step for furan acylation reaction. But the increase in barrier suggest a shift in kinetically relevant step or an enhanced contribution of C-C coupling step in degree of rate control.

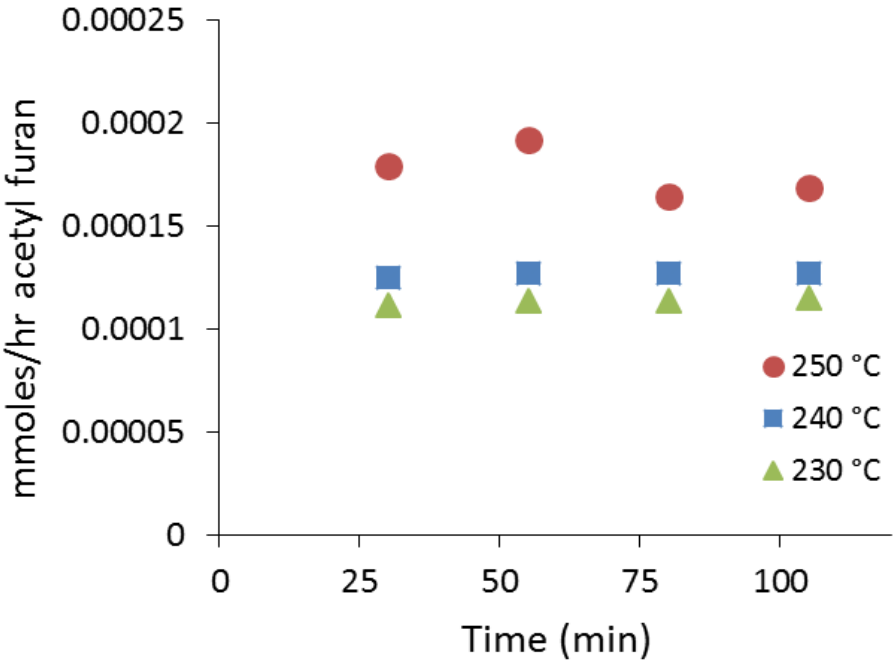

Figure 26 :- Yields of acetyl furan product as a function of time at different temperatures.

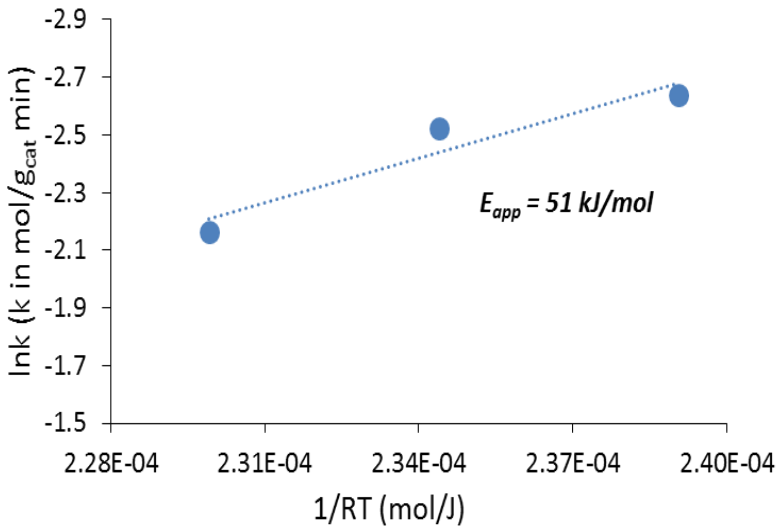

Figure 27 :- Arrhenius plot for furan acylation with acetic acid over HZSM-5

Conclusion

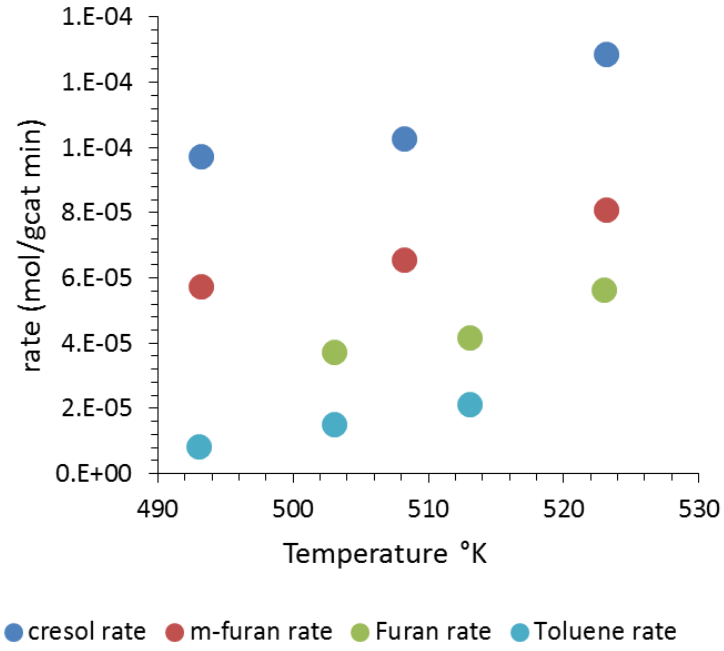

Figure 28 :- Comparing the rates of acylation of m-cresol, m-furan, furan and toluene with acetic acid as acylating agent over HZSM-5

Figure 28 shows the wide range of rates that result over the same catalyst under identical conditions when feeding a furanic, phenolic or aromatic compound. As the rate decreases and the barrier increases (the apparent barrier for toluene acylation is greater than that for ketonization), the rate limiting step shifts. In other words, selectivity for various acylation reactions can be tuned by manipulating the population of surface acyl species and the local environment. The rates and barriers can be correlated to the electron density of the substrate and its ability to stabilize the charge to ease C-C coupling step in the reaction.

Chapter 6: Effect of water on cracking reaction

All the data presented in this chapter is obtained at University of Oklahoma. The DFT calculations as a part of this work were performed by Dr. Bin Wang.

Introduction

Solid-acid catalysts are valuable in many existing industrial hydrocarbon conversion processes, the majority of which occur in the gas-phase, but are also promising for new applications in biomass utilization and environmental remediation[42, 97, 98]. Microporous zeolites with pore diameters in the sub-nanometer range are the most commonly employed solid-acid catalysts, although variations in hydrocarbon distributions from currently available petroleum sources have generated interest in mesoporous aluminosilicates possessing Brønsted acid sites[99-101]. In addition, new solid-acid catalyzed upgrading of renewable feedstocks in the liquid-phase demonstrates the diversity of zeolite structures[102, 103].

Water can be incorporated in the reaction system in the feed or evolved as a side product inside the solid acid catalyst during reaction. For example, in biomass conversion processes, water is a major component of the feedstock[104, 105] and in reactions involving oxygenates (alcohols, aldehydes, acids) water may be produced stoichiometrically. Such reactions include methanol-to-hydrocarbon, aldol condensation, ketonization, and alkylation catalyzed by zeolites and other solid acids. Multiple reports discuss the difficulty in completely removing water from acidic zeolites[106, 107]. Due to the high internal surface area of microporous zeolites and their mesoporous analogues, and the hydrophilicity of Brønsted acid sites, water is

likely present at some level in many existing reactions, including gas phase chemistry at elevated temperatures.

Water is generally considered deleterious in solid-acid chemistry. First, water is a competitive base that strongly adsorbs at the acid site, thereby inhibiting proton availability for hydrocarbon reagents[108-110]; Second, at high-temperatures, the presence of water may lead to lattice dealumination and loss of acidity[111]. Finally, in the case of zeolites, the presence of condensed water causes severe losses in crystallinity and catalytic activity[112]. There are a few instances in which water has been found to exhibit a positive effect on selectivity by virtue of its ability to prevent secondary reactions by strongly adsorbing at Brønsted acid sites and competing with readsorption of products. For example, selectivity enhancements for methanol-to-hydrocarbon conversions through water co-addition have been reported for many years, and even very recently the origin of this effect has been attributed to water's competitive adsorption properties. Interestingly, for an alcohol reagent like methanol, which generates water in the condensation step to dimethyl ether, addition of even more water leads to increased selectivity to primary products like small olefins. Recent work on another alcohol system, propanol, indicated that propanol adsorbs more strongly than water, but water helped stabilize adsorbed intermediate, i.e. pre-transition, states relative to stabilization of the transition state itself such that reduced reaction rates were observed.

All of the cases cited above demonstrate that catalyst activity is generally reduced when additional water is introduced, which may be used to improve selectivity, not intrinsic activity. More interesting, and only recently recognized, are cases in which

the catalytic activity is actually promoted by the presence of water[104]. For example, in a gas-phase Fischer-Tropsch study involving Ru catalysts, Hibbitts et al.[105] showed that CO activation is increased through water-mediated hydrogen transfer. Similarly, Yoon et al.[113] demonstrated that activity in Rh-catalyzed biphasic conversions of lignin-derived molecules increased in the presence of co-fed water by enhancing a key hydrodeoxygenation step on the bifunctional catalyst. Water's role in each of these cases proceeded through interaction with the metal. Two recent reports in the literature indicate that introduction of small amounts of water can increase reactions rates in purely solid-acid catalysts. First, Motokura et al.[114, 115] demonstrated that addition of water in the range of 1-5 wt% relative to the mass of the proton-exchanged montmorillonite catalyst increased reaction rates between bulky alkenes by over an order of magnitude. In a study utilizing the industrially-important HZSM-5 catalyst, Chen and coworkers[116] demonstrated a one-order of magnitude increase in the reaction rate, relative to the completely dry catalyst, for isobutane isotopic exchange with Brønsted acid sites when less than one equivalent of water (on an acid site basis) was introduced to the reaction mixture. Water loadings in excess of ca. 1 equivalent were shown to lead to decreased reaction rate constants versus that obtained with a dry HZSM-5.

To our knowledge, these are the only few reports of catalyst activity enhancement involving solid Brønsted acids, and even though alkenes versus alkanes were used in the two studies, it is interesting that the significant increases in catalyst activity were realized only at very low water amounts. These data indicate that water can actively participate in reactions that occur at Brønsted acid sites, but little to no

mechanistic information was provided in these reports. In this contribution, we show that contrary to conventional thinking, water can significantly enhance the reactivity of solid acid catalysts in a variety of reactions relative to the dry catalysts, including some very well-known reactions involving aromatic reagents in zeolites. These surprising findings are encouraging for design of catalysts for processing new feedstocks, like those from biomass, where water is present. More importantly, the results indicate that water actively participates in hydrocarbon transformations in acidic zeolite and other solid acid zeotypes, a heretofore unrealized conclusion. These new fundamental insights about the role of water in solid acid catalysis also have immediate practical implications, including the potential to conduct chemistry at lower temperatures and realize longer catalyst lifetimes in the presence of appropriate water concentrations in the catalyst. Possible explanations for how water increases activity in solid acids are proposed.

Experimental and Theoretical Methods

Catalytic materials

ZSM-5 (CBV-2314) with a $SiO_2/Al2O_3$=23 and CBV8014 with a $SiO_2/Al2O_3$=80 were purchased in its ammonium form from Zeolyst International. To obtain the protonated HZSM-5, the zeolite in ammonium form was calcined at 600 °C for 5 h in dry air. The calcined sample was then pelletized and subsequently crushed and sieved to particles with sizes ranging from 90 to 250 μm.

X-Ray diffraction (XRD) measurements for both catalyst were obtained using Bruker axs Inc. D8 DISCOVER with a GADDS detector. It was operated at 40 kV and

35 mA in the angle range 5–55°. The result shown in Appendix-D approves the catalyst sample to be MFI framework with good crystallinity.

Scanning electron microscopy (SEM) technique was used to estimate the particle diameter for catalyst. The SEM measurements performed on a Zeiss-NEON FEG-SEM instrument reveal agglomeration of small crystals.

Isopropylamine (IPA) temperature-programmed desorption (TPD) was performed to investigate the concentration of Brønsted acid sites in the zeolite sample. A catalyst sample size of 50 mg was taken in a quartz reactor (1/4" OD) and preheated to 300 °C with flushing in helium flow (20 ml/min) for 1 h. After pretreatment, the temperature was reduced to 100 °C and 2 lL pulses of IPA were injected into the reactor through a septum using a syringe. Saturation of acid sites in the catalyst bed with IPA was ensured by tracking the mass-to-charge ratios (m/z) of 44 and 58 at the exit of the reactor with an MKS Cirrus 200 quadrupole mass spectrometer (MS). IPA pulses were continued until constant peak heights corresponding to m/z = 44 and 58 were observed as sequential pulses were injected. After adsorption of IPA onto the catalyst bed, physically adsorbed IPA was flushed off using helium as carrier gas was flushed at a rate of 20 ml/min at 100 °C for 4 h. After flushing the temperature was ramped from 100 to 600 °C at a rate of 10 °C/min. IPA, propylene and ammonia desorbing from the reactor during the temperature ramp as shown in figure were tracked via MS. Products were quantified through calibration of the MS signal using standards and a sample loop. Based on the number of moles of propylene desorbed per gram catalyst Brønsted acid site density is calculated to be 1.01 mmoles/g for CBV2314 and 0.396 mmoles/g for CBV8014. These values correlate well with literature.

Vapor and Liquid phase reactions

Vapor phase reactions to study dealkylation of cumene and n-hexane cracking were performed in a quartz tube reactor (1/4" OD) at atmospheric pressure and desired reaction temperatures. The catalyst sample was diluted with acid washed glass beads (Sigma Aldrich, 150-212 µm) and packed into the reactor between plugs of quartz wool. A thermocouple was attached to the outer wall of the reactor to control the catalyst bed temperature. The catalyst bed was preheated to 300 °C and flushed with helium flowing at 125 ml/min for 1 h before cumene (Sigma Aldrich, 98%) was introduced via a syringe pump. The product distribution at the desired time on stream (TOS) were analyzed using a Hewlett Packard 6890 gas chromatograph equipped with a flame ionization detector and an Innowax column of dimensions 30 m and 0.25 lm. For any offline analysis, the vapors downstream of the six-port valve were condensed in a sample bubbler using ice and water as the coolant medium. For reactions with water co-feeding, double distilled water was fed via a second syringe pump.

Results and discussion

Cumene cracking was studied over CBV2314 in a vapor phase reactor at 300 °C and atmospheric pressure. As expected, the product distribution consisted of two dealkylation products, propylene and benzene. The carbon balance for this reaction was above 95%, and insignificant catalyst deactivation was observed across the reaction times studied here. The same reaction was repeated while co-feeding water along with cumene in a mole ratio of water : cumene = 3.8 : 1. It is important to mention that both of these reactions were performed at a constant W/F with respect to cumene and

constant partial pressure of cumene. Reaction conversion and product yields for cumene cracking with and without water are presented in figure-1. Surprisingly, a slight enhancement in the cracking reaction rate to form benzene and propylene was observed while co-feeding water. Similar experiments were conducted at lower temperature of 285 °C and 275 °C. The behavior of rate enhancement in presence of water was still present at these lower temperatures too. As expected the product distribution was 100 % selective to propylene and benzene. No side reactions were observed and very minimal deactivation was observed. The data presented in Figure 29 (a,b,c) shows conversion of cumene to propylene and benzene in presence and absence of water at different reaction temperatures. To ensure the rate enhancement is true and not due to the artifact of deactivation we have extrapolated the reaction to 0 time on stream by fitting exponential model. The percentage rate enhancement at 0 time for these different temperatures is shown in Table 3.

There is a slightly higher enhancement at lower temperatures for the same partial pressure of water suggesting an increase in surface coverage with reduction in temperature could be responsible for this phenomena.

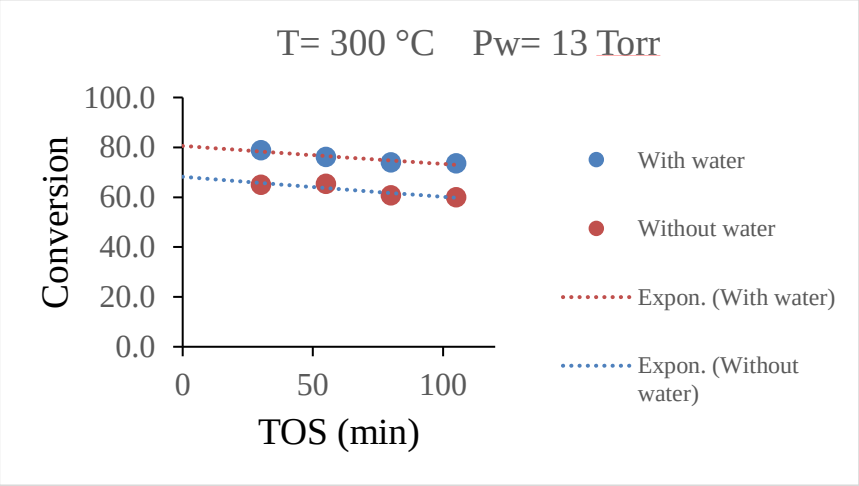

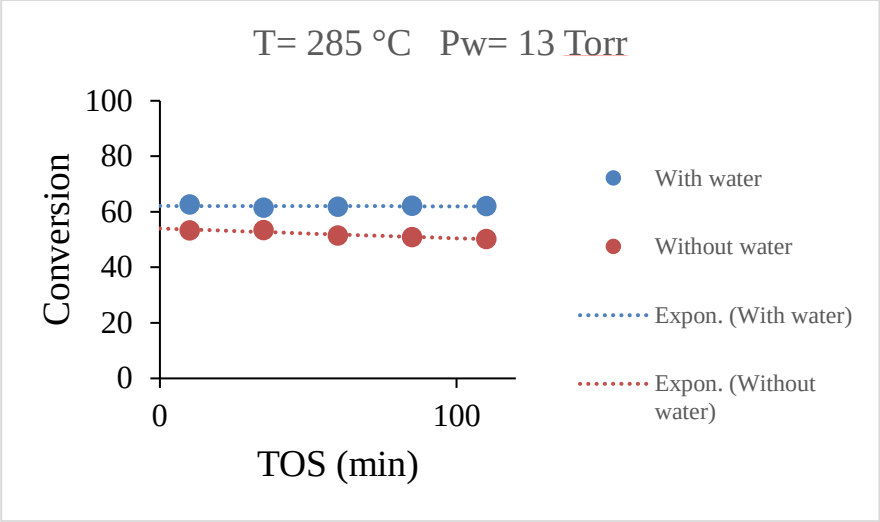

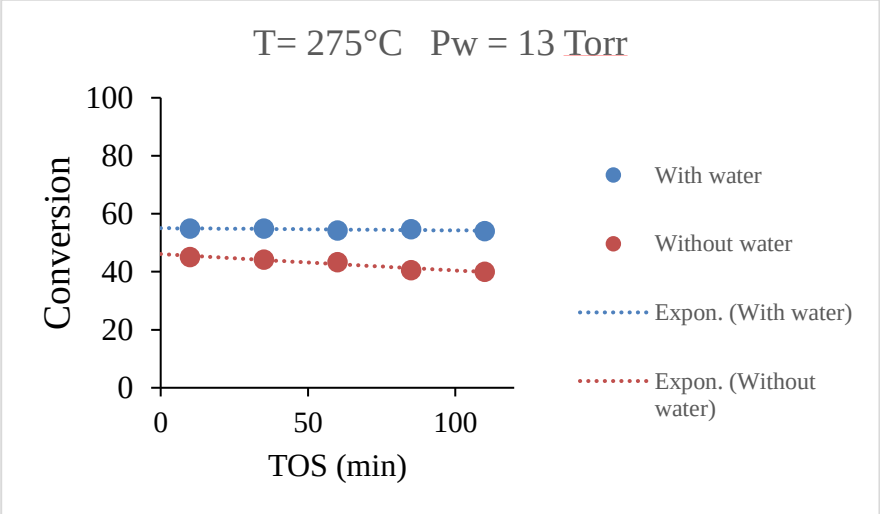

Figure 29 (a,b,c) :- Cumene conversion over CBV2314 at a reaction temperature of 300, 285,275 °C with water and without water.

Temperature (C)	rate (W/O water)	rate (W water)	% enhancement
300	0.245	0.283	13.8 ±1
285	0.19	0.222	14 ±1
275	0.161	0.194	17 ±1.5

Table 3 :- Rate enhancement for cumene cracking at 0 time on stream

To further support and verify whether the increase in activity observed is true or error, an experiment was designed to start cofeeding water intermittently and observe the rate. Figure 30 shows the conversion of cumene cracking as a function of time on stream. At a time of 120min water cofeeding was started into the reactor at a ratio of 3.8:1 of water: cumene. We observed a sudden jump in the conversion in the presence of water while it gradually leveled off after stopping cofeeding of water at 200min time on stream. A similar experiment but in reverse order to the previous was performed to observe the activity behavior. Water was cofed along with cumene right from 0 reaction time and was suddenly stopped at 120 min time on stream. As seen in Figure 31after stopping the water the rate of reaction gradually dropped and regained immediately after starting the water back into the reaction. The slow drop in the activity instead of a sudden decrease could be due to the presence of residual water on the catalyst bed.

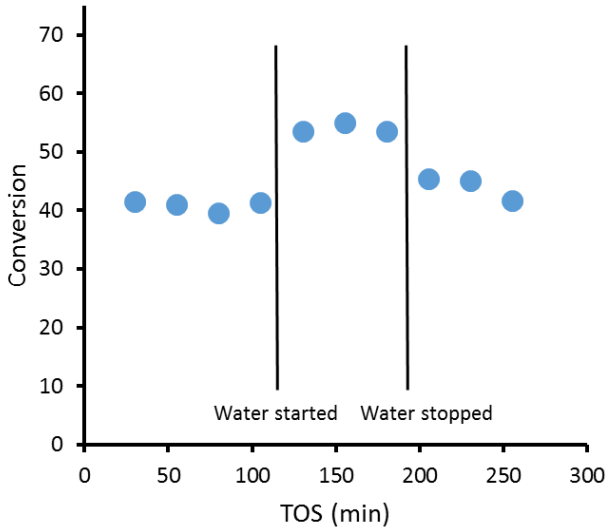

Figure 30 :- Conversion of cumene as a function of time on stream with intermittent cofeeding of water at a reaction temperature of 275 °C over CBV2314 catalyst.

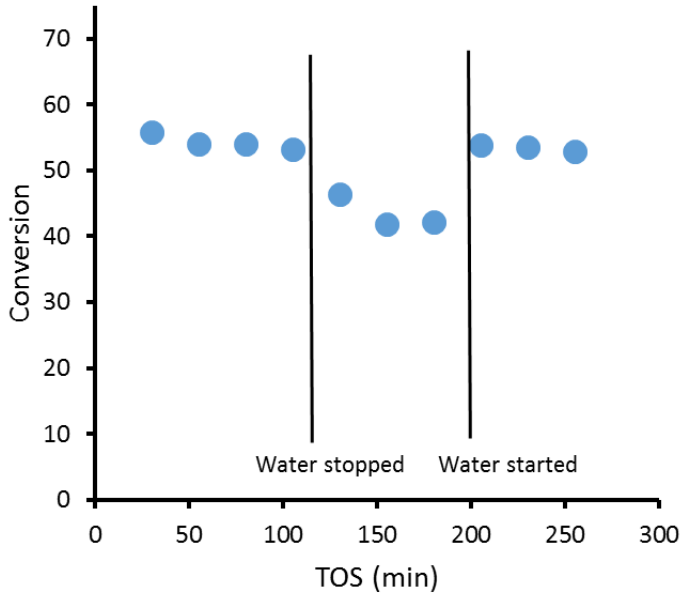

Figure 31 :- Conversion of cumene to products as a function of time on stream in presence of water at 275 °C over CBV2314. Water was intermittently stopped and started back to observe the activity behavior.

Similar experiments were performed over HZSM-5 catalyst with higher Si/Al ratio of 40 in comparison to Si/Al=11.5 used in above section. Surprisingly we have not observed any rate enhancement for cumene cracking in presence of water for Si/Al=40 while using the partial pressures the same. Increasing the partial pressure of water also did not show any activity increment but instead reduced the conversion of cumene cracking. This could be due to competition by water for active sites at higher temperatures. This results suggests that the proximity of Brønsted acid sites is very critical to observe the enhancement with water.

It can be argued that the presence of extra framework alumina (EFAl) in CBV2314 could be responsible for the enhancement in activity. Water can interact with these EFAl sites by hydrogen bonding to create some surface bound hydroxyl group which may catalyze cumene cracking. To eliminate this argument we have acid washed

CBV2314 with very mild acid to remove all the penta-coordinated and octahedral EFAl. After acid washing the catalyst was tested for cumene cracking activity in presence and absence of water and we still observed the enhancement in the rate with water. This shows that the EFAl species are not responsible for increase in activity. This surprising positive phenomena of water at lower temperatures has significant practical implications and needs further investigation for better understanding. Assuming a first order reaction rate as a function of cumene partial pressure, the apparent activation energy was estimated for the reactions with water and without water. A drop of 5 kJ/mole in apparent barrier was observed while cofeeding water. This results suggest that water may not just play an entropic role of stabilizing the transition state but participates in the reaction.

Ab-initio molecular dynamics (AIMD) simulations

To investigate the interplay between the Brønsted acid sites (BAS) and water molecules, AIMD simulations were performed using the VASP package[77] with an exchange-correlation potential derived from the Perdew-Burke-Ernzerhof (PBE) Generalized-Gradient-Approximation (GGA) [78] and electron-core interactions treated in the projector augmented wave (PAW) method. A cluster of water molecules was represented by hexamers in their most stable configurations (Prism, Cage, Book and Cyclic)[117]. It was observed that in the pristine zeolite containing no BAS, water molecules migrate in the cage and channel and weakly interact with the zeolite framework. However, in the presence of the BAS, the water hexamers form stable, ordered structures interacting with the acid sites as shown by Figure 32. We find that

the water molecules can bridge two acid sites via a chain (Figure 32A) or clusters (Figure 32B). These two typical configurations last a couple of picoseconds (a few thousand of steps) suggesting that they are relatively stable. In both cases the BAS protons are connected to the H-bonded water network and become delocalized. Particularly, Figure 32B shows that a $H_5O_2^+$ dimer is able to stabilize the charges remaining in the zeolite framework, while the other BAS proton is immersed in water. It becomes difficult to identify the precise position of the H_3O^+ in the simulations due to the dynamic nature of the protons. The delocalization of protons (charges), as compared to the protons (charges) initially at the BAS, provides enhanced flexibility and increased freedom for catalyzing the reactions.

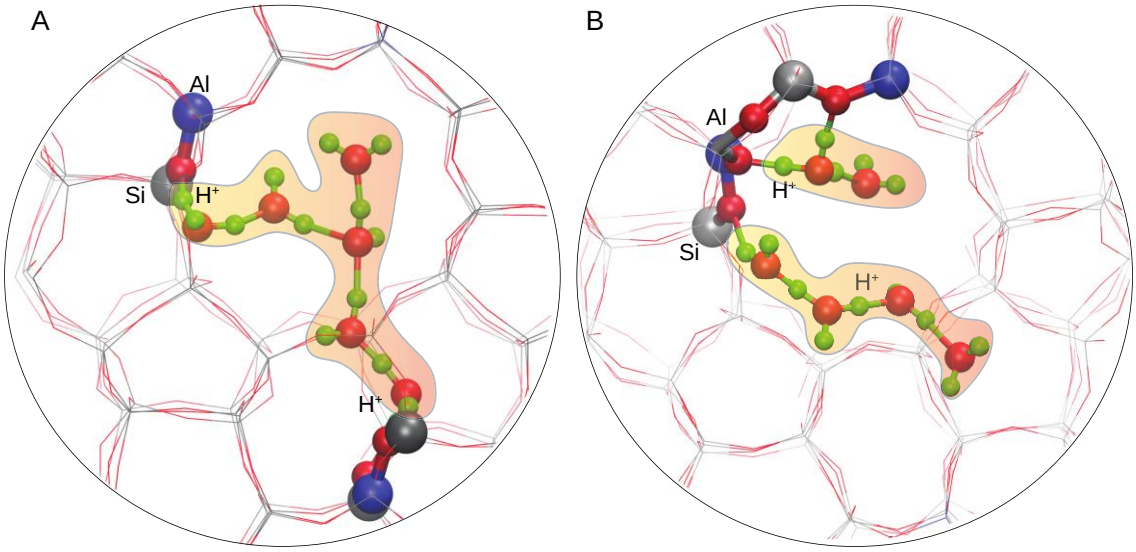

Figure 32 :- Snapshots in AIMD simulations. (A) water hexamer forms a chain between two acid sites. (B) the water hexamer breaks to form two clusters, a dimer and a tetramer. In both cases, the protons are delocalized in the H-bonded environment. The Si, Al, O, H are colored grey, blue, red and green, respectively.

Conclusions

HZSM-5 with low Si/Al ratio of 11.5 shown a peculiar and very interesting behavior in presence of water. The catalyst activity for cumene cracking reaction was significantly enhanced for a wide range of temperatures when water was cofed along with cumene. It was ensured that EFAl present in CBV2314 is not responsible for this surprising behavior. There was a decrease in the apparent barrier by 5 kJ/mol suggesting water does not only have an entropic effect but also might be stabilizing the transition state and may contribute to the enthalpy of the reaction. Acid site proximity plays a detrimental role in this behavior as we have not observed any enhancement for HZSM-5 catalyst with Si/Al=40 while all the remaining conditions were maintained constant. DFT studies revealed that the water molecules can bridge two acid sites via a chain or clusters thereby delocalizing the proton on Brønsted acid sites. This delocalization of protons (charges), as compared to the protons (charges) initially at the BAS, could be providing enhanced flexibility and increased freedom for catalyzing the reactions.

Chapter 7: Synthesis of ZSM-5 Nanoparticles Encapsulated within an Ultrathin Silicalite-1 Coating of Tunable Thickness

The work in this chapter is a collaboration between our group at University of Oklahoma and Dr. Jeff Rimer's group at University of Houston. The encapsulated zeolites were synthesized by Dr. Rimer's group, while part of the characterization (IPA-TPD, XPS, Al-NMR) and activity testing were performed by OU group. This work is published in ACS Nano journal. Complete article and supporting information can found using the citation "Ghorbanpour, A., Gumidyala, A., Grabow, L. C., Crossley, S. P., & Rimer, J. D. (2015). Epitaxial growth of ZSM-5@ Silicalite-1: A core–shell zeolite designed with passivated surface acidity. ACS nano, 9(4), 4006-4016."

Abstract

The design of materials with spatially-controlled chemical composition has potential advantages for wide-reaching applications that span energy to medicine. Here, we present a novel method for preparing a core-shell aluminosilicate zeolite with continuous translational symmetry of nanopores and an epitaxial shell of tunable thickness that passivates Brønsted acid sites (≡ $AlOH$ groups) on exterior surfaces. For this study, we selected the commercially relevant *MFI* framework type and prepared core-shell particles consisting of an aluminosilicate core (ZSM-5) and a siliceous shell (silicalite-1). Transmission electron microscopy and gas adsorption studies confirmed that silicalite-1 forms an epitaxial layer on ZSM-5 crystals without blocking pore openings. Scanning electron microscopy and dynamic light scattering were used in combination to confirm that the shell thickness can be tailored with nanometer resolution. X-ray photoelectron spectroscopy and temperature programmed desorption

measurements revealed the presence of a siliceous shell, while probe reactions using molecules that were either too large or sufficiently sized to access MFI pores confirmed the uniform shell coverage. The synthesis of ZSM-5@silicalite-1 offers a pathway for tailoring the physicochemical properties of MFI-type materials – notably in the area of catalysis, where surface passivation can enhance product selectivity without sacrificing catalyst activity. The method described here provides a general platform for core-shell design that may prove to be broadly applicable to other porous materials.

Introduction

Zeolites are used in a variety of applications owing to their unique acidity and nanoporous structures that are well-suited for catalysis, ion-exchange, sorption, and separations. The acidity of H-zeolites is attributed to Brønsted acid sites, which are located on oxygen atoms that bridge Si and Al atoms in the crystalline framework. In catalytic applications, Brønsted acid sites located within confined nanopores impose shape-selectivity to achieve narrow product distributions; however, acid sites on the exterior surfaces of zeolite crystals reduce product selectivity and can exhibit properties that differ from bulk sites.[118, 119] A catalyst "passivation" method was patented by Mobil in the 1970's to coat ZSM-5 (MFI type) surfaces with a catalytically inactive silica layer.[120] Surface passivation has proven to be a useful method for enhancing product selectivity in the production of para-xylene[121] and para-selective disproportionation and alkylation of aromatics.[122] Additional examples include the production of methylamines using a passivated zeolite RHO catalyst with enhanced selectivity for dimethylamine.[123]

Details regarding the synthesis and characterization of passivated zeolites are difficult to extract from patents. In addition, techniques reported in the literature tend to have associated drawbacks. Examples include post-synthesis dealumination by acid treatment,[124, 125] which can generate crystal defects and/or mesopores.[125, 126] An alternative approach is the modification of external functional groups on zeolite surfaces with a passivating agent. Examples include the use of metal oxides (e.g., Sb_2O_3)[127] and hydride, alkyl, or alkoxy compounds that chemisorb to the hydroxyl groups on zeolite surfaces.[128] This is frequently performed using chemical vapor deposition (CVD) or chemical liquid deposition (CLD) techniques.[129-133] These methods enhance shape selectivity by narrowing surface pore openings and eliminating surface active sites; however, they also result in pore blockage and/or increased internal diffusion resistance due to pore mouth narrowing, which reduce molecular flux during sorption and separations and reduce catalytic activity.[127, 129, 134, 135]

The aforementioned drawbacks of zeolite passivation can be circumvented by growing an epitaxial zeolite shell on the surface of a zeolite core with identical or congruent structure. Synthesis of core-shell structures has been demonstrated for a wide range of inorganic and organic materials[136] with applications ranging from semiconductors[137, 138] and drug delivery[139] to catalysis.[140, 141] A key factor in the fabrication of zeolite core-shell composite structures is sufficient compatibility between core and shell in terms of framework composition, growth conditions, and crystal structure in order to facilitate oriented (or epitaxial) growth of one crystal on the surface of another.[135, 142, 143] In the literature, many combinations of core-shell zeolites are reported, such as LTA@FAU,[144] SOD@CAN,[145] FAU@BEA,[146]

MOR@MFI,[129] MFI@BEA,[142, 147] and BEA@MFI.[148, 149] These materials can be formed through heterogeneous nucleation and growth of the shell on the core. Alternatively, the shell layer can be formed through the use of nanocrystalline seeds that are first deposited on the core surface and then transformed into a contiguous layer via secondary growth.[129, 142, 147, 150] One disadvantage of the latter approach is the need to calcine the seeded cores prior to shell growth in order to firmly fix the seeds to the core surface – a process that can introduce defects at the core/shell boundary.[151]

Herein, we focus on the formation of a MFI@MFI core-shell zeolite comprised of an aluminosilicate ZSM-5 (catalytically active) core and a siliceous silicalite-1 (catalytically benign) shell, both of which possess an orthorhombic crystal structure with identical unit cell parameters (MFI type). Prior attempts to passivate MFI zeolite have resulted in incomplete silicalite-1 coverage,[152, 153], misaligned (non-epitaxial) shell growth,[154] and/or individual silicalite-1 particles adhered to ZSM-5 seeds.[153, 154] Core-shell MFI has been prepared by a one-step procedure using fluoride growth media;[155] however, the silicalite-1 shell thickness typically exceeds 1 μm and fluoride-based protocols are commercially restrictive. Prior examples have shown that MFI core-shell structures can improve catalyst selectivity, but often at the expense of reduced catalytic activity due to pore blockage or narrowing.[151] Moreover, structural mismatch between the core and shell can introduce molecular diffusion barriers that facilitate carbonaceous coke buildup.[156] Here, we report a robust protocol for realizing nanocrystalline ZSM-5@silicalite-1 with an ultrathin (< 10 nm), epitaxial silicalite-1 shell of tunable thickness. Performance tests using model reactions showed

that the shell layer preserves catalytic activity, thus avoiding pore blockage/narrowing and validating the overall effectiveness of this approach for rational design.

Experimental Section

Materials

The following chemicals were purchased from Sigma Aldrich: tetraethylorthosilicate (TEOS, 98%), aluminum isopropoxide (98%), sodium hydroxide pellets (NaOH, 98%), 1,3,5-tri-isopropyl-benzene (TIPB, 95%), acetic acid (ACS reagent, ≥99.7%), isopropylamine (IPA >99.5%), and 2,6-di-tert-butylpyridine (DTBPy, >97%). Tetrapropylammonium hydroxide (TPAOH, 40%) was purchased from Alfa Aesar. The deionized (DI) water used for all synthesis and analytical measurements was purified with an Aqua Solutions RODI-C-12A purification system (18.2 MΩ). All gases necessary for reactions and gas chromatography analysis (He, N_2, H_2, and air) were obtained from Airgas. The N_2 for textural analysis was obtained from Praxair.

Synthesis of ZSM-5 Seeds

Growth solutions were prepared with a molar composition of 6 TPAOH:0.1 Na_2O:25 SiO_2:0.25 Al_2O_3:480 H_2O:100 EtOH. We first added TEOS dropwise to a solution of TPAOH, NaOH, and DI water (25 mL total volume). This solution was stirred overnight at room temperature. Aluminum isopropoxide was added and the mixture was aged for an additional 24 hours at room temperature with continuous stirring. The solution was then placed in an acid digestion bomb (Parr Instruments) and was heated in a ThermoFisher Precision 3050 Series gravity oven at 100 °C. The solution was removed after 60 hours and immediately cooled to room temperature. The

crystalline product was isolated from the supernatant by three centrifugation and washing cycles of the mother liquor with DI water at 13,000 rpm for 40 minutes. The water was decanted, leaving behind a gel containing the ZSM-5 crystals. For protocols without an annealing step, a portion of the ZSM-5 gel was removed and dried in air for further characterization, while the remaining gel was directly added to a silicalite-1 growth solution (without drying) to prepare core-shell particles. For protocols employing an annealing step, the entire ZSM-5 gel was transferred to a solution with composition 10 TEOS:14 TPAOH:9500 H_2O. This solution was prepared by adding an appropriate amount of TEOS (dropwise) to a solution containing TPAOH and DI water (25 mL total volume). The solution was stirred at room temperature overnight prior to the addition of ZSM-5 seed crystals (1 wt%). The solution containing ZSM-5 seeds was thoroughly mixed, placed in an acid digestion bomb, and heated for 12 days at 170 ºC. The solution was removed from the oven and cooled to room temperature. A similar centrifugation/washing procedure was used to isolate the ZSM-5 crystals as a gel, which was fully transferred to a silicalite-1 growth solution (without drying).

Synthesis of ZSM-5@silicalite-1

A layer of silicalite-1 was grown on ZSM-5 seeds using a growth solution with a molar composition of x TEOS:14 TPAOH:9500 H_2O (with x = 17 – 40). This solution was prepared by adding an appropriate amount of TEOS (dropwise) to a solution containing TPAOH and DI water (25 mL total volume). The solution was stirred at room temperature overnight. Shell growth was carried out by adding ZSM-5 seeds (1 wt%) to the silicalite-1 growth solution. Prior to hydrothermal treatment, the solution pH was measured using an Orion 3-star Plus pH benchtop meter and 8102BNUWP

ROSS Ultra electrode. The suspension was placed in an acid digestion bomb and heated for 24 hours at 100 °C. The solution was removed from the oven and cooled to room temperature. A similar centrifugation/washing procedure was used to isolate ZSM-5@silicalite-1 crystals as a gel. For protocols without an annealing step, the entire gel was dried in air for further characterization. For processes employing an annealing step, the gel was directly transferred (without drying) to a solution with composition 10 TEOS:14 TPAOH:9500 H_2O, which was heated for 12 days at 170 ºC. The solution was then removed from the oven, the solid was isolated as a gel by centrifugation and washing, and the product was dried in air for further analysis.

Preparation of H-Zeolites

ZSM-5 and ZSM-5@silicalite-1 samples were calcined to remove occluded TPA^+ from the pores using a ThermoScientific Lindberg Blue M tubular furnace. Calincation was performed with a temperature ramp rate of 1 ºC/min and a dwell time of 5 h at 550 ºC under the constant flow of compressed air (purchased from Praxair). An appropriate amount of each sample was then mixed with DI water to yield a 5 wt% suspension. This suspension was heated at 70 ºC for 12 h, and washed with DI water by centrifugation and decanting, such that the pH of the supernatant was within the range 6 to 7. The precipitate was mixed with a 1.0 M ammonium nitrate solution to yield a 5 wt% suspension. This suspension was then heated at 80 ºC for 5 h to allow the exchange of extraframework Na^+ ions with NH_4^+. The solid material was recovered by centrifugation. This entire process was performed for a total of three cycles, and the final product was dried at room temperature and calcined at the same condition as

above. The resulting H-form zeolite samples were used for BET, XRD, XPS, IPA TPD, probe reactions, and di-tert-butylpyridine adsorption experiments.

Materials Characterization

The MFI crystal structure of core and core-shell samples was verified by powder X-ray diffraction (XRD) using a Siemens D5000 X-ray diffractometer with CuKα radiation (40 kV, 30 mA, λ = 1.54 nm). The elemental composition of zeolite samples was determined by inductively coupled plasma atomic emission spectroscopy (ICP-AES) at Galbraith Laboratories (Knoxville, TN). The BET surface area of H-zeolite samples was measured by N_2 adsorption using a Micromeritics ASAP2020 instrument. Crystal morphology, size, and particle size distribution were assessed by scanning electron microscopy (SEM) using a FEI model Strata235 instrument. To prepare SEM samples, a small amount of the zeolite aqueous suspension was placed on a glass slide and dried overnight. The crystals were then transferred onto carbon grids and coated with carbon (ca. 30 nm). Transmission electron microscopy (TEM) was performed at the Texas A&M University Microscopy and Imaging Center using a FEI Tecnai G2 F20 ST FE-TEM instrument. TEM samples were microtomed (ca. 80 nm thickness) and carbon coated for stability.

X-ray photoelectron spectroscopy (XPS) analysis of samples was performed using a PHI 5800 ESCA (Physical Electronics) multi-technique system equipped with a standard achromatic AlKα X-ray source (1486.6 eV) operating at 300 W (15kV and 20 mA) and a concentric hemispherical analyser. The samples were filled in the specimen holder and outgassed in the introduction chamber prior to analysis. Survey spectra (0 - 1400 eV) and high-resolution spectra were collected with a pass energy of 187.85 eV

and 23.50 eV, respectively. All data were collected at a 45° take-off angle. To compensate for surface charging effects, all spectra were referenced to the hydrocarbon C1s peak at 284.6 eV.

Growth solutions for dynamic light scattering (DLS) measurements were prepared with molar composition 14 TEOS:7 TPAOH:9500 H_2O (pH = 10.8) using the same protocol for silicalite-1 synthesis. To this solution was added an aliquot of stock ZSM-5 seed solution (3 g zeolite in 19 mL DI water) in the amount of 5 g seed solution per 75 g growth solution. After 30 min of stirring, the mixture was divided equally into three acid digestion bombs, and placed in an oven regulated at 100 °C. At various time points, a sample was removed from the oven, quenched to room temperature, filtered through a 0.45 mm nylon membrane (Pall Corp.), and diluted to obtain a transparent solution prior to DLS measurements. The degree of dilution was adjusted to ensure equal scattering count rates for each sample. Samples labeled as the *zero time point* refer to the solution without any heating. A total of three DLS measurements were taken for each sample (2 min per measurement) to obtain an average crystal size and standard deviation. Autocorrelation functions were analyzed using the method of cumulants to obtain an average hydrodynamic diameter. All measurements were performed using a Brookhaven Instruments BI-200SM machine equipped with a TurboCorr Digital Correlator, a HeNe laser (637 nm), and a refractive index matching decalin bath. The temperature of the DLS sample was regulated at 25 °C.

The ^{27}Al NMR experiments were performed on a Bruker AVIII HD NMR spectrometer operating at a magnetic field strength of 11.74 T, equipped with a 4 mm Bruker MAS probe. For the MAS experiments of ^{27}Al (130.3754 MHz), a single pulse

acquisition was applied with a spinning speed of 14 KHz and a short RF pulse (less than 15°) with a recycle delay of 0.5-1 s. Spectra were collected after 10240 scans and referenced to $AlCl_3$ (aq. 1 M) at 0 ppm.

Material Testing in a Fixed Bed Reactor

Flow reaction studies were performed in a quartz tube reactor (1/4" OD) at 400 °C and at atmospheric pressure. The H-zeolite catalyst was diluted with acid washed glass beads packed in the reactor between plugs of quartz wool. The inlet of the reactor was heated to create a vaporization zone and the outlet stream of the reactor as well as the six port valve for injection to the gas chromatograph (GC) were heated to 250 °C to prevent condensation. The temperature of the catalyst bed was controlled by a thermocouple attached to the outer wall of the reactor. The catalyst was preheated and flushed with helium (50 mL/min) for one hour at 400 °C before introducing the reactant via a syringe pump. The results and product distribution were analyzed using a HP-6890GC equipped with a flame ionization detector and innowax column (30m and 0.25 μm). Reaction products were condensed in a sample bubbler using ice and water as a coolant medium for identification via GCMS.

Flow reaction studies of TIPB were performed at 400 °C and atmospheric pressure, keeping the W/F=0.2. The acetic acid ketonization reaction was performed at 320 °C and atmospheric pressure with W/F=0.3. Reactant and helium (carrier gas) feed rates for the probe reactions were 0.1 mL/hr and 50 mL/min, respectively. For all reactions, the catalyst was first preheated and flushed with helium (50 mL/min) for one hour at 300 °C prior to introducing the reactant via a syringe pump.

For temperature programmed desorption (TPD) experiments, 50 mg of H-zeolite sample was packed in a quartz reactor (1/4" OD) between two quartz plugs and flushed at 400 °C for 1 h with helium as the carrier gas (50 mL/min). After pre-treatment, the temperature was reduced to 100 °C and 2 μL pulses of isopropyl amine (IPA) were injected into the reactor through a septum using a syringe. The IPA was tracked by following a mass-to-charge ratio (m/z) of 58 exiting the reactor with a MKS Cirrus 200 quadrupole mass spectrometer (MS) until the signal remained constant with additional pulses to ensure that all of the acid sites in the catalyst bed were saturated. After adsorption of IPA on to the catalyst bed, it was flushed with carrier gas at 20 mL/min and 100 °C for 4 h to remove any physically absorbed IPA, after which the temperature was ramped from 100 to 600 °C at a rate of 10 °C/min under a flow of He (20 mL/min). The outlet stream of the reactor was connected to the MS to analyze the desorbing species from the catalyst bed. Quantification of the number of moles of product evolved in the MS was conducted by injecting standards, with propylene gas injected through a sample loop. The Brønsted acid sites for each H-zeolite sample were quantified by integrating the moles of propylene (m/z = 41) desorbed during the IPA-TPD experiment.

Adsorption measurements with 2,6-di-tert-butylpyridine (DTBP) were conducted in a PerkinElmer Spectrum 100 FT-IR Spectrometer equipped with a Harrick Praying Mantis^{TM} chamber. After pre-treating the H-zeolite sample at 300 °C in helium flow for 1 hour, the temperature was reduced to 50 °C and a blank spectrum of the zeolite surface was taken as a reference. DTBP was then adsorbed onto the surface for 30 min at 50 °C through a sample bubbler maintained at -7 °C while flowing helium at a rate of

50 mL/min (using a Porter mass flow controller). This was followed by flushing for 2 hours at 50 °C under a flow of 50 mL/min to remove physically adsorbed DTBP. After flushing, the spectrum of the H-zeolite surface adsorbed with DTBP was collected at 50 °C and then the temperature was raised at a steady rate of 10 °C/min. Analysis at each desired temperature was conducted by stopping the ramp and holding at a fixed temperature to obtain the spectrum (64 scans) prior to continuing the temperature ramp.

Results and discussion

Preparation of ZSM-5@silicalite-1

ZSM-5 and its purely-siliceous analogue silicalite-1 have an identical crystal structure (MFI type) possessing an orthorhombic *Pnma* space group comprised of 3-dimensional channels (ca. 5.6 Å diameter). ZSM-5 was synthesized according to a procedure reported by Persson et al. [157] with slight modifications. We prepared ZSM-5 crystals with a Si/Al molar ratio of 44, which was confirmed by inductively coupled plasma atomic emission spectroscopy (ICP-AES, Galbraith Labs). The crystal size was measured by dynamic light scattering (DLS) and electron microscopy. DLS analysis of a suspension of crystallites in aqueous solution revealed a relatively monodisperse distribution of crystals with an average hydrodynamic diameter equal to 156 nm. Scanning electron microscopy (SEM) images of ZSM-5 confirmed their average size and size distribution (Figure 33A). High magnification SEM images (inset) revealed that crystals are spheroidal with highly roughened surfaces. It is well documented in the literature that ZSM-5 and other zeolites grow by nonclassical routes [158-160] involving the aggregation of amorphous precursors. For instance, Subotić and coworkers [161, 162] suggest that ZSM-5 crystallization proceeds via a complex series

of pathways involving (i) precursor aggregation, (ii) precursor disorder-to-order transitions, (iii) aggregate growth and coarsening, and (iv) the densification of aggregates. Increased synthesis time often leads to “annealing” by Ostwald ripening to form relatively smooth and faceted crystals. If syntheses are performed at low temperatures where the timescales for coarsening are sufficiently long, the final crystal is typically rough. There are many examples of highly corrugated crystals similar to the ones shown in Figure 33 where particles appear to be fractal aggregates of smaller crystallites or have surfaces comprised of protrusions with dimensions spanning 5 to 20 nm. Notable examples include the syntheses of LTA (zeolite A),[163-165] FAU (zeolite X),[164] and MFI (silicalite-1).[158, 159]

An epitaxial layer of silicalite-1 was grown on ZSM-5 by seeded growth. During the synthesis of ZSM-5 seeds, the crystals were isolated by centrifugation and washed with deionized (DI) water to remove the supernatant. The crystals were then transferred as a gel (without drying) to a silicalite-1 growth solution. We used the gel transfer procedure to minimize ZSM-5 crystal aggregation and to prevent the potential alteration of its exterior surface that may occur upon drying. The silicalite-1 growth solution was prepared with tetraethylorthosilicate (TEOS) and tetrapropylammonium (TPA^+) as an organic structure-directing agent (OSDA) to facilitate the formation of the MFI structure. We employed a dilute supersaturated silica solution with molar composition x TEOS:14 TPAOH:9500 H_2O (with x = 17 – 40). The rationale for selecting a dilute solution was to minimize the homogeneous nucleation of silicalite-1, as well as achieve ultrathin (nanometer thick) silicalite-1 layers on the surface of ZSM-5 seeds. The silicalite-1 shell thickness was quantified by light scattering and electron microscopy.

DLS measurements revealed that the hydrodynamic diameter increased by 10 nm or more depending on the TEOS concentration. The autocorrelation functions in DLS measurements showed no evidence of a bimodal size distribution that would be indicative of homogeneous silicalite-1 nucleation. SEM images of the core-shell particles (Figure 33B) revealed larger particles on average compared to the original seeds. Transmission electron microscopy (TEM) images indicated that the core-shell particles were rough (Figure 33C) with features similar to those of the ZSM-5 core. High resolution TEM (HRTEM) revealed the presence of lattice fringes on the exterior surface (Figure 33D) with the same orientation as the particle interior, suggesting the shell formed via epitaxial growth of silicaltie-1 on ZSM-5.

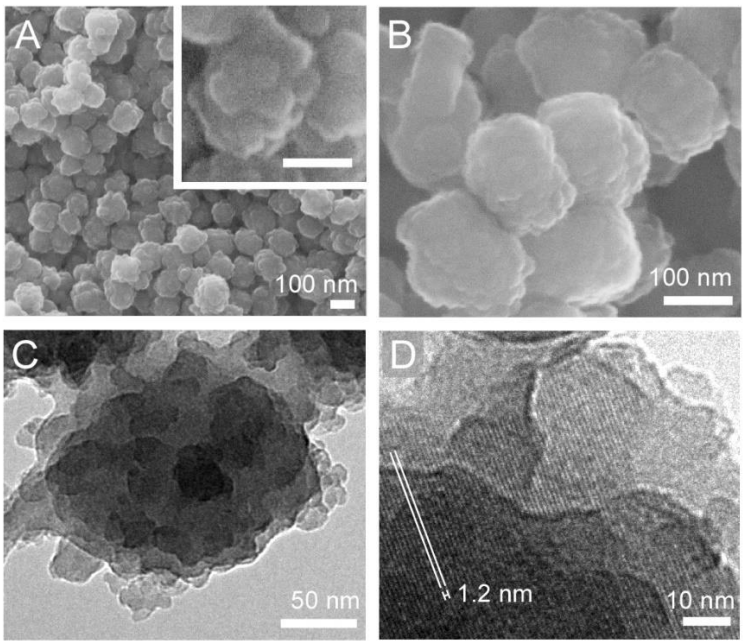

Figure 33 :- Electron microscopy images of ZSM-5 (core) and ZSM-5@silicalite-1 (core-shell) crystals prepared without thermal annealing. (A) SEM image of ZSM-5 crystals prepared at 100 °C for 60 h. (B) SEM image of ZSM-5@silicalite-1 prepared with a 10 nm shell thickness. (C) TEM image of a core-shell particle shows the rough crystal surface comprised of protrusions with dimensions spanning ca. 5 to 20 nm. (D) HRTEM image of the core-shell particle reveals the

presence of lattice fringes with translation symmetry extending from the exterior to interior of the crystal (1.2 nm periodicity, white lines).

Rough surfaces impose challenges for the analysis of shell growth and the characterization of silicalite-1 uniformity on ZSM-5 crystals. In order to obtain definitive proof of a continuous epitaxial layer of silicalite-1, we prepared spheroidal ZSM-5 crystals with smoother surfaces that were easier to characterize by scattering and microscopy techniques. This was accomplished by introducing an annealing step in the previous synthesis protocol. Following the completion of ZSM-5 crystallization, the gel product was transferred to a solution with molar composition 10 TEOS:14 TPAOH:9500 H_2O (with 1 wt% solid content) and was heated at 170 °C for 12 days. For this step we selected a silica concentration that was approximately equal to the solubility of silicalite-1 in order to minimize ZSM-5 dissolution and prevent silicalite-1 crystallization. During hydrothermal annealing, protrusions on the exterior surfaces of ZSM-5 seed crystals coarsened, most likely as a result of Ostwald ripening, to produce crystals with smoother surfaces (Figure 34A). The annealed ZSM-5 seeds were then used to prepare ZSM-5@silicalite-1. Electron micrographs of the core-shell particles revealed a spheroidal morphology (Figure 34B) and showed no evidence of protrusions on their exterior surfaces (Figure 34C).

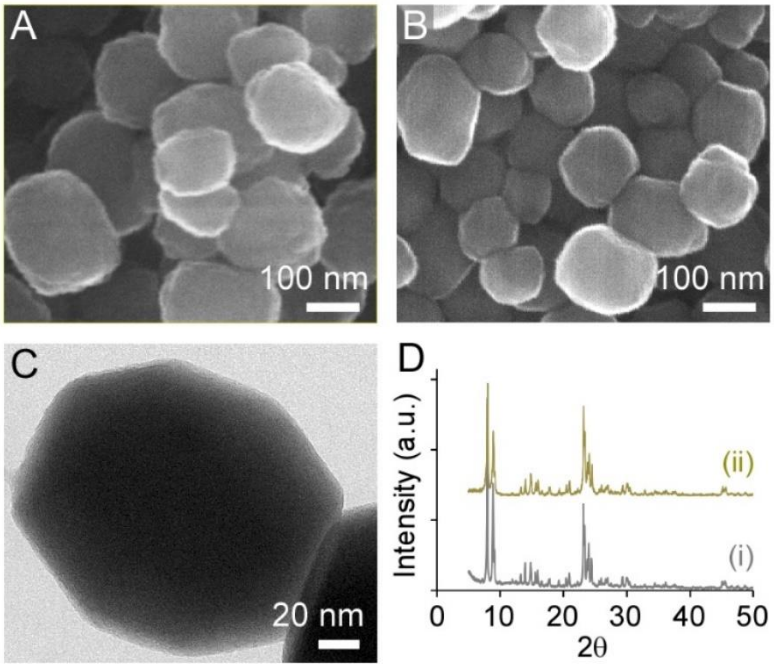

Figure 34 :- Characterization of ZSM-5 (core) and ZSM-5@silicalite-1 (core-shell) crystals prepared with thermal annealing. (A) SEM image of ZSM-5 crystals after 170 °C annealing for 12 days. (B) SEM image of ZSM-5@silicalite-1 crystals after 170 °C annealing of the core for 12 days and growth of a 10 nm silicalite-1 layer. (C) TEM image of a ZSM-5@silicalite-1 crystal reveals a smooth, faceted surface. (D) Powder XRD patterns confirm the crystallinity of annealed (i) ZSM-5 and (ii) ZSM-5@silicalite-1 as having the MFI structure (*Pnma* space group). XRD data are offset along the y-axis for visual clarity.

Powder X-ray diffraction (XRD) patterns of ZSM-5 (core) and ZSM-5@silicalite-1 (core-shell) confirmed that the products were fully crystalline (Figure 34D), i.e., an amorphous peak in the region 2θ = 20 – 30º was not observed in the core-shell XRD pattern. ICP-AES analysis revealed Si/Al molar ratios of 44 and 53 for the core and core-shell samples, respectively. These results confirmed the expected increase in Si content due to shell growth. Moreover, N_2 adsorption measurements revealed that the BET surface area of ZSM-5 crystals (475 m^2/g) was approximately equal to the ZSM-5@silicalite-1 core-shell particles (454 m^2/g). These studies revealed that the silica layer on the surface of ZSM-5 seeds is not an amorphous phase and that shell formation

does not result in pore blockage, thereby circumventing the undesired outcome of surface passivation techniques reported in the literature.

Validation of the Silicalite-1 Shell Structure

In order to confirm that the silica shell was a continuous epitaxial layer of silicalite-1, we used a combination of TEM, X-ray photoelectron spectroscopy (XPS), and catalytic testing with two probe reactions. Electron dispersive spectroscopy (EDS) revealed the presence of a silica layer surrounding the ZSM-5 core with an approximately uniform thickness of ca. 10 nm (Figure 35A). The ZSM-5 core in EDS mappings appears to be yellow due to the superposition of Si (green) and Al (red) elements. Conversely, the exterior of the particle is green due to the presence of a Si-rich shell. High resolution TEM (HRTEM) analysis of these particles shows the presence of lattice fringes (Figure 35B). HRTEM images confirm that there is a translational symmetry between the core and shell, as determined by the continuous orientation of lattice fringes without any apparent discontinuity at the core/shell interface. The continuous channels, which span from one end of the core-shell particle to the other, permit unhindered access of ions and molecules to diffuse within the 3D porous network of the MFI framework structure.

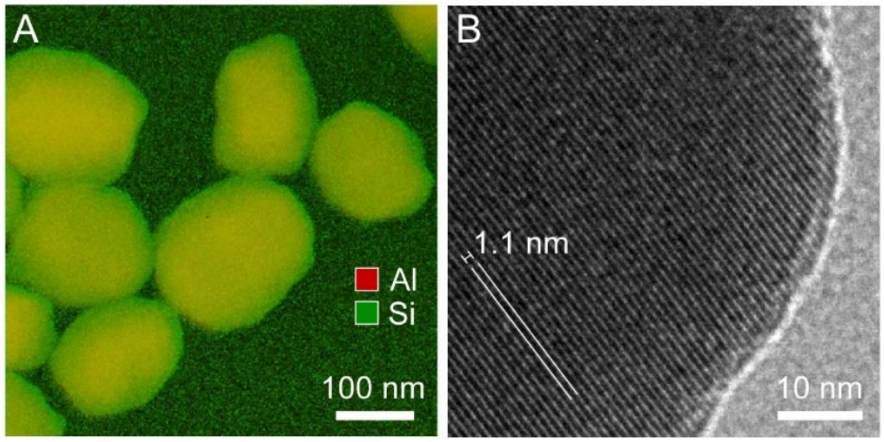

Figure 35 :- (A) Superimposed EDS mapping of annealed ZSM-5@silicalite-1 crystals prepared with a 10 nm silicalite-1 shell. The elements are color coded: Al (red) and Si (green). (B) HRTEM image of a core-shell crystal reveals the presence of lattice fringes that extend from the exterior to the interior of the particle without any discontinuity. The orientation of fringes (1.1 nm periodicity) is highlighted by the white lines. HRTEM images confirm the translational symmetry between the core and shell due to the epitaxial growth of a silicalite-1 layer on the surface of ZSM-5 seeds.

The formation of a thin silicalite-1 shell was further confirmed through the combined use of several analytical techniques, as summarized in Table 4. As synthesized ZSM-5 and ZSM-5@silicalite-1 samples were activated to their proton forms (H-zeolites) prior to XPS and catalytic studies. XPS results indicate a significant increase in the Si/Al ratio after growth of the silicalite-1 shell. The fact that the Si/Al ratio of the ZSM-5@silicalite-1 sample significantly increases, but is still a finite value, indicates that the shell formed is very thin due to the short sampling depth of XPS (i.e., on the order of nanometers). Comparison of the Si/Al ratios of ZSM-5 core particles reveals slight differences between ICP-AES and XPS. The Si/Al ratio provided by the latter is biased to the elemental composition near the exterior of the particle, whereas ICP-AES provides a bulk average elemental analysis. A lower Si/Al ratio from XPS measurements suggests the presence of so called “Al zoning” in ZSM-5. This is a

common phenomenon in ZSM-5 synthesis (notably in the presence of an organic structure-directing agent [166]), which leads to a Si/Al gradient within the crystal that decreases from its interior to its exterior.[166-171]

TABLE . Si/Al ratios and Shell thickness δ for HZSM-5 (core) and HZSM-5@Silicalite-1 (core-shell)

	Si/Al ratio		
Technique	**Core**	**Core-Shell**	**δ (nm)**
XPS [a]	39	82	----
ICP-AES [a]	44	53	9
IPA-TPD [ab]	45 ± 1	51 ± 2	7 ± 1
DLS	----	----	10 ± 2

[a] Experiments performed on H form of zeolite

[b] 10% weight loss due to moisture loss of zeolite during pretreatment is considered. Extra-framework Al estimated from ^{27}Al NMR (Table S1) is also included in the Si/Al ratio

Table 4 :- Si/Al ratios and Shell thickness δ for HZSM-5 (core) and HZSM-5@Silicalite-1 (core-shell)

Techniques such as temperature programmed desorption (TPD) and ^{27}Al NMR provide additional means of analyzing the Al content in zeolite particles. The temperature programmed desorption of isopropylamine (IPA TPD) measures the Brønsted acid sites, which directly correlate with the tetrahedral Al content in H-zeolites.[73,74] The extraframework Al was quantified by ^{27}Al NMR (Figure 36) to be 9.1% for the core and 5.1% for core-shell, both of which are significantly lower than the

percentages reported for commercial MFI catalysts (i.e., values can reach as high as 25%).[172, 173] The Si/Al data in Table 4 was used to estimate the shell thickness, δ, assuming a spherical morphology for all zeolite crystals. Knowing the Al content of the core and core-shell, the weight ratios of each were calculated, which is equivalent to volume ratio assuming the same density. The difference in volume for H-ZSM-5 (core) and H-ZSM-5@silicalite-1 (core-shell) was used to calculate the silicalite-1 shell thickness. The resulting δ values estimated from IPA TPD and ICP-AES are comparable to DLS measurements (within experimental error), thus providing additional evidence of a thin silicalite-1 shell.

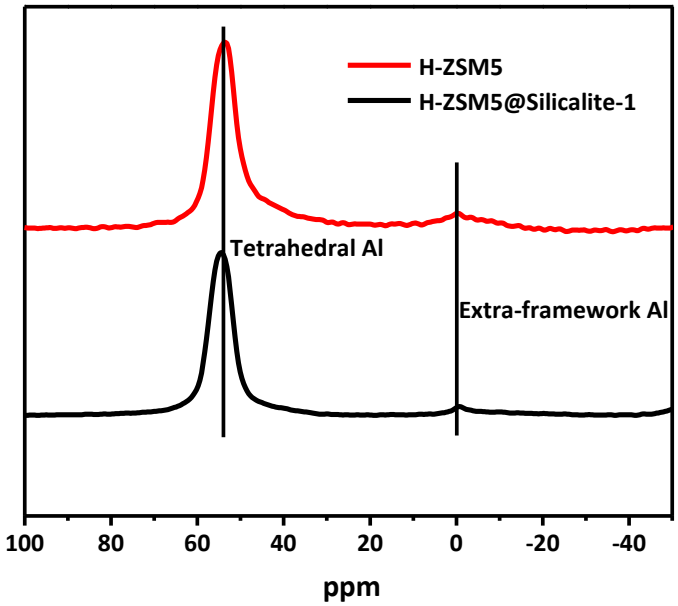

Figure 36 :- ^{27}Al NMR was used to quantify the amount of extra-framework alumina in H-ZSM5 (core) and H-ZSM5@silicalite-1 (core-shell). The intensities at 60 ppm and 0 ppm correspond to framework and extra-framework alumina, respectively.

Two probe chemical reactions were used to confirm the surface passivation of H-ZSM-5 and the unhindered access to Brønsted acid sites within H-ZSM-5@silicalite-1. Triisopropylbenzene (TIPB) is a bulky molecule with three reactive isopropyl groups and a kinetic diameter of 8.5 Å, which is larger than the pores of MFI (5.6 Å). This

limits the reactivity of TIPB to the external surface of the zeolite.[174-176] The second probe molecule selected for this study was acetic acid, which reacts via decarboxylative ketonization over Brønsted sites in zeolites to produce acetone.[7] The kinetic diameters of acetic acid and the reaction products (acetone, CO_2 and H_2O) are small enough to diffuse through the micropores of MFI. Figure 37A shows a dramatic reduction in the reactivity of TIPB over H-ZSM-5@silicalite-1 when compared to H-ZSM-5. On an equivalent acid site basis, the surface activity is limited to less than 6% of the activity of the parent zeolite, indicating a near complete silicalite-1 coating on H-ZSM-5. The removal of external surface Brønsted acid sites in H-ZSM-5@silicalite-1 was also demonstrated by infrared (IR) spectroscopy of an adsorbed bulky pyridine, di-tertbutyl pyridine (see Figure S4 in Appendix-C). A signal at 1616 cm^{-1}, corresponding to protonation of di-tertbutyl pyridine,[177, 178] is observed for the core, with little to no peak in this region for the core-shell sample, indicating the absence of external Brønsted acid sites. The rate of acetic acid conversion normalized per total acid site, as shown in Figure 37B, identical for the samples with and without a silicalite-1 shell. The rate of catalyst deactivation as a function of time is identical for both catalysts as well. This identical catalytic activity after incorporating the silicalite-1 shell demonstrates that the internal acid sites are accessible for this reaction, which is consistent with the results from TEM and BET analysis. This finding also validates the ability to passivate ZSM-5 surfaces without hindering the intrinsic activity of the catalyst, which is a significant advancement in zeolite core-shell design.

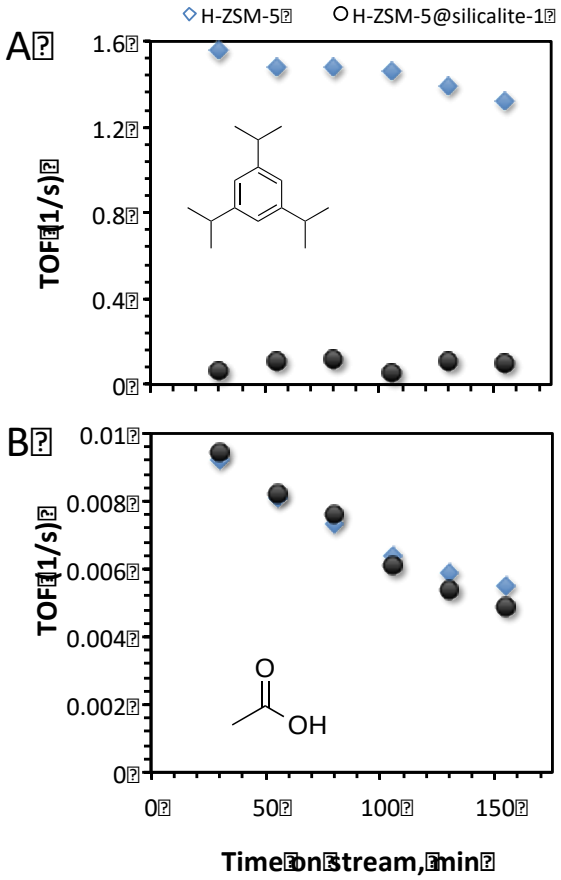

Figure 37 :- Gas phase turnover frequency (TOF) in a flow reactor of (A) triisopropylbenzene and (B) acetic acid over H-ZSM-5@silicalite-1 prepared with a 10 nm silicalite-1 shell, as well as the annealed H-ZSM-5 core. The reactions were performed at 1 atm after pre-treating the catalyst in He flow at 300 °C for one hour to remove physisorbed water from the catalyst surface. Cracking of triisopropylbenzene (A) was done at 400 °C and ketonization of acetic acid (B) was done at 320 °C. The outlet stream from the flow reactor is connected to a GC-FID equipped with innowax column to quantify the products. The number of Brønsted sites was estimated via IPA TPD (excluding extra-framework Al from ^{27}Al NMR).

Tailoring the Silicalite-1 Shell Thickness.

We investigated two approaches to tune the shell thickness. The synthesis can either be quenched at a specific time of hydrothermal treatment to achieve the desired thickness (leaving a fraction of unreacted silica in the growth solution), or an exact concentration of TEOS can be selected such that shell growth is terminated once the

solution reaches thermodynamic equilibrium (i.e., silicalite-1 solubility). We carried out the first approach and monitored the rate of shell growth using *ex situ* DLS measurements of ZSM-5@silicalite-1 particles that were heated for various times in a silicalite-1 growth solution. In order to measure shell growth over a reasonable timescale, we used a silicalite-1 growth solution with lower pH (molar composition 14 TEOS:7 TPAOH: 9500 H_2O), which increases the rate of crystallization. As shown in Figure 38, DLS measurements revealed a monotonic increase in the hydrodynamic diameter of ZSM-5@silicalite-1 with heating time. The linear rate of silicalite-1 growth is consistent with trends in the literature.[179] The measured growth rate of 3.8 nm/h (i.e., change in particle diameter with time) is approximately equal to the 4.0 nm/h value reported by Li et al. [135] in their study of silicalite-1 growth at similar conditions. CONTIN analysis of the DLS autocorrelation functions revealed a single particle size distribution for all extracted samples, which suggests that homogeneous silicalite-1 nucleation and crystal growth is negligible. Indeed, if the latter were to occur with any appreciable frequency, we would anticipate the presence of a bimodal size distribution. The absence of a smaller particle size population in the DLS data suggests that ZSM-5@silicalite-1 growth is the dominant pathway.

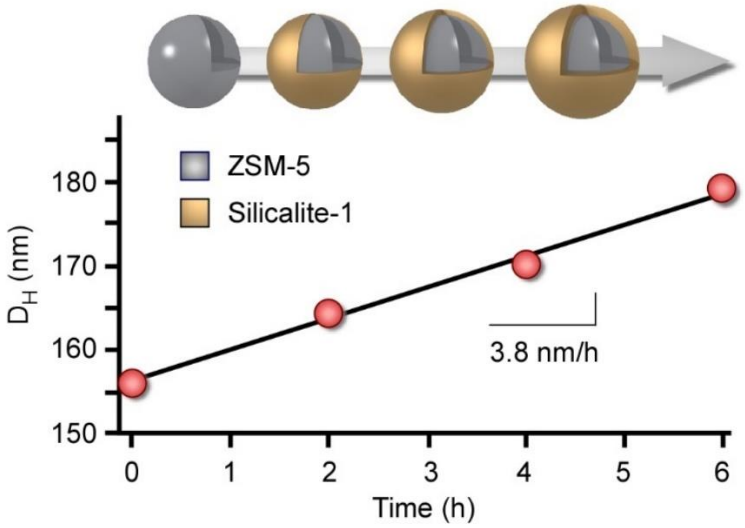

Figure 38 :- *Ex situ* DLS measurements of ZSM@silicalite-1 growth. The temporal change in hydrodynamic diameter D_H was analyzed by heating a 1 wt% dispersion of ZSM-5 seeds (D_H = 156 nm) in a silicalite-1 growth solution with molar composition 14 TEOS:7 TPAOH:9500 H_2O. Samples were removed from the oven (100 ± 1 °C) at periodic times and were quenched to room temperature for DLS analysis. The symbols are an average of three measurements with standard deviation of ± 2 nm. The slope of linear regression (solid line) reveals a 3.8 nm/h rate of silicalite-1 growth, which agrees with a prior study by Li et al.. [135]

A disadvantage of the previous approach is that silicalite-1 growth is terminated prior to reaching silicalite-1 solubility. As such, TEOS is wasted in this process and the extraction of crystals from the supernatant could lead to the potential deposition of amorphous silica from solution to the exterior surfaces of ZSM-5@silicalite-1 (thereby leading to pore blockage).[159] An alternative, and more practical approach, is to select the exact amount of TEOS needed to achieve the desired thickness, such that silicalite-1 growth is terminated once equilibrium is reached. The ability to control the thickness of the silicalite-1 shell, however, requires knowledge of solution chemistry and the approximate solubility of MFI crystals. Prior studies have shown that silicalite-1 growth solutions prepared with TEOS are comprised of silica nanoparticle precursors (1 – 6 nm) that self-assemble at a critical aggregation concentration (CAC), which is defined

by the silica concentration at a 1:1 molar ratio of TEOS:TPAOH.[180, 181] The kinetic phase diagram for silicalite-1 growth solutions depicted in Figure 39A reveals the presence of two distinct regions divided by the CAC (solid line). Region I (TEOS/TPAOH < 1) consists of soluble silica species (i.e., silicic acid and silica oligomers), while region II (TEOS/TPAOH > 1) consists of silica molecules in quasi-equilibrium with silica nanoparticles. There have been many studies that focused on characterizing the physicochemical properties of silica nanoparticles and identifying their role(s) in silicalite-1 crystallization.[180-186] We recently showed that silicalite-1 growth occurs by the addition of both precursors and silica molecules to crystal surfaces.[159] During the course of silicalite-1 crystallization, silica is consumed from the growth solution, thereby resulting in the depletion of silica nanoparticles (i.e., a temporal shift from right to left along the dashed line in Figure 39A). The final stages of silicalite-1 growth involve an exothermic-to-endothermic transition in the heat of crystallization when crossing the CAC that is accompanied by an increase in pH.[187] Crystal growth is completed once the concentration of silica in solution reaches the thermodynamic solubility of silicalite-1 (estimated as the dotted line in Figure 39A).

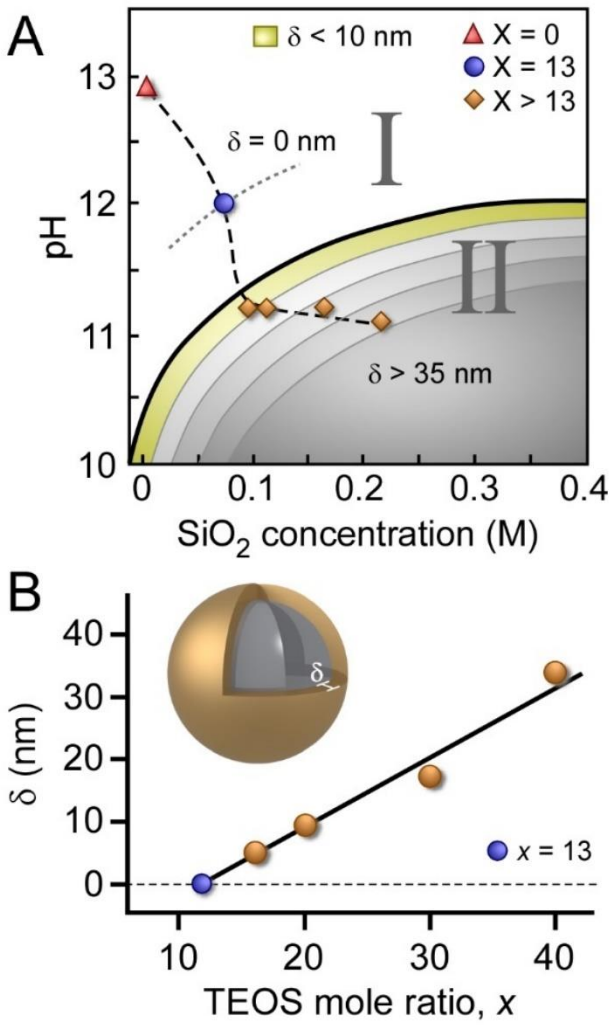

Figure 39 :- (A) Kinetic phase diagram of silicalite-1 growth solutions comprised of two regimes: Region I contains soluble silica molecules (monomers and oligomers) and Region II is comprised of soluble species in quasi-equilibrium with silica nanoparticle precursors.[187] The CAC (solid line) divides the two regions. The pH was measured for solutions used to prepare core-shell particles (diamond symbols), to estimate ce (blue circle), and to assess a silica-free solution (red triangle). The dashed line is interpolated between data points and the dotted line is an estimated solubility of silicalite-1. The color coded segments in Region II illustrate the progressive increase in shell thickness with increased silica supersaturation. (B) Synthesis conditions used to tailor the shell thickness of ZSM-5@silicalite-1. Growth solutions of molar composition x TEOS:14 TPAOH: 9500 H2O and ZSM-5 crystals (0.25 g seeds per 25 g growth solution) were heated for 24 hours at 100 °C, followed by 12 days of 170 °C annealing. The solid line is a linear regression (R2 = 0.97) extrapolated to zero shell thickness, which corresponds to ce of silicalite-1 (i.e., x = 13 TEOS).

The design of ZSM-5@silicalite-1 must take into account the relative ratio of seed and silica concentrations. Here, we used a concentration of 2.5×10^{15} seeds/L growth solution (i.e., N = 6.3×10^{13} seeds). If the concentration of seeds is sufficiently low, there is a higher probability of silicalite-1 nucleation and growth occurring in solution rather than on the surface of ZSM-5 seeds. This would lead to a mixture of ZSM-5, silicalite-1, and/or ZSM-5@silicalite-1 crystals in the final product. There is evidence in the literature [152, 154, 188] that suggests silicalite-1 crystallites can attach to the surface of ZSM-5 crystals, thus generating fractal aggregates as opposed to a continuous epitaxial silicalite-1 shell. Depending on the size of silicalite-1 crystals and their coverage on ZSM-5 surfaces, these layers may appear to be a uniform shell that would go undetected by cursory inspection using bulk characterization techniques such as DLS or SEM, whereas higher resolution techniques, such as TEM, are capable of discerning these differences.

The preparation of ZSM-5@silicalite-1 with predictable shell thickness requires the selection of an appropriate silica supersaturation. To this end, we prepared several growth solutions of varying silica concentration and measured the resulting shell thickness (Figure 39B). For these studies we used 0.095 – 0.22 M SiO_2 to adjust the shell thickness between 5 and 40 nm. We observe an approximately linear correlation between shell thickness and silica concentration that enables one to predictively tune the thickness as desired. It is reasonable to assume that molecular layers of silica ($\delta < 2$ nm) can be achieved by working at lower silica concentrations; however, for the purpose of this study, we used an appreciable shell thickness (ca. 10 nm) in order to confirm

silicalite-1 growth on ZSM-5 seeds. The shell thickness δ can be controlled using Eq. 1 with the judicious selection of silica concentration c(δ) for seeded crystallization:

$$c(\delta, T, pH) = \frac{4\pi N \rho_{SiO_2}}{3VM_{SiO_2}} \cdot ((R+\delta)^3 - R^3) + c_e(T, pH) \quad (1)$$

The parameter R is the average radius of ZSM-5 seeds, N is the number of crystal seeds, ρ is density of silicalite-1, V is the total volume of the growth solution, and M is molar mass of SiO_2. Assuming ca. 2.0 g/cm^3 as the silicalite-1 density and 78 nm as the average radius of ZSM-5 seeds, the calculated silicalite-1 solubility c_e is 0.05 ± 0.02 M. The selection of c(δ) equal to c_e corresponds to δ = 0 nm. An estimate of this value using a linear extrapolation of the data points in Figure 39B results in c_e = 0.06 M (i.e., 13 TEOS:14 TPAOH molar ratio), which is in good agreement with the calculated value from Eq. 1. To experimentally validate the estimated c_e, we prepared a 0.06 M TEOS solution without ZSM-5 seeds (Figure 39A, blue circle) and compared its pH to that of the seeded growth solutions after 24 hours of heating. We observed nearly identical pH values (12.0 and 11.8, respectively), suggesting our estimated value of c_e is accurate within experimental error.

Conclusions

In summary, we have demonstrated an ability to synthesize a core-shell zeolite with compositionally distinct, but structurally identical domains. For this study we selected the MFI framework structure, which is one of the most commercially relevant zeolites used in the petrochemical industry. Using a broad combination of experimental techniques, we have shown that ZSM-5@silicalite-1 can be prepared with tunable shell thickness. Electron microscopy and textural analysis confirmed that silicalite-1 forms an epitaxial layer on ZSM-5 crystals without blocking pore openings. SEM and DLS were

used in combination to confirm that the shell thickness can be tailored with nanometer resolution. XPS and TPD measurements revealed the presence of a siliceous shell, while probe reactions using molecules that were either too large (i.e., triisopropylbenzene) or sufficiently sized (i.e., acetic acid) to access MFI pores confirmed the uniform shell coverage. Moreover, these studies revealed that the activity and lifetime of ZSM-5 catalysts are not compromised by the overgrowth of a passivation layer. This finding is a distinct advantage of our synthetic protocol relative to alternative techniques that have been used in the past to generate surface passivated zeolites.

The synthesis of ZSM-5@silicalite-1 offers a pathway for tuning the physicochemical properties of MFI-type materials – notably for their use as catalysts where surface passivation can enhance product selectivity. Knowledge of solution chemistry for aluminosilicate zeolites and their siliceous analogues affords the opportunity to selectively design novel materials with tailored properties. To this end, the method described here provides a general platform for core-shell design that may prove to be applicable to other nanoporous zeolite structures.

Acknowledgment

We are grateful to Dr. Hansoo Kim (TAMU-MIC) for assistance with TEM measurements. We thank Dr. Banghao Chen (Florida State University) for performing the Al-NMR experiments, Dr. Mallikharjuna Komarneni for conducting the XPS measurements and Manasa Godavarthy for assistance with the flow reactions. We acknowledge financial support from the American Chemical Society (grant PRF 52422-DNI5), the National Science Foundation, (grant CAREER 1151098), The Welch

Foundation (grant E-1794), NIFA-USDA BRDI (2012-10008-20271), and the Department of Energy (grant DE-EE0006287).

Chapter 8 :- Mechanism of Ketonization of Carboxylic acids over ZSM 5 – role of Alpha Hydrogen

All the experimental work and data analysis in this Chapter was performed by Manasa Godavarthy and myself.

Introduction

Bio-oil derived from the fast pyrolysis of biomass, which is one of the promising renewable fuels also contains considerable amounts of phenolics, furanics, carboxylic acids and light oxygenates[1, 13, 189-193]. Bio-oil is a promising alternative fuel and the recent increased interest in bio – oil upgradation calls for better understanding of various challenges associated with bio-oil. Similarly, carboxylic acids present in the crude oil, pose severe problems when refining the crude oil. The highly reactive carboxylic acids are very corrosive and difficult for handling and storage. Ways to reduce the amounts of acidic content in the crude have been under research. The conversion of these acids into non acidic molecules is a very interesting area of study.

One reaction of significance for converting these problematic carboxylic acids is ketonization [7, 34, 194-196], where two carboxylic acids react to produce a ketone, CO_2, and H_2O as depicted in Figure 1. The product of this reaction is ketone which is not corrosive like the carboxylic acid. Better understanding of the mechanism behind the conversion of carboxylic acids into ketones could lead to improvements in catalyst design for the processing of problematic crude oils.

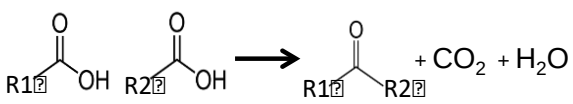

The most commonly used zeolites in the refining industry are HZSM-5 and HY, and zeolites are a good catalyst for ketonization reactions. As this is a popular and an important reaction, we can assume that it is well understood, however, literature has very few studies.

Various groups have studied the ketonization mechanism over oxide catalysts but fewer studies have been conducted on protonated zeolites. Previous studies in our group have established that HZSM-5 demonstrates promise to convert acetic acid into ketone. Also, studies on this reaction is subject to some controversy regarding the mechanism of ketonization on heterogeneous catalysts[197]. Understanding the intermediate species formed for ketonization can benefit the research about this reaction.

Performing ^{13}C experiments and gas phase flow experiments with various carboxylic acids with varying carbon chain length and number of alpha hydrogens like Pivalic acid, benzoic acid, propionic acid, hexanoic acid will further improve our understanding the ketonization mechanism.

In this contribution, we report the importance of the presence of α- hydrogen in one of the reacting carboxylic acids for the ketonization reaction over HZSM-5. Experiments for ketonization with carboxylic acids having no alpha hydrogens and ^{13}C labelled acids gave interesting perceptions into the importance of the α- hydrogen importance for the intermediates for the ketonization reaction.

Experimental Methods

Catalyst preparation

The zeolite used for the experiments is a commercial catalyst (CBV 8014) purchased from Zeolyst International in ammonium form with a Si/Al ratio of 40. Here on in this paper the catalyst would be referred as HZSM-5. The catalyst was calcined in dry air at 600^{o}C for 5 hrs. to thermally decompose NH_4^+ to NH_3 and H^+ and obtain the protonated form of the zeolite. The catalyst was pelletized and sieved to obtain particles of size in the range of 90-250 µm.

Catalyst characterization

X-Ray Diffraction studies were performed on the zeolite sample for checking the crystallinity of the zeolite. The catalyst sample was put on a plastic slide, with the surface made very flat. The analysis was performed using Rigaku automatic diffractor (model D-Max A) with a curved crystal monochromator. It was operated at 40 kV and 35mA between the angle ranges of 5- 55^{o} using Cu Kα as radiation source.

SEM (Scanning electron microscopy) measurement of the sample was performed using a Zeiss- NEON FEG-SEM instrument to estimate the particle diameter. A small amount of the zeolite was suspended in aqueous medium and placed on carbon tape and dried before analyzing.

IPA (Isopropyl Amine) Temperature - programmed desorption experiment was performed on the ZSM-5 sample (CBV 8014) to quantify the number of Brønsted acid sites in the catalyst sample. 50mg of the catalyst sample was held between quartz wool plugs in a ¼"OD quartz reactor. This sample was pretreated at 300 ^{o}C with 20ml/min helium flowing as carrier gas for 2 hours. The temperature was then reduced to 100^{o}C

and IPA was injected into the reactor as 2 microliter pulses until saturation. An MKS cirrus 200 mass spectrometer was used to track the m/e (mass to charge ratio) of IPA 44 and 58 for a constant signal indicating saturation. The catalyst bed was flushed with a helium flow of 20ml/min for 4 hours to ensure that the bed was free of any physically adsorbed IPA. The temperature of the catalyst bed was ramped from 100 ^{o}C to 600 ^{o}C at a rate of 10^{o}C/min and the products desorbing from the surface are tracked. Propylene gas was pulsed from a known volume sample loop to quantify the products.

Flow experiments

The continuous flow reactions were conducted at atmospheric pressure in a ¼"OD quartz reactor and at various temperatures ranging between 220 ^{o}C and 320 ^{o}C. The catalyst was mixed with acid washed glass beads of size ranging between 150 μm – 250 μm to avoid channeling and this was packed into a bed into the reactor held between quartz wool plugs. A thermocouple was attached to the outer side wall of the reactor to monitor the temperature of the catalyst bed. A vaporization zone is created at the inlet of the reactor by heating it to appropriate temperatures sufficient to vaporize the reactants. The outlet lines are heated to a temperature of 250 ^{o}C to prevent any condensation in the lines and the outlet of the reactor is connected to a six port valve and to a HPGC equipped with a flame ionization detector and an innowax column with dimensions 30m and 0.25micrometer for product analysis.

The acid reactants, Pivalic acid (Aldrich, 99%), benzoic acid (Sigma Aldrich, ACS reagent, ≥99.5%) and acetic acid (Sigma Aldrich, ACS reagent, ≥99.7%) were introduced into the reactor with a syringe pump. The products made in the reaction were condensed into a sample bubbler using ice as a cooling medium, at the downstream of

the six port valve. The reactions were conducted at various temperatures and Weight/ flow ratios.

Temperature programmed reactions

The set up for these experiments is a similar set up used for IPA TPD experiments.

Temperature programmed desorption experiments of acid (pivalic acid or benzoic acid) on the Brønsted acid sites present in the HZSM – 5 catalyst sample was studied in the reactor. 50 mg of catalyst was packed between two quartz wool plugs in a ¼" OD reactor and pre-treated for 2 hours at a temperature of 300 ^{o}C in 50ml/min continuous flow of carrier gas, helium. During the pre-treatment, water (m/e = 18) was tracked in the MS connected at the reactor outlet. The temperature was brought down to 100 ^{o}C, and carboxylic acid (pivalic acid or benzoic acid) was pulsed in 2µL pulses using an air – tight syringe, until the catalyst bed was saturated. This was ensured by tracking Pivalic acid (m/e = 57) or benzoic acid (m/e = 105) at the exit of the reactor to be at a constant MS signal. The catalyst bed was flushed for 4 hours in helium flow (50ml/min) to remove any physically adsorbed species. The temperature was ramped from 100 ^{o}C to 600 ^{o}C at a rate of 10 ^{o}C/ min and the products that are desorbing were tracked using the MS. The products were quantified using standard sample injections.

When performing TPD experiments with two carboxylic acids to study for cross ketonization, the temperature was ramped up to a previously determined dehydration temperature for the first carboxylic acid and the second carboxylic acid (acetic acid, benzoic acid or ^{13}C labelled benzoic acid based on the experiment) was pulsed in with an air tight syringe. The temperature was then ramped to 600 ^{o}C and the products

desorbing were tracked using the MS. The idea behind these experiments was to saturate the zeolite surface with one acid molecule, dehydrate and supply the surface with a second acid molecule to analyse the products formed

Results and Discussion

Characterization results

XRD patterns of the commercial HZSM-5 sample, CBV 8014 indicate that this is the MFI structure. SEM images show that the crystal sizes of the catalyst vary between 100-500nm.

In the IPA TPD experiments, the number of moles of propylene desorbed from the catalyst is a direct indicator of the number of Brønsted acid sites. This is explained as IPA reacts on the Brønsted acid site of the protonated zeolite to produce propylene and ammonia. From IPA TPD experiments, the Brønsted acid density of the ZSM-5 zeolite is 0.39 milli-moles per gram of catalyst. A theoretical calculation for the Brønsted acid site density estimates 0.406 milli-moles per gram of catalyst. The experimental and theoretical values are close.

Flow reaction results

As benzoic acid is a crystalline solid, a solution was prepared with benzene as a solvent. This solution of molar ratios of benzoic acid to benzene of 1: 10 will be hereby referred as benzoic acid. Flow reaction experiments were performed at reaction temperature of 300 ^{o}C with a W/F of 0.22 and no conversion of the benzoic acid was observed. Various reaction temperatures were experimented with, but benzoic acid displayed no conversion into ketones or any other products.

Figure 40 shows the species desorbing from a temperature programmed desorption study of benzoic acid over HZSM-5 surface. This indicates an initial dehydration step at a temperature of suggesting the production of surface acyl species on the catalyst surface.

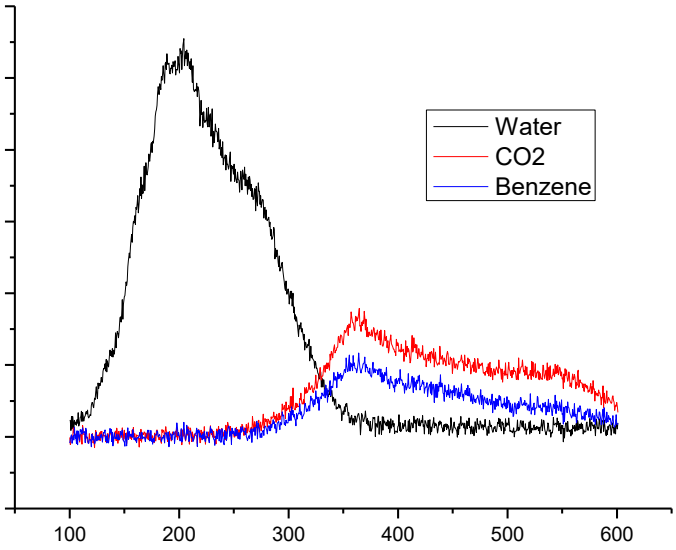

Figure 40 :- Benzoic acid TPD on HZSM-5 showing an initial dehydration step

To ensure that the water desorbed is produced by the reaction of the benzoic acid on the Brønsted acid sites, the water formed on the catalyst surface was quantified corresponding to the available Brønsted acid sites in the catalyst sample. The number of moles of water desorbed was quantified to be 20.7 micromoles, and the number of Brønsted acid sites in the catalyst sample is 20.3 micromoles. The water generated corresponds to nearly 100% of the Brønsted acid sites, indicating that water is produced by reaction on the acid sites and not physically adsorbed water. So we can clearly assume that the benzoic acid forms surface acyl species.

Previous studies in the group have reported similar results while working with acetic acid over HZSM-5 catalyst, where an initial dehydration step resulting in the formation of acyl intermediate was observed followed by a ketone and CO_2. The reaction mechanism was proposed to be the interaction of the surface acyl intermediate with a second activated surface acid species followed by decomposition of the intermediate into acetone and CO_2. [198]

Chang et al. [199], from their studies proposed that the mechanism of ketonization occurs with the nucleophilic attack of an acyl ion, by an acetate species with CO2 elimination. Work by Ponec et al. [194, 195, 200] about ketonization on various oxides with different acid reactants indicates that the presence of alpha hydrogen is important for ketonization over oxide catalysts. But 2,2,5,5, tetra methyl adipic acid, which lacks an alpha hydrogen forms a ketone over BaO and K [201].However, no discussion about the necessity of an alpha hydrogen for ketonization over zeolites was available in literature. It may be noted that benzoic acid has no alpha hydrogen and this may be a reason that ketonization of benzoic acid on zeolites is not observed.

To further understand the role of alpha hydrogen in ketonization, co-feeding experiments with benzoic acid and another carboxylic acid containing alpha hydrogens seemed to be an interesting headway. Acetic acid seemed to be the best choice as it has three alpha hydrogens and from previous work in the group, it was established that acetic acid readily forms acetone [198] at similar reaction conditions.

Flow experiments co-feeding benzoic acid and acetic acid in a molar ratio of 1: 8 at a reaction temperature of 300 ^{o}C at a W/F of 0.22 were performed, and the results are

shown in Figure 41. As expected, we see acetone formation but an observation of great interest here, is the formation of acetophenone, a cross ketone between benzoic acid and acetic acid.

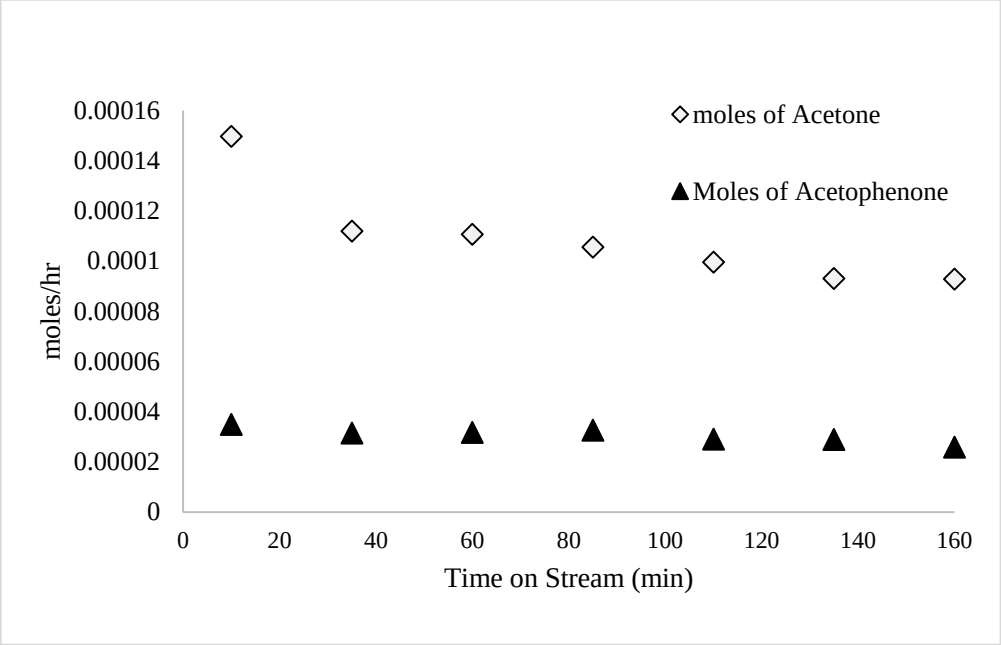

Figure 41 :- Flow reaction studies co-feeding acetic acid with benzoic acid at T=300C showing formation of two ketones

To probe the reaction mechanism, temperature programmed desorption studies were done by saturating the surface of the catalyst bed with benzoic acid and flushed for a certain amount of time. From previous experiments, the dehydration temperature is known just beyond which and the catalyst surface is believed to contain surface acyl species. The temperature was ramped at 10 ^{o}C/min to 220 ^{o}C and acetic acid was pulsed in through the septum on to the catalyst bed. The desorption of the ketones was tracked in the MS and are shown in Figure 42a,b as a function of number of pulses.

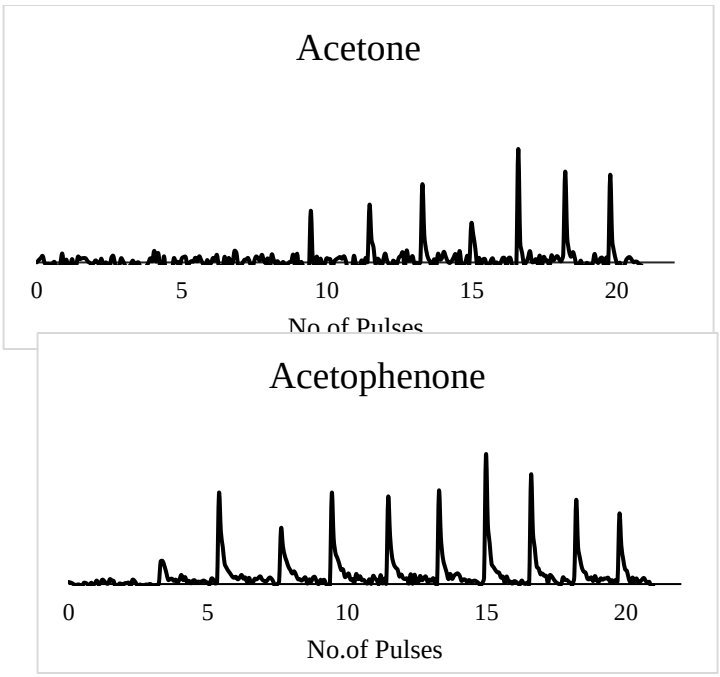

Figure 42 :- a, b: Benzoic acid TPD studies pulsing in acetic acid on benzoyl adsorbed HZSM5 showing acetone and acetophenone respectively

It was evident that a cross ketone is formed with acetic acid pulses. Also, an interesting observation is that with increase in number of pulses of acetic acid, the acetone produced increases. This suggests that the surface adsorbed acyl species from benzoic acid interacts with the acetic acid molecules pulsed in to form acetophenone and desorb from the surface of the catalyst. With increased number of pulses, the surface acyl species are reduced as they couple with acetic acid and leave the surface making the Brønsted acid sites available for acetic acid ketonization. Therefore, the acetone formation occurs after few pulses and seems to be more significant in the later pulses.

It can be established that for ketonization over zeolites, it is neccesary that one of the two carboxylic acids has an alpha hydrogen. To verify this, experiments with

pivalic acid were conducted as it does not have any alpha hydrogens. Pivalic acid was made into a solution in a molar ratio of solute to solvent 10:1 with benzene as a solvent. This solution will be referred as pivalic acid in furthere discussion. Flow reactions with pivalic acid over HZSM - 5 at a reaction temperature of 300 ^{o}C and a W/F of 0.12 show 100% selectivity towards isobutylene. Observing no ketones, the possibility of ketone formation with various temperatures was examined by conducting reaction over varying reaction temperatures over a range of 220^{o}C to 300^{o}C. The conversion of the pivalic acid slightly changed at various temperatures, but the selectivity remained 100% towards isobutylene, thereby indicating the fast decomposition of the pivalic acid and no ketonization.

To investigate the probability of cross ketonization, similar co-feeding experiments with pivalic acid and acetic acid in a molar ratio of 5:1 were conducted at reaction temperature of 300 ^{o}C and a W/F of 0.3. Surprisingly, the products formed were acetone and isobutylene, and no cross ketone was formed between both acids.

Figure 43 shows the amounts of acetone produced by reacting acetic acid over HZSM - 5 at same temperature and W/F and the amount of acetone formed when both acids were co-fed. Comparing the amounts of acetone produced, it can be noticed that the activity of acetic acid when co-fed with pivalic acid is significantly low. But, when the flow of pivalic acid was stopped, it can be observed that the amount of acetone produced increased and is comparable to acetone produced when acetic acid is fed alone. Re-starting the pivalic acid flow, inhibits the amounts of acetone produced. This suggests that the pivalic acid only competes for the sites on the surface but does not adsorb irreversibly on Brønsted acid sites.

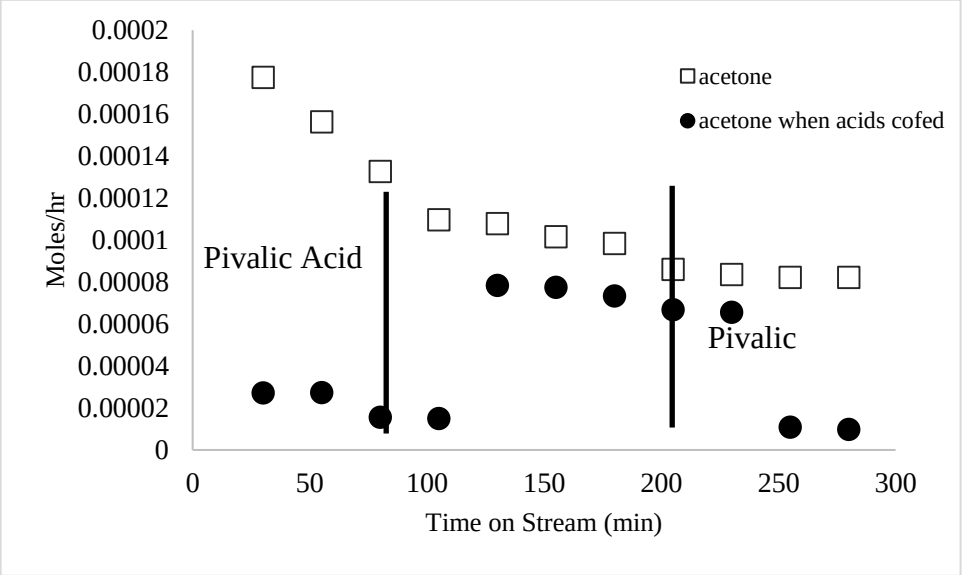

Figure 43 :- Flow reaction studies co feeding Pivalic acid and acetic acid at T=300ºC

The temperature programmed desorption studies of pivalic acid over HZSM-5 indicate decomposition of pivalic acid, as shown in Figure 44. This implies that the pivalic acid does not dehydrate to form a surface acyl, instead it decomposes. These observations are in line with the flow reaction results from which we observe that pivalic acid does not undergo ketonization

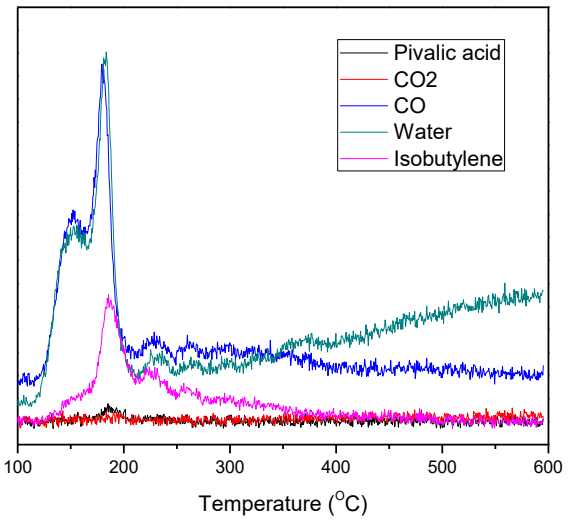

Figure 44 :- Pivalic acid TPD on HZSM-5 showing decomposition into isobutylene, water and CO_2

Mark Davis et al.[202] reported in their study of acylation of biphenyl that with pivalic acid, the t-butyl cation is more stable than the tri-methyl cation and therefore pivalic acid could not form an acyl species.

From previous experiments, it was understood that one of the two acids reacting over HZSM-5 needs to have an alpha hydrogen to produce a ketone. But benzoic acid, which does not have an alpha hydrogen can produce surface acyl species was another result from the experiments. To support this observation, carbon labelled studies might help understanding the contribution from each acid for forming a ketone and thereby the reaction mechanism.

Temperature programmed experiments as described above were conducted with benzoic acid with ^{13}C labelled carboxylic group and acetic acid. The catalyst surface was saturated with ^{13}C labelled benzoic acid and the temperature was ramped to the

dehydration temperature and acetic acid was pulsed in and the ketones were tracked for analysis and shown in Figure 45a,b.

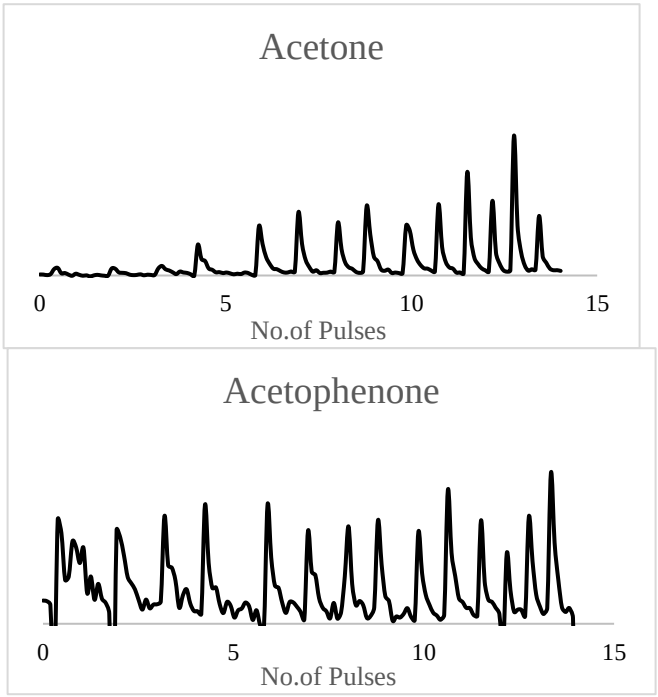

Figure 45 :- a, b: TPD studies pulsing in acetic acid on ^{13}C benzoyl adsorbed HZSM5

The observation of significance from this experiment is that, the mass number (m/e 105) for the cross ketone, acetophenone shifted by 1. This indicates that the cross ketone contains the labelled carbon. This is strong evidence that the acyl species present in the cross ketone is contributed by the benzoic acid and not the acetic acid. The acyl couples with a second activated carboxylic acid forming the intermediate for decomposing into a ketone and CO_2.

Conclusions:

Benzoic acid produces a cross ketone when co-fed with acetic acid. At least one of the carboxylic acids requires the presence of an alpha hydrogen for ketonization

reaction to occur over zeolites, this is similar to the observation reported for reducible oxides. An initial dehydration step required to form surface acyl species can occur even with acids that do not have an alpha hydrogen.

However, pivalic acid behaves different undergoing a fast decomposition. Also pivalic acid reversibly inhibits the ketonization activity of acetic acid on HZSM-5. Carbon labelled experiments confirm that an alpha hydrogen is needed in the second acid molecule for it to couple with the surface acyl species, forming an intermediate which decomposes into ketone and CO_2.

Chapter 9: Synthesis of thin layers of ZSM-5 over carbon nanotubes for improved selectivities

This manuscript was prepared together by me and Dr. Nick Briggs which will be submitted for publication. The nanotubes used in this study were synthesized and characterized by Dr. Briggs.

Introduction

Zeolites have become an important material in catalysis and have been used for a wide range of reactions. Zeolites are used in fluidized catalytic cracking where low value high molecular weight hydrocarbons are converted to high value olefinic gases, gasoline and diesel oil[203, 204]. However, since zeolites are composed of solely microspores intracrystalline diffusion limitations can limit the applicability of zeolites unless micropores are added. Hierarchical zeolites allow for the diffusion paths to be modified which can change reaction selectivity[205-210]. Modification of the diffusion path can be done to increase the ability of molecules to diffuse in and out of the zeolite so that the molecules do not become trapped.

Several approaches have been taken to create hierarchical zeolites by using templates and chemicals. One approach is to etch away portions of the zeolite with an alkaline solution. The alkaline solution attacks defects on the zeolite creating mesopores[211-214]. However, this method suffers from the inability to control where and how the alkaline solution etches the zeolites. A different approach Mesoporous zeolites have been synthesized using surfactants which create rod-like micelles creating the well-known MCM-41[215, 216] and SBA 15[217, 218]. However, these catalysts can have low acidity due to the synthesis. Another approach is to construct zeolites

using a template, such as carbon nanotubes[219-224]. Carbon nanotubes have also been used to construct metal-oxide nanotubes[225-230]. By building the zeolite around the carbon nanotube a pore is formed and then carbon can then be burned away leaving the zeolite with a pores the size of the carbon nanotubes. This approach suffers from the form in which carbon nanotubes and carbon particulates are received. Particulates of carbon can agglomerate together and can become trapped if the zeolite grows entirely around the carbon wasting zeolite material. Carbon nanotubes are typically in a random orientation and agglomerated together. Therefore, it is difficult to control the position of the pores and pore spacing. Carbon nanotubes can be grown vertically, however, approaches taken so far have been with the carbon nanotubes grown on a silicon wafer, which offers low surface area and is difficult to scale up[231, 232]. Therefore, there is a necessity to create a process which is scalable and can finely control the pores properties.

In this report, we have created a hierarchical zeolite using vertically aligned multi-walled carbon nanotubes (VMWNTs) in a scalable method. This is accomplished by growing VMWNTs between mica sheets which was initially proven by Wei's group[233] and then improved upon by our group[234]. Zeolite crystals are grown on the outside of VMWNTs and then the VMWNTs are removed by oxidation. The result is a hierarchical zeolite with large pores the diameter and width of the VMWNTs. The VMWNTs are grown between mica sheets and this keeps the ends of the VMWNTs open allowing for molecules to diffuse into the large pores. By varying the amount of VMWNTs added to the solution for zeolite growth the density of zeolite crystals around the VMWNTs can be changed. Zeolite rods can be made or a zeolite block with large

pores can be made. This hierarchical zeolite has enhanced selectivity for cracking bulky molecules such as triisopropylbenzene. Zeolite with solely micropores results in molecules resulting from cracking of triisopropylbenzene becoming trapped in the zeolite pores and carbon deposited on the outside of the catalyst resulting in catalyst deactivation. With the the hierarchical zeolite the triisopropylbenzene and the products formed from cracking can diffuse in and out of the zeolite due to the large pores. This prolongs catalyst life and enhances reaction selectivity.

Experimental Details

VMWNTs Synthesis

VMWNTs were grown between mica sheets by following the conditions to grown sample HRRx650D-D.

Zeolite Synthesis:

Zeolite precursor was prepared with a gel composition of 9TPAOH/0.16NaOH/Al/25Si/495H2O/100EtOH[235]. The reagents used for the synthesis are tetraethyl orthosilicate (98%, Sigma-Aldrich), tetrapropylammonium hydroxide (40% W/W, Alfa-Aesar), aluminum isopropoxide (98%, Sigma-Aldrich), sodium hydroxide (>98%, Sigma-Aldrich) and double distilled water. Precursor gel was stirred at 500 rpm for 24hrs for incubation. Several batches of this gel were prepared and for each batch 500 mg, 750 mg, 1000 mg or 2000 mg of CNT's were added and stirred for 1 hr. The samples made with 500 mg are labelled Z-CNT-1, 750 mg are labelled Z-CNT-2, 1000 mg Z-CNT-3, and 2000 mg Z-CNT-4. Each batch was transferred into a Parr vessel and left in the oven at 165 °C for 120 hrs. The obtained

sample after synthesis was washed with water several times. The obtained cake was dried for twelve hours at 85 ˚C in an oven. The dried sample is ion-exchanged from sodium form to ammonia form with 2M ammonium nitrate solution at 80˚C for three hours. The ion-exchange procedure was repeated five times to ensure complete exchange. This was followed by washing with double distilled water three times and drying for twelve hours at 85˚C. Obtained ammonium form zeolite was calcined at 600˚C (ramp rate 2 ˚C/min) for five hours to burn off the CNT's and to get proton form of zeolite.

Nitrogen Adsorption for Surface Area Measurements

A Micrometrics ASAP 2020 Surface Area and Porosity Analyzer (Micrometrics; Norcross, GA) was used to perform nitrogen adsorption experiments to determine the total pore volume, micropore volume, and by difference the mesopore volume of the catalysts.

IPA-TPD

Isopropyl amine (IPA) temperature-programmed desorption (TPD) is a proven technique for estimating the number of Brønsted acid sites in H-form zeolites[236]. IPA reacts on a Brønsted acid site of H-zeolite to produce propylene and ammonia. IPA-TPD experiments were done on all the H-Zeolite samples used in this study to investigate the amount of Brønsted acid sites. 50mg of catalyst was loaded into a quartz reactor (1/4" OD) and flushed at 300˚C for two hours with helium as carrier gas (20ml/min). After flushing the sample the temperature was reduced to 100˚C and 2 μL pulses of IPA were injected into the reactor through a septum via a syringe. Mass to charge ratio (m/e) of 44 and 58 were tracked at exit of the reactor with a MKS Cirrus

200 quadrupole mass spectrometer (MS), to ensure saturation of all the acid sites in the catalyst bed with IPA. Pulses of IPA were continued until a constant signal m/e=44 and 58 was observed. After adsorption of IPA on to the catalyst bed, it was flushed with carrier gas (20ml/min) at 100˚C for 4hrs to remove all the physically absorbed IPA. Flushing was followed by a temperature ramp from 100˚C to 600˚C at a rate of 10˚C/min. The products desorbing from the reactor with temperature ramp were tracked by MS. Quantification of the products was done by injecting standards and propylene gas pulsed using a sample loop.

X-Ray Diffraction

For checking the crystallinity of the sample, X-ray diffraction studies using Rigaku automatic diffractor (Model D-MAX A) with a curved crystal monochromator were performed. A flat surface of the well ground samples was prepared on a plastic slide for the experiments. The instrument has Cu-Kα as a radiation source and was operated at 40kV and 35 mA between the angle range of 5-60˚.

Reaction Studies

Flow reaction studies are performed in a quartz tube reactor (1/4" OD) at 400 °C and at atmospheric pressure. The H-zeolite catalyst is diluted with acid washed glass beads packed in the reactor between plugs of quartz wool. The inlet of the reactor is heated to create a vaporization zone and the outlet stream of the reactor as well as the six port valve for injection to the gas chromatograph (GC) were heated to 250 °C to prevent condensation. The temperature of the catalyst bed was controlled by a thermocouple attached to the outer wall of the reactor. The catalyst was preheated and flushed with helium (125 mL/min) for one hour at 400 °C before introducing the

reactant using a syringe pump. The products were analyzed using a HP-6890GC equipped with a flame ionization detector and innowax column (30m and 0.25 μm). Reaction products were condensed in a sample bubbler using ice and water as a coolant medium for identification via GCMS.

Probe chemical reactions are used to confirm the activity and stability of CNT-HZSM-5 in comparison of commercial HZSM-5. Triisopropylbenzene (TIPB) is a bulky molecule with three reactive isopropyl groups and a kinetic diameter of 8.5 Å, which is larger than the pores of MFI (5.6 Å). This limits the reactivity of TIPB to the external surface of the zeolite. Commercial zeolite which does not have any mesoporisity is to have activity only due to external sites if any present. On an equivalent acid site basis, the activity on commercial zeolite is limited to the surface activity. In contrast CNT-HZSM-5 should have stable activity due to high mesoporisity reducing the diffusion limitations. Thus a dramatic reduction in the reactivity of TIPB over H-ZSM-5 is seen compared to CNT-HZSM-5

Electron Microscopy

Scanning electron microscopy (SEM) was performed with a Zeis Neon 40 EsB scanning electron miscrocpe operating at an accelerating voltage of 2 kV or 5 kV. The accelerating voltage was chosen to minimize charging of the sample due to its non-conductive nature. Transmission electorn microscopy was performed with a JEOL 2000 FX equipped with a LaB_6 filament operating at 2000 kV.

Results and Discussion

Catalyst

VMWNTs deposited in a solution for growth of zeolites results in a layer of zeolites on the outside of the VMWNTs, Figure 46. After growth of the zeolites the

VMWNTs can be removed by heating the sample to 600°C at which point carbon nanotubes decompose[237].

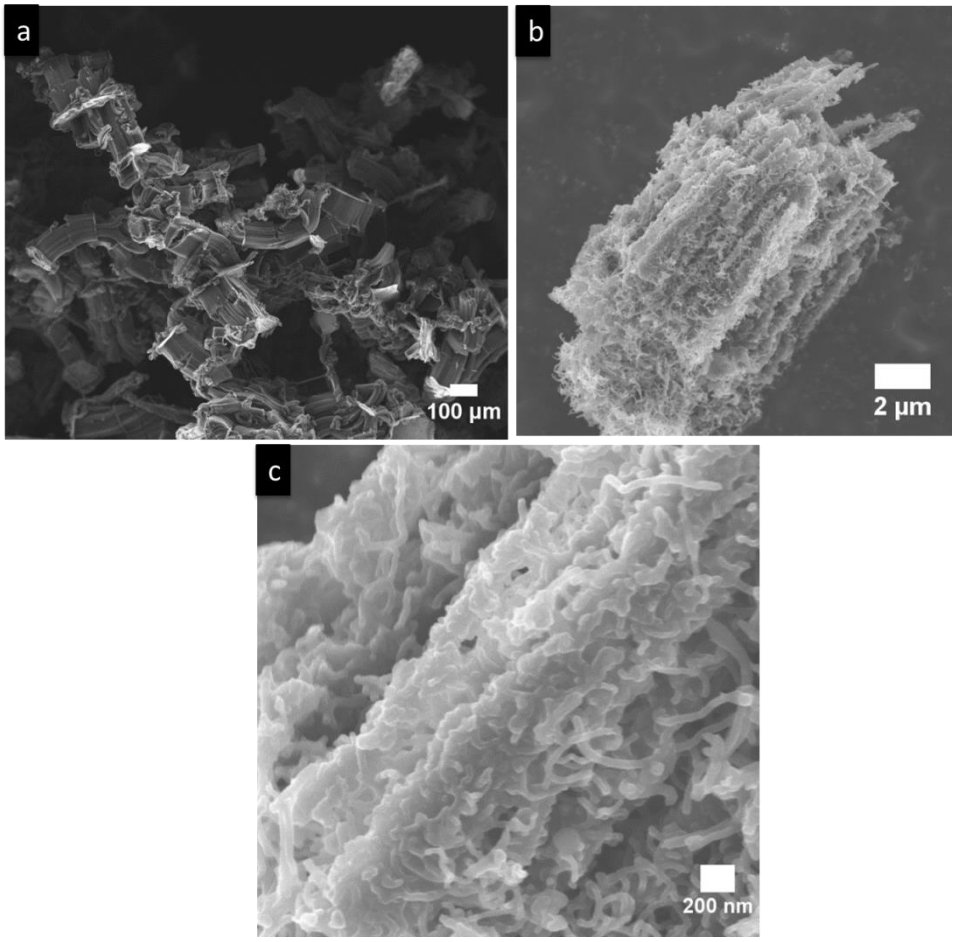

Figure 46 :- (a) VMWNTs grown between mica sheets and (b &c) after growth of zeolites on the VMWNTs.

The zeolites remain and the structure is maintained after the VMWNTs have been decomposed, Figure 47. As can be seen in the SEM images the zeolites maintain the shape of the VMWNTs and holes can be seen where possibly the ends of the carbon nanotubes protruded. This observation along with with TEM images, Figure 48 indicates after removal of the carbon nanotubes the zeolites do not collapse on themselves and retain the spacing the VMWNTs once provided. This is evident since

the diameter of the pores created after removal of the VMWNTs are comparable with the outer diameter of the VMWNTs.

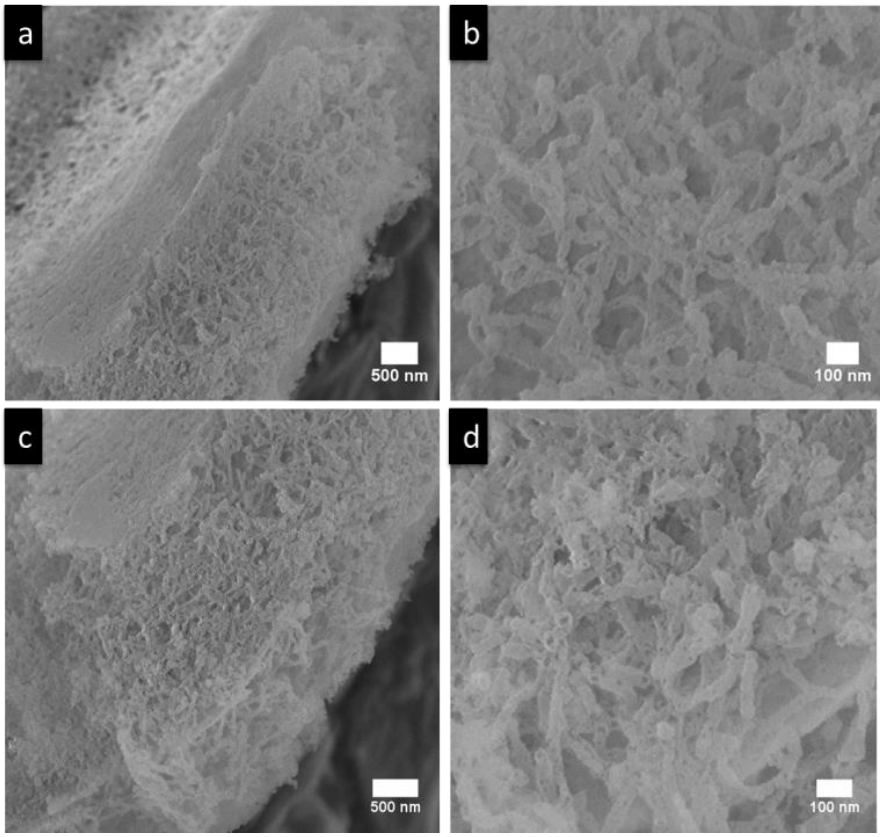

Figure 47 :- Images of zeolites after burning out the carbon nanotube template. (a) Low magnification image of the the middle of the VMWNT array (b) high magnification image of the middle of the VMWNT array, (c) low magnication image of the end of a VMWNT array, and (d) high magnification image of the end of the VMWNT array.

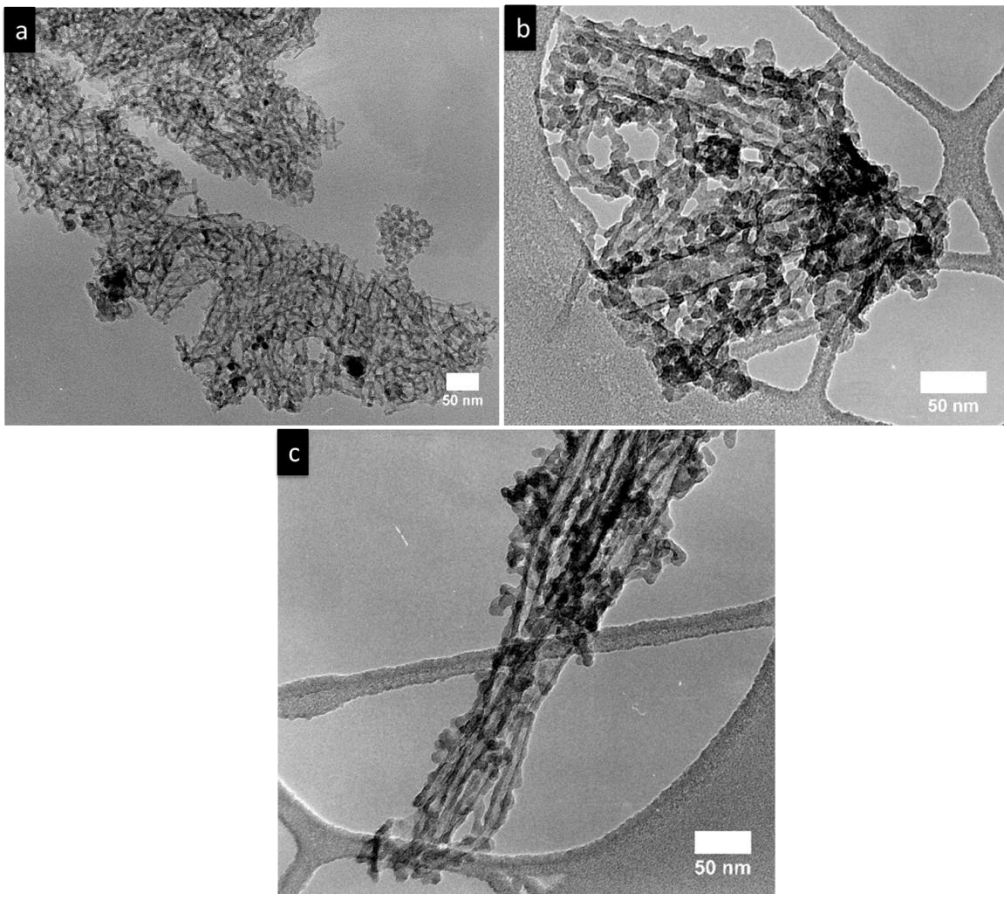

Figure 48 :- TEM images of sample Z-CNT-3 (a) low magnification showing arrays of zeolites and (b & c) high magniciation showing the channels created where the VMWNTs once resided.

From nitrogen adsorption experiments the surface area and presence of micropores and mesopores can be measured using the BET equation, Figure 49. From the nitrogen adsorption experiments the surface area was 309 m^2/g with a micropore volume of 0.0321 cm^2/g and a mesopore volume of 0.923 cm^2/g. The average pore diameter was 11.8 nm, which is an average of the mesoporous and microporous pores present, Figure 50.

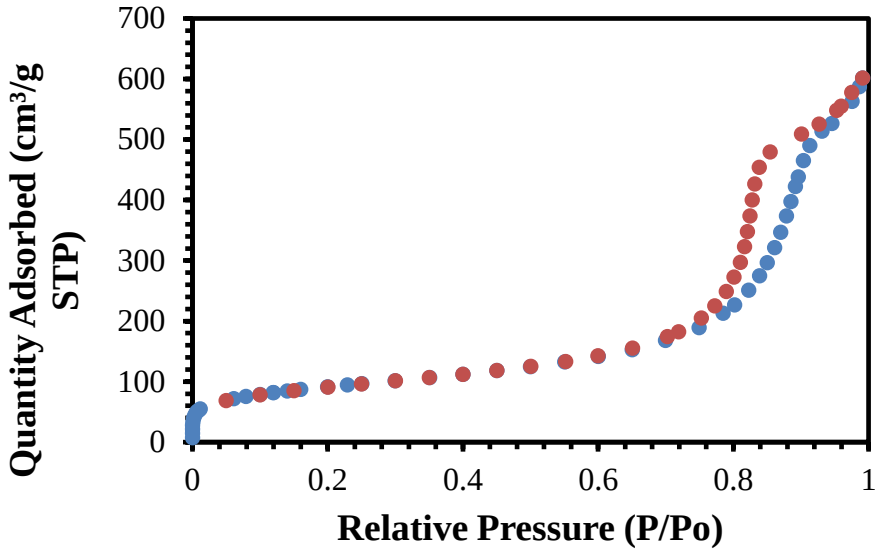

Figure 49: Nitrogen adsorption used to calculate the volume of the micropores and mesopores for sample Z-CNT-1.

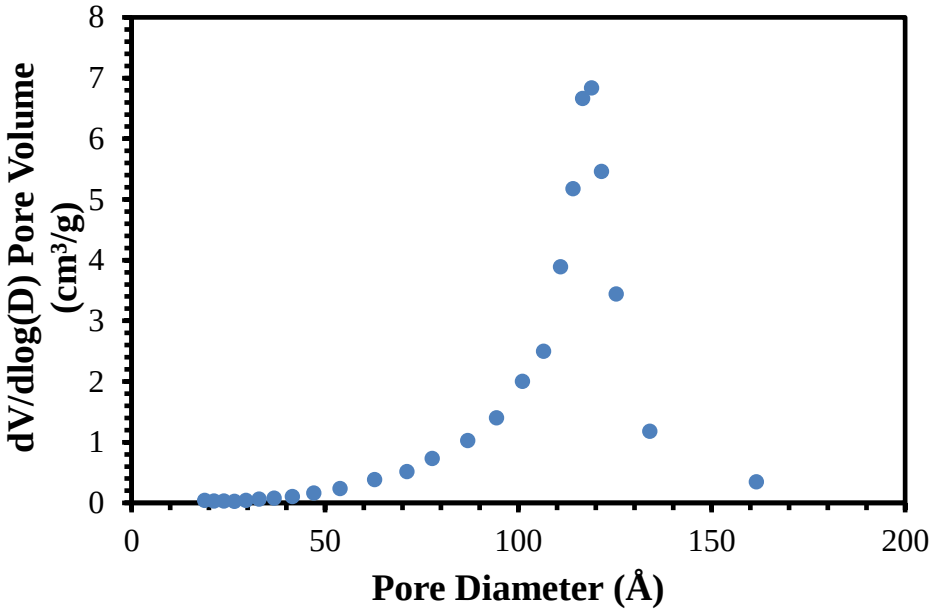

Figure 50: Average pore diameter of the Z-CNT-1 sample.

Reactions

To determine if our hierarchical zeolite changes the diffusion paths which allow for more selective cracking of bulky molecules compared to microporous zeolites triispropylbenzene (TIPB) was used as a probe molecule. Using HZSM5 with a Si/Al=40 the conversion of TIPB quickly drops off, Figure 51. In addition no cracking products are observed. This is likely due to the TIPB molecules and resulting products from the cracking becoming trapped in the micropores of the zeolite and coking up the catalyst due to poor diffusion. Using a HZSM5 with a Si/Al=11resutls in a slower deactivation. This is attributed to a few acid sites on the outside of the zeolite crystals which can crack the TIPB molecules before entering the pores. Active sites on the outside of the zeolite results in better conversion and propylene and benzene are observed, Figure 52. However, there is still not enough diffusion as the TIPB and resulting products from TIPB cracking become trapped in the zeolite. Thus, the zeolite catalyst deactivates from coking.

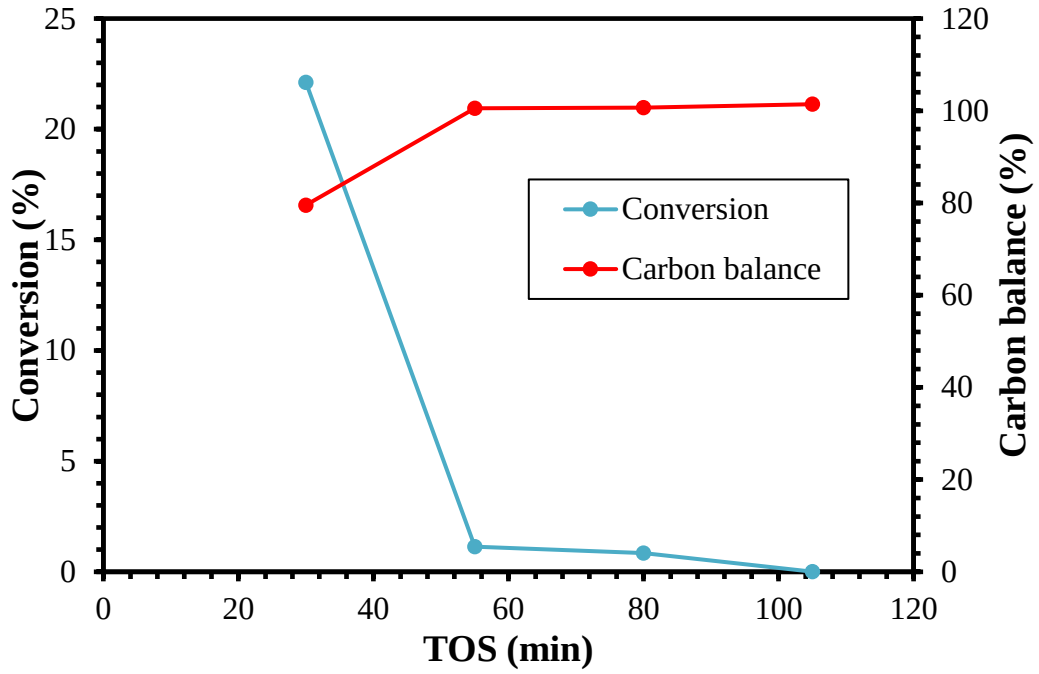

Figure 51: Conversion and carbon balance for HZSM5 with a Si/Al=40.

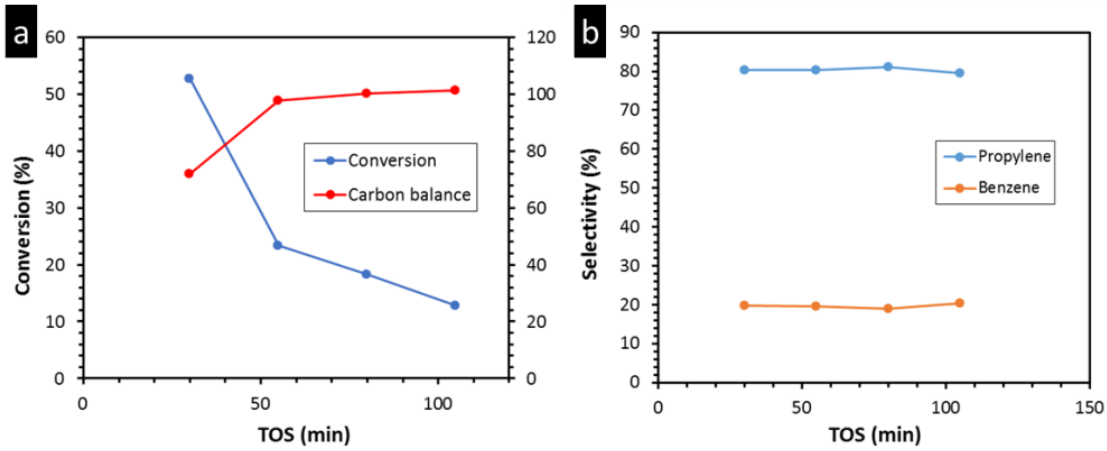

Figure 52: For HZSM5 with a Si/Al=11 the (a) conversion and carbon balance and (b) the selectivity for propylene and benzene.

The CNT-Zeolite-1 catalyst results in a stable conversion over the time tested and in a greater number of products, unlike the HZSM5 zeolites, Figure 53 (a). Benzene, cumene, diisopropylbezne, and propylene are all observed from the cracking

of TIPB, Figure 53 (b). Due to the hierarchical zeolite structure there are more diffusion pathways for the TIPB molecules and the resulting products to enter and leave the micropores of the zeolite. Molecules can enter and leave from the outside of the zeolite nanotubes or can enter and leave from the pores created by the VMWNTs. The hierarchical structure created yields greater reaction selectivity and less catalyst deactivation than HZSM5.

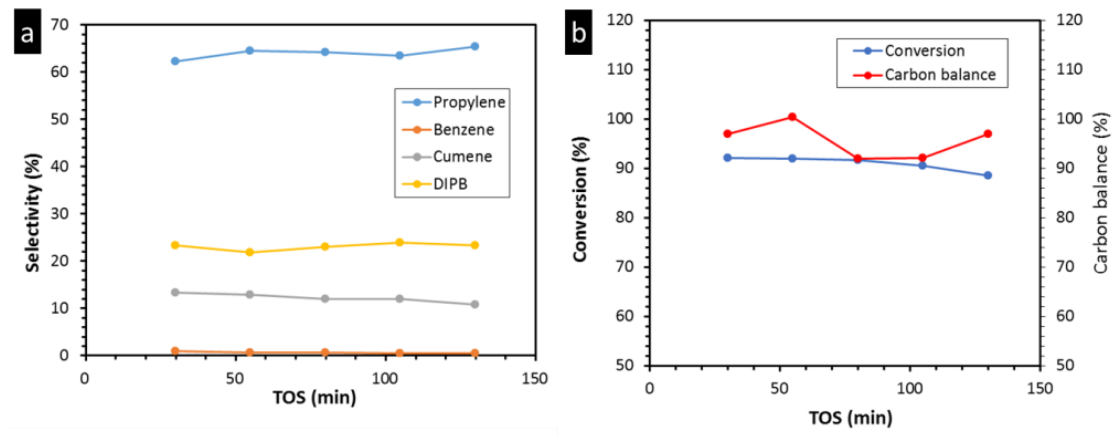

Figure 53: Reactions results for Z-CNT-1 (a) selectivity and (b) conversion and carbon balance.

Modification of the Zeolite Catalyst

By changing the amount of VMWNTs placed in the solution for zeolite growth the nucleation during the growth of the zeolites if changed, Figure 54. The higher the amount of VMWNTs in the solution the more surface area the zeolite has to nucleate over. With lower VMWNT surface area for the zeolite to nucleate over the zeolite grows outwards from the VMWNT forming a block. These differences can possibly be used to change the diffusion of molecules to the zeolites. Therefore, the reaction selectivity for the cracking of TIPB can be further tuned.

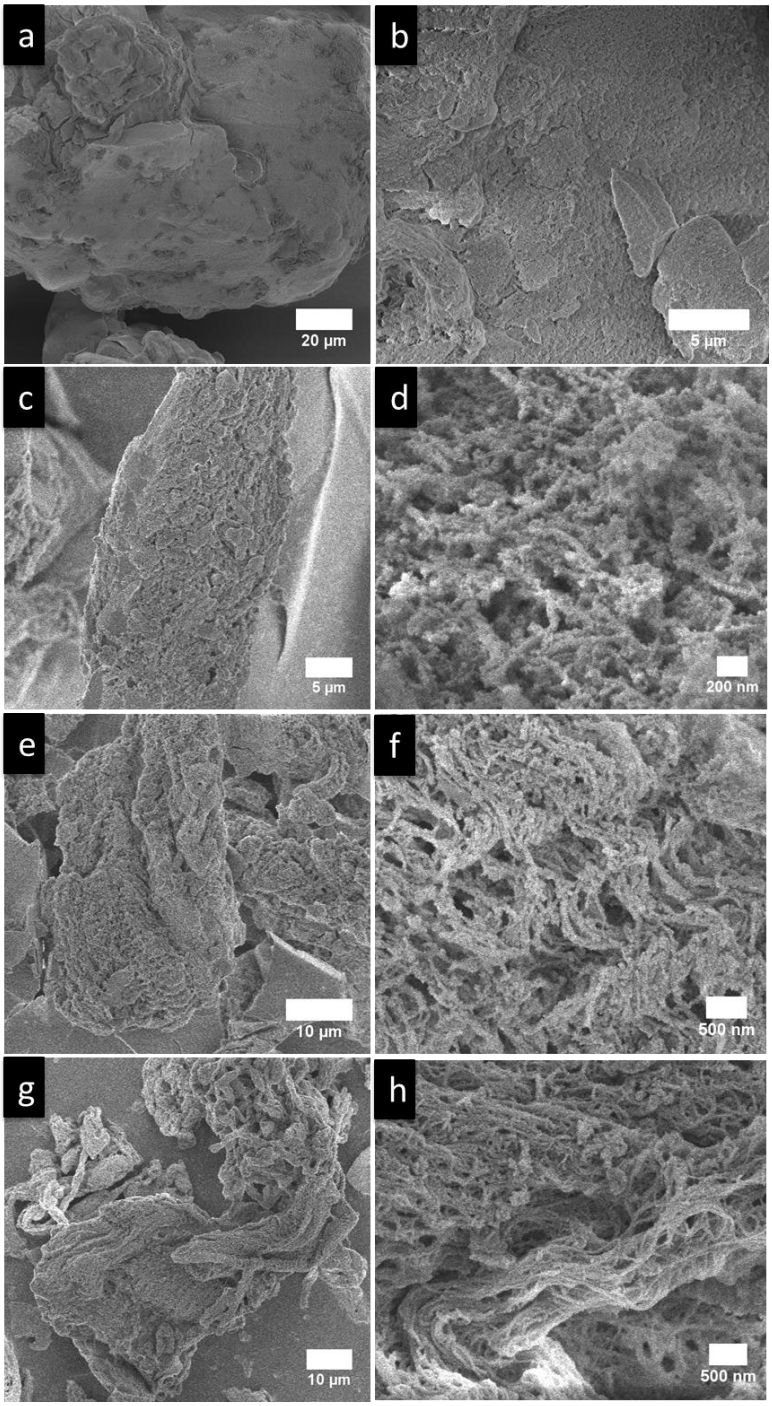

Figure 54: SEM images of samples (a & b) Z-CNT-1, (c & d) Z-CNT-2, (e & f) Z-CNT-3, (g & h) Z-CNT-4.

Conclusion

A hierarchical zeolite has been created which allows for bulky molecules such as triisopropyl benzene to diffuse in and out of the zeolite micropores because of the large pores. These large pores are formed by using VMWNTs for the zeolite crystals to grow around and then removing the VMWNTs through oxidation leaving a pore roughly the size of the VMWNT. With the large pores the hierarchical zeolites allow for molecules to diffuse in and out of the micropores, unlike the commercial zeolite with only micropores which can trap molecules and results in coking of the catalyst. The VMWNTs are grown between layers of mica sheets which allows for VMWNT growth in a fluidized bed, which allows for the manufacturing hierarchical zeolites to be scaled up. Additionally, the VMWNTs can be grown to different lengths and diameters offering further flexibility for tuning pore size which can change the molecules diffusion path. The diffusion path of the molecules can also be changed by varying the density of zeolite crystals surrounding the VMWNTs. These results in zeolite nanorods or a zeolite block with pores the size of the VMWNTs. Therefore, several routes are available to further enhance reaction selectivity by modification of the hierarchical zeolite which will be explored.

Chapter 10: The Role of Diffusion Path on the Catalytic Upgrading of Biomass Pyrolysis Vapors over ZSM-5

This manuscript was prepared together by me, Adam Stevens, Tyler Vann and Manasa Godavarthy which will be submitted for publication. Adam and Tyler are responsible for activity testing and anlysis using pyroprobe, while Manasa and myself have synthesized the zeolite series and characterized them.

Introduction

With rising concerns on the effects of CO_2 in the atmosphere from the use of fossil fuels, governments and companies worldwide have invested heavily into developing a carbon neutral process to supplement the transportation fuel industry. When biomass, more specifically lignocellulosic biomass, undergoes fast pyrolysis, the cellulose, hemicellulose, and lignin that compose the biomass begins to thermally decompose to lighter molecules. While these compounds may be highly valuable, they are also oxygenated, unstable, and react easily to polymerize and form side-products. Biomass pyrolysis yields numerous products including acetic acid, light oxygenates, furfurals, methoxyphenols, and levoglucosan/sugars; many of which are acidic/corrosive and harmful to equipment and those who may be handling the raw bio-oil. Separation of these products is nearly impossible due to the high distribution of products and an added difficulty is encountered when the pyrolysis vapors are condensed because polymerization occurs almost immediately. While there are many difficulties inherent with this process, research has been done to develop novel methods of overcoming these challenges.

Catalytic fast pyrolysis (CFP) is a rising method of taking the biomass and converting it to usable chemicals and products; more specifically gasoline and diesel range molecules. Immediately after the biomass is pyrolyzed, the vapors are passed over a solid catalyst to deoxygenate the molecules while attempting to retain the carbon. This overcomes the problems with raw liquid biofuel and creates a much more stable product that can be stored and potentially further upgraded. Some CFP reactions are done in situ[1, 238] while others are done ex situ[239-242]. In general, zeolite catalysts have been found to be very effective in the deoxygenation of biofuels and so are the major focus of this study.

The challenge of determining the optimal zeolite catalyst for this process has been taken on by many research groups. Zeolites that have been investigated include, HY, ZSM-5, H-Beta, ZSM-11, MCM-22, and SAPO-34; among others. Multiple research groups have found that the family of zeolites that converted the pyrolysis vapors best, towards aromatics, was the MFI family particularly ZSM-5.[243-245] It has been found that by using ZSM-5, dehydration, decarboxylation, decarbonylation, oligomerization, and dehydration reactions can be performed within the same zeolite to deoxygenate the highly oxygenated products produced from fast pyrolysis. The pore size of ZSM-5 is also optimal to facilitate aldol condensation toward aromatics. This is possible due to the confining effect imposed by the pore walls on the reactants.[246] To further improve ZSM-5 performance, it can be modified through the use of metals, external coatings, and changing the morphology to increase the activity of the catalyst or change the reaction mechanism.

Some of the proposed methods to increase the activity of a zeolite and/or decrease the rate of deactivation focus on affecting the diffusion path molecules have to travel to reach an active site within the pores or escape the pores. These include varying the crystallite size or introducing mesopores into the framework of the zeolite.[247-251] By decreasing the diffusion path, the zeolite is expected to show higher activity toward aromatics and less coking of the catalyst. In a previous work done by our group, it was shown that small crystal zeolites had greater stability and production of alkyl aromatics from light oxygenates due to the increased removal of products.[247] Mesoporous ZSM-5 zeolites were investigated by Wang et al. as a catalyst for upgrading of pyrolysis vapors. They found that creating mesopores post-synthesis at increasing concentrations of NaOH to get larger mesopores increased the aromatic production noticeably.[249] In this work an in-depth study was carried out focused on what role the diffusion path to the active sites inside the catalyst had on aromatic production.

Results and Discussion

Catalyst Characterization

SEM images of the crystallite series were taken. Imaging of the parent (Sample C) and mesoporous catalyst was also done using SEM and as seen in Figure 55, the parent zeolite's surface is relatively uniform and consistent with other ZSM-5 zeolites. Samples A, B, C have approximate crystal sizes of 0.5, 5, 10 μm respectively. After attacking Sample C with NaOH to create mesopores, Figure 55 shows that the surface is noticeably different. There are many large pockets and craters but the spherical form is maintained. This led us to believe that the zeolite structure was maintained and the pore

structure had not collapsed. These images are supported in the literature, showing a removal of the interior zeolite.[252] After acid washing, no noticeable change was observed to the zeolite structure.

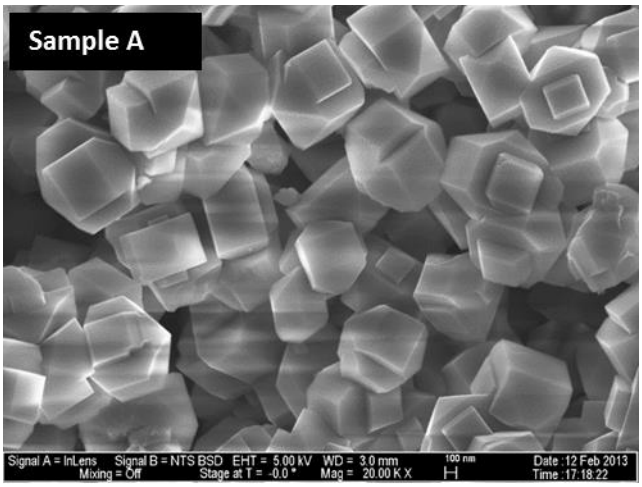

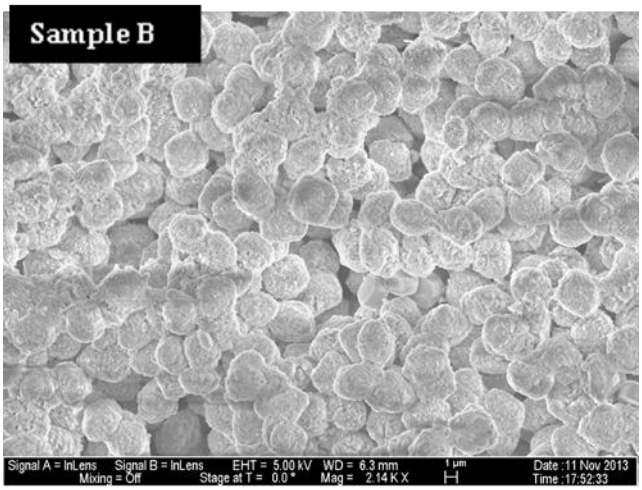

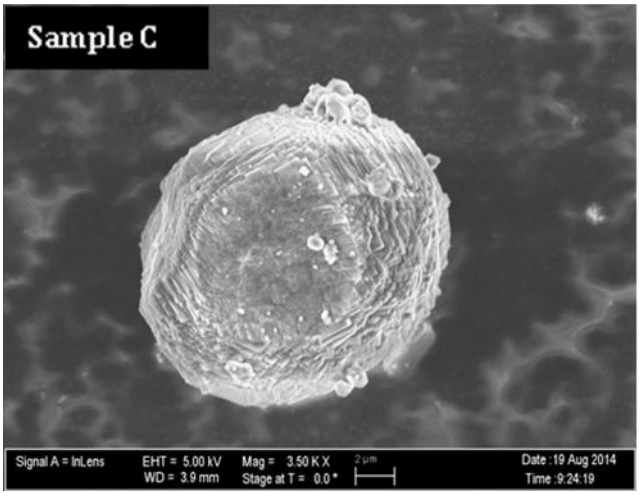

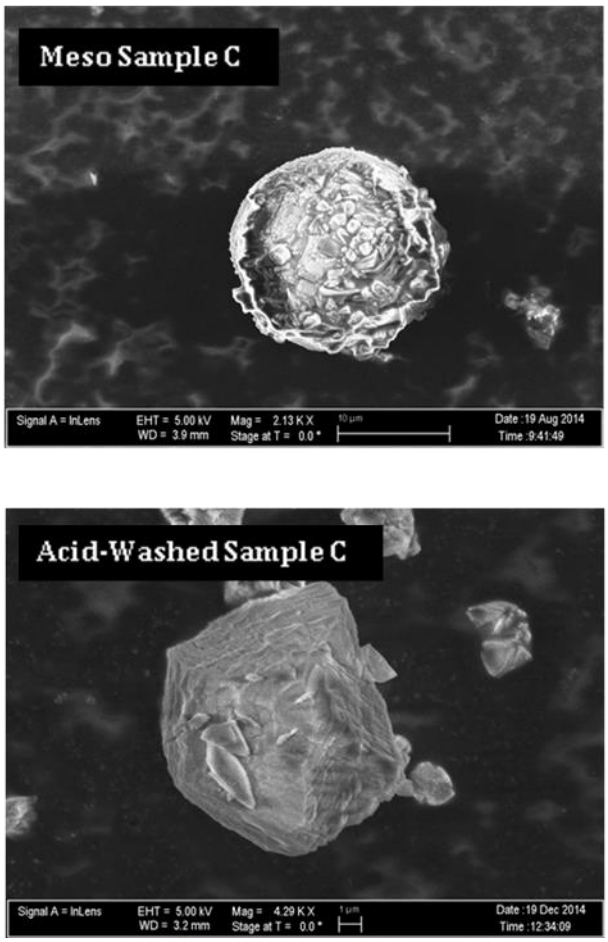

Figure 55 : SEM images of the ZSM-5 samples (A,B,C), mesoporous sample C and acid washed sample C.

Nitrogen adsorption experiments were performed on the 3 Sample C series catalysts to determine if extra-framework alumina (EFA) created by the NaOH attack blocks the pores of the zeolite and is included in Table 5. The micropore volume was found to decrease due to EFA after NaOH attack, but when an acid wash was performed removing the EFA, micropore volume returned to levels seen with the parent zeolite. The mesopore volume and external surface area increased with each step in the creation of the final catalyst. This was expected and helped confirm the creation of mesopores.

The increase in surface area also leads us to believe the zeolite crystal structure was also maintained.

	Micropore Volume cm^3/g	Micropore Area cm^2/g	Total Pore Volume cm^3/g	Mesopore Volume cm^3/g	External Surface Area m^2/g
Sample C	0.186	355	0.222	0.035	19.5
Meso Sample C	0.165	314.9	0.305	0.140	51.6
Acid-Washed Sample C	0.189	361	0.357	0.168	61.0
[a] measured via t-plot method					

Table 5 :- Nitrogen adsorption results for mesopore series

To further confirm that the crystallinity was maintained after NaOH attack, X-Ray Diffraction (XRD) was performed on the parent and mesopore catalysts. While a minor loss in crystallinity can be seen, Figure 56, it is evident that the MFI structure of the zeolite was maintained and XRD patterns agree with what is currently found in literature.[253]

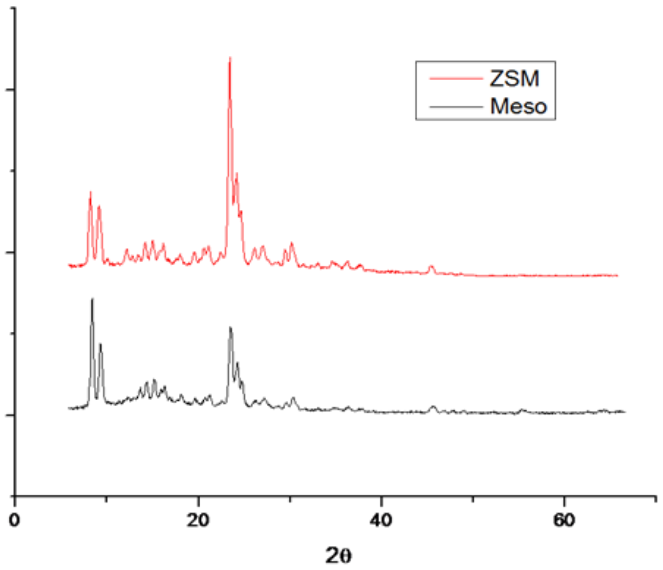

Figure 56 : XRD of parent and mesoporous zeolite

IPA-TPD was used to determine the Brønsted acid site density of each catalyst. For the Sample C mesoporous series catalyst, it was found that the density of acid sites decreased after NaOH attack but was then increased higher than the initial parent catalyst after the acid wash; see Table 6. The decrease in acid site density when linked with what was learned from the nitrogen adsorption, gives further credence to the hypothesis of pore blockage by EFA. This correlates well with literature and the activity seen in pyroprobe experiments. Also, when compared on a per acid site basis, the acid-washed mesopore zeolite was far superior

	Sample A	Sample B	Sample C	Meso Sample C	Acid-Washed Sample C
Brønsted Acidity (mmol/gm catalyst)	0.850	0.673	0.189	0.160	0.216
Si/Al Ratio	19.6	23.7	90	103	76

[a] measured by TPD of isopropylamine

Table 6 :- Measured Brønsted sites and calculated Si/Al ratio for mesopore series[a]

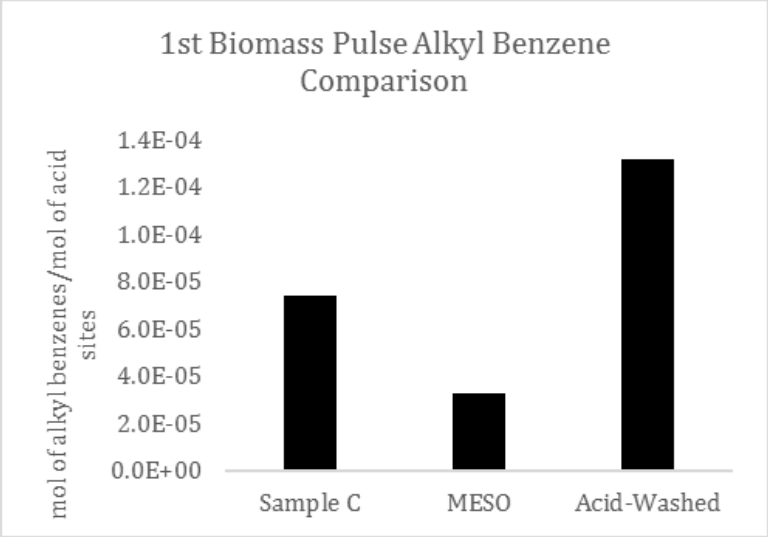

Figure 57 :- 1st biomass pulse alkyl benzenes for mesopore series on a per acid site basis

Catalyst Activity

Effect of Crystallite Size

ZSM-5 catalyst of differing crystallite sizes were synthesized to study the influence of pore diffusion on aromatic production. It was hypothesized that the internal diffusion path distance would be inversely proportional to the yield of alky benzenes products. As there is a higher ratio of internal to external sites, the molecules should not have to diffuse so far to reach the inner sites.

In pyroprobe experiments we did see improved results when using the smaller crystal size as seen in Figure 58 and Figure 59. The alkyl benzenes and naphthalenes produced from the catalyst were noticeably different and greatly improved. After a few pulses the 5μm catalyst shows significant deactivation and then appears to level off a steady conversion . For the 500nm zeolite the aromatic yield has been increased three-fold throughout the pulse experiments. The deactivation behavior for both crystallites is not uncommon for pyrolysis vapor upgrading and correlates well with literature and previous experience with low Si/Al ratio ZSM-5 zeolites.[64]

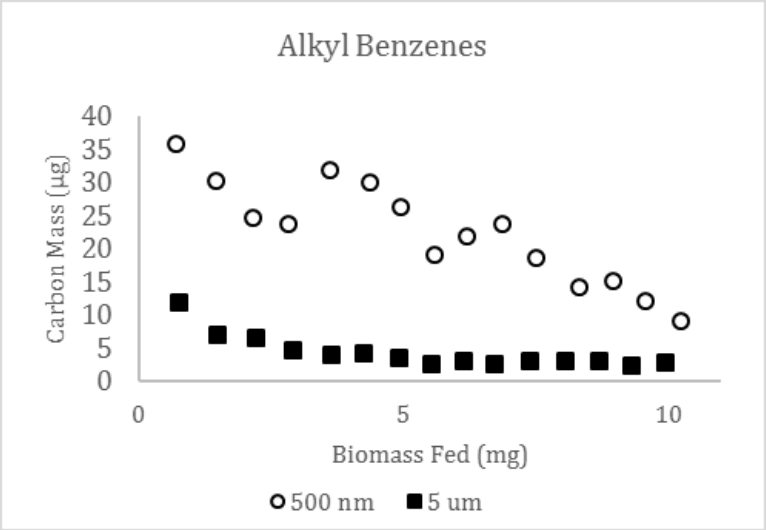

Figure 58 :- Alkyl benzenes in crystallite size series

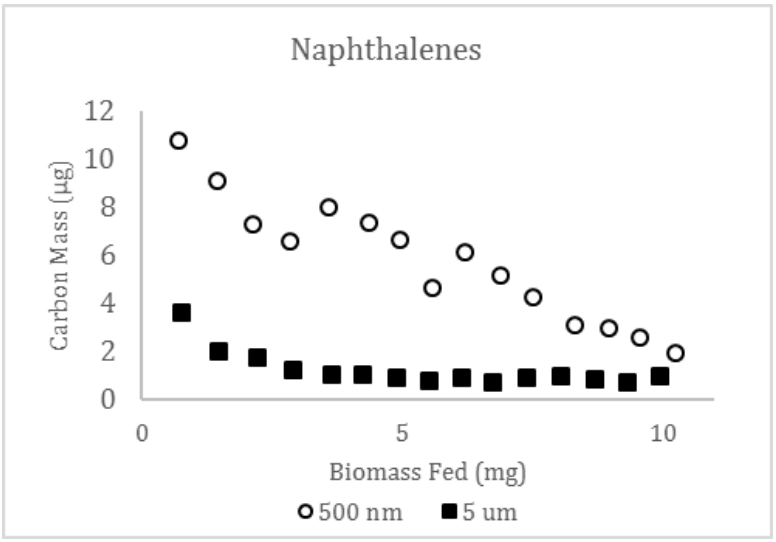

Figure 59 :- Napthalenes in crystallite size series

Role of Extra-Framework Alumina

When the parent zeolite (Sample C) was attacked using NaOH, there were visible differences in the surface of the zeolite when observed through SEM. From the images it was apparent that a mesoporous material had been formed. To determine if the zeolite crystallinity was maintained after creating the mesopores, XRD was performed on the parent (Sample C) and the NaOH attacked catalyst. While a minor loss in crystallinity was observed, the XRD results suggest that the MFI structure was maintained to a large extent.

When both zeolites were used to upgrade the pyrolysis vapors on a constant mass basis, it was seen that the activity of the mesoporous ZSM-5 was much lower when compared to the parent. We hypothesized that this was due to a plugging of the pores by EFA that was redeposited after the NaOH attack. To test this the mesoporous

zeolite was washed with hydrochloric acid to remove the EFA and then repeated the experiment in the pyrolysis system.

Effect of Acid Washing and Mesopores

Remarkably a nearly order of magnitude difference was observed in the initial creation of alkyl benzenes; see Figure 60. Other products like naphthalenes (Figure 61), indanes, and acetone also increased significantly over the mesoporous catalyst. The initial cause in the increase in activity is due to the acid washing removing the EFA and opening the pores and thus making more active sites accessible to the pyrolysis vapor reactants. In addition to the increase in accessible acid sites, the creation of mesopores also leads to a decrease in the diffusion path to the active. It would be expected that trend observed with the 500nm vs 5μm would also hold true in this case. This would explain the substantial difference in alkyl benzene yield between the parent and acid-washed mesoprous zeolite. As discussed previously the shorter diffusion path should decrease the amount of subsequent aromatic reaction to form polyaromatics and coke that remain in the zeolite pores.

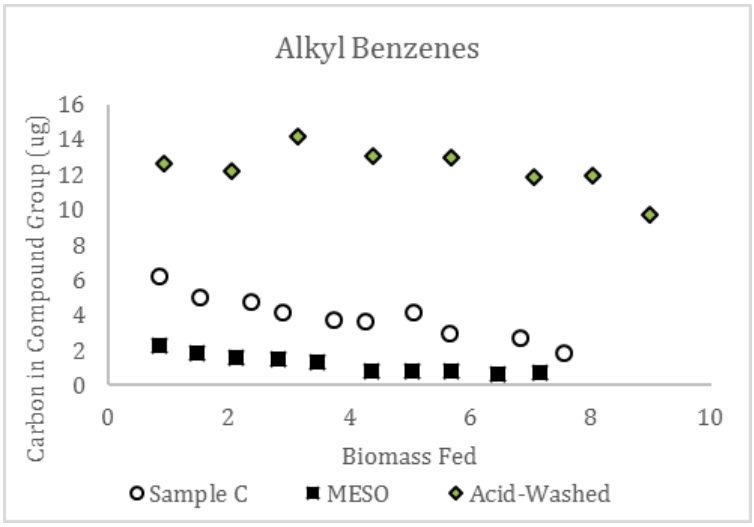

Figure 60 :- Alkyl benzenes in mesopore series

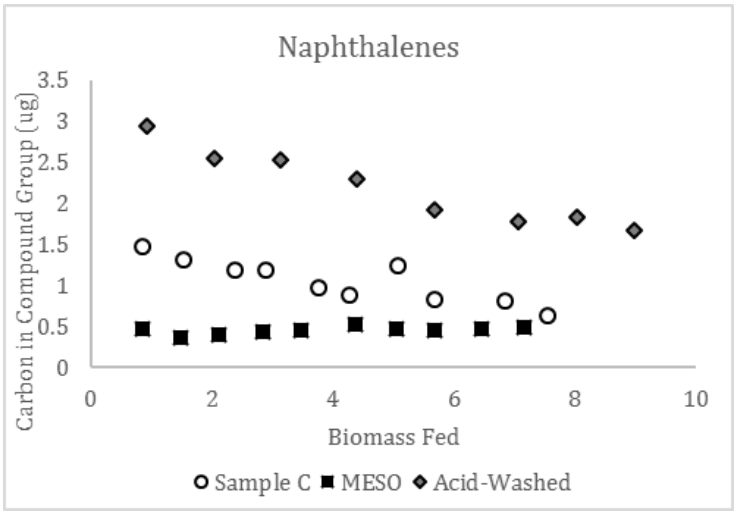

Figure 61 :- Naphthalenes in mesopore series

One trend that was noticed is that the acetone and furans, both products of catalytic upgrading, increased as biomass was fed to the acid-washed catalyst. This is due to the compounds undergoing secondary reactions to form naphthalenes, indanes, or coke. There was no increase or decrease in the light combustible gas peak.

It appears that the creation of mesopores, which reduce the diffusion path a compound travels through the zeolite, increases the production of alkyl benzenes and naphthalenes.

The conversion of furanic compounds were increased in the mesopore zeolite as were other light oxygenates. This is due to an increased accessibility to internal active sites and both furfurals and light oxygenates are compounds that can undergo aldol condensation to form alkyl benzenes and naphthalenes.

By examing specific molecules found in the pyrolysis vapors we can also examine the role of internal vs external sites on catalytic activity. Two prevalent compounds in pyrolysis vapors are acetic acid derived from hemicelluose and lignin derived syringol. It would be expected that a small compound such as acetic acid would have little difficulty diffusing into the internal pore structure of HZSM-5. Syringol on the other hand with its larger kinetic diameter has a hard time fitting inside the catalyst. Any reaction of syringol thus must be taking place on the external surface of the catalysts. In Figure 62 and Figure 63 signifcant difference can be see in the conversion of each of the species over the different catalysts. Similar to the trends seen with the alkyl benzenes production. The mesoporous Sample C appears to have the lowest activity. Interestingly, if we look at the activity normalized to the number of acid sites available for reaction, calculated from the IPA-TPD, we see almost no difference between the three samples. This further confirms that the loss in activity in mesoporous Sample C is due to blocking of the internal sites. With the syringol the change in acid site density should have minimal effect on the conversion. This molecule should be more strongly correlated to the external surface area that is available for reaction. Using BET analsysis it is known that the surface area of the mesopore series increases as NaOH attack and acid washing is carried out. From Figure 63 it can be observed that conversion does to follow the trend of the external surface area. The increased surface

area that is exposed from the NaOH attack lead to much higher conversion levels with the mesoporous samples. If we examine the intial pulses of biomass fed another interesting observation can be seen. The non acid-washed sample actually leads to a higher conversion of these large bulky molecules per external S.A.,Figure 65. We credit this to the reactions taking place on the EFA that was created from the NaOH attack. Looking at the conversion it is evident that the effect of these EFA sites is only prevalent initally and then are deactivated rapidly. In other work it has been shown that it is possible to inhibit these external sites. If the methoxyphenolic compounds remain unreacted from the zeolite upgrading they can be separated from the resultant liquid and more targeted chemistries for methoxyphenolics can be utilized.

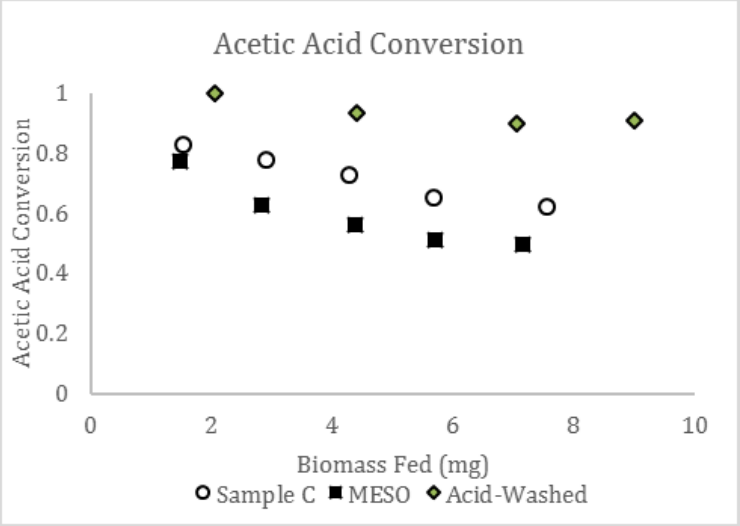

Figure 62 :- Acetic acid conversion mesopore series

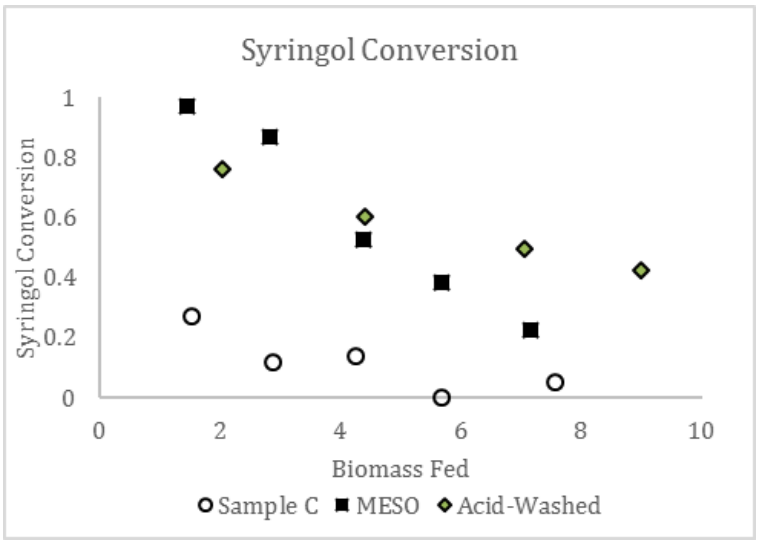

Figure 63 :- Syringol conversion mesopore series

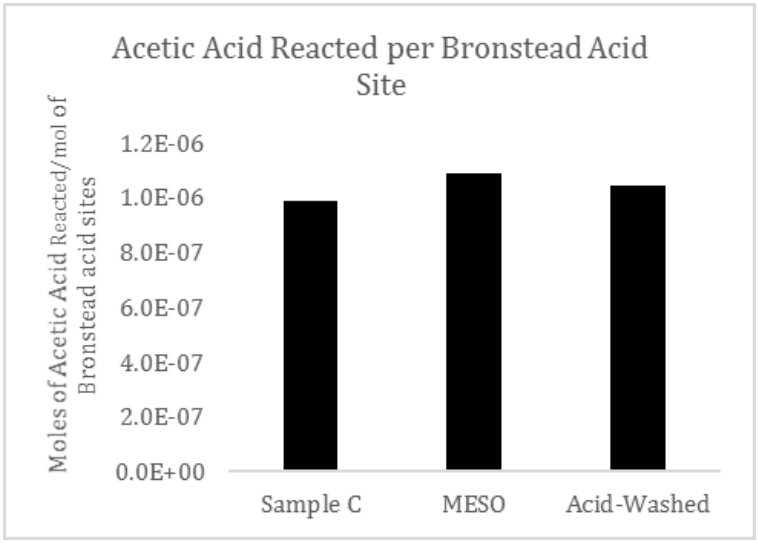

Figure 64 :- Acetic acid reacted per site basis on mesopore series

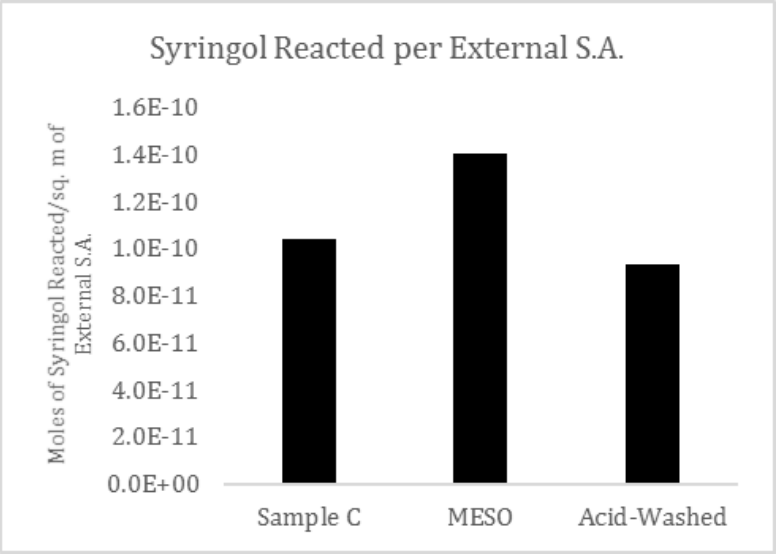

Figure 65 :- Syringol converted per site basis on mesopore series

Deactivation

The deactivation rate of the Acid-Washed Sample C zeolite showed a slower deactivation curve for the production of alkyl benzenes. This could be due to a decrease in the production of coke through conversion of naphthalenes to higher polyaromatics which get easily trapped in the cages and pores of the ZSM-5 structure. As the diffusion path is shortened, the products of alkyl benzenes and naphthalenes are more likely to escape the pores before further reacting to form polyaromatics which lead to coke.

Conclusions

Catalytic fast pyrolysis is a constantly changing and growing topic and manipulation of the catalyst can improve the products produced. By controlling the length a pyrolysis product travels through a zeolite, it is possible to increase the production of alkyl benzenes and naphthalenes. This diffusion length can be controlled through changing the size of the zeolite crystal or by creating mesopores in the zeolite

structure by NaOH attack. A subsequent acid wash is needed to remove any extra-framework alumina that has been redeposited after mesopore creation which can plug the pores of the zeolite and block access to active sites. It was determined in this study that the length of the diffusion path can be adjusted to increase the catalytic conversion of pyrolysis products, with shorter paths found to be more favorable than longer paths. A higher production of products would in turn decrease the production of coke and increase the life of the catalyst.

Experimental Section

Catalyst Synthesis

Three different ZSM-5 crystals were hydrothermally synthesized following Armaroli et al.'s procedure. The precursor gel composition was varied keeping the synthesis conditions same as reported.[i] The reagents used for the synthesis are tetraethyl orthosilicate (98%, Sigma-Aldrich), tetrapropylammonium hydroxide (40% W/W, Alfa-Aesar), aluminum isopropoxide (98%, Sigma-Aldrich), sodium hydroxide (>98%, Sigma-Aldrich) and double distilled water. Synthesized samples were washed three times with doubly distilled water and filtered by centrifugation. The obtained cake was dried overnight (12hrs) at 85 ˚C in an oven. The dried sample is ion-exchanged from sodium form to ammonia form with 2M ammonium nitrate solution at 80˚C for 3 hours. The ion-exchange procedure was repeated 5 times to ensure complete exchange. This was followed by washing with double distilled water 3 times and drying overnight (12hrs) at 85˚C. Obtained ammonium form zeolite was calcined at 600˚C (ramp rate 2 ˚C/min) for 5 hrs to get proton form of zeolite. These three H-ZSM-5 samples will be

referred as A, B and C in further discussion. Characterization results of all three synthesized samples are tabulated in Table 7.

Sample	Crystal size (SEM, μm)
A	0.4-0.5
B	5
C	10
Meso C	10
Acid-washed Meso C	10

Table 7 :- Hydrothermally synthesized samples

Mesopore Creation

It is well established that alkaline treatment of crystalline ZSM5 can create mesopores by de-silication.[254-257] In our study, 0.2M sodium hydroxide solution was used for the alkaline treatment of Sample C. The zeolite and NaOH solution was mixed in a ratio of 1:30 for the experimental procedure.[258] The solution was well stirred at a temperature of 80˚C for 5 hours. The mixture was cooled in an ice bath and was washed with double distilled water for three times. The washed sample was oven dried at 85˚C for 12 hours. The dried sample was ion-exchanged and calcined following the procedure described in the previous section. This sample is referred to as Meso Sample C further.

Acid Washing

Acid wash of the Mesoporous Sample C was done following the procedure as published in literature.[259] The Mesoporous Sample C was washed with 0.2M hydrochloric acid in a ratio of 1:10 at a temperature of 80˚C under vigorous stirring for

3 hours. The sample was then washed three times and oven dried at 85˚C for 12 hours. This sample is termed as Acid-Washed Sample C further.

Catalyst characterization

SEM- To estimate the particle diameter of all the samples scanning electron microscopy (SEM) measurements were performed by a Zeiss-NEON FEG-SEM instrument. To prepare samples for SEM, a small amount of the zeolite was dispersed in water. A drop of zeolite aqueous suspension was placed on carbon tape and dried for one hour at 75˚C before doing the experiments.

Nitrogen Adsorption- A Micrometrics ASAP 2020 Surface Area and Porosity Analyzer (Micrometrics; Norcross, GA) was used to perform nitrogen adsorption experiments to determine the total pore volume, micropore volume, and by difference the mesopore volume of the catalysts.

IPA-TPD- Isopropyl amine (IPA) temperature-programmed desorption (TPD) is a proven technique for estimating the number of Brønsted acid sites in H-form zeolites.[260, 261] IPA reacts on a Brønsted acid site of H-zeolite to produce propylene and ammonia. IPA-TPD experiments were done on all the H-Zeolite samples used in this study to investigate the amount of Brønsted acid sites. 50mg of catalyst was taken in a quartz reactor (1/4” OD) and flushed at 300˚C for two hours with helium as carrier gas (20ml/min). After flushing the sample, temperature was reduced to 100˚C and 2 μL pulses of IPA were injected into the reactor through a septum via a syringe. Mass to charge ratio (m/e) of 44 and 58 were tracked at exit of the reactor with a MKS Cirrus 200 quadrupole mass spectrometer (MS), to ensure saturation of all the acid sites in the

catalyst bed with IPA. Pulses of IPA were continued until a constant signal m/e=44 and 58 was observed. After adsorption of IPA on to the catalyst bed, it was flushed with carrier gas (20ml/min) at 100˚C for 4hrs to remove all the physically absorbed IPA. Flushing was followed by a temperature ramp from 100˚C to 600˚C at a rate of 10˚C/min. The products desorbing from the reactor with temperature ramp were tracked by MS. Quantification of the products was done by injecting standards and propylene gas pulsed using a sample loop.

XRD- For checking the crystallinity of the sample, X-ray diffraction studies using Rigaku automatic diffractor (Model D-MAX A) with a curved crystal monochromator were performed. A flat surface of the well ground samples was prepared on a plastic slide for the experiments. The instrument has Cu-Kα as a radiation source and was operated at 40kV and 35 mA between the angle range of 5-60˚.

Pyrolysis GCMS-FID

Pyroprobe Description – The instrument used for pyrolysis of biomass was the CDS analytical pyroprobe model 5250 fitted with an autosampler. Pyrolysis vapors travel through1/16 inch Silco-stainless steel transfer line tubing that is kept at 300°C. Reactor Description – A 6" long quartz reactor was placed between two heated transfer lines for ex situ catalytic upgrading of the biomass vapors. A furnace oven was used to heat the catalyst bed to the reaction temperature. 5 mg of catalyst was used for all experiments and was mixed thoroughly with 200 mg acid washed borosilicate glass beads obtained from Sigma Aldrich (G1145) to prevent channeling through the catalyst bed. The catalysts were pelletized and sieved to a similar size as the glass beads, 90-250 μm, and held in position by a pinch in the quartz tube and two plugs of 30 mg of quartz

wool. To maintain proper temperature, a thermocouple was secured to the outside of the quartz tube and placed in the middle of the catalyst bed. Quartz wool was used as insulation on top and bottom of the furnace to maintain the desired temperature.

GCMS-FID Description – To analyze the pyrolysis vapors or catalytically upgraded vapor products, a Shimadzu QP2010 GCMS-FID system was used with a RTX-1701 column 60m×0.25mm with a 0.25 μm film thickness. The oven ramp rate was programmed to hold for 4 min at 45°C then ramp at 3°C/min to 280°C and hold for 20 min. The injector temperature was set at 280°C with the injector split ratio set to 90:1. The carrier gas was helium (ultra high purity from Airgas) and the column flow rate was maintained at 1 mL/min. Products were identified using the mass fragmentation patterns and literature while yields were determined using the FID area of a peak normalized to 1 mg of biomass fed. The FID/MS split ratio was set to 10:1. A calibration was then applied to determine the μgrams of carbon/mg biomass. This was done using an effective carbon number (ECN) model that takes in to account the various effects of C-O bonds on the FID signal. Due to the large amount of compounds seen in pyrolysis vapors, traditional model compound injection calibrations were not feasible.

Pyroprobe conditions

The biomass samples used consisted of locally sourced red oak sawdust that was ground to 0.25-0.45 mm and dried in a vacuum (0.02 MPa) at 60˚C overnight. Typical red oak composition has been found to have a lignin, hemicellulose, and cellulose content of 21, 47, and 27 wt % respectively.[262] An estimated ash content of 2% was determined by calcination in a TGA unit at 800°C. 0.7-1.0mg of oak was packed in a

quartz tube with a quartz wool plug on bottom to prevent any loss of particles when the tube drops from the autosampler into the pyrolysis chamber of the pyroprobe.

The pyrolysis chamber consists of a quartz chamber wrapped in a platinum wire that is heated to 500°C while sealed in an inert environment of helium for 60 seconds. All pyrolysis experiments were done under these conditions. In a previous work, it was found that 500°C was an optimum temperature for the catalytic upgrading of pyrolysis vapors over a ZSM-5 and so all catalytic experiments were performed under the same conditions.

Acknowledgements

The work has been financially supported by the NIFA-USDA BRDI (2012-10008-20271), the National Science Foundation (EPSCoR 0814361) and the US Department of Energy (DE-FG36GO88064). The assistance of Dr. Charles Mullen, of the Agricultural Research Service of the USDA, with the GCMS analysis is gratefully acknowledged. We would also like to thank Zhenxi Liang for help with the char analysis.

References

1. Huber, G.W., S. Iborra, and A. Corma, *Synthesis of transportation fuels from biomass: chemistry, catalysts, and engineering.* Chemical reviews, 2006. **106**(9): p. 4044-4098.
2. Czernik, S. and A.V. Bridgwater, *Overview of applications of biomass fast pyrolysis oil.* Energy & Fuels, 2004. **18**(2): p. 590-598.
3. Herron, J.A., et al., *A Systems-Level Roadmap for Biomass Thermal Fractionation and Catalytic Upgrading Strategies.* Energy Technology, 2016.
4. Pestman, R., et al., *Reactions of carboxylic acids on oxides .1. Selective hydrogenation of acetic acid to acetaldehyde.* Journal of Catalysis, 1997. **168**(2): p. 255-264.
5. Pestman, R., et al., *Reactions of carboxylic acids on oxides .2. Bimolecular reaction of aliphatic acids to ketones.* Journal of Catalysis, 1997. **168**(2): p. 265-272.
6. Pham, T.N., D.C. Shi, and D.E. Resasco, *Kinetics and Mechanism of Ketonization of Acetic Acid on Ru/TiO2 Catalyst.* Topics in Catalysis, 2014. **57**(6-9): p. 706-714.
7. Pham, T.N., et al., *Ketonization of Carboxylic Acids: Mechanisms, Catalysts, and Implications for Biomass Conversion.* Acs Catalysis, 2013. **3**(11): p. 2456-2473.
8. Rasmussen, D.B., et al., *Ketene as a Reaction Intermediate in the Carbonylation of Dimethyl Ether to Methyl Acetate over Mordenite.* Angewandte Chemie International Edition, 2015.
9. Gumidyala, A., T. Sooknoi, and S. Crossley, *Selective ketonization of acetic acid over HZSM-5: The importance of acyl species and the influence of water.* Journal of Catalysis, 2016. **340**: p. 76-84.
10. Reddy, P.R., M. Subrahmanyam, and S. Kulkarni, *Vapour phase acylation of furan and pyrrole over zeolites.* Catalysis letters, 1998. **54**(1-2): p. 95-100.
11. Bui, T.V., S. Crossley, and D.E. Resasco, *C-C Coupling for Biomass-Derived Furanics Upgrading to Chemicals and Fuels.* Chemicals and Fuels from Bio-Based Building Blocks, 2016: p. 431-494.
12. Goyal, H.B., D. Seal, and R.C. Saxena, *Bio-fuels from thermochemical conversion of renewable resources: A review.* Renewable & Sustainable Energy Reviews, 2008. **12**(2): p. 504-517.
13. McKendry, P., *Energy production from biomass (part 2): conversion technologies.* Bioresource technology, 2002. **83**(1): p. 47-54.
14. Zhang, Q., et al., *Review of biomass pyrolysis oil properties and upgrading research.* Energy Conversion and Management, 2007. **48**(1): p. 87-92.
15. Mortensen, P.M., et al., *A review of catalytic upgrading of bio-oil to engine fuels.* Applied Catalysis a-General, 2011. **407**(1-2): p. 1-19.
16. Alonso, D.M., J.Q. Bond, and J.A. Dumesic, *Catalytic conversion of biomass to biofuels.* Green Chemistry, 2010. **12**(9): p. 1493-1513.
17. Demirbas, A., *Hydrocarbons from pyrolysis and hydrolysis processes of biomass.* Energy Sources, 2003. **25**(1): p. 67-75.

18. Huber, G.W. and A. Corma, *Synergies between bio- and oil refineries for the production of fuels from biomass.* Angewandte Chemie-International Edition, 2007. **46**(38): p. 7184-7201.
19. Kim, K.S. and M.A. Barteau, *Structure and Composition Requirements for Deoxygenation, Dehydration, and Ketonization Reactions of Carboxylic-Acids on Tio2(001) Single-Crystal Surfaces.* Journal of Catalysis, 1990. **125**(2): p. 353-375.
20. Martinez, R., M.C. Huff, and M.A. Barteau, *Ketonization of acetic acid on titania-functionalized silica monoliths.* Journal of Catalysis, 2004. **222**(2): p. 404-409.
21. Doornkamp, C. and V. Ponec, *The universal character of the Mars and Van Krevelen mechanism.* Journal of Molecular Catalysis a-Chemical, 2000. **162**(1-2): p. 19-32.
22. Snell, R.W. and B.H. Shanks, *Insights into the ceria-catalyzed ketonization reaction for biofuels applications.* ACS Catalysis, 2013. **3**(4): p. 783-789.
23. Resasco, D.E. and S.P. Crossley, *Implementation of concepts derived from model compound studies in the separation and conversion of bio-oil to fuel.* Catalysis Today, 2014.
24. Oasmaa, A., D.C. Elliott, and J. Korhonen, *Acidity of Biomass Fast Pyrolysis Bio-oils.* Energy & Fuels, 2010. **24**: p. 6548-6554.
25. Pham, T.N., D.C. Shi, and D.E. Resasco, *Evaluating strategies for catalytic upgrading of pyrolysis oil in liquid phase.* Applied Catalysis B-Environmental, 2014. **145**: p. 10-23.
26. Pham, T.N., et al., *Aqueous-phase ketonization of acetic acid over Ru/TiO2/carbon catalysts.* Journal of Catalysis, 2012. **295**: p. 169-178.
27. Pestman, R., et al., *The Formation of Ketones and Aldehydes from Carboxylic-Acids, Structure-Activity Relationship for 2 Competitive Reactions.* Journal of Molecular Catalysis a-Chemical, 1995. **103**(3): p. 175-180.
28. Nie, L. and D.E. Resasco, *Improving carbon retention in biomass conversion by alkylation of phenolics with small oxygenates.* Applied Catalysis a-General, 2012. **447**: p. 14-21.
29. Zapata, P.A., et al., *Condensation/Hydrogenation of Biomass-Derived Oxygenates in Water/Oil Emulsions Stabilized by Nanohybrid Catalysts.* Topics in Catalysis, 2012. **55**(1-2): p. 38-52.
30. Wan, S.L., et al., *Direct catalytic upgrading of biomass pyrolysis vapors by a dual function Ru/TiO2 catalyst.* Aiche Journal, 2013. **59**(7): p. 2275-2285.
31. Yakerson, V., L. Lafer, and A. Rubinshtein, *Catalytic preparation of ketones of the pyridine series.* Bulletin of the Academy of Sciences of the USSR, Division of chemical science, 1966. **15**(2): p. 280-285.
32. Schwartz, T.J., A.R. van Heiningen, and M.C. Wheeler, *Energy densification of levulinic acid by thermal deoxygenation.* Green Chemistry, 2010. **12**(8): p. 1353-1356.
33. Snell, R.W. and B.H. Shanks, *Ceria calcination temperature influence on acetic acid ketonization: Mechanistic insights.* Applied Catalysis A: General, 2013. **451**: p. 86-93.

34. Vervecken, M., et al., *Zeolite-induced selectivity in the conversion of the lower aliphatic carboxylic acids*, in *Chemical Reactions in Organic and Inorganic Constrained Systems*. 1986, Springer. p. 95-114.
35. Martens, J.A., et al., *Acid-Catalyzed Ketonization of Mixtures of Low-Carbon Number Carboxylic-Acids on Zeolite H-T.* Heterogeneous Catalysis and Fine Chemicals Iii, 1993. **78**: p. 527-534.
36. Chang, C.D., et al., *Synergism in Acetic-Acid Methanol Reactions over Zsm-5 Zeolites.* Abstracts of Papers of the American Chemical Society, 1983. **185**(Mar): p. 49-Fuel.
37. Bedard, J., H. Chiang, and A. Bhan, *Kinetics and mechanism of acetic acid esterification with ethanol on zeolites.* Journal of Catalysis, 2012. **290**: p. 210-219.
38. Gayubo, A.G., et al., *Transformation of oxygenate components of biomass pyrolysis oil on a HZSM-5 zeolite. H. Aldehydes, ketones, and acids.* Industrial & Engineering Chemistry Research, 2004. **43**(11): p. 2619-2626.
39. Kresnawahjuesa, O., R.J. Gorte, and D. White, *Characterization of acylating intermediates formed on H-ZSM-5.* Journal of Molecular Catalysis a-Chemical, 2004. **208**(1-2): p. 175-185.
40. Venuto, P.B., *Organic catalysis over zeolites: a perspective on reaction paths within micropores.* Microporous Materials, 1994. **2**(5): p. 297-411.
41. Tanabe, K. and W.F. Hölderich, *Industrial application of solid acid–base catalysts.* Applied Catalysis A: General, 1999. **181**(2): p. 399-434.
42. Corma, A., *Inorganic solid acids and their use in acid-catalyzed hydrocarbon reactions.* Chemical Reviews, 1995. **95**(3): p. 559-614.
43. Sartori, G. and R. Maggi, *Update 1 of: Use of Solid Catalysts in Friedel− Crafts Acylation Reactions.* Chemical reviews, 2011. **111**(5): p. PR181-PR214.
44. Bejblova, M., D. Prochazkova, and J. Čejka, *Acylation reactions over zeolites and mesoporous catalysts.* ChemSusChem, 2009. **2**(6): p. 486-499.
45. Martín-Aranda, R.M. and J. Čejka, *Recent advances in catalysis over mesoporous molecular sieves.* Topics in Catalysis, 2010. **53**(3-4): p. 141-153.
46. Corma, A., et al., *Design of synthetic zeolites as catalysts in organic reactions: acylation of anisole by acyl chlorides or carboxylic acids over acid zeolites.* Applied catalysis, 1989. **49**(1): p. 109-123.
47. Bonati, M.L., R.W. Joyner, and M. Stockenhuber, *A temperature programmed desorption study of the interaction of acetic anhydride with zeolite beta (BEA).* Catalysis today, 2003. **81**(4): p. 653-658.
48. Bonati, M., et al., *Adsorption studies of acylation reagents and products on zeolite beta catalysts.* Studies in Surface Science and Catalysis, 2004. **154**: p. 2724-2730.
49. Bonati, M.L., R.W. Joyner, and M. Stockenhuber, *On the mechanism of aromatic acylation over zeolites.* Microporous and mesoporous materials, 2007. **104**(1): p. 217-224.
50. Ren, N., et al., *A seed surface crystallization approach for rapid synthesis of submicron ZSM-5 zeolite with controllable crystal size and morphology.* Microporous and Mesoporous Materials, 2010. **131**(1): p. 103-114.

51. Garcia, L., et al., *Phenol alkylation with methanol: effect of sodium content and ammonia selective poisoning of an HY zeolite.* Catalysis letters, 1996. **37**(1-2): p. 121-123.
52. Fogler, H.S., *Elements of Chemical Reaction Enginering, 2006.* R12. **3**.
53. Ison, A. and R.J. Gorte, *The adsorption of methanol and water on H-ZSM-5.* Journal of Catalysis, 1984. **89**(1): p. 150-158.
54. Pope, C.G., *Adsorption of ethanoic acid on zeolites NaY and HY.* Journal of the Chemical Society-Faraday Transactions, 1996. **92**(19): p. 3647-3651.
55. Kukulska-Zajac, E., K. Gora-Marek, and J. Datka, *IR and TPD studies of the reaction of acetic acid in zeolites NaHY.* Microporous and Mesoporous Materials, 2006. **96**(1-3): p. 216-221.
56. Przystajko, W., R. Fiedorow, and I.G.D. Lana, *Base Properties of Zeolite Catalysts.* Zeolites, 1987. **7**(5): p. 477-480.
57. Cheung, P., et al., *Site requirements and elementary steps in dimethyl ether carbonylation catalyzed by acidic zeolites.* Journal of Catalysis, 2007. **245**(1): p. 110-123.
58. Boronat, M., C. Martínez, and A. Corma, *Mechanistic differences between methanol and dimethyl ether carbonylation in side pockets and large channels of mordenite.* Physical Chemistry Chemical Physics, 2011. **13**(7): p. 2603-2612.
59. Kresnawahjuesa, O., *Characdterization of H-[Fe]ZSM -5 and an investigation of adsorption complexes formed in acylation reactions over zeolite acids.* Thesis dissertation, University of Pennsylvania, Philadelphia, PA, 2003.
60. Chiang, H. and A. Bhan, *Catalytic consequences of hydroxyl group location on the rate and mechanism of parallel dehydration reactions of ethanol over acidic zeolites.* Journal of Catalysis, 2010. **271**(2): p. 251-261.
61. Lowry, T.H. and K.S. Richardson, *Mechanism and theory in organic chemistry.* 1981.
62. Stocker, M., *Biofuels and Biomass-To-Liquid Fuels in the Biorefinery: Catalytic Conversion of Lignocellulosic Biomass using Porous Materials.* Angewandte Chemie-International Edition, 2008. **47**(48): p. 9200-9211.
63. Bridgwater, A.V. and G.V.C. Peacocke, *Fast pyrolysis processes for biomass.* Renewable & Sustainable Energy Reviews, 2000. **4**(1): p. 1-73.
64. Wan, S., et al., *Decoupling HZSM-5 Catalyst Activity from Deactivation during Upgrading of Pyrolysis Oil Vapors.* ChemSusChem, 2015. **8**(3): p. 552-559.
65. Meng, J.J., et al., *The effect of torrefaction on the chemistry of fast-pyrolysis bio-oil.* Bioresource Technology, 2012. **111**: p. 439-446.
66. Prins, M.J., K.J. Ptasinski, and F.J.J.G. Janssen, *Torrefaction of wood - Part 2. Analysis of products.* Journal of Analytical and Applied Pyrolysis, 2006. **77**(1): p. 35-40.
67. Carlson, T.R., T.R. Vispute, and G.W. Huber, *Green gasoline by catalytic fast pyrolysis of solid biomass derived compounds.* Chemsuschem, 2008. **1**(5): p. 397-400.
68. Lange, J.P., *Lignocellulose conversion: an introduction to chemistry, process and economics.* Biofuels Bioproducts & Biorefining-Biofpr, 2007. **1**(1): p. 39-48.

69. Zhou, C.H., et al., *Catalytic conversion of lignocellulosic biomass to fine chemicals and fuels.* Chemical Society Reviews, 2011. **40**(11): p. 5588-5617.
70. Elliott, D.C. and T.R. Hart, *Catalytic hydroprocessing of chemical models for bio-oil.* Energy & Fuels, 2008. **23**(2): p. 631-637.
71. French, R.J., J. Hrdlicka, and R. Baldwin, *Mild Hydrotreating of Biomass Pyrolysis Oils to Produce a Suitable Refinery Feedstock.* Environmental Progress & Sustainable Energy, 2010. **29**(2): p. 142-150.
72. Resasco, D.E., B. Wang, and S. Crossley, *Zeolite-catalysed C–C bond forming reactions for biomass conversion to fuels and chemicals.* Catalysis Science & Technology, 2016. **6**(8): p. 2543-2559.
73. Sartori, G. and R. Maggi, *Advances in Friedel-Crafts acylation reactions: catalytic and green processes*. 2009: CRC Press.
74. Resasco, D.E. and S.P. Crossley, *Implementation of concepts derived from model compound studies in the separation and conversion of bio-oil to fuel.* Catalysis Today, 2015. **257**: p. 185-199.
75. Gallezot, P., *Conversion of biomass to selected chemical products.* Chemical Society Reviews, 2012. **41**(4): p. 1538-1558.
76. Sitthisa, S., W. An, and D.E. Resasco, *Selective conversion of furfural to methylfuran over silica-supported Ni Fe bimetallic catalysts.* Journal of Catalysis, 2011. **284**(1): p. 90-101.
77. Kresse, G. and J. Furthmuller, *Efficient iterative schemes for ab initio total-energy calculations using a plane-wave basis set.* Physical Review B, 1996. **54**(16): p. 11169-11186.
78. Perdew, J.P., K. Burke, and M. Ernzerhof, *Generalized gradient approximation made simple.* Physical Review Letters, 1996. **77**(18): p. 3865-3868.
79. Blochl, P.E., *Projector Augmented-Wave Method.* Physical Review B, 1994. **50**(24): p. 17953-17979.
80. Kresse, G. and D. Joubert, *From ultrasoft pseudopotentials to the projector augmented-wave method.* Physical Review B, 1999. **59**(3): p. 1758-1775.
81. Grimme, S., et al., *A consistent and accurate ab initio parametrization of density functional dispersion correction (DFT-D) for the 94 elements H-Pu.* Journal of Chemical Physics, 2010. **132**(15): p. 154104.
82. Grimme, S., S. Ehrlich, and L. Goerigk, *Effect of the Damping Function in Dispersion Corrected Density Functional Theory.* Journal of Computational Chemistry, 2011. **32**(7): p. 1456-1465.
83. Heyd, J., G.E. Scuseria, and M. Ernzerhof, *Hybrid functionals based on a screened Coulomb potential (vol 118, pg 8207, 2003).* Journal of Chemical Physics, 2006. **124**(21).
84. Heyd, J., G.E. Scuseria, and M. Ernzerhof, *Hybrid functionals based on a screened Coulomb potential.* Journal of Chemical Physics, 2003. **118**(18): p. 8207-8215.
85. Cohen, A.J., P. Mori-Sanchez, and W.T. Yang, *Insights into current limitations of density functional theory.* Science, 2008. **321**(5890): p. 792-794.
86. Henkelman, G., B.P. Uberuaga, and H. Jonsson, *A climbing image nudged elastic band method for finding saddle points and minimum energy paths.* Journal of Chemical Physics, 2000. **113**(22): p. 9901-9904.

87. Ghorbanpour, A., J.D. Rimer, and L.C. Grabow, *Periodic, vdW-corrected density functional theory investigation of the effect of Al siting in H-ZSM-5 on chemisorption properties and site-specific acidity.* Catalysis Communications, 2014. **52**: p. 98-102.
88. Vankoningsveld, H., *High-Temperature (350-K) Orthorhombic Framework Structure of Zeolite H-Zsm-5.* Acta Crystallographica Section B-Structural Science, 1990. **46**: p. 731-735.
89. Cheng, Y.-T. and G.W. Huber, *Chemistry of furan conversion into aromatics and olefins over HZSM-5: a model biomass conversion reaction.* ACS catalysis, 2011. **1**(6): p. 611-628.
90. Sitthisa, S. and D.E. Resasco, *Hydrodeoxygenation of Furfural Over Supported Metal Catalysts: A Comparative Study of Cu, Pd and Ni.* Catalysis Letters, 2011. **141**(6): p. 784-791.
91. Yu, W., et al., *One-step hydrogenation–esterification of furfural and acetic acid over bifunctional Pd catalysts for bio-oil upgrading.* Bioresource technology, 2011. **102**(17): p. 8241-8246.
92. Padró, C. and C. Apesteguıa, *Gas-phase synthesis of hydroxyacetophenones by acylation of phenol with acetic acid.* Journal of Catalysis, 2004. **226**(2): p. 308-320.
93. Gumidyala, A., B. Wang, and S. Crossley, *Direct carbon-carbon coupling of furanics with acetic acid over Brønsted zeolites.* Science Advances, 2016. **2**(9): p. e1601072.
94. Schimka, L., et al., *Accurate surface and adsorption energies from many-body perturbation theory.* Nature Materials, 2010. **9**(9): p. 741-744.
95. Stroppa, A. and G. Kresse, *The shortcomings of semi-local and hybrid functionals: what we can learn from surface science studies.* New Journal of Physics, 2008. **10**.
96. Duong, N., et al., *Enhancing the Acylation Activity of Acetic Acid by Forming an Intermediate Aromatic Ester.* ChemSusChem, 2017: p. n/a-n/a.
97. Moliner, M., Y. Roman-Leshkov, and M.E. Davis, *Tin-containing zeolites are highly active catalysts for the isomerization of glucose in water.* Proceedings of the National Academy of Sciences of the United States of America, 2010. **107**(14): p. 6164-6168.
98. Kabalan, I., et al., *New Generation of Zeolite Materials for Environmental Applications.* Journal of Physical Chemistry C, 2016. **120**(5): p. 2688-2697.
99. Wang, H. and T.J. Pinnavaia, *MFI zeolite with small and uniform intracrystal mesopores.* Angewandte Chemie-International Edition, 2006. **45**(45): p. 7603-7606.
100. Choi, M., et al., *Amphiphilic organosilane-directed synthesis of crystalline zeolite with tunable mesoporosity.* Nature Materials, 2006. **5**(9): p. 718-723.
101. Corma, A., et al., *High-throughput synthesis and catalytic properties of a molecular sieve with 18-and 10-member rings.* Nature, 2006. **443**(7113): p. 842-845.
102. Gounder, R. and M.E. Davis, *Beyond shape selective catalysis with zeolites: Hydrophobic void spaces in zeolites enable catalysis in liquid water.* Aiche Journal, 2013. **59**(9): p. 3349-3358.

103. Ennaert, T., et al., *Potential and challenges of zeolite chemistry in the catalytic conversion of biomass.* Chemical Society Reviews, 2016. **45**(3): p. 584-611.
104. Davies, P.R., *On the Role of Water in Heterogeneous Catalysis: A Tribute to Professor M. Wyn Roberts.* Topics in Catalysis, 2016. **59**(8-9): p. 671-677.
105. Hibbitts, D.D., et al., *Mechanistic Role of Water on the Rate and Selectivity of Fischer-Tropsch Synthesis on Ruthenium Catalysts.* Angewandte Chemie-International Edition, 2013. **52**(47): p. 12273-12278.
106. Huo, H., L.M. Peng, and C.P. Grey, *Low Temperature H-1 MAS NMR Spectroscopy Studies of Proton Motion in Zeolite HZSM-5.* Journal of Physical Chemistry C, 2009. **113**(19): p. 8211-8219.
107. Kanellopoulos, J., et al., *NMR investigation of proton mobility in zeolites.* Journal of Catalysis, 2008. **255**(1): p. 68-78.
108. Zhao, Y.X. and B.W. Wojciechowski, *The consequences of steam dilution in catalytic cracking .1. Effect of steam dilution on reaction rates and activation energy in 2-methylpentane cracking over USHY.* Journal of Catalysis, 1996. **163**(2): p. 365-373.
109. Corma, A., O. Marie, and F.J. Ortega, *Interaction of water with the surface of a zeolite catalyst during catalytic cracking: a spectroscopy and kinetic study.* Journal of Catalysis, 2004. **222**(2): p. 338-347.
110. Kletnieks, P.W., et al., *Adsorbate clustering and proton transfer in zeolites: NMR spectroscopy and theory.* Chemphyschem, 2006. **7**(1): p. 114-116.
111. White, J.L., *Methanol-to-hydrocarbon chemistry: The carbon pool (r)evolution.* Catalysis Science & Technology, 2011. **1**(9): p. 1630-1635.
112. Zhang, L., et al., *Factors that Determine Zeolite Stability in Hot Liquid Water.* Journal of the American Chemical Society, 2015. **137**(36): p. 11810-11819.
113. Yoon, J.S., et al., *Water-Assisted Selective Hydrodeoxygenation of Lignin-Derived Guaiacol to Monooxygenates.* Chemcatchem, 2015. **7**(17): p. 2669-2674.
114. Motokura, K., et al., *Allylsilylation of alkenes catalyzed by H+-exchanged montmorillonite with water.* Catalysis Today, 2014. **226**: p. 141-149.
115. Motokura, K., et al., *Water-Accelerated Allylsilylation of Alkenes Using a Proton-Exchanged Montmorillonite Catalyst.* Acs Catalysis, 2012. **2**(9): p. 1942-1946.
116. Chen, K., et al., *Trace water amounts can increase benzene H/D exchange rates in an acidic zeolite.* Journal of Catalysis, 2017. **351**: p. 130-135.
117. Santra, B., et al., *On the accuracy of van der Waals inclusive density-functional theory exchange-correlation functionals for ice at ambient and high pressures.* Journal of Chemical Physics, 2013. **139**(15).
118. Kim, K., et al., *Spatial distribution, strength, and dealumination behavior of acid sites in nanocrystalline MFI zeolites and their catalytic consequences.* Journal of Catalysis, 2012. **288**: p. 115-123.
119. Seo, Y., et al., *Characterization of the Surface Acidity of MFI Zeolite Nanosheets by P-31 NMR of Adsorbed Phosphine Oxides and Catalytic Cracking of Decalin.* Acs Catalysis, 2013. **3**(4): p. 713-720.
120. Rollmann, L.D., in *US Patent 4088605*. 1978.
121. Chang, C.D. and P.G. Rodewald, in *US Patent 5475179*. 1995.

122. Wichterlova, B. and J. Cejka, *A Comparison of the Ethylation of Ethylbenzene and Toluene on Acid, Cationic and Silylated ZSM-5 Zeolites.* Catalysis Letters, 1992. **16**(4): p. 421-429.
123. Corbin, D.R., S. Schwarz, and G.C. Sonnichsen, *Methylamines synthesis: A review*. Catalysis Today, 1997. **37**(2): p. 71-102.
124. Kwak, B.S. and J. Sung, *Skeletal isomerization of 1-butene over surface modified ferrierite catalysts.* Catalysis Letters, 1998. **53**(1-2): p. 125-129.
125. Foster, A.J., et al., *Optimizing the aromatic yield and distribution from catalytic fast pyrolysis of biomass over ZSM-5.* Applied Catalysis a-General, 2012. **423**: p. 154-161.
126. Yan, Z.M., et al., *On the acid-dealumination of USY zeolite: a solid state NMR investigation.* Journal of Molecular Catalysis a-Chemical, 2003. **194**(1-2): p. 153-167.
127. Zheng, S.R., A. Jentys, and J.A. Lercher, *On the enhanced para-selectivity of HZSM-5 modified by antimony oxide.* Journal of Catalysis, 2003. **219**(2): p. 310-319.
128. Choplin, A., *Surface Organometallic Chemistry on Zeolites - A Tool for Modifying the Sorption Properties of Zeolites.* Journal of Molecular Catalysis, 1994. **86**(1-3): p. 501-512.
129. Bouizi, Y., L. Rouleau, and V.P. Valtchev, *Bi-phase MOR/MFI-type zeolite core-shell composite.* Microporous and Mesoporous Materials, 2006. **91**(1-3): p. 70-77.
130. Niwa, M., et al., *Fine Control of the Pore-Opening Size of the Zeolite Mordenite by Chemical Vapor Deposition of Silicon Alkoxide.* Journal of the Chemical Society-Faraday Transactions I, 1984. **80**: p. 3135-3145.
131. Cheng, Y.T., et al., *Production of p-Xylene from Biomass by Catalytic Fast Pyrolysis Using ZSM-5 Catalysts with Reduced Pore Openings.* Angewandte Chemie-International Edition, 2012. **51**(44): p. 11097-11100.
132. Tominaga, K., et al., *HZSM-5 modified by silica CVD for shape-selective production of p-xylene: Influence of in situ and ex situ preparation conditions of the zeolite.* Microporous and Mesoporous Materials, 2009. **117**(3): p. 523-529.
133. Weber, R.W., et al., *The characterization and elimination of the external acidity of ZSM-5.* Microporous Materials, 1996. **7**(1): p. 15-25.
134. Zheng, S., et al., *On the enhanced selectivity of HZSM-5 modified by chemical liquid deposition.* Topics in Catalysis, 2003. **22**(1-2): p. 101-106.
135. Li, Q.H., et al., *Synthesis and characterization of colloidal zoned MFI crystals.* Microporous and Mesoporous Materials, 2005. **78**(1): p. 1-10.
136. Chaudhuri, R.G. and S. Paria, *Core/Shell Nanoparticles: Classes, Properties, Synthesis Mechanisms, Characterization, and Applications.* Chemical Reviews, 2012. **112**(4): p. 2373-2433.
137. Dabbousi, B.O., et al., *(CdSe)ZnS core-shell quantum dots: Synthesis and characterization of a size series of highly luminescent nanocrystallites.* Journal of Physical Chemistry B, 1997. **101**(46): p. 9463-9475.
138. Reiss, P., M. Protiere, and L. Li, *Core/Shell Semiconductor Nanocrystals.* Small, 2009. **5**(2): p. 154-168.

139. Zhu, Y.F., et al., *Stimuli-responsive controlled drug release from a hollow mesoporous silica sphere/polyelectrolyte multilayer core-shell structure.* Angewandte Chemie-International Edition, 2005. **44**(32): p. 5083-5087.
140. Alayoglu, S., et al., *Ru-Pt core-shell nanoparticles for preferential oxidation of carbon monoxide in hydrogen.* Nature Materials, 2008. **7**(4): p. 333-338.
141. Zhang, X. and Z.H. Su, *Polyelectrolyte-Multilayer-Supported Au@Ag Core-Shell Nanoparticles with High Catalytic Activity.* Advanced Materials, 2012. **24**(33): p. 4574-4577.
142. Bouizi, Y., L. Rouleau, and V.P. Valtchev, *Factors controlling the formation of core-shell zeolite-zeolite composites.* Chemistry of Materials, 2006. **18**(20): p. 4959-4966.
143. Ji, Y.J., et al., *Core/shell-structured Al-MWW@B-MWW zeolites for shape-selective toluene disproportionation to para-xylene.* Journal of Catalysis, 2011. **283**(2): p. 168-177.
144. Porcher, F., et al., *Epitaxial growth of zeolite X on zeolite A and twinning in zeolite A: structural and topological analysis.* Mineralogical Magazine, 2000. **64**(1): p. 1-8.
145. Okubo, T., et al., *Heteroepitaxial growth of a zeolite.* Angewandte Chemie-International Edition, 2001. **40**(6): p. 1069-+.
146. Zheng, J.J., et al., *Synthesis and catalytic performance of a bi-phase core-shell zeolite composite.* Journal of Porous Materials, 2009. **16**(6): p. 731-736.
147. Bouizi, Y., et al., *Beads comprising a hierarchical porous core and a microporous shell.* Journal of Physical Chemistry C, 2007. **111**(12): p. 4535-4542.
148. Bouizi, Y., et al., *Core-shell zeolite microcomposites.* Advanced Functional Materials, 2005. **15**(12): p. 1955-1960.
149. Pirngruber, G.D., et al., *Core-shell zeolite composite with enhanced selectivity for the separation of branched paraffin isomers.* Microporous and Mesoporous Materials, 2013. **169**: p. 212-217.
150. Lovallo, M.C., L. Boudreau, and M. Tsapatsis, *Preparation of supported zeolite films and layers: Processing of zeolite suspensions and in situ growth from homogeneous solutions*, in *Microporous and Macroporous Materials*, R.F. Lobo, et al., Editors. 1996. p. 225-236.
151. Okamoto, M. and Y. Osafune, *MFI-type zeolite with a core-shell structure with minimal defects synthesized by crystal overgrowth of aluminum-free MFI-type zeolite on aluminum-containing zeolite and its catalytic performance.* Microporous and Mesoporous Materials, 2011. **143**(2-3): p. 413-418.
152. Van Vu, D., et al., *Selective formation of para-xylene over H-ZSM-5 coated with polycrystalline silicalite crystals.* Journal of Catalysis, 2006. **243**(2): p. 389-394.
153. Van Vu, D., et al., *Catalytic activities and structures of silicalite-1/H-ZSM-5 zeolite composites.* Microporous and Mesoporous Materials, 2008. **115**(1-2): p. 106-112.
154. Vu, D.V., et al., *Morphology Control of Silicalite/HZSM-5 Composite Catalysts for the Formation of Para-Xylene.* Catalysis Letters, 2009. **127**(3-4): p. 233-238.

155. Lombard, A., et al., *Synthesis and characterization of core/shell Al-ZSM-5/silicalite-1 zeolite composites prepared in one step.* Microporous and Mesoporous Materials, 2010. **129**(1-2): p. 220-227.
156. Mores, D., et al., *Core-shell H-ZSM-5/silicalite-1 composites: Bronsted acidity and catalyst deactivation at the individual particle level.* Physical Chemistry Chemical Physics, 2011. **13**(35): p. 15985-15994.
157. Persson, A.E., et al., *Synthesis of Stable Suspensions of Discrete Colloidal Zeolite (Na, TPA)ZSM-5 Crystals.* Zeolites, 1995. **15**(7): p. 611-619.
158. Davis, T.M., et al., *Mechanistic principles of nanoparticle evolution to zeolite crystals.* Nature Materials, 2006. **5**(5): p. 400-408.
159. Lupulescu, A.I. and J.D. Rimer, *In Situ Imaging of Silicalite-1 Surface Growth Reveals the Mechanism of Crystallization.* Science, 2014. **344**(6185): p. 729-732.
160. Cundy, C.S. and P.A. Cox, *The hydrothermal synthesis of zeolites: Precursors, intermediates and reaction mechanism.* Microporous and Mesoporous Materials, 2005. **82**(1-2): p. 1-78.
161. Ren, N., et al., *Unusual Pathway of Crystallization of Zeolite ZSM-5 in a Heterogeneous System: Phenomenology and Starting Considerations.* Chemistry of Materials, 2012. **24**(10): p. 1726-1737.
162. Ren, N., et al., *Role of Subcolloidal (Nanosized) Precursor Species in the Early Stage of the Crystallization of Zeolites in Heterogeneous Systems.* Langmuir, 2014.
163. Hasan, F., et al., *Direct synthesis of hierarchical LTA zeolite via a low crystallization and growth rate technique in presence of cetyltrimethylammonium bromide.* Journal of Colloid and Interface Science, 2012. **382**: p. 1-12.
164. Maldonado, M., et al., *Controlling Crystal Polymorphism in Organic-Free Synthesis of Na-Zeolites.* Journal of the American Chemical Society, 2013. **135**(7): p. 2641-2652.
165. Itani, L., et al., *Investigation of the Physicochemical Changes Preceding Zeolite Nucleation in a Sodium-Rich Aluminosilicate Gel.* Journal of the American Chemical Society, 2009. **131**(29): p. 10127-10139.
166. Althoff, R., et al., *CONTROLLING THE SPATIAL-DISTRIBUTION OF ALUMINUM IN ZSM-5 CRYSTALS.* Microporous Materials, 1993. **1**(3): p. 207-218.
167. Ristanovic, Z., et al., *Intergrowth Structure and Aluminium Zoning of a Zeolite ZSM-5 Crystal as Resolved by Synchrotron-Based Micro X-Ray Diffraction Imaging.* Angewandte Chemie-International Edition, 2013. **52**(50): p. 13382-13386.
168. Groen, J.C., et al., *Creation of hollow zeolite architectures by controlled desilication of Al-zoned ZSM-5 crystals.* Journal of the American Chemical Society, 2005. **127**(31): p. 10792-10793.
169. Danilina, N., et al., *Where Are the Active Sites in Zeolites? Origin of Aluminum Zoning in ZSM-5.* Journal of Physical Chemistry C, 2010. **114**(14): p. 6640-6645.

170. Vonballmoos, R. and W.M. Meier, *ZONED ALUMINUM DISTRIBUTION IN SYNTHETIC ZEOLITE ZSM-5.* Nature, 1981. **289**(5800): p. 782-783.
171. Chao, K.J. and J.Y. Chern, *ALUMINUM DISTRIBUTION IN LARGE ZSM-5 CRYSTALS.* Zeolites, 1988. **8**(1): p. 82-85.
172. Jones, A.J., et al., *Acid strength and solvation in catalysis by MFI zeolites and effects of the identity, concentration and location of framework heteroatoms.* Journal of Catalysis, 2014. **312**: p. 58-68.
173. Gounder, R. and E. Iglesia, *Catalytic Consequences of Spatial Constraints and Acid Site Location for Monomolecular Alkane Activation on Zeolites.* Journal of the American Chemical Society, 2009. **131**(5): p. 1958-1971.
174. O'Connor, C.T., K.P. Moller, and H. Manstein, *The effect of silanization on the catalytic and sorption properties of zeolites.* Cattech, 2001. **5**(3): p. 172-182.
175. Odedairo, T., R.J. Balasamy, and S. Al-Khattaf, *Influence of mesoporous materials containing ZSM-5 on alkylation and cracking reactions.* Journal of Molecular Catalysis a-Chemical, 2011. **345**(1-2): p. 21-36.
176. Sun, Y.Y., et al., *Microporosity in ordered mesoporous aluminosilicates characterized by catalytic probing reactions.* Journal of Physical Chemistry B, 2003. **107**(8): p. 1853-1857.
177. Corma, A., et al., *2,6-di-tert-butyl-pyridine as a probe molecule to measure external acidity of zeolites.* Journal of Catalysis, 1998. **179**(2): p. 451-458.
178. Koo, J.-B., et al., *Direct synthesis of carbon-templating mesoporous ZSM-5 using microwave heating.* Journal of Catalysis, 2010. **276**(2): p. 327-334.
179. Hedlund, J., S. Mintova, and J. Sterte, *Controlling the preferred orientation in silicalite-1 films synthesized by seeding.* Microporous and Mesoporous Materials, 1999. **28**(1): p. 185-194.
180. Fedeyko, J.M., et al., *Spontaneous Formation of Silica Nanoparticles in Basic Solutions of Small Tetraalkylammonium Cations.* Journal of Physical Chemistry B, 2004. **108**(33): p. 12271-12275.
181. Rimer, J.D., R.F. Lobo, and D.G. Vlachos, *Physical Basis for the Formation and Stability of Silica Nanoparticles in Basic Solutions of Monovalent Cations.* Langmuir, 2005. **21**: p. 8960-8971.
182. de Moor, P., et al., *In situ investigation of Si-TPA-MFI crystallization using (ultra-) small- and wide-angle X-ray scattering.* Journal of Physical Chemistry B, 1997. **101**(51): p. 11077-11086.
183. Watson, J.N., L.E. Iton, and J.W. White, *In situ observation of the growth of silicalite nuclei by small-angle X-ray and neutron scattering.* Chemical Communications, 1996(24): p. 2767-2768.
184. Schoeman, B.J., *Analysis of the nucleation and growth of TPA-silicalite-1 at elevated temperatures with the emphasis on colloidal stability.* Microporous and Mesoporous Materials, 1998. **22**(1-3): p. 9-22.
185. Kragten, D.D., et al., *Structure of the silica phase extracted from silica/(TPA)OH solutions containing nanoparticles.* Journal of Physical Chemistry B, 2003. **107**(37): p. 10006-10016.
186. Kumar, S., et al., *A Structural Resolution Cryo-TEM Study of the Early Stages of MFI Growth.* Journal of the American Chemical Society, 2008. **130**(51): p. 17284-+.

187. Rimer, J.D., et al., *Silica self-assembly and the synthesis of microporous and mesoporous silicates.* Chemistry-a European Journal, 2006. **12**(11): p. 2926-2934.
188. Miyamoto, M., et al., *Single crystals of ZSM-5/silicalite composites.* Advanced Materials, 2005. **17**(16): p. 1985-+.
189. Czernik, S. and A. Bridgwater, *Overview of applications of biomass fast pyrolysis oil.* Energy & Fuels, 2004. **18**(2): p. 590-598.
190. Goyal, H., D. Seal, and R. Saxena, *Bio-fuels from thermochemical conversion of renewable resources: a review.* Renewable and Sustainable Energy Reviews, 2008. **12**(2): p. 504-517.
191. Kumar, A., D.D. Jones, and M.A. Hanna, *Thermochemical biomass gasification: a review of the current status of the technology.* Energies, 2009. **2**(3): p. 556-581.
192. Mortensen, P.M., et al., *A review of catalytic upgrading of bio-oil to engine fuels.* Applied Catalysis A: General, 2011. **407**(1): p. 1-19.
193. Zhang, Q., et al., *Review of biomass pyrolysis oil properties and upgrading research.* Energy conversion and management, 2007. **48**(1): p. 87-92.
194. Pestman, R., et al., *Reactions of carboxylic acids on oxides: 1. Selective hydrogenation of acetic acid to acetaldehyde.* Journal of catalysis, 1997. **168**(2): p. 255-264.
195. Pestman, R., et al., *Reactions of carboxylic acids on oxides: 2. Bimolecular reaction of aliphatic acids to ketones.* Journal of catalysis, 1997. **168**(2): p. 265-272.
196. Pham, T.N., D. Shi, and D.E. Resasco, *Evaluating strategies for catalytic upgrading of pyrolysis oil in liquid phase.* Applied Catalysis B: Environmental, 2014. **145**: p. 10-23.
197. Renz, M., *Ketonization of carboxylic acids by decarboxylation: mechanism and scope.* European journal of organic chemistry, 2005. **2005**(6): p. 979-988.
198. Gumidyala, A.S., T.; and Crossley, S. submitted, . , 2016.
199. Chang, C., et al., *Synergism in acetic acid/methanol reactions over ZSM-5 zeolites.* Prepr. Pap.-Am. Chem. Soc., Div. Fuel Chem.;(United States), 1983. **28**(CONF-830303-).
200. Pestman, R., et al., *The formation of ketones and aldehydes from carboxylic acids, structure-activity relationship for two competitive reactions.* Journal of molecular catalysis A: chemical, 1995. **103**(3): p. 175-180.
201. Rand, L., et al., *Reactions Catalyzed by Potassium Fluoride. II. The Conversion of Adipic Acid to Cyclopentanone.* The Journal of Organic Chemistry, 1962. **27**(3): p. 1034-1035.
202. Escola, J. and M. Davis, *Acylation of biphenyl with acetic anhydride and carboxylic acids over zeolite catalysts.* Applied Catalysis A: General, 2001. **214**(1): p. 111-120.
203. Sadeghbeigi, R., *Fluid catalytic cracking handbook: an expert guide to the practical operation, design, and optimization of FCC units*. 2012: Elsevier.
204. Biswas, J. and I. Maxwell, *Recent process-and catalyst-related developments in fluid catalytic cracking.* Applied Catalysis, 1990. **63**(1): p. 197-258.

205. Gobin, O.C., et al., *Comparison of the Transport of Aromatic Compounds in Small and Large MFI Particles.* Journal of Physical Chemistry C, 2009. **113**(47): p. 20435-20444.
206. Reitmeier, S.J., et al., *Influence of Postsynthetic Surface Modification on Shape Selective Transport of Aromatic Molecules in HZSM-5.* Journal of Physical Chemistry C, 2009. **113**(34): p. 15355-15363.
207. Christensen, C.H., et al., *Crystals in crystals-nanocrystals within mesoporous zeolite single crystals.* Journal of the American Chemical Society, 2005. **127**(22): p. 8098-8102.
208. Christensen, C.H., et al., *Catalytic benzene alkylation over mesoporous zeolite single crystals: Improving activity and selectivity with a new family of porous materials.* Journal of the American Chemical Society, 2003. **125**(44): p. 13370-13371.
209. Perez-Ramirez, J., et al., *Hierarchical zeolites: enhanced utilisation of microporous crystals in catalysis by advances in materials design.* Chemical Society Reviews, 2008. **37**(11): p. 2530-2542.
210. Christensen, C.H., I. Schmidt, and C.H. Christensen, *Improved performance of mesoporous zeolite single crystals in catalytic cracking and isomerization of n-hexadecane.* Catalysis Communications, 2004. **5**(9): p. 543-546.
211. Verboekend, D. and J. Perez-Ramirez, *Design of hierarchical zeolite catalysts by desilication.* Catalysis Science & Technology, 2011. **1**(6): p. 879-890.
212. Ogura, M., et al., *Formation of uniform mesopores in ZSM-5 zeolite through treatment in alkaline solution.* Chemistry Letters, 2000(8): p. 882-883.
213. Groen, J.C., et al., *Mesoporosity development in ZSM-5 zeolite upon optimized desilication conditions in alkaline medium.* Colloids and Surfaces a-Physicochemical and Engineering Aspects, 2004. **241**(1-3): p. 53-58.
214. Groen, J.C., J. Perez-Ramirez, and L.A.A. Peffer, *Formation of uniform mesopores in ZSM-5 zeolite upon alkaline post-treatment?* Chemistry Letters, 2002(1): p. 94-95.
215. Kresge, C.T., et al., *Ordered Mesoporous Molecular-Sieves Synthesized by a Liquid-Crystal Template Mechanism.* Nature, 1992. **359**(6397): p. 710-712.
216. Kresge, C.T., et al., *M41S: A new family of mesoporous molecular sieves prepared with liquid crystal templates.* Science and Technology in Catalysis 1994, 1995. **92**: p. 11-19.
217. Zhao, D.Y., et al., *Triblock copolymer syntheses of mesoporous silica with periodic 50 to 300 angstrom pores.* Science, 1998. **279**(5350): p. 548-552.
218. Zhao, D.Y., et al., *Nonionic triblock and star diblock copolymer and oligomeric surfactant syntheses of highly ordered, hydrothermally stable, mesoporous silica structures.* Journal of the American Chemical Society, 1998. **120**(24): p. 6024-6036.
219. Pham-Huu, C., et al., *BETA zeolite nanowire synthesis under non-hydrothermal conditions using carbon nanotubes as template.* Carbon, 2004. **42**(10): p. 1941-1946.
220. Schmidt, I., et al., *Carbon nanotube templated growth of mesoporous zeolite single crystals.* Chemistry of Materials, 2001. **13**(12): p. 4416-+.

221. Egeblad, K., et al., *Templating mesoporous zeolites.* Chemistry of Materials, 2007. **20**(3): p. 946-960.
222. Gu, L.J., et al., *Structured zeolites catalysts with hierarchical channel structure.* Chemical Communications, 2010. **46**(10): p. 1733-1735.
223. Tao, Y.S., et al., *Mesopore-modified zeolites: Preparation, characterization, and applications.* Chemical Reviews, 2006. **106**(3): p. 896-910.
224. Tang, K., et al., *Carbon nanotube templated growth of nano-crystalline. ZSM-5 and NaY zeolites.* Materials Letters, 2006. **60**(17-18): p. 2158-2160.
225. Ajayan, P.M., et al., *Carbon Nanotubes as Removable Templates for Metal-Oxide Nanocomposites and Nanostructures.* Nature, 1995. **375**(6532): p. 564-567.
226. Satishkumar, B.C., et al., *Oxide nanotubes prepared using carbon nanotubes as templates.* Journal of Materials Research, 1997. **12**(3): p. 604-606.
227. Zhu, K.K., et al., *Carbon as a hard template for nano material catalysts.* Journal of Natural Gas Chemistry, 2012. **21**(3): p. 215-232.
228. Min, Y.S., et al., *Ruthenium oxide nanotube arrays fabricated by atomic layer deposition using a carbon nanotube template.* Advanced Materials, 2003. **15**(12): p. 1019-+.
229. Sun, X.M., et al., *The synthesis of porous materials with macroscopically oriented mesopores interconnected by branched mesopores.* Journal of Materials Chemistry A, 2013. **1**(15): p. 4693-4698.
230. Ogihara, H., et al., *Synthesis, characterization and formation process of transition metal oxide nanotubes using carbon nanofibers as templates.* Journal of Solid State Chemistry, 2009. **182**(6): p. 1587-1592.
231. Zhang, L., Y.Q. Tan, and D.E. Resasco, *Controlling the growth of vertically oriented single-walled carbon nanotubes by varying the density of Co-Mo catalyst particles.* Chemical Physics Letters, 2006. **422**(1-3): p. 198-203.
232. Zhang, L., et al., *Influence of a top crust of entangled nanotubes on the structure of vertically aligned forests of single-walled carbon nanotubes.* Chemistry of Materials, 2006. **18**(23): p. 5624-5629.
233. Zhang, Q., et al., *Energy-absorbing hybrid composites based on alternate carbon-nanotube and inorganic layers.* Advanced Materials, 2009. **21**(28): p. 2876-2880.
234. Briggs, N.M. and S.P. Crossley, *Rapid growth of vertically aligned multi-walled carbon nanotubes on a lamellar support.* Rsc Advances, 2015. **5**(102): p. 83945-83952.
235. Song, W., et al., *Synthesis, characterization, and adsorption properties of nanocrystalline ZSM-5.* Langmuir, 2004. **20**(19): p. 8301-8306.
236. Tittensor, J.G., R.J. Gorte, and D.M. Chapman, *Isopropylamine Adsorption for the Characterization of Acid Sites in Silica-Alumina Catalysts.* Journal of Catalysis, 1992. **138**(2): p. 714-720.
237. Kitiyanan, B., et al., *Controlled production of single-wall carbon nanotubes by catalytic decomposition of CO on bimetallic Co-Mo catalysts.* Chemical Physics Letters, 2000. **317**(3-5): p. 497-503.
238. Agblevor, F.A., et al., *Fractional catalytic pyrolysis of hybrid poplar wood.* Industrial & Engineering Chemistry Research, 2010. **49**(8): p. 3533-3538.

239. Cooper, M., et al., *Catalytic upgrading of biomass pyrolysis vapors.* TCS, 2010.
240. Wan, S., et al., *Direct catalytic upgrading of biomass pyrolysis vapors by a dual function Ru/TiO2 catalyst.* AIChE Journal, 2013. **59**(7): p. 2275-2285.
241. Corma, A., S. Iborra, and A. Velty, *Chemical routes for the transformation of biomass into chemicals.* Chemical Reviews, 2007. **107**(6): p. 2411-2502.
242. Mukarakate, C., et al., *Real-time monitoring of the deactivation of HZSM-5 during upgrading of pine pyrolysis vapors.* Green Chemistry, 2014. **16**(3): p. 1444-1461.
243. French, R. and S. Czernik, *Catalytic pyrolysis of biomass for biofuels production.* Fuel Processing Technology, 2010. **91**(1): p. 25-32.
244. Carlson, T.R., et al., *Catalytic fast pyrolysis of glucose with HZSM-5: the combined homogeneous and heterogeneous reactions.* Journal of Catalysis, 2010. **270**(1): p. 110-124.
245. Jae, J., et al., *Investigation into the shape selectivity of zeolite catalysts for biomass conversion.* Journal of Catalysis, 2011. **279**(2): p. 257-268.
246. Gounder, R. and E. Iglesia, *The catalytic diversity of zeolites: confinement and solvation effects within voids of molecular dimensions.* Chemical Communications, 2013. **49**(34): p. 3491-3509.
247. Hoang, T.Q., et al., *Effects of HZSM-5 crystallite size on stability and alkyl-aromatics product distribution from conversion of propanal.* Catalysis Communications, 2010. **11**(11): p. 977-981.
248. Armaroli, T., et al., *Effects of crystal size and Si/Al ratio on the surface properties of H-ZSM-5 zeolites.* Applied Catalysis A: General, 2006. **306**: p. 78-84.
249. Li, J., et al., *Catalytic fast pyrolysis of biomass with mesoporous ZSM-5 zeolites prepared by desilication with NaOH solutions.* Applied Catalysis A: General, 2014. **470**: p. 115-122.
250. Bjørgen, M., et al., *Methanol to gasoline over zeolite H-ZSM-5: Improved catalyst performance by treatment with NaOH.* Applied Catalysis A: General, 2008. **345**(1): p. 43-50.
251. Zhu, X., et al., *Tailoring the mesopore structure of HZSM-5 to control product distribution in the conversion of propanal.* Journal of Catalysis, 2010. **271**(1): p. 88-98.
252. Dessau, R., E. Valyocsik, and N. Goeke, *Aluminum zoning in ZSM-5 as revealed by selective silica removal.* Zeolites, 1992. **12**(7): p. 776-779.
253. Wu, E., et al., *ZSM-5-type materials. Factors affecting crystal symmetry.* Journal of Physical Chemistry, 1979. **83**(21): p. 2777-2781.
254. Verboekend, D. and J. Pérez-Ramírez, *Design of hierarchical zeolite catalysts by desilication.* Catalysis Science & Technology, 2011. **1**(6): p. 879-890.
255. Groen, J.C., J.A. Moulijn, and J. Pérez-Ramírez, *Desilication: on the controlled generation of mesoporosity in MFI zeolites.* Journal of Materials Chemistry, 2006. **16**(22): p. 2121-2131.
256. Van Donk, S., et al., *Generation, characterization, and impact of mesopores in zeolite catalysts.* Catalysis Reviews, 2003. **45**(2): p. 297-319.

257. Groen, J., et al., *On the introduction of intracrystalline mesoporosity in zeolites upon desilication in alkaline medium.* Microporous and Mesoporous Materials, 2004. **69**(1): p. 29-34.
258. Ogura, M., et al., *Formation of Uniform Mesopores in ZSM-5 Zeolite through Treatment in Alkaline Solution.* Chemistry letters, 2000(8): p. 882-883.
259. Caicedo-Realpe, R. and J. Pérez-Ramírez, *Mesoporous ZSM-5 zeolites prepared by a two-step route comprising sodium aluminate and acid treatments.* Microporous and mesoporous materials, 2010. **128**(1): p. 91-100.
260. Kofke, T.G., et al., *Stoichiometric adsorption complexes in H-ZSM-5, H-ZSM-12, and H-mordenite zeolites.* Journal of Catalysis, 1989. **115**(1): p. 265-272.
261. Gorte, R., *What do we know about the acidity of solid acids?* Catalysis Letters, 1999. **62**(1): p. 1-13.
262. Gardner, D.J., et al., *Dynamic wettability of wood.* Langmuir, 1991. **7**(11): p. 2498-2502.

Appendix-A : Supporting information for chapter-2

1. X-ray diffraction results

Figure S1 (a,b) shows the typical powder diffraction spectrum for calcined zeolite with MFI framework. These XRD patterns confirms the framework and the crystallinity of the samples used in this study.

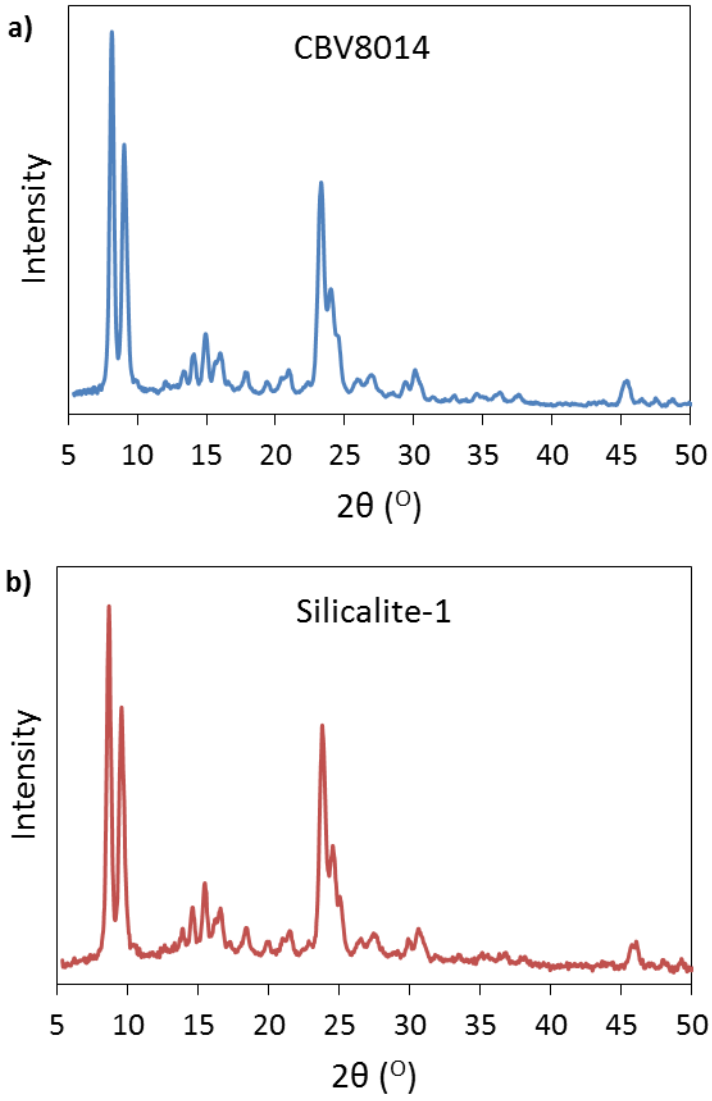

Figure S1:- XRD data for (a) CBV8014 and (b) silicalite-1 showing the samples are perfectly crystalline MFI zeolite.

2. Scanning electron microscopy.

Particle diameter of the catalyst was estimated based on the SEM images shown in Figure S2 (a,b). The reported value for the diameter of the crystal was based on measurements of 20 different crystals using ImageJ software. CBV8014 was observed to have varying crystal structure in contrast to silicalite-1 which had very uniform size.

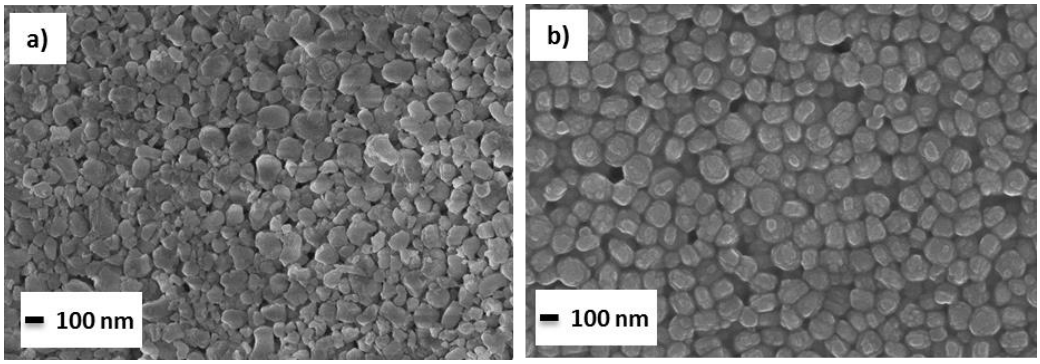

Figure S2 (a, b):- SEM images of (a) CBV 8014 (b) Silicalite-1 to estimate the crystal size of both the catalyst.

XRD patterns of the CBV8014 and silicalite-1 samples are shown in **Figure S1 (a,b)** indicating that both samples exhibit MFI crystal structure. SEM images for both samples, shown in **Figure S2 (a,b),** indicate that the silicalite-1 sample crystal size is approximately 100nm while the crystal size for the commercial catalyst CBV8014 varies across a range from 100-500nm.

3. FTIR

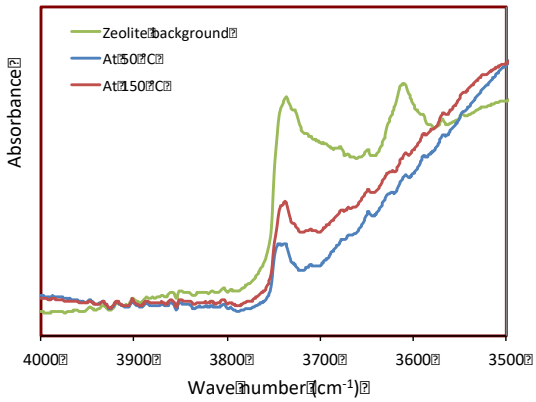

Figure S3: FTIR spectra of region corresponding to Brønsted sites of the zeolite before exposure to acetic acid, after exposure to acetic acid at 50°C, and after subsequent heating to 150°C.

4. Reaction data and TPO profile of spent catalyst

Figure S4 (a) shows the reaction data at 300°C with 0.025g of fresh catalyst and used catalyst regenerated by temperature programmed oxidation (TPO). The evolution of CO_2 as a function temperature is shown in TPO plot Figure S6 (b). 50 ml/min of 5% O_2 in Helium is used for TPO experiment.

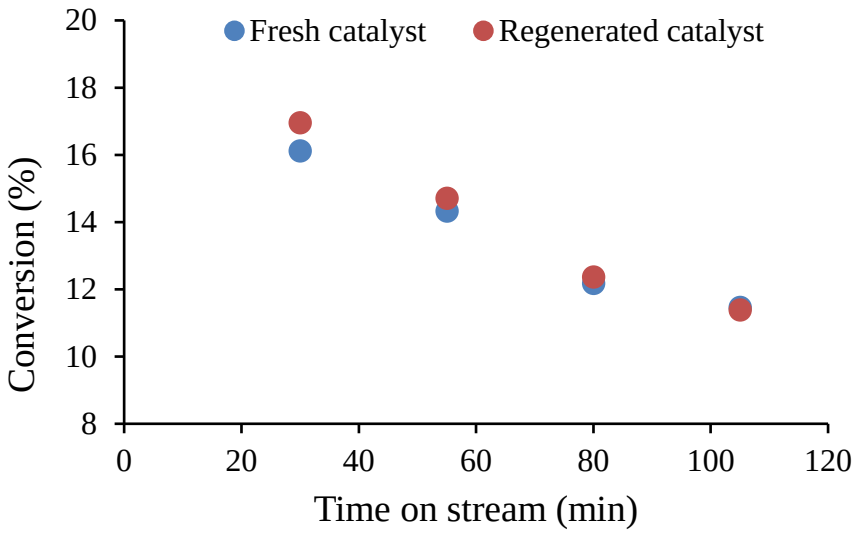

Figure S4 (a):- Acetic acid conversion as a function of time over fresh and regenerated catalyst of 0.025g at 300°C.

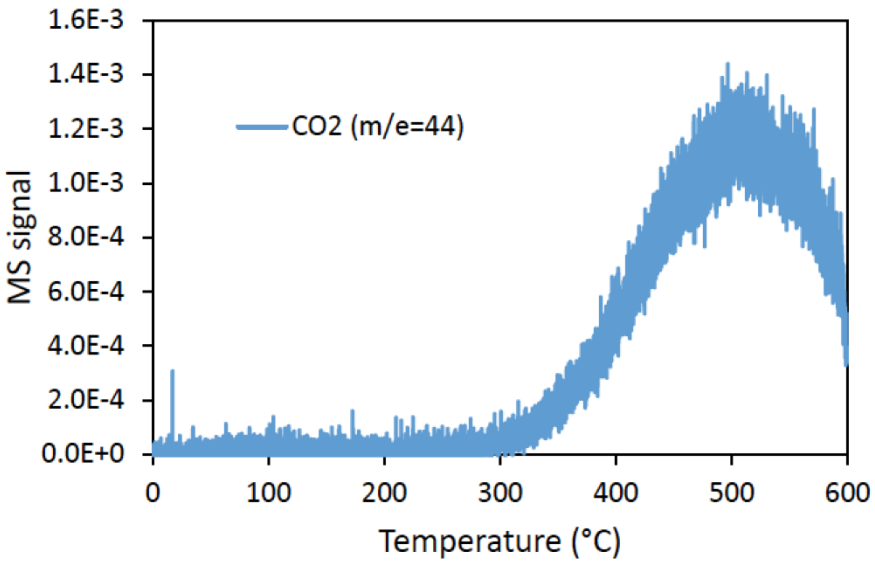

Figure S4 (b):- TPO profile of spent catalyst showing MS signal of CO_2 evolving as a function of temperature.

5. Flow reaction studies with Silicalite-1

Flow reaction of acetic acid over Silicalite-1 at 300 °C has no conversion. We observed no yields of acetone with increasing time on stream as shown in Figure S5. Traces of acetic acid at earlier time on stream was unaccounted which can be understood to be due to physisorption on the catalyst bed. This suggests the necessity of the Brønsted acid site for acetic acid ketonization reaction to proceed.

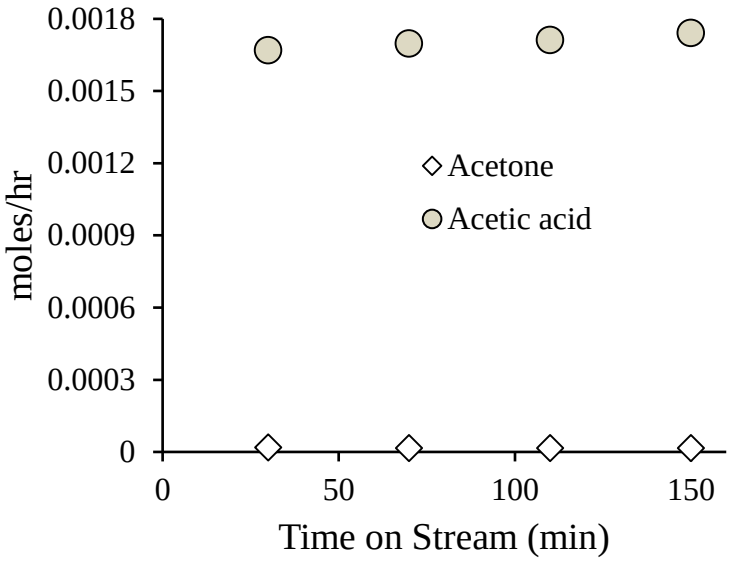

Figure S5:- Flow reaction studies of acetic acid on silicalite-1 at 300 ^{O}C showing no conversion of acetic acid

6. IPA TPD profiles

Isopropyl amine TPD is a precise technique to estimate the number of Brønsted acid sites present in the zeolite. In the Figure S6 profile (a) shows evolution of IPA, propylene and ammonia with an increase in temperature for CBV8014 commercial zeolite. Based on the number of moles of propylene desorbed per gram catalyst Brønsted acid site density is calculated. Different amount of sodium was loaded on to the parent zeolite CBV8014 as explained in section 2.3. With increase in sodium loading the number of protons exchanged with sodium increased resulting in the decrease in Brønsted acid density. This phenomenon is quantified based on IPA TPD profiles shown Figure S6 (b, c, d).

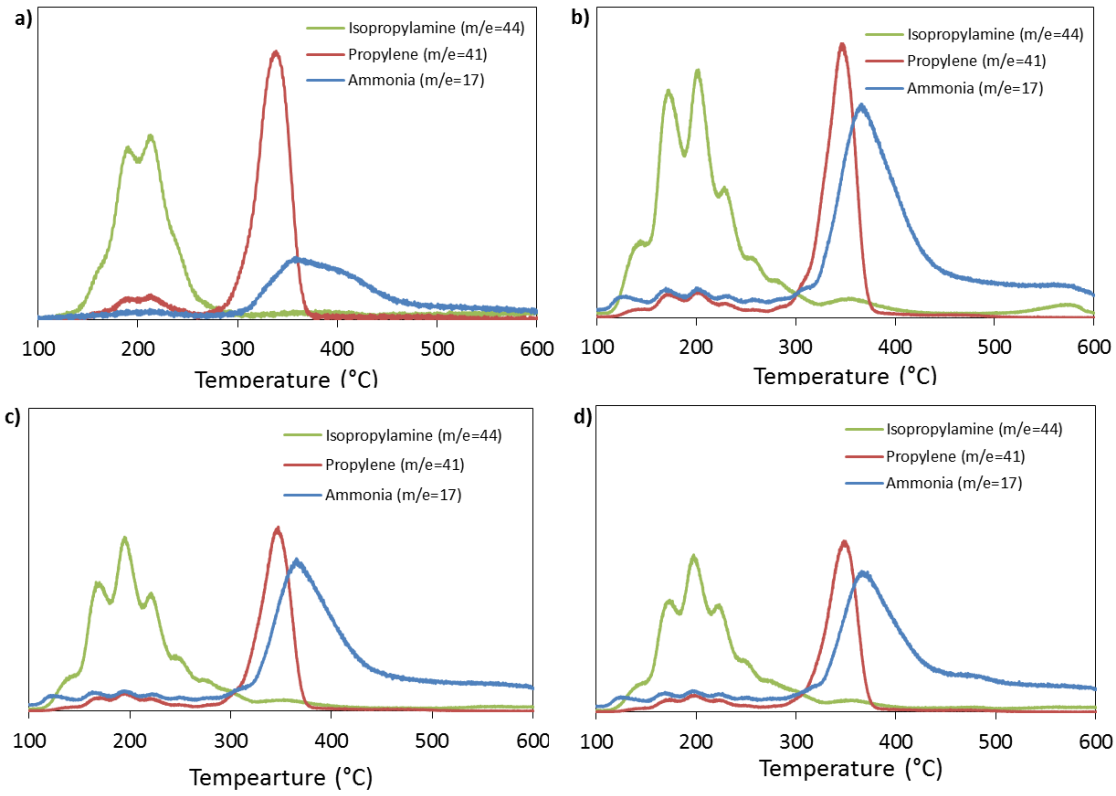

Figure S6 (a, b, c, d):- IPA TPD profiles of CBV8014 and Sample (1, 2, 3) respectively showing evolution of IPA, propylene and ammonia as a function of temperature.

The concentration of Brønsted acid sites in CBV8014 and sample-1,2,3 calculated from IPA-TPD are tabulated in **Table 1**. The theoretical Brønsted acid site density of CBV8014 is 0.406 mmoles/g based on the Si/Al ratio, which is very close to estimated sites from IPA TPD. The nearly 30% drop in Brønsted acid site concentration induced through Na poisoning provides a wide range to probe internal diffusion limitations and verify the absence of mass transfer corruptions on the kinetic results.

	Brønsted acid site density (mmol/g)	**Percent poisoned (%)**
CBV8014	0.396	0
Sample 1	0.335	17
Sample 2	0.312	23
Sample 3	0.295	27

Table S1:- Brønsted acid site density of CBV8014 and Na loaded samples (sample 1,2,3) as measured via IPA TPD.

7. Derivation of rate expression

H^+ represents acid sites, while RCO^+ represent surface bound acyl species.

Elementary steps

$$RCOOH + H^+ \xleftrightarrow{K_{Acid}} RCOOH \cdot H^+$$

$$RCOOH \cdot H^+ \xleftrightarrow{K_{equilibrium}} RCO^+ + H_2O$$

$$RCO^+ + RCOOH \xleftrightarrow{Kcom} RCOOH / RCO^+$$

$$RCOR + H^+ \xleftrightarrow{K_{Ketone}} RCOR \cdot H^+$$

$$H_2O + H^+ \xleftrightarrow{K_{H_2O}} H_2O \cdot H^+$$

$$CO_2 + H^+ \xleftrightarrow{K_{CO_2}} CO_2 \cdot H^+$$

Rate limiting step

$$RCOOH / RCO^+ \xrightarrow{k} RCOR \cdot H^+ + CO_2$$

Adsorption/Equilibrium constants

$$K_{Acid} = \frac{[RCO^+]P_{H_2O}}{P_{Acid}[H^+]} \longrightarrow [RCO^+] = \frac{K_{Acid}P_{Acid}[H^+]}{P_{H_2O}}$$

$$K_{Com} = \frac{[RCOOH / RCO^+]}{P_{Acid}[RCO^+]} = \frac{[RCOOH / RCO^+]P_{H_2O}}{P_{Acid}K_{Acid}P_{Acid}[H^+]} \longrightarrow$$

$$[RCOOH / RCO^+] = \frac{K_{Com}P_{Acid}K_{Acid}P_{Acid}[H^+]}{P_{H_2O}}$$

$$K_{Ketone} = \frac{[RCOR \cdot H^+]}{P_{Ketone}[H^+]} \longrightarrow [RCOR \cdot H^+] = K_{Ketone}P_{Ketone}[H^+]$$

$$K_{CO_2} = \frac{[CO_2 \cdot H^+]}{P_{CO_2}[H^+]} \longrightarrow [CO_2 \cdot H^+] = K_{CO_2}P_{CO_2}[H^+]$$

$$K_{H_2O} = \frac{[H_2O \cdot H^+]}{P_{H_2O}[H^+]} \longrightarrow [H_2O \cdot H^+] = K_{H_2O}P_{H_2O}[H^+]$$

Site balance

$$C_t = [H^+] + [RCO^+] + [RCOOH / RCO^+] + [RCOR \cdot H^+] + [H_2O \cdot H^+] + [CO_2 \cdot H^+]$$

$$C_t = [H^+] + \frac{K_{Acid}P_{Acid}[H^+]}{P_{H_2O}} + \frac{K_{Com}P_{Acid}K_{Acid}P_{Acid}[H^+]}{P_{H_2O}} + K_{Ketone}P_{Ketone}[H^+] + K_{H_2O}P_{H_2O}[H^+] + K_{CO_2}P_{CO_2}[H^+]$$

$$C_t = [H^+]\left(1 + \frac{K_{Acid}P_{Acid}}{P_{H_2O}} + \frac{K_{Com}P_{Acid}K_{Acid}P_{Acid}}{P_{H_2O}} + K_{Ketone}P_{Ketone} + K_{H_2O}P_{H_2O} + K_{CO_2}P_{CO_2}\right)$$

Rate equation

$$rate = k'\,[RCOOH / RCO^+] = \frac{kK_{Acid}K_{Com}P_{acid}^2[H^+]}{P_{H_2O}}$$

$$rate = \frac{\frac{kK_{Com}K_{equilibrium}K_{Acid}P_{Acid}^{\ 2}}{P_{H_2O}}}{\left(1 + K_{Acid}P_{Acid} + \frac{K_{equilibrium}K_{Acid}P_{Acid}}{P_{H_2O}} + \frac{K_{Com}K_{equilibrium}K_{Acid}P_{Acid}^{\ 2}}{P_{H_2O}} + K_{Ketone}P_{Ketone} + K_{H_2O}P_{H_2O} + K_{CO_2}P_{CO_2}\right)}$$

$$rate = \frac{kK_{Com}K_{equilibrium}K_{Acid}P_{Acid}^2}{P_{H_2O}\left(1 + K_{Acid}P_{Acid} + \frac{K_{equilibrium}K_{Acid}P_{Acid}}{P_{H_2O}} + \frac{K_{Com}K_{equilibrium}K_{Acid}P_{Acid}^2}{P_{H_2O}} + K_{Ketone}P_{Ketone} + K_{H_2O}P_{H_2O} + K_{CO_2}P_{CO_2}\right)}$$

At very high partial pressures of water, where water occupies most sites, the rate simplifies to negative 2nd order with respect to water and positive 2nd order with respect to acetic acid.

$$rate = \frac{kK_{Com}K_{equilibrium}K_{Acid}P_{Acid}^2}{\left(K_{H_2O}P_{H_2O}^2\right)}$$

At very low conversions, with very low surface coverage of all species (acid, acyl, and water), the rate equation reduces to: (2nd order wrt acid, -1 order wrt water)

$$rate = \frac{kK_{Com}K_{equilibrium}K_{Acid}P_{Acid}^2}{P_{H_2O}}$$

Under conditions where all sites are occupied by acid derived species (acid, acyl and complex) plus vacant sites, the rate equation simplifies to:

$$rate = \frac{kK_{Com}K_{equilibrium}K_{Acid}P_{Acid}^2}{\left(P_{H_2O} + K_{Acid}P_{Acid}P_{H_2O} + K_{equilibrium}K_{Acid}P_{Acid} + K_{Com}K_{equilibrium}K_{Acid}P_{Acid}^2\right)}$$

These conditions yield a fractional negative order with respect to water (0 to -1), with an order closer to -1 as the number of vacant sites or adsorbed acid increases. Order from 2nd to 0th of acid depending on relative number of vacant sites and percentage of sites occupied by acid, acyl or complex

If the most abundant surface intermediates (MASI) are surface acyl groups, the order with respect to water ranges from 0 to -1, and the order with respect to acid ranges from 1 to 2. This can shift depending on fraction of vacant sites.

$$rate = \frac{kK_{Com}K_{equilibrium}K_{Acid}P_{Acid}^2}{\left(P_{H_2O} + K_{equilibrium}K_{Acid}P_{Acid}\right)}$$

If MASI are species other than acyl groups, e.g. adsorbed carboxylic acid, the equation ranges from -1 order with respect to water if acetic acid dominates the surface to -2nd order with respect to water as water begins to occupy more sites. This, when compared with the -0.46 order with respect to water observed experimentally, indicates that surface acyl groups and acyl/acetic acid complex species occupy a significant portion of the surface.

$$rate = \frac{kK_{Com}K_{equilibrium}K_{Acid}P_{Acid}^2}{P_{H_2O}\left(1 + K_{Acid}P_{Acid} + K_{H_2O}P_{H_2O}\right)}$$

The catalyst is not completely covered by surface acyl species, as in this case, the reaction order with respect to acid would drop significantly, behaving as 1st order with respect to acetic acid as with all sites occupied by acyl groups (with a driving force to form the acyl/acid complex).

$$rate = \frac{kK_{Com}K_{equilibrium}K_{Acid}P_{Acid}^2}{\left(P_{H_2O} + K_{equilibrium}K_{Acid}P_{Acid}\right)}$$

Similarly, if the acyl/acetic acid complex occupied all sites, the reaction would behave as 0th order with respect to acetic acid.

$$rate = \frac{kK_{Com}K_{equilibrium}K_{Acid}P_{Acid}^2}{\left(P_{H_2O} + K_{Com}K_{equilibrium}K_{Acid}P_{Acid}^2\right)}$$

An order of 1.6 with respect to acetic acid indicates that sites are not all occupied by acyl groups or an acyl/acid complex, but clearly a significant fraction of the sites are occupied by these species in order to justify an order with respect to water that is between 0 and -1.

8. Initial rates and orders

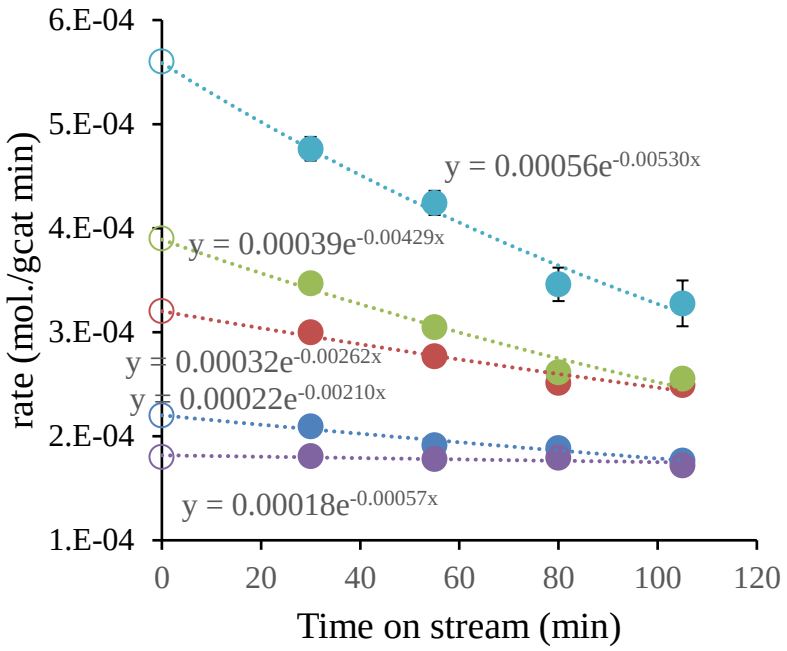

Figure S8a: Exponential decay of reaction rates as a function of water partial pressure at a constant acetic acid partial pressrue. Projected initial rates are highlighted by hollow points while solid points indicate experimental data. Acetic acid was maintained at 10.8 Torr. The concentration of water was varied from 0 Torr (dark blue), 2.7 Torr (gray), 5.4 Torr (orange), 10.8 Torr (light blue), and 14.6 Torr (yellow).

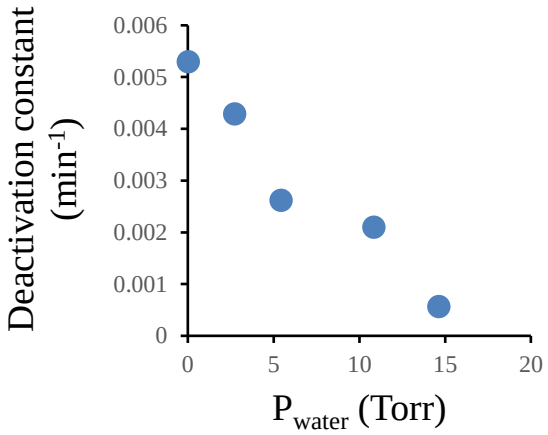

Figure S8b: Exponential constants shown in Figure S8a expressed as a deactivation constant as a function of water partial pressure.

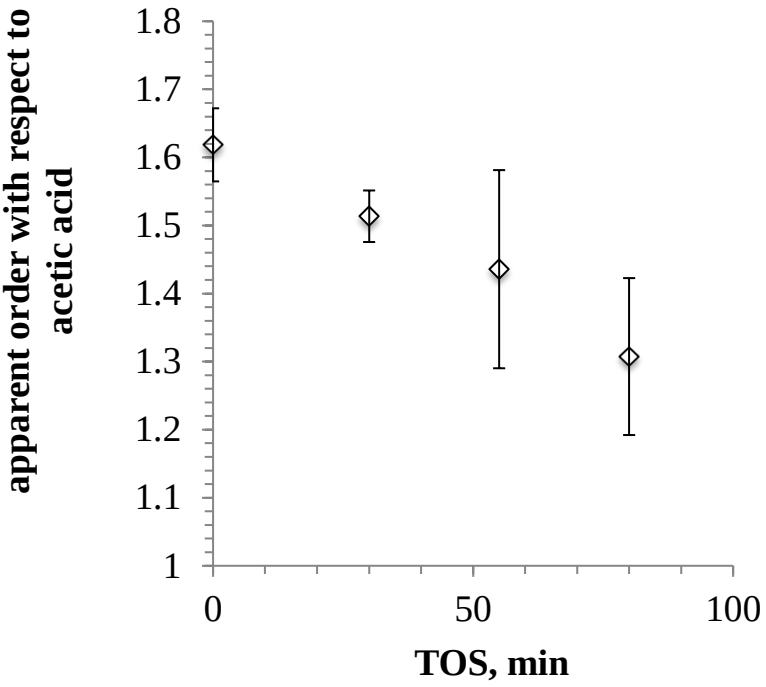

Figure S8c: Order of reaction rate with respect to increasing initial acetic acid concentration as measured at varying TOS values. Orders were measured over CBV8014 at 300°C, 0.025 g catalyst, with initial rates extrapolated to 0 min TOS using exponential decay curves identical to those outlined for varying water partial pressure in Figure S8a. Eror bars represent ±1 standard error value of the reaction order coefficient.

Appendix-B :- Supporting information for chapter-3

1.1. Catalyst preparation

The catalyst used in this study CBV8014 (Si/Al=40), which is an MFI zeolite was purchased from Zeolyst international in ammonium form. The catalyst was calcined in dry air at 600 °C for 5hours using a ramp rate of 2 °C/min to obtain proton form. In all the experiments, the catalyst particle size distribution was maintained to be 90-250 μm, which was obtained by pelletizing and sieving.

1.2. Isopropyl amine Temperature-Programmed Desorption (IPA-TPD):

IPA-TPD experiment was done on H-form of zeolite to estimate the Brønsted acid site density. The experimental setup consists of an oven for temperature control, a quarter inch quartz reactor to hold the catalyst bed and an MKS Cirrus 200 quadrupole mass spectrometer (MS) connected at the end of reactor to analyze products. IPA was adsorbed on to the 50mg of catalyst bed after removing moisture by pre-treatment at 300 °C in helium flow (20 ml/min) for one hour. 2 μL pulses of IPA was injected on to catalyst bed using a syringe through a septum at 100 °C. IPA pulses were continued until we observed a constant mass to charge ratio (m/e) of 44 and 58 in MS to ensure complete saturation of bed. Physically adsorbed IPA was removed by flushing catalyst bed for one hour with helium after which the temperature was ramped from 100 °C to 600 °C at a rate of 10 °C/min. Propylene, ammonia and IPA were tracked by MS and propylene was quantified by injecting standards through gas sample loop. Figure S1 shows the MS signal intensity of desorbing products as a function temperature. Brønsted acid density of CBV8014 and CP814C are accounted to 0.394 mmoles/g and 0.744 mmoles/g respectively.

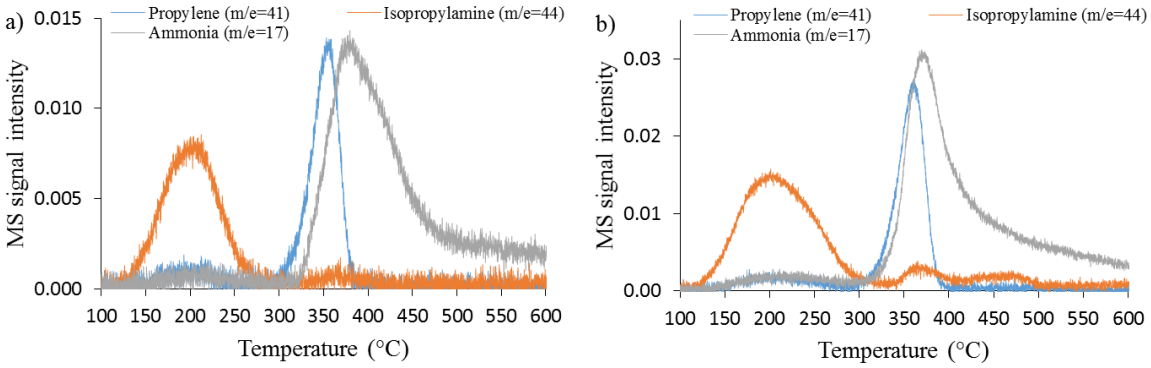

Figure S1(a,b) : IPA TPD profile of CBV8014 and CPC814C showing evolution of IPA, propylene and ammonia as a function of temperature.

1.3. Scanning electron microscopy (SEM)

SEM measurements using a Zeiss-NEON FEG-SEM instrument were done to estimate particle diameter. Catalyst sample for SEM were prepared by placing a small amount of the zeolite aqueous suspension on carbon tape and dried for one hour. Particle diameter of the catalyst was estimated based on the SEM images shown in Figure S2. The reported value for the diameter of the crystal was based on measurements of 20 different crystals using ImageJ software. Varying crystal size was observed for CBV8014 ranging from 100-500nm which is believed to be due to agglomeration.

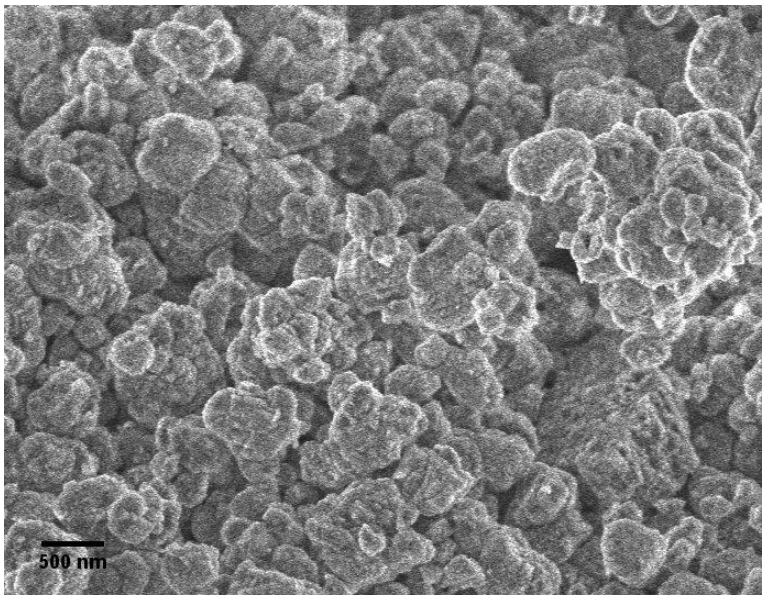

Figure S2: SEM image of CBV 8014 to estimate the crystal size of the catalyst.

1.4. X-Ray Diffraction (XRD)

XRD study of CBV8014 for crystallinity was done using Rigaku automatic diffractor (Model D-MAX A) equipped with a curved crystal monochromator. Sample spread evenly on a plastic slide was analyzed with Cu Kα as radiation source and was operated at 40kV and 35mA between the angle range of 5-55°. Figure S3 shows the zeolite to be MFI.

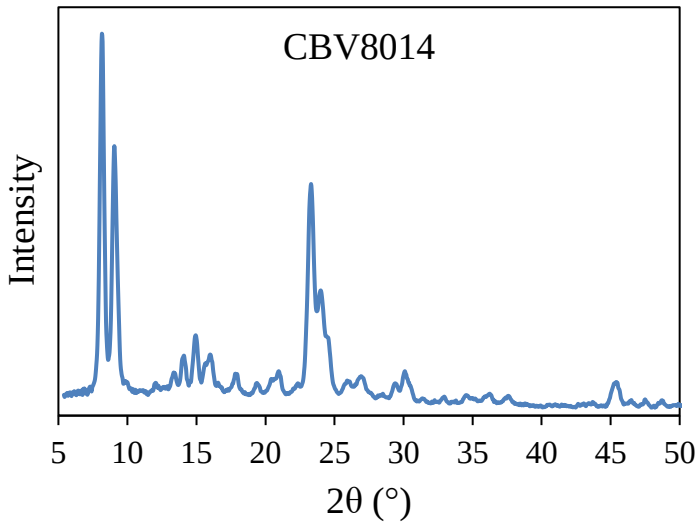

Figure S3: XRD data for CBV8014 showing the sample is perfectly crystalline MFI zeolite.

1.5. Role of water

Effect of water on the reaction rate was tested at 250 °C. Partial pressure of water was changed keeping all other parameters like catalyst (0.0198 mmoles), carrier gas flowrate (125 ml/min), feed rate of acetic acid (0.00437 moles/hr) and methyl furan (0.00113 moles/hr) constant. Figure S4 shows the turnover frequency for different acetic acid to water mole ratios.

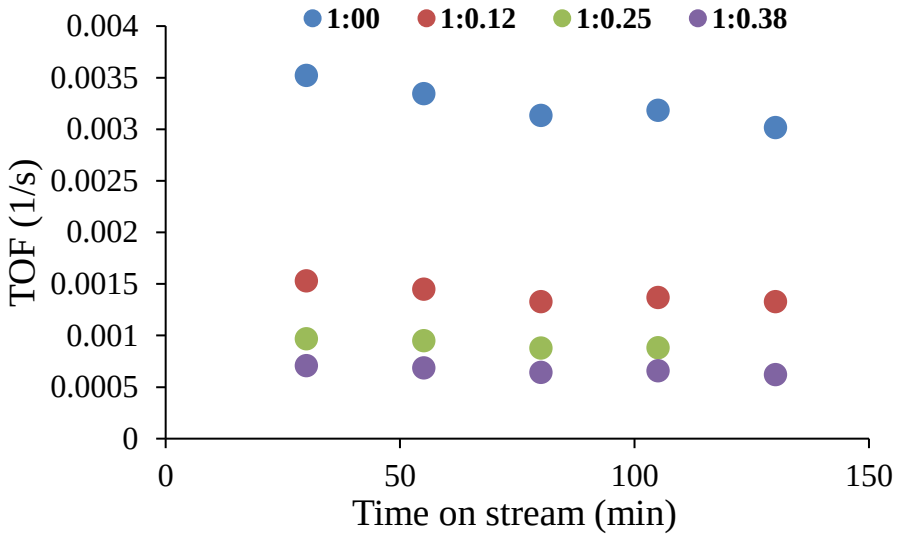

Figure S4: Comparing TOF with increasing water co feeding at a reaction temperature of 250 °C. Legend in the figure is mole ratio of acetic acid to water. The catalyst moles used for this study was 0.0198 mmoles with reactants fed at a rate of acetic acid= 0.00437 moles/hr, methyl furan=0.00113 moles/hr under the helium flow of 125 ml/min.

1.6. Effect of partial pressure of methylfuran

Role of methyl furan partial pressure for deactivation was tested at 250 °C. Partial pressure of methylfuran was changed keeping catalyst (0.0198 mmoles), molar flowrate of acetic acid (0.00437 moles/hr) and helium flowrate (125ml/min) constant. Figure S5 shows the turnover frequency for different acetic acid to methylfuran mole ratios. With increase in partial pressure of methylfuran deactivation rate increased as it promotes polymerization and coking.

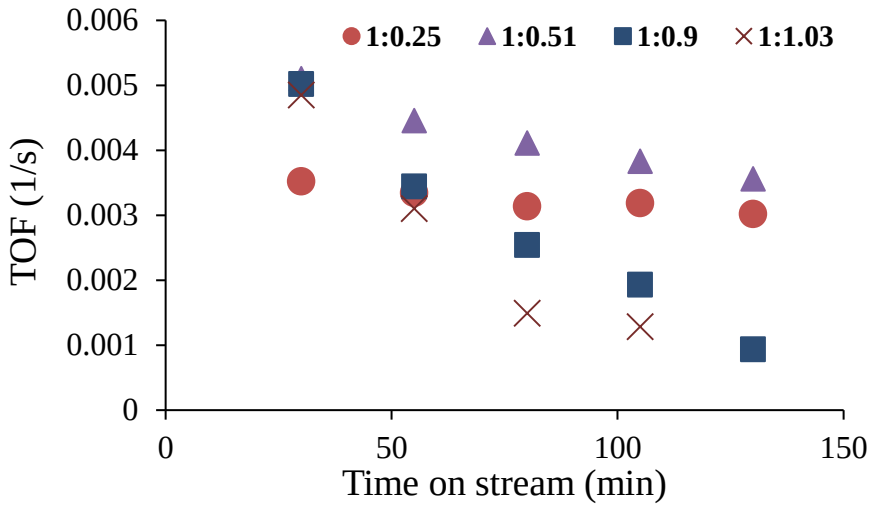

Figure S5: Comparing TOF with increasing partial pressure of methylfuran at a reaction temperature of 250 °C. Legend in the figure is mole ratio of acetic acid to methylfuran. The catalyst used for this study was 0.0198 mmoles with feed rate of acetic acid= 0.00437 moles/hr under the helium flow of 125 ml/min.

1.7. Diffusion Limitations

Internal diffusion limitations were tested by exchanging a fraction of acid sites in CBV8014 with sodium as per procedure reported in literature (45). After exchange the acid site density measured with IPA-TPD reduced to 0.295 mmoles/g in comparison to 0.396 mmoles/g before exchange. Figure S6 shows a drop in the rate corresponding to the reduction in acid site density, yielding a constant TOF of 0.0035(1/s) for each catalyst, suggesting no internal diffusion limitations.

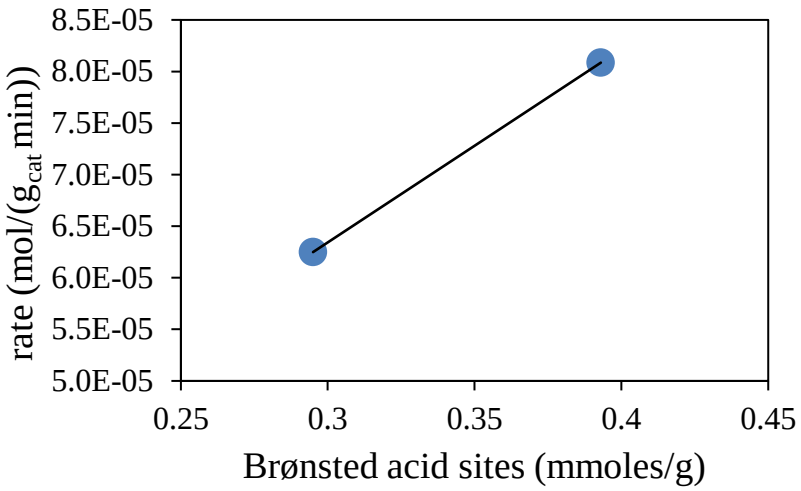

Figure S6: Comparing rate of acylation between CBV80114 and Na exchanged CBV8014 to test internal diffusion limitations. The catalyst weight used for this study was 50mg with reactants fed at a rate of acetic acid= 0.00437 moles/hr, methyl furan=0.00113 moles/hr under the helium flow of 125 ml/min.

1.8. DFT calculations

The plane-averaged electron density difference along the [010] direction, which is correspondingly the b (or y) axes of ZSM5, has been calculated as follows:

$$Dr(xz) = \frac{\sum_{0}^{y} Dr(x,y,z)}{\text{Number of grid points along y}}$$

where Δρ is calculated by Δρ = ρ(total)- ρ(zeolite)- ρ(molecule). The molecule is the desorbed acyl or acyl + methylfuran (see text).

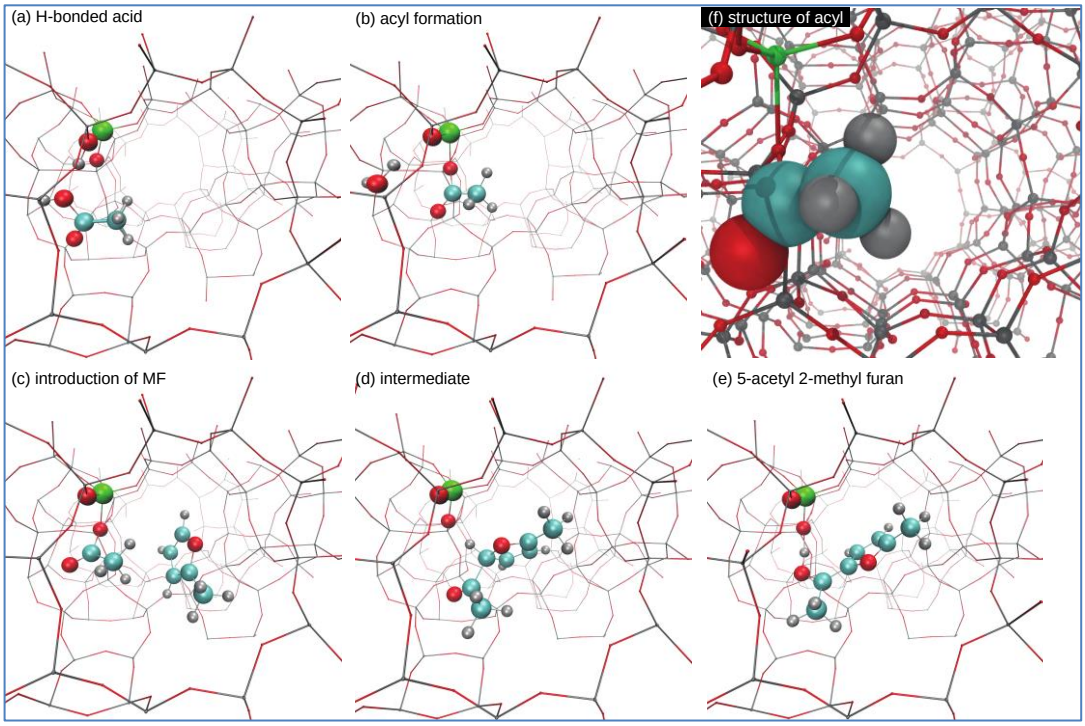

Figure S7. The optimized structures from DFT calculations. (a-e) These structures correspond to the schematic figures showing in Figure 3. (f) ball and stick figure to show the structure of the surface acyl species. The C, O, H, Si, and Al atoms colored cyan, red, grey, black and green, respectively.

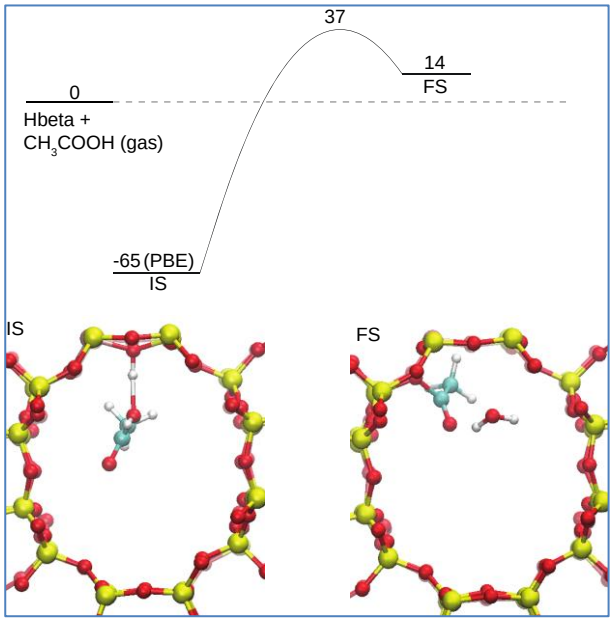

Figure S8. DFT calculations of acyl formation from acetic acid in Hbeta. The initial structure (H-bonded acetic acid) and final structure (surface acyl with a water molecule) are also shown.

1.9. Activation barrier for acetic acid self coupling

By operating in the kinetically limited regime, the apparent activation energy for acetic acid ketonization over CBV8014 was estimated using an Arrhenius plot. Reaction rate constants were estimated for this reaction between the temperature range 270-310°C keeping all the other parameters constant. Using the Arrhenius equation, the activation energy was estimated plotting natural log of k against 1/RT. As shown in **Figure S9**, the obtained apparent activation energy is 67 kJ/mole. This is comparable to the apparent activation energy reported by Martens *et al.* (46) of 73 kJ/mole for butyric acid ketonization over H-T zeolite.

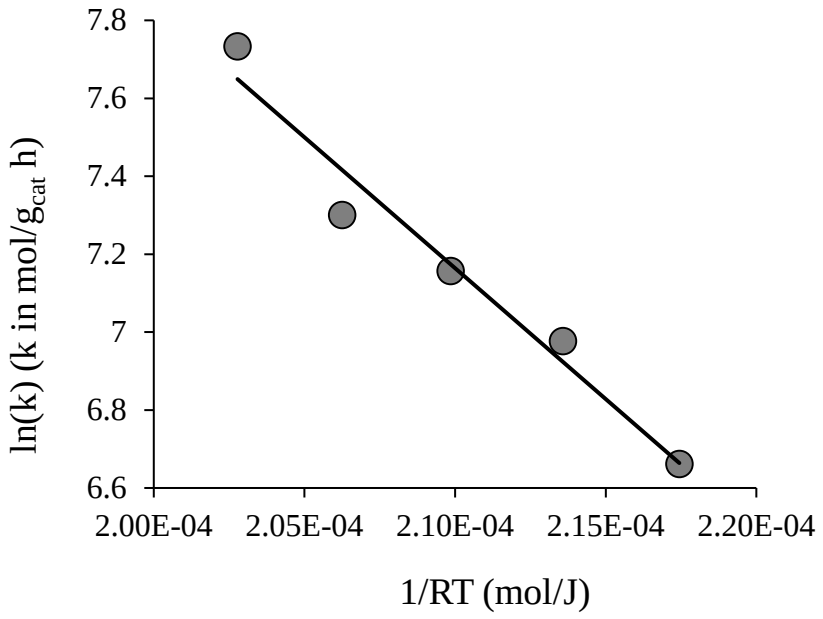

Figure S9. Apparent activation energy of acetic acid ketonization over CBV8014 estimated for a temperature range of 270-310 °C. Acetic acid partial pressure was maintained at 10.67 Torr. Rates at each temperature were taken at a W/F of 0.09 h at 30 min TOS.

1.10. Activity as a function of catalyst weight

Catalyst activity was tested using different catalyst weights at a reaction temperature of 250 °C. The ratio and partial pressure of acetic acid and 2-methyl furan were kept constant for this study. Figure S10 shows the conversion of 2-methyl furan almost doubled when doubling the catalyst amount indicating this reaction can be performed at higher conversions. It is important to mention that there was no change in the product selectivities at higher conversion.

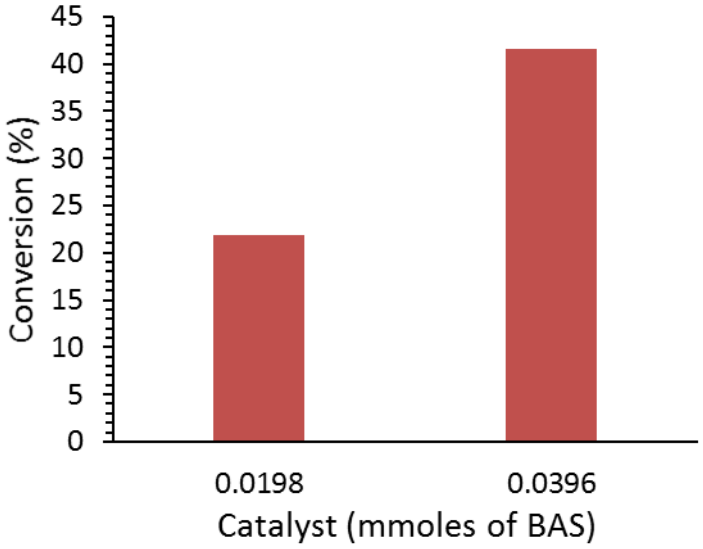

Figure S10: Comparing the conversion of 2-methyl furan at using different catalyst amounts. A constant feed rate of acetic acid= 0.00437 moles/hr, methyl furan=0.00113 moles/hr in helium flow of 125 ml/min was used in both the reactions. The conversions reported here are at 30min time on stream.

1.11. Calculations

Below table presents further details of the calculation regarding the data reported in the paper. Column-1 in the table indicated the reaction temperature in °C. Number of moles of Brønsted acid sites used in the reaction are presented in column-2 which is a product of catalyst weight used in the reaction and Brønsted acid site density obtained from

IPA-TPD experiment reported in section 1.2. Column-3 and 4 are the moles/hr of 2-methyl furan fed to the reactor and acetyl methyl furan isomers formed respectively. Yield in column-5 is calculated as (moles of acetyl methyl furan isomers)/(moles of 2-methyl furan fed). Comparing yield with conversion in column-6 which is disappearance of 2-methyl furan we have very high carbon balances (>99%) given in column-8.

	Catalyst weight *BAS density from IPA-TPD	Methylfuran feed	Acetyl methylfuran formed	(mol Acetyl methylfuran/mol methylfuran fed) *100	Disapperance of methyl furan	Rate of formation of Acetyl methylfuran TOF (1/hr)	Carbon balance with respect to methylfuran and products
Temperature (°C)	Catalyst (moles of BAS)	Moles fed (moles/hr)	Moles formed (moles/hr)	Yield (%)	Conversion (%)		
250	1.97E-05	1.13E-03	2.43E-04	21.5	21.8	12.31	99.7
235	1.97E-05	1.13E-03	1.97E-04	17.5	18.1	10.02	99.4
220	1.97E-05	1.13E-03	1.72E-04	15.2	15.5	8.73	99.7

1.12. Analysis and product identification

Quantification of the reactant and product is done using an online GC-FID (Agilent 6890 series) connected at the outlet of the reactor. Innowax column is used in GC-FID for compound separation based on polarity. Figure S11 shows a typical spectrum for 2-methyl furan reaction with acetic acid at a conversion of 15%. After identification of the products, the peak areas from the GC-FID spectrum are quantified by manual injection of standards. To identify the compounds for any new reaction the outlet stream from the reactor is condensed in a cold trap using a solvent. The condensed mixture is analyzed using GC-MS for identification of compounds in the mixture with the help of GC-MS library. Figure S12 shows the GC-MS spectrum for 2-methyl furan acylation with acetic acid. To confirm the compound suggested by GC-MS library, commercial standard is injected into the GC-FID to match for the retention time.

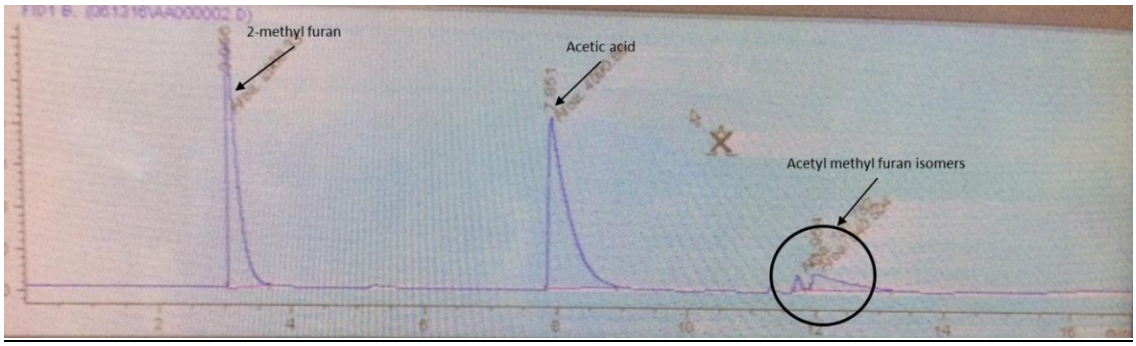

Figure S11: Online GC-FID spectrum for 2-methyl furan acylation with acetic acid at a conversion level of 15%. All the peak areas are converted to moles based on the response factors obtained from injecting standard model compounds.

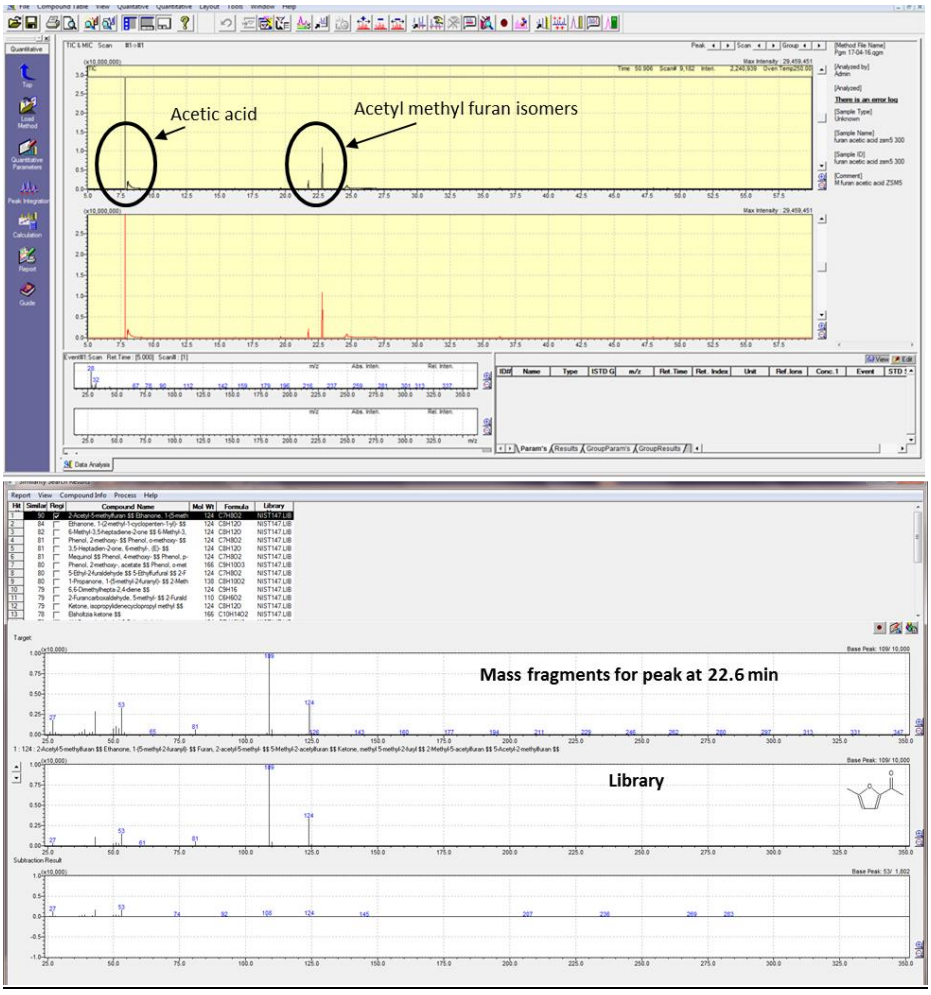

Figure S12: GC-MS spectrum to identify compounds of 2-methyl furan acylation reaction with acetic acid. The mass fragments of the peak at 22.6 min corresponds to 2-acetyl 5-methyl furan as seen with a perfect match to the library.

1.13. Product separation

All the data reported for acylation reaction we have used acetic acid to 2-methyl furan ratio of 1:0.258. Assuming 100% conversion of limiting reactant which is 2-methyl furan we form a product stream of acetic acid and acetyl methyl furan isomers in a ratio of 1:0.35. For practical application product separation from reactants plays a key role. This can be achieved either by traditional distillation process or by using a biphasic system. To demonstrate this, we prepared a model compound mixture of acetic acid and 2-aectyl 5-methyl furan in the ratios 1:0.35 similar to the ratio assuming 100% conversion of 2-methyl furan. This compound mixture was added to a biphasic system of water and decalin of equal volume. At t=0 min the concentration of acetyl methyl furan and acetic acid in water phase were 0.15 M and 0.42 M respectively. After 2hrs of stirring at t=120 min the concentration of acetyl methyl furan reduced to 0.044 M, while acetic acid remains unchanged. 71 % extraction in terms of concentration was achieved just by stirring at room temperature for 2hrs. This extraction can be further enhanced either by adding more oil phase or stirring it for longer times.

Acetic acid to 2-acetyl 5-methyl furan mole ratio	
Before extraction	1 : 0.35
After extraction	1: 0.1

Appendix-C :- Supporting information for chapter-7

S1. Powder X-ray diffraction (XRD)

Powder XRD measurements were performed to verify the crystallinity and MFI structure (orthorhombic, *Pnma* space group) of the annealed and non-annealed H-ZSM-5 samples. The resulting curves were compared to a standard XRD pattern of calcined MFI zeolite.[73] Figure S1 indicates that both samples possess an MFI framework structure and that the annealing step did not alter the crystallinity.

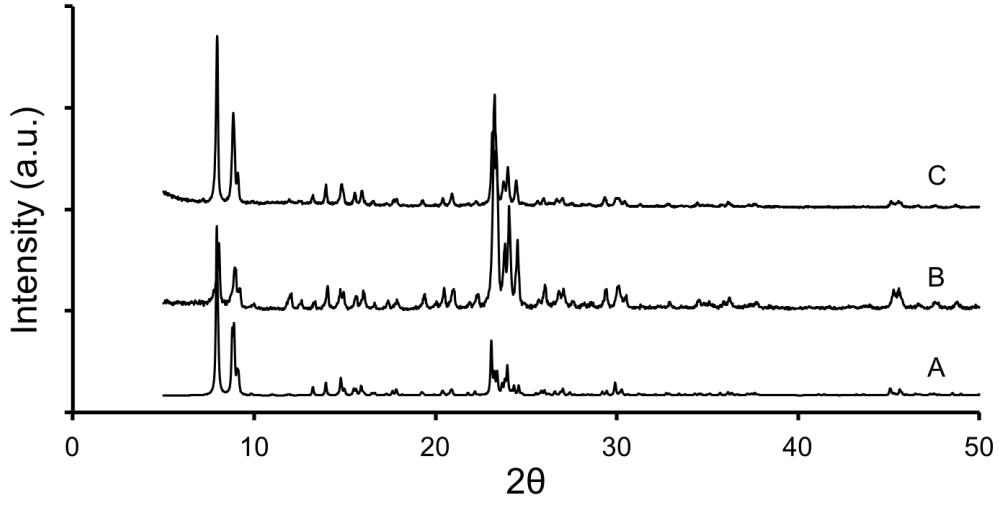

Figure S1. Powder XRD patterns of (A) reference calcined MFI zeolite [73] along with (B) the non-annealed and (C) annealed H-ZSM-5 crystals synthesized in this study. Comparison to the reference pattern reveals that both non-annealed and annealed H-ZSM-5 samples possess the MFI crystal structure.

S2. Physisorption measurements

Adsorption/desorption measurements using N_2 at 77 K were carried out to characterize the microstructure of the core and core-shell samples and inquire if the external surface passivation of ZMS-5 crystals through the silicalite-1 shell growth resulted in the blockage of access to the internal pores of ZSM-5 or not. The adsorption/desorption

isotherms are shown in Figure S2, indicating a type I pattern of microporous materials for both samples.

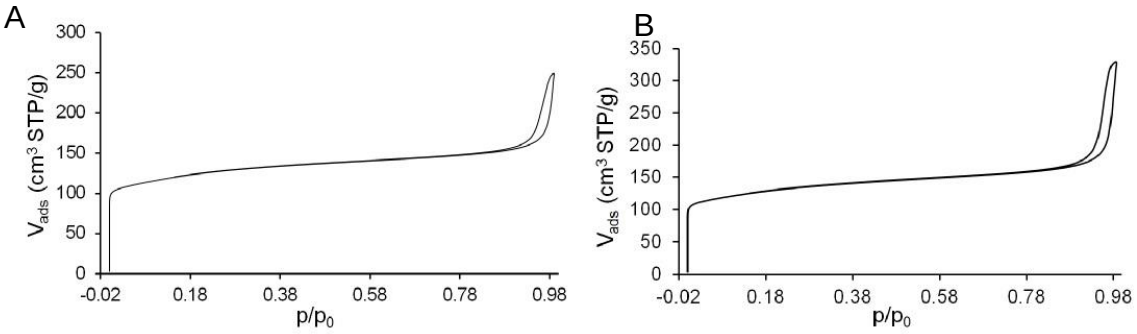

Figure S2. Nitrogen adsorption/desorption isotherms for H-ZSM-5 core (A) and core-shell (B) samples. The core-shell used for BET analysis was synthesized using a silicalite-1 growth solution with a molar composition of 20 TEOS:14 TPAOH:9500 H_2O (i.e., 10 nm shell thickness).

S3. Dynamic light scattering (DLS) studies

A representative autocorrelation function and CONTIN particle size distribution for DLS analysis of ZSM-5@silicalite-1 particles are provided in Figure S3.

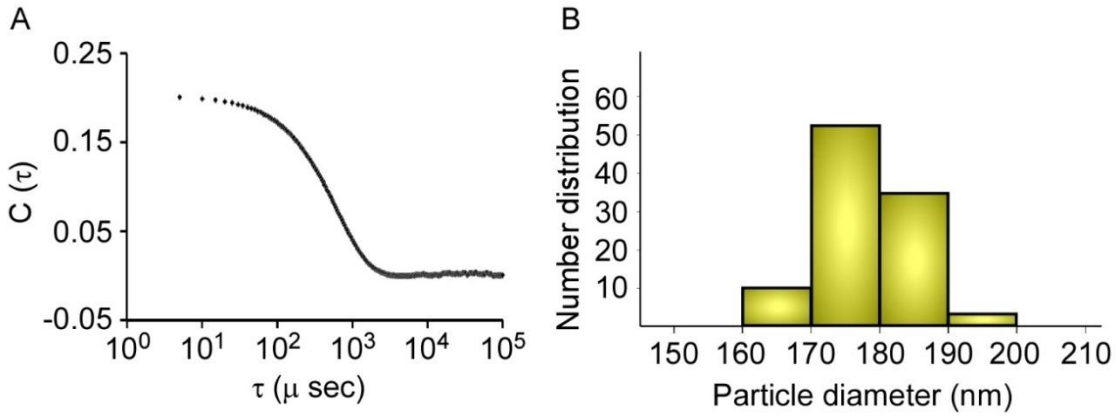

Figure S3. (A) DLS autocorrelation function of a ZSM-5@silicalite-1 sample that was prepared in a silicalite-1 growth solution with a molar composition of 14 TEOS:7 TPAOH: 9500 H_2O (heated for 6 h at 100 °C). (B) The corresponding CONTIN analysis of the autocorrelation function in (A) reveals a single particle size distribution.

S4. Di-tertbutylpyridine (DTBP) adsorption infrared (IR) spectroscopy

IR Spectra of H-ZSM-5 and H-ZSM-5@silicalite-1 catalysts were compared before and after adsorption of a bulky pyridine Di-tertbutylpyridine, the protonation of which appears at 1616 $cm.^{-1}$

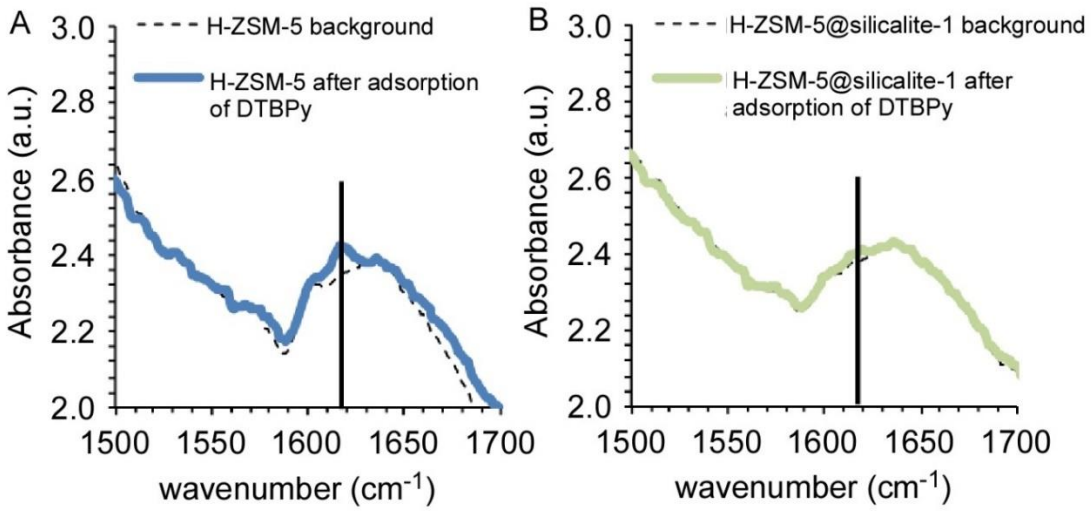

Figure S4. Di-tert-butylpyridine (DTPB) adsorption and analysis via IR for (A) H-ZSM-5 and (B) H-ZSM-5@silicalite-1 samples. Experiments were conducted on PerkinElmer Spectrum 100 FT-IR Spectrometer equipped with a Harrick Praying MantisTM chamber. For (A) H-ZSM-5 a signal at 1616 cm-1, corresponding to protonation of di-tertbutyl pyridine, is observed, whereas little to no peak in this region for the (B) H-ZSM-5@silicalite-1, indicating the absence of external Brønsted acid sites.

S5. Isopropylamine (IPA) temperature programmed desorption (TPD)

IPA TPD spectra of both H-ZSM-5 (core) and (B) H-ZSM-5@silicalite-1 samples. Brønsted sites were quantified by integrating the propylene resulting from the decomposition of IPA.

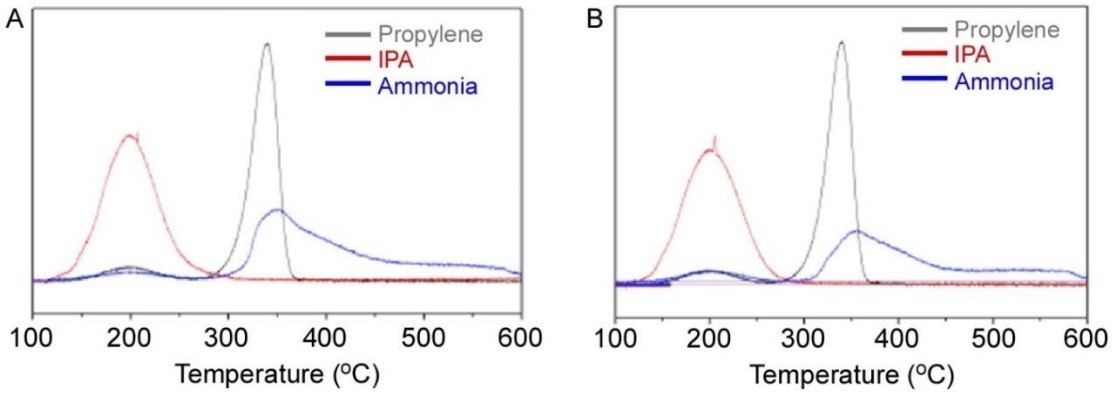

Figure S5. Isopropylamine (IPA) TPD signals resulting from (A) H-ZSM-5 (core) and (B) H-ZSM-5@silicalite-1 (core-shell) samples. The analysis of reactants and products was done using MKS Cirrus 200 quadrupole mass spectrometer (MS), tracking m/z=58, 41, 17 for IPA, propylene and ammonia respectively.

S6. X-ray photoelectron spectroscopy (XPS)

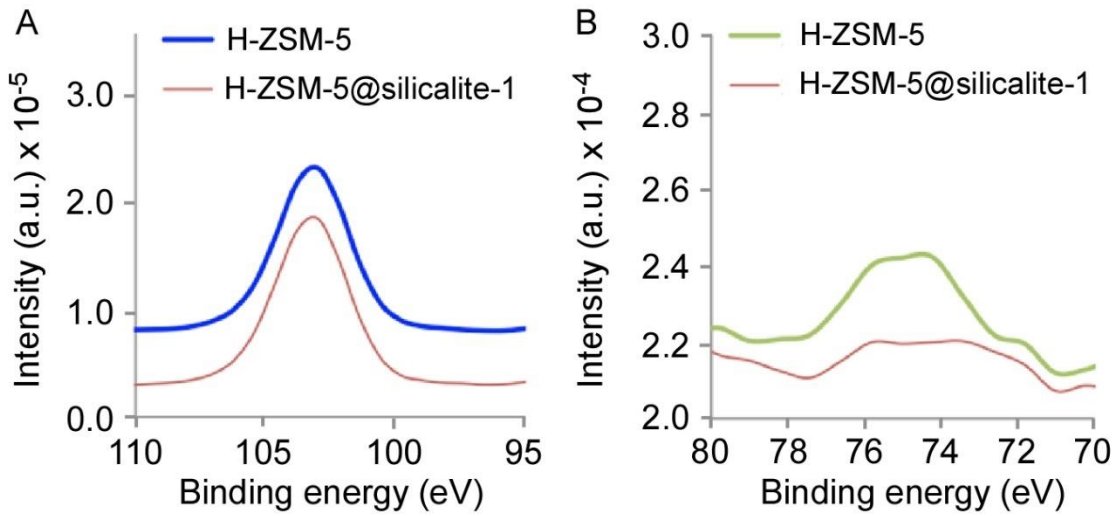

Figure S6. XPS results of (A) Si 2p and (B) Al 2p binding energy regions for H-ZSM-5 (core) and H-ZSM-5@silicalite-1 (core-shell) samples. The H-ZSM-5 samples are offset in the y-axis for clarity. All the data was collected at 45º takeoff angle and to compensate for surface charging effects, all spectra were referenced to the hydrocarbon C1s peak at 284.6 eV.

S7. ^{27}Al NMR measurements

The extra-framework Al content in H-ZSM-5 and H-ZSM-5@silicalite-1 samples was quantified by ^{27}Al NMR. As shown in Figure 4, the intensities at 60 and 0 ppm correspond to framework and extra-framework alumina, respectively. Using these intensities we calculated the percentage of extra-framework alumina (Table S1) using the following expression

$$\left(\frac{Si}{Al}\right)_{framework} = \left(\frac{Si}{Al}\right)_{total} \cdot \frac{I_{60}+I_0}{I_{60}} \quad (1)$$

where I_x are the intensities (x = 60 or 0 ppm) and $(Si/Al)_{total}$ accounts for both framework and extra-framework alumina in the zeolite. The amount of extra-framework Al reported here is lower than the amount typically reported for commercial MFI catalysts.[172, 173]

TABLE S1. Total Si/Al ratio and framework Si/Al ratio of the H-ZSM-5 and H-ZSM-5@silicalite-1 estimated from ^{27}Al NMR

	Si/Al $_{total}$ [a]	Si/Al $_{framework}$	% Extra framework Alumina
Core	44	48.5	9.1
Core-Shell	53	55.8	5.0

[a] Si/Al $_{total}$ from ICP-AES

S8. Supporting references

1. *http://www.iza-structure.org/databases/*.
2. Jones, A.J., R.T. Carr, S.I. Zones, and E. Iglesia, *Acid strength and solvation in catalysis by MFI zeolites and effects of the identity, concentration and location of framework heteroatoms*. Journal of Catalysis, 2014. **312**: p. 58-68.
3. Gounder, R. and E. Iglesia, *Catalytic Consequences of Spatial Constraints and Acid Site Location for Monomolecular Alkane Activation on Zeolites*. Journal of the American Chemical Society, 2009. **131**(5): p. 1958-1971.